

Syracuse University

SURFACE

Dissertations - ALL

SURFACE

December 2015

Shape Memory Polymers as 2D Substrates and 3D Scaffolds for the Study of Cell Mechanobiology and Tissue Engineering

Richard McClary Baker
Syracuse University

Follow this and additional works at: <https://surface.syr.edu/etd>



Part of the [Engineering Commons](#)

Recommended Citation

Baker, Richard McClary, "Shape Memory Polymers as 2D Substrates and 3D Scaffolds for the Study of Cell Mechanobiology and Tissue Engineering" (2015). *Dissertations - ALL*. 378.

<https://surface.syr.edu/etd/378>

This Dissertation is brought to you for free and open access by the SURFACE at SURFACE. It has been accepted for inclusion in Dissertations - ALL by an authorized administrator of SURFACE. For more information, please contact surface@syr.edu.

Shape Memory Polymers as 2D Substrates and 3D Scaffolds for the Study of Cell Mechanobiology and Tissue Engineering

Abstract

By

Richard M. Baker

Tissue engineering is a promising, fast-growing field that combines cells, signals, and scaffolds to regenerate damaged tissues. To develop new, functional, engineered tissues, it is becoming increasingly important to understand how cell-material interactions affect the cell mechanobiological response. As a result, recent efforts have focused on developing complex synthetic materials that can mimic the dynamic *in vivo* cell environment. In this work, shape memory polymers (SMPs) were employed to develop dynamic 2D substrates and 3D scaffolds that undergo programmed changes in shape under cell compatible conditions. These substrates and scaffolds were applied *in vitro* and *in vivo* to demonstrate their potential as platforms to study cell mechanobiology and as functional tissue engineered constructs.

The first part of this dissertation describes the fabrication and application of an SMP bilayer system capable of forming nano-scale wrinkles under cytocompatible conditions. Wrinkled substrates with easily tunable characteristics were employed to control the degree of cell alignment, with increased wrinkle amplitude and wrinkle orientation resulting in increased cell alignment until reaching a point of saturation. Active wrinkling with attached and viable cells was found to enable cell alignment to be “turned-on” on command. Additionally, cell migration on wrinkled substrates was assessed using quantitative, statistical-physics-based metrics which revealed cell motility atop anisotropic wrinkled substrates and which was more oriented and persistent than cell motility atop flat isotropic controls

The second part of this dissertation describes the fabrication and application of porous 3D SMPs capable of expanding under physiological temperatures. A modified porogen-leaching approach was employed to fabricate highly porous, interconnected SMP scaffolds with tunable properties. The potential of SMP foams for use as synthetic bone substitutes was demonstrated in a mouse segmental defect model, where expanding foams were deployed intraoperatively to fill and conform to a critical size defect. Stiff SMP foams were able to maintain defect stability in a load-bearing application and integrated with the native bone after 12 weeks. Furthermore, deployable SMP foams showed potential for use as deployable cell-based therapies to facilitate bone repair, as expanding foams were able to support osteogenic differentiation of attached stem cells.

This work demonstrates the potential of SMPs to be employed as dynamic materials to study cell-material interactions in dynamic environments and to aid in the development of functional tissue engineered constructs.

**SHAPE MEMORY POLYMERS AS 2D SUBSTRATES AND 3D SCAFFOLDS FOR THE
STUDY OF CELL MECHANOBIOLOGY AND TISSUE ENGINEERING**

By

RICHARD M. BAKER

B.S. Biomedical Engineering, Rose-Hulman Institute of Technology, 2009
B.S. Mechanical Engineering, Rose-Hulman Institute of Technology, 2009

DISSERTATION

Submitted in partial fulfillment of the requirements for the
degree of Doctor of Philosophy in Bioengineering
in the Graduate School of Syracuse University

December 2015

Copyright © 2015 Richard M. Baker

All Rights Reserved

In memory of my beloved grandfather, Richard E. Baker. . . I miss you

Acknowledgements

First and foremost I'd like to thank my advisors, Professors Patrick T. Mather and James H. Henderson for their patience, support, and guidance these past six years. I started my PhD studies having no prior research experience, and their mentorship has been invaluable to my growth into an independent researcher. A special thanks to Prof. Mather for encouraging creativity and promoting innovation, which have driven my passion for research. Dr. Henderson has been instrumental in my personal development, helping with goal setting and achieving those goals, for which I am very grateful. Both have been pivotal to my academic and personal growth, and their intellect and pursuit of knowledge has been an inspiration.

I would also like to thank my committee members, Prof. Jeremy L. Gilbert, Prof. Radhakrishna "Suresh" Sureshkumar, Prof. Megan E. Oest, and Prof. Mathew M. Maye for their thought-provoking comments and invaluable suggestions to my dissertation.

I have had the fortunate opportunity to collaborate with several people during my PhD studies, and I am grateful for all their help. Specifically I want to thank Dr. Pine Yang, Dr. Hossein Birjandi-Nejad, Megan Brasch, Dr. Lisa Manning, and Kevin Davis. Also, I would like to thank Dr. Megan Oest for her guidance and mentorship during our collaboration at SUNY Upstate Medical. A special thanks is reserved for Jing Wang and Ling-Fang Tseng (Team Awesome), who have been a wealth of knowledge and a pleasure to work with.

My sincere thanks goes out to all past and current members of the Henderson Lab and Mather Research Group (MRG) with whom I have had the privilege of working. I would like to acknowledge all of the undergraduate and graduate mentees I have the pleasure of working with: Yong Chen, Dakota Jones, Sanjay Dialani, Ashkan Noushabadi, and Xinchu Yi. Also, I am grateful for all the behind the scenes hard work and support from the administrative staff at Syracuse University, especially Karen Low, Lynore De La Rosa, and Dawn Long.

Last but certainly not least none of this would have been possible without the love, support, and encouragement of my family, my friends, and my confidant. Thank you to my

parents, Stephanie and Robert, for your endless love and support; a huge thank you to my grandmother, Jayna, who has been a huge emotional and spiritual supporter; to my siblings Robert, Nicholas, Brittany, and Brandon, thank you for your encouragement and keeping me sane; and to my confidant, Erika, thank you for your love, support, motivation, and patience throughout my doctoral studies.

Table of Contents

List of Tables	xv
List of Schemes	xviii
List of Figures.....	xxiii
Chapter One: Introduction	1
1.1 Tissue Engineering and Cell Mechanobiology: Bridging the Gap	1
1.2 Cell-Material Interactions	1
1.2.1 Surface Chemistry Affects Cell Behavior.....	2
1.2.2 Topography Affects Cell Behavior	3
1.2.3 Elasticity Affects Cell Behavior	5
1.3 Dynamic Microenvironment During Development and Disease Progression.....	6
1.3.1 ECM Dynamics During Development.....	7
1.3.2 ECM Dynamics During Disease Progression	7
1.4 Shape Memory Polymers	8
1.4.1 Overview of SMPs.....	8
1.4.1.1 Surface Shape Memory	10
1.4.1.2 Two-Way Shape Memory Polymers.....	10
1.4.1.3 Multi-Shape Memory Polymers.....	11
1.4.2 Applications of SMPs	12
1.5 Active Cell Culture	13
1.5.1 Cell-Material Interactions in Dynamic Environments	13
1.5.2 Shape Memory Polymers as Active Cell Culture Substrates	15
1.5.3 Current Challenges with Active Cell Culture Materials	16
1.6 Scope of Dissertation	17
1.7 References	18
Chapter Two: Shape Memory Induced Wrinkle Formation Directs Cell Alignment In Vitro.....	32
2.1 Synopsis	32
2.2 Introduction.....	32
2.3 Methods and Materials.....	35

2.3.1 Materials	35
2.3.2 Substrate Preparation	35
2.3.3 Substrate Characterization	36
2.3.3.1 Thermal Characterization.....	36
2.3.3.2 Thermomechanical Characterization	37
2.3.3.3 Hydrated Recovery at 37 °C	38
2.3.4 Wrinkle Formation.....	39
2.3.4.1 Wrinkle Formation in Dry State	39
2.3.4.2 Wrinkle Formation in Hydrated State.....	39
2.3.5 Wrinkle Characterization	40
2.3.6 Cell Culture.....	40
2.3.6.1 Cell Culture on Previously Wrinkled Substrates	41
2.3.6.2 Cell Culture on Actively Wrinkling Substrates	41
2.3.7 Cell Staining and Imaging	42
2.3.8 Determining Cell Alignment.....	43
2.3.8.1 Cell Nuclear Alignment Determination	43
2.3.8.2 Cell Cytoskeleton Alignment Determination.....	44
2.3.9 Statistics	44
2.4 Results.....	45
2.4.1 Substrate Material Properties	45
2.4.1.1 Tuning the Glass Transition Temperature (T_g).....	45
2.4.1.2 Thermomechanical Properties	45
2.4.2 Strain Effect on Wrinkle-Crack Properties	46
2.4.3 Cell Culture on Previously Wrinkled Substrates	47
2.4.4 Wrinkle Formation in Simulated Cell-Culture Conditions.....	49
2.4.5 Cell Culture on Actively Wrinkling Substrates	49
2.4.6 Comparing Cell Nuclear and Cell Cytoskeleton Alignment.....	50
2.5 Discussion	51
2.6 Conclusion	56
2.7 Acknowledgements.....	56
2.8 References.....	56

Chapter Three: Effect of Surface Topography and Surface Chemistry on Cell Motility <i>In Vitro</i>	84
3.1 Synopsis	84
3.2 Introduction	84
3.3 Methods and Materials	87
3.3.1 Overview of the Cell Tracking Algorithm (ACTIVE)	87
3.3.2 Substrate Preparation	88
3.3.2.1 Gold-Coated Wrinkled Substrate Preparation	88
3.3.2.2 Gold-Coated Flat Substrate	88
3.3.2.3 TCPS Substrate	89
3.3.3 Cell Culture	89
3.3.4 Nuclear Staining and Imaging	90
3.3.5 Quantification of Cell Motility	90
3.3.5.1 Mean Squared Displacement (MSD)	90
3.3.5.2 Velocity Autocorrelation	91
3.3.5.3 Cell Track Asphericity	92
3.3.6 Assessing Division Directionality	93
3.3.7 Statistics	94
3.3.7.1 Statistics for Effect of Density on Cell Motility Parameters	94
3.3.7.2 Statistics for Effect of Substrate on Cell Motility Parameters	94
3.3.7.3 Statistics for Cell Division Directionality	94
3.4 Results	95
3.4.1 ACTIVE Tracking	95
3.4.2 Cell Trajectory Analysis	96
3.4.3 Cell Motility Analysis	96
3.4.3.1 Mean Squared Displacement (MSD)	96
3.4.3.2 Velocity Autocorrelation	97
3.4.3.3 Cell Diffusion and Track Asphericity	98
3.4.3.4 Motility Parameters and Effect of Cell Density	99
3.4.4 Division Angle Analysis	99
3.5 Discussion	100

3.6 Conclusion	104
3.7 Acknowledgements.....	104
3.8 References.....	104
Chapter Four: Shape Memory Poly(ϵ-caprolactone)-co-Poly(ethylene glycol) Foams with Body Temperature Actuation.....	128
4.1 Synopsis	128
4.2 Introduction.....	128
4.3 Methods and Materials.....	131
4.3.1 Materials	131
4.3.1.1 PCL Macromer Functionalization.....	131
4.3.1.2 PEG Macromer Functionalization	131
4.3.2 Scaffold Preparation.....	132
4.3.2.1 Salt Fusion	132
4.3.2.2 Scaffold Fabrication.....	133
4.3.2.3 Example Formulation.....	133
4.3.3 Thermal Characterization.....	134
4.3.3.1 Thermogravimetric Analysis	134
4.3.3.2 Differential Scanning Calorimetry.....	134
4.3.4 Thermomechanical Characterization	135
4.3.4.1 One-Way Shape Memory	135
4.3.4.2 Two-Way Shape Memory.....	135
4.3.4.3 Varying Deformation Temperature to Control Recovery	136
4.3.5 Architecture Characterization	137
4.3.5.1 Scanning Electron Microscopy (SEM)	137
4.3.5.2 Microcomputed Tomography (μ CT)	138
4.4 Results.....	138
4.4.1 Scaffold Fabrication.....	138
4.4.2 Scaffold Architecture	139
4.4.3 Controlling Melt Transition Temperature Through Chemical Composition.....	139
4.4.4 One-Way Shape Memory Behavior.....	140

4.4.5 Controlling Shape Recovery Temperature Through Deformation Temperature.....	141
4.4.6 Two-Way Shape Memory Behavior	143
4.5 Discussion	143
4.6 Conclusion	148
4.7 References.....	148
Chapter Five: Shape Memory Scaffolds for Treating Critical Size Defects.	174
5.1 Synopsis	174
5.2 Introduction.....	174
5.3 Methods and Materials.....	177
5.3.1 Materials	177
5.3.2 Scaffold Fabrication.....	177
5.3.2.1 Semi-crystalline SMP Foams.....	178
5.3.2.2 Amorphous SMP Foams	178
5.3.3 Thermal Characterization.....	179
5.3.4 Thermomechanical Characterization	180
5.3.5 Scanning Electron Microscopy	181
5.3.6 Preparing Foams for <i>In Vivo</i> Testing	181
5.3.7 Scaffold Sterilization	182
5.3.8 Surgical Procedure	183
5.3.9 X-ray Radiography.....	184
5.3.10 Histology.....	184
5.3.11 Microtomography	184
5.3.12 Torsional Testing and Analysis	185
5.3.13 Statistics	186
5.4 Results.....	186
5.4.1 Scaffold Characterization.....	186
5.4.1.1 Semi-crystalline SMP Foams (80PCL-20PEG-20HA).186	
5.4.1.2 Amorphous SMP Foams (92tBA-8BA).....	188
5.4.2 Defect Stability and Graft Integration.....	189
5.4.3 Histology.....	190
5.4.4 Torsional Testing and Analysis	191
5.5 Discussion	192

5.6 Conclusion	195
5.7 Acknowledgements.....	196
5.8 References.....	196
Chapter Six: Osteogenic Differentiation in Expanding Shape Memory	
Scaffolds.....	222
6.1 Synopsis	222
6.2 Introduction.....	222
6.3 Methods and Materials.....	225
6.3.1 Materials	225
6.3.2 Scaffold Preparation.....	225
6.3.3 Scaffold Characterization.....	226
6.3.4 Scaffold Sterilization	227
6.3.5 Cell Culture.....	227
6.3.5.1 Cell Expansion.....	227
6.3.5.2 Cell Seeding In Foams	228
6.3.6 Assessing Calcium Deposition	229
6.3.6.1 Xylenol Orange Staining.....	229
6.3.6.2 Scanning Electron Microscopy	229
6.3.6.3 Microcomputed Tomography	230
6.3.7 Alkaline Phosphatase Activity.....	230
6.3.8 Real-Time Polymerase Chain Reaction (qPCR).....	231
6.3.8.1 Total RNA Extraction and cDNA Analysis.....	231
6.3.8.2 Determining Best Housekeeper Gene for qPCR.....	232
6.3.8.3 qPCR Procedure.....	232
6.3.9 Histology.....	233
6.3.10 Statistics	233
6.4 Results.....	233
6.4.1 Scaffold Architecture Reorganization.....	233
6.4.2 Cell Seeding in Programmed Scaffolds	234
6.4.3 Mineral Formation	235
6.4.3.1 Xylenol Orange (XO) Analysis	235
6.4.3.2 Scanning Electron Microscopy (SEM) Analysis	236
6.4.3.3 Microcomputed Tomography Analysis	236

6.4.4 Protein Expression	237
6.4.5 Gene Expression	238
6.4.6 Histology.....	238
6.5 Discussion	239
6.6 Conclusion	243
6.7 References.....	244
Chapter Seven: Conclusions and Future Directions.....	265
7.1 Overall Conclusion	265
7.2 Recommendations for Future Work.....	268
7.2.1 Shape Memory 2D Substrates for Active Cell Culture.....	268
7.2.2 Cell Tracking in Dynamic Environments	270
7.2.3 SMP Scaffolds for Bone Tissue Engineering	271
7.2.4 SMP Scaffolds as Deployable Cell-Based Therapy.....	272
7.2.5 SMP Scaffolds as 3D Active Cell Culture Scaffolds.....	273
7.2.6 Shape Memory Assisted Cell Seeding (SMACS).....	273
7.3 References.....	274
Appendix One: MATLAB Analysis for Wrinkle Amplitude and Cell Nuclear Alignment	276
A1.1 MATLAB Algorithm for Wrinkle Amplitude Analysis	276
A1.2 MATLAB Algorithm for Calculating Nuclear Angle Spread	280
Appendix Two: ACTIVE Tracking User's Manual	283
Appendix Three: MATLAB Analysis for Biomechanical Torsion Testing of Femurs	296
Appendix Four: Functionalized Hydroxyapatite.....	302
Appendix Five: Biodegradable Amorphous SMP Foams	308
Appendix Six: Shape Memory Assisted Cell Seeding (SMACS)	317
VITA.....	333

List of Tables

Table 2-1. Comparing cell nuclear angular spread to cell cytoskeletal angular spread. Values for the average nuclear spread are comparable to values obtained from the cytoskeletal spread for all time points. Prior to triggering wrinkle formation (30 °C 5 h) cell nuclear and cytoskeletal alignment is random, as noted by the large spread values (52 ° being completely random). Upon wrinkle formation, cell nuclei and cytoskeleton become highly oriented as shown by the low angular spreads. Averages were calculated from 6 samples for the before and after wrinkling groups, and 5 samples for the control group.	82
Table 3-1. Average number of cells identified by <i>ACTIVE</i> for various frames at each density and substrate type.....	114
Table 3-2. Average slopes and mobility parameters are reported for the non-decomposed and decomposed MSD profiles. Standard deviations are in parentheses. For substrates, wrinkled = W, non-wrinkled = NW, and tissue culture polystyrene = TCPS. For a given metric (column), statistical comparisons were made between substrate type (W vs. NW vs. TCPS). For each metric, substrates sharing a label are statistically different. Substrates that do not share a label are not statistically different.....	119
Table 3-3. Velocity auto-correlation and track asphericity for different substrates. Average track asphericity and the decay constants fit to the velocity autocorrelation function, where x is the direction parallel to the wrinkles for the wrinkled substrate, are reported. Standard deviations are in parentheses. For a given metric (column), statistical comparisons were made between substrate type (W vs. NW vs. TCPS). For each metric, substrates sharing a label are statistically different. Substrates that do not share a label are not statistically different.	121

Table 3-4. Angular spread of division angles atop anisotropic and isotropic substrates. Average angular spread for the wrinkled substrate is lower than the non-wrinkled and TCPS substrates, indicative of more directed division atop the wrinkled topography.	127
Table 4-1. Summary of fixing (R_f) and recovery (R_r) ratios for 80PCL-20PEG foams deformed at different temperatures. All samples show excellent recovery, but fixing ratios decrease as deformation temperature decreases. R_f and R_r were calculated according to equations Eq 2-4 and Eq 2-5 , respectively, discussed in Chapter 2	170
Table 5-1. Summary of torsional mechanical properties for limbs treated with an SMP graft (92tBA-8BA) or an allograft control, and a contralateral intact control. The SMP graft exhibited a trend of lower torsional mechanical properties compared to the allograft group, although not statistically significant. Mechanical properties of both treatment groups were significantly lower than the contralateral intact control.	221
Table 6-1. Mineral fractions (V_{100}/V_{40}) of <i>active</i> and <i>static</i> foam scaffolds over time. Three replicates for (top) active and (bottom) static scaffolds reveal that average mineral fractions for replicates 2 and 3 are consistent and increasing over time, while the mineral fraction for replicate 1 is high at the early time point and decreases at the later time points. This inconsistency for replicate 1 is attributed to inconsistent initial cell seeding density. No significant difference was found between <i>active</i> and <i>static</i> groups.	260
Table A6-1. Sample groups used for each salt fusion template for cell culture. A total of 7 groups were used for each salt fusion condition investigated (6%, 10%, 15% water), for a final total of 21 groups for the cell experiments.	326

Table A6-2. Composition effect on Dry and Wet Tg. A range of Tgs were achieved from 45.1 °C to 26.3 °C in the dry state, and a range of 38.3 °C to 20.3 °C in the wet state.	329
--	-----

List of Schemes

- Scheme 2-1.** Chemical structure of synthesized substrate; tert-butyl acrylate (tBA) and butyl acrylate (BA) monomers are crosslinked with tetraethylene glycol dimethacrylate (TEGDMA) and photo-polymerized using DMPA as a photoinitiator.....63
- Scheme 2-2.** Using an SMP bilayer system to form nano-scale wrinkles. A uniaxial tensile strain is fixed in the SMP substrate by heating, deforming, and subsequently cooling. Following fixing, a thin film of gold is deposited on the surface of the SMP substrate. Upon heating the substrate recovers and induces surface buckling into the gold film.....64
- Scheme 2-3.** Process for determining cell body and nuclear orientation. Fluorescent micrographs of the cell body (actin cytoskeleton) and cell nucleus were manually traced using ImageJ software. Traced cell bodies and nuclei were then thresholded and fitted with an ellipse. The angle of the major axis of the fit ellipse was used to describe cell orientation.65

Scheme 3-1. Overview of ACTIVE tracking algorithm. The tracking algorithm accomplishes 4 main tasks: segmentation, linking, post-processing, and analysis. (a-b) Cells are stained with Hoechst 33342 dye and imaged for 24 h. (c) Images are initially processed using a bandpass filter and (d) contour profiles are established based on nuclear intensity fluctuations. (e) For single peak contours, cells are fit with a representative ellipse, while multi-peak instances are tagged as two separate ellipses for division and merging event cases. (f-i) Cell identification tags (IDs) are established and (f-ii) IDs are linked between consecutive frames. (g-i) Post-tracking, interaction events are identified, (ii) processed using a customized cost function and (iii) cell track information is updated for more complete and accurate complex interaction event analysis. To characterize the diffusivity and velocity dynamics of cell behavior, cell motility behavior is then quantified using (h) MSD (I and II for x and y data, respectively), (i) velocity-autocorrelation analyses (I and II for x and y data, respectively), (j) diffusion plots of cell tracks in which the final position for each cell was plotted after the starting location was renormalized to the plot origin and (k) final cell locations rotated by the principal axis of the gyration tensor.....	113
Scheme 4-1. PCL functionalization through end-capping with acryloyl chloride.	154
Scheme 4-2. PEG functionalization through end-capping with allyl isocyanate.	155
Scheme 4-3. SMP network formation using photo-initiated addition reactions between oligomeric macromers and the shown tetrathiol.	156

Scheme 4-4. Fabricating foams using a modified porogen-leaching technique. (a)(i) Salt particles with the desired diameter are sieved and added to a 20 mL glass vial; (ii)salt particles are fused in a humidity chamber for 24 h; (iii) a prepolymer solution consisting of PCL, PEG, tetrathiol crosslinker, and DMPA photoinitiator are added to the salt template; (iv) the solution is UV cured for 2 h; (v) foams are removed from the glass vials, surface skins are cut off, and salt is extracted by soaking in water for 48 h; (vi) upon first heating, densification occurs. (b) A picture of a foam following salt extraction.157

Scheme 5-1. Concept of deployable scaffolds for treatment of critical size defects. (i) An SMP scaffold could be radially compressed and fixed into a shape smaller than the defect site; (b) the SMP could then be delivered to the defect site where it remains in its stable temporary shape; (c) upon heating, the SMP would recover and expand to fill the defect. Adopted with permission from ref [19].202

Scheme 5-2. Preparation of tBA/BA scaffolds coated with polydopamine. (a) A modified porogen-leaching technique is employed where (i) salt particles with the desired diameter are sieved and added to a 20 mL glass vial; (ii) salt particles are fused in a humidity chamber for 24 h; (iii) a comonomer solution consisting of tBA, BA, TEGDMA crosslinker, and DMPA photoinitiator are added to the salt template; (iv) the solution is UV cured for 2 h; (v) foams are removed from the glass vials, surface skins are cut off, and salt is extracted by soaking in water for 48 h. (b) Time progression images of polydopamine coating show a darkening of the polydopamine solution, indicating successful coating; (c) prior to polydopamine coating, tBA/BA scaffolds are white. After coating and drying, scaffolds turn dark brown/grey.203

Scheme 5-3. Sterilization setup using NOx. (a) Schematic and (b) picture of the NO sterilization setup. Programmed SMP foams are placed in Tyvek pouches and sealed in the sample chamber. NO gas is injected into the sample chamber through the NO inlet. After 1 h, 120 mL of humid air is injected into the sample chamber. After 18 h, sample pouches are removed and aerated.....204

Scheme 5-4. Surgical procedure for implanting deployable SMP scaffolds. (i) femur is exposed and (ii) a 25 G needle is inserted into the medullary cavity; (iii) a 4 mm segmental defect is cut into mid-diaphysis; (iv) programmed foams are inserted on the intramedullary nail and 50 μ L of bone cement (brown circle) injected into the proximal end of the femur; (v) the intramedullary nail is inserted in the proximal end of the femur; (vi) SMP foam expansion is triggered by irrigating with 45 °C saline. Following expansion, foams are irrigated with room temperature saline to cool foams below their glass transition temperature; (vii) the intramedullary nail is cut and the bent between the distal condyles.....205

Scheme A4-1. Hydroxyapatite nanoparticles (HAp) are functionalized with a reactive vinyl group following a 3-step process. First unmodified HAp is grafted with hexamethylene diisocyanate with dibutyltin dilaurate as the catalyst. Next ethylene glycol is added to the reaction flask and grafted to the free isocyanate group on the modified HAp. Finally allyl isocyanate is reacted with the hydroxyl groups of the grafted ethylene glycol to add a vinyl terminated end group to the HAp. Detailed reaction processes for steps 1 and 2 are shown in **Scheme A4-2a**, and a detailed reaction process for step 3 is shown in **Scheme A4-2b**.305

Scheme A4-1. Reaction protocol for (a) grafting ethylene glycol (EG) to HAp to form HAp-EG and (b) end-capping allyl isocyanate to the HAp-EG particles for form functionalized HAp-EG-DA. For (a) HAp particles are reacted with hexamethylene diisocyanate, using dibutyltin dilaurate as a catalyst, for 8 h at 50 °C in DMF; next ethylene glycol is added to the reaction flask and the reaction carried out at 60 °C for 12 h; finally the HAp-EG particles were centrifuged and washed 3 times with DCM. For (b) the HAp-EG particles were reacted with allyl isocyanate, using dibutyltin dilaurate as the catalyst, at 90 °C for 4 h, followed by centrifugation and washing with DCM 3 times, and finally drying.306

Scheme A5-1. Thiol-ene mediated crosslinking of PDLLA macromers. (a) PDLLA diol is fabricated using ring opening polymerization of D,L Lactide initiated by 1,4 butanediol; (b) the PDLLA diol is functionalized by end-capping with allyl isocyanate to fabricate a PDLLA diallyl acrylamide; (c) The PDLLA diallyl acrylamide is crosslinked via thiol-ene mediation.313

Scheme A5-2. Chemical structure of the PDLLA thermoplastic polyurethane (TPU). PDLLA diol (polyol) was reacted with hexamethylene diisocyanate (HDI) and polyhedral oligomeric silsesquioxane (POSS) under typical urethane polymerization conditions. Reprinted with permission from ref [3].314

List of Figures

- Figure 1-1.** One-way shape memory behavior. (a) Schematic depicting a one-way shape memory cycle. Starting at the (*) above the sample's thermal transition temperature, the sample is (i) deformed, (ii) cooled to fix the temporary strain, (iii) unloaded to observe fixing, and (iv) heated to trigger recovery; (b) a corresponding one-way shape memory cycle of crosslinked poly(cyclooctene), with (i-iv) corresponding to the schematic in (a). Figure in (b) is adopted with permission from ref [48].....29
- Figure 1-2.** Two-way shape memory behavior. (a) The one-way shape memory cycle of poly(cyclooctene) shows a stretch-induced crystallization upon cooling (blue arrow), indicative of two-way shape memory capacity; (b) two-way shape memory behavior of a poly(cyclooctene) sample at different stresses, (i) 500, (ii) 600, and (iii) 700 kPa upon heating/cooling; (c) schematic showing the difference between one-way and two-way shape memory. Two-way shape memory is achieved through repeated heat/cool cycles while maintaining load (weight). Figures in (a) and (b) adapted with permission from ref [52].....31
- Figure 2-1.** Copolymer glass transition temperature (T_g) is tuned through composition control; (a) DSC thermograms of copolymers with different compositions of tBA-BA show that T_g increases as the amount of tBA increases. (b) DSC thermograms of samples before methanol extraction, after methanol extraction, and after hydration show that methanol extraction increases T_g , while water plasticization decreases T_g . All DSC thermograms are from the second heat.....66

Figure 2-2. Temperature dependent dynamic mechanical response (1 Hz, under tension) of the 95tBA-5BA substrate. (a) Effect of temperature on the tensile storage modulus for dry and wet films shows a drop in modulus of 3 orders of magnitude upon heating through the glass transition temperature. (b) Isothermal storage modulus of a dry film heated to 55 °C and a wet film heated to 37 °C, temperatures used for forming wrinkles in the dry and wet state, respectively.....	67
Figure 2-3. Shape memory characterization of the 95tBA-5BA substrate (a) dry and (b) wet show excellent shape fixing and shape recovery.	68
Figure 2-4. Effect of composition on recovery kinetics in 37 °C water. Increased amounts of tBA in the SMP substrate result in slower recovery once hydrated at 37 °C.	69
Figure 2-5. Fixed SMP prestrain affects wrinkle and crack formation. (left) AFM wrinkle images and (right) optical micrograph crack images with prestrain values of (a) 2%, (b) 7%, (c) 12%, (d) 17%, (e) 23%. Increasing prestrain increases wrinkle amplitude and crack density. Heights in the AFM images are given in color scale and range from $z=0$ nm black pixels to $z=700$ nm bright pixels. Scale bar is 20 μm for AFM images and 200 μm for optical micrographs. Arrow indicates the strain direction.....	70
Figure 2-6. Characterization of wrinkles using 2D FFT. (a) Wavelength distributions of uniaxial wrinkles with controlled thickness of gold at varying prestrain; (b) 2D FFT pattern of wrinkled surfaces; (c) relative degree of alignment characterization using 2D FFT pattern. “1” and “2” in the left frame indicate the first and second populations of uniaxial wrinkle wavelengths.	71

- Figure 2-7.** Characterization of static and active wrinkles. (a) Wavelength change with respect to the prestrain, (b) amplitude dependence of wrinkle prestrain, (c) relative degree of alignment as a function of prestrain. The controlled gold thickness in (a), (b), and (c) is 33 nm. “1” and “2” in (a) indicate the first and second populations of uniaxial wrinkle wavelengths.....72
- Figure 2-8.** Cell viability on wrinkled substrates. LIVE/DEAD assay performed on cells seeded on (a) non-wrinkled, (b) 2%, (c) 7%, (d) 12%, (e) 17%, and (f) 23% prestrain. Scale bar is 200 μm . Green cells represent live cells while red cells represent dead cells. Cells showed >95% viability for all samples.73
- Figure 2-9.** Wrinkle effect on cell alignment. Phalloidin (cytoskeleton) and DAPI (nuclear) assays performed on cells seeded on (a) non-wrinkled, (b) 2%, (c) 7%, (d) 12%, (e) 17%, and (f) 23% prestrain. Scale bar is 200 μm . Cytoskeleton stain is shown in red and nuclear stain in blue. Cells on the non-wrinkled sample appear randomly distributed whereas cells on all wrinkled samples how alignment parallel to the wrinkle direction.74
- Figure 2-10.** Wrinkle effect on cell nuclear distribution. Angular histograms of cells seeded on (a) non-wrinkled, (b) 2%, (c) 7%, (d) 12%, (e) 17%, and (f) 23% prestrained wrinkled substrates show the distribution of cell nuclear angles, with a broad distribution of angles representing no alignment and a narrow distribution representing a high degree of alignment. Increased prestrain results in a narrowing of the cell nuclear angle distribution, indicating increased cell alignment. The 90° angle in the angular histogram represents the angle parallel to the wrinkles.75
- Figure 2-11.** Effect of prestrain on cell orientation and crack density. With increasing prestrain, a decrease in angular spread is observed, indicating increased cell orientation. Crack density increases with increasing prestrain, with a critical prestrain of 2.6% required for crack formation.76

- Figure 2-12.** Optical micrographs of water triggered wrinkle formation with 100 s gold coating and 12% prestrain. Prestrained samples are soaked in water (a) at 30 °C for 5 h, (b) at 30 °C for 29 h, and (c) at 30 °C for 5 h and 37 °C for 24 h, simulating conditions for cell culture. Scale bar is 50 μm77
- Figure 2-13.** Cells remain viable following wrinkle formation. LIVE/DEAD assay performed on cells seeded (a) at 30 °C for 5 h, (b) at 30 °C for 29 h, and (c) at 30 °C for 5 h and 37 °C for 24 h. (Scale bar is 200 μm). Green cells represent live cells while red cells represent dead cells. Cells showed >95% viability for all samples.78
- Figure 2-14.** Cell morphology is affected by active wrinkle formation. Phalloidin (cytoskeleton) and DAPI (nuclear) assays were performed on cells seeded (a) at 30 °C for 5 h, (b) at 30 °C for 29 h, and (c) at 30 °C for 5 h followed by 37 °C for 24 h. For conditions (a) and (b), the substrate is flat as wrinkle formation has not been triggered. In condition (c) wrinkle formation is triggered while cells are attached. Scale bar is 200 μm . Cells show no orientation prior to wrinkle formation and subsequently align parallel to the wrinkle direction (denoted by arrow) after wrinkle formation is triggered.79
- Figure 2-15.** Active wrinkling results in narrowed nuclear angle distribution. Angular histograms of cells seeded (a) at 30 °C for 5 h, (b) at 30 °C for 29 h, and (c) at 30 °C for 5 h followed by 37 °C for 24 h show that before wrinkling (condition (a)) cell nuclear angle has a broad distribution that narrows upon active wrinkling.(condition (c)). The 90° angle in the angular histogram represents the angle parallel to the wrinkles for condition (c).80

Figure 2-16. Representative cell cytoskeleton and cell nuclear angular distributions during active wrinkling. Angular histograms of cells seeded (a) at 30 °C for 5 h, (b) at 30 °C for 29 h, and (c) at 30 °C for 5 h followed by 37 °C for 24 h show that both cytoskeleton and nuclear angular distributions are broad before wrinkling (condition (a)) and narrow upon wrinkling (condition (c)). The 90° angle in the angular histogram represents the angle parallel to the wrinkles for condition (c).....81

Figure 2-17. Histograms showing the difference between measured cell nuclear angle and the corresponding cell cytoskeletal angle for cells seeded (a) at 30 °C for 5 h, (b) at 30 °C for 29 h, and (c) at 30 °C for 5 h followed by 37 °C for 24 h. Prior to wrinkling angles between cell nuclei and cell cytoskeleton can vary significantly, however upon wrinkling nuclei and cytoskeletal angles are identical, as noted by over 50% of the measured angles being within $\pm 5^\circ$. Δ Angle is the difference in nuclear and cytoskeletal angle, measured cell-by-cell.....83

Figure 3-1. Representative fluorescent micrographs of stained nuclei seeded at different densities. (a) Cells were stained with Hoechst 33342 nuclear dye after seeding on a wrinkled substrate at three different densities: low density (5,000 cells/cm²); medium density (10,000 cells/cm²); and high density (20,000 cells/cm²). (b) Cells segmented in the first frame for each sample image on wrinkled, non-wrinkled and TCPS substrates (n=12 samples per substrate; samples ordered first by cell number).115

Figure 3-2. Raw fluorescent images and the corresponding tracked images with overlaid tracks. Time progression of cell nuclei with overlaid tracks shows accurate full tracks are constructed. Only the first 45 min are shown for ease of visualizing all cell tracks.....116

Figure 3-3. Representative cell trajectories for cells seeded on (top) wrinkled, (middle) non-wrinkled, and (bottom) TCPS substrates at (left) low, (middle) medium and (right) high densities. The resulting trajectory information qualitatively shows that wrinkled samples yield directional migration of C3H10T1/2 mouse fibroblast cells. Representative tracks for non-wrinkled and TCPS isotropic substrates qualitatively show no preferential directional migration. For the wrinkled images, black double headed arrows indicate wrinkle direction.117

Figure 3-4. Representative MSD plots for cells seeded on anisotropic and flat substrates at various densities. Cells seeded on (top) wrinkled, (middle) non-wrinkled, and (bottom) TCPS at (left) 5,000, (middle) 10,000 and (right) 20,000 cells/cm² were analyzed using a mean squared displacement correlation analysis. Slopes of the MSD plots were calculated at small timescales and large timescales to determine the diffusive nature of migration. Linear regression was used on the first 5 data points for short timescale slopes and a range of 60 data points for the long timescale slope, using the same range for each sample. Blue lines depict MSD traces of the x-direction (parallel to wrinkle direction for wrinkled samples) and magenta lines depict MSD traces of the y-direction (perpendicular to wrinkle direction for wrinkled samples).118

Figure 3-5. Representative velocity autocorrelation plots for cells seeded on anisotropic and flat substrates at various densities. Cells seeded on (top) wrinkled, (middle) non-wrinkled, and (bottom) TCPS at (left) 5,000, (middle) 10,000 and (right) 20,000 cells/cm² were analyzed using a velocity autocorrelation function. Anisotropic substrates showed distinct preferential migration along the grooved direction, while non-wrinkled and TCPS controls demonstrated no statistically significant difference in their x- and y-velocity autocorrelation components. An exponential decay was fit to each profile after removing the first 5 points due to noise. A decay constant was extracted and compared amongst all samples.120

Figure 3-6. Representative cell diffusion plots for cells seeded on anisotropic and flat substrates at various densities. Cells seeded on (top) wrinkled, (middle) non-wrinkled, and (bottom) TCPS at (left) 5,000, (middle) 10,000 and (right) 20,000 cells/cm² were analyzed when the final position for each cell was plotted after renormalizing the starting location to the plot origin. Anisotropic substrates showed directed cell migration as noted by the location of most cells along the x-axis (parallel to the wrinkle direction). In contrast, cells atop both isotropic substrates showed no preferential migration as noted by the radial distribution of cells from the origin. .122

Figure 3-7. Representative cell track terminal points for cells seeded on anisotropic and flat substrates at various densities. Terminal points for cell tracks are shown for cells seeded on (top) wrinkled, (middle) non-wrinkled, and (bottom) TCPS at (left) 5,000, (middle) 10,000 and (right) 20,000 cells/cm². Terminal points were rotated so that the largest eigenvector of the gyration tensor (**Eq. 3-3** in the main text) lies along the x-axis. Therefore, the anisotropy of the points is a visualization of average track asphericity. Surprisingly, cell track asphericity was significantly higher atop flat gold substrates when compared to flat TCPS substrates, indicative of a dependence of cell motility on surface chemistry.123

Figure 3-8. Cell motility behavior correlation with average cell density. (a) Short timescale slopes extracted from the non-decomposed MSD, (b) long timescale slopes extracted from the non-decomposed MSD, and (c) cell track asphericity are plotted as a function of the average cell density for a given sample. Short timescale slopes exhibit a negative correlation with cell density, while long timescale slopes have no correlation with cell density. Cell track asphericity is positively correlated with cell density particularly atop the anisotropic wrinkled substrate. Average cell density is determined as the average number of particles segmented in the beginning and ending frames....124

Figure 3-9. Cell divisions and determining cell division orientation. A timelapse sequence of a dividing cell (yellow arrow in t=0 frame) shows a cell condensing its nucleus and dividing into two daughter cells. For cell division orientation, a line is drawn between the two nuclei centroids, and the angle of that line is used as the cell division angle (noted by double headed arrow).....125

Figure 3-10. Representative angular histograms of the division angles of cells seeded on anisotropic and flat substrates at various densities. Angular histograms of cell division angles are shown for cells seeded on (top) wrinkled, (middle) non-wrinkled, and (bottom) TCPS at (left) 5,000, (middle) 10,000 and (right) 20,000 cells/cm². Histograms show a narrow distribution of division angles for the wrinkled substrates, centered around 90° (parallel to the wrinkle direction), and broad distributions of division angles for both the non-wrinkled and TCPS substrates, independent of seeding density. ..126

Figure 4-1. Salt fusion forms thick salt bridges between salt particles. SEM micrographs of salt particles (a) before fusion and (b) after fusion reveal that upon exposure to a humid atmosphere for 24 h, salt particles form thick salt bridges at contact sites. Scale bars are 100 µm for all SEM micrographs.....158

Figure 4-2. Thermal degradation profile of a salt-extracted foam. Following salt extraction the foam nearly completely degrades when heated to 600 °C. Salt crystals are thermally stable to this temperature, indicating salt was successfully extracted from the foam. Samples were heated at 20 °C-min⁻¹.159

Figure 4-3. Microcomputed tomography 3D reconstructions of an SMP foam. (a) 3D reconstruction of a circular disc with 3 mm thickness and 10.2 mm diameter; (b) cross-sectional views. In (b), the image on the right is a thin slice of the cross-section shown in the image on the left. Scaffolds appear highly porous with interconnected pores. Scale bars are 1 mm for (a) and 400 µm for (b).160

Figure 4-4. SEM micrograph of SMP foam. A freeze-fractured cross-section of an 80PCL-20PEG foam shows large cuboidal pores with small round interconnections. Scaffolds appear highly porous and interconnected. Scale bar is 500 µm.161

Figure 4-5. Effect of PCL-PEG composition on thermal properties of SMP foams. DSC 2 nd heat traces of foams with weight ratios of PCL-PEG ranging from 100PCL-0PEG to 60PCL-40PEG in the (a) dry and (b) wet state show T_m decreases with increasing PEG content. This effect is more prominent in the wet state. (c) Hydration lowers the T_m of each composition.	162
Figure 4-6. Effect of PCL-PEG composition on water uptake. As the weight percent of hydrophilic PEG increases, the amount of water uptake increases for both foams and films.	163
Figure 4-7. Shape memory behavior of SMP foams. (a) Dry one-way shape memory testing of 80PCL-20PEG in compression reveals excellent shape fixing and recovery; (b) wet one-way shape memory testing of 80PCL-20PEG in compression also shows excellent shape fixing and recovery.	164
Figure 4-8. Shape memory effect on SMP foam architecture. (left) Optical micrographs and (right) SEM images of foam cross-sections prior to compressing 50% (top), after compressing 50% (middle), and after triggering recovery (bottom) reveal the porous architecture collapses upon fixing but is subsequently restored following shape recovery. Scale bars are 200 μm	165
Figure 4-9. Hydrated recovery of 80PCL-20PEG foam at 37 °C. A sample with a hydrated T_m of 36 °C is triggered to fully expand within seconds of being exposed to 37 °C water. Prior to the addition of the water, the foam was heated to 80 °C, compressed between two steel plates, and fixed in a -4 °C freezer for 10 min.	166
Figure 4-10. Shape memory behavior of 80PCL-20PEG foams deformed at different temperatures. Deformation temperatures (T_{def}) at (a) $T_m + 30$ °C, (b) $T_m + 10$ °C, (c) T_m , (d) $T_m - 5$ °C, (e) $T_m - 10$ °C, and (f) $T_m - 15$ °C, reveal that foams fully recover regardless of T_{def} , however shape fixing decreases as T_{def} decreases below T_m	169

Figure 4-11. Effect of deformation temperature on the stability of fixed foams at room temperature. (a) Recovery traces of foams deformed below and above T_m reveal deforming at lower temperatures leads to a decrease in stability near room temperature. Fixed samples were heated at $3\text{ }^{\circ}\text{C}\cdot\text{min}^{-1}$ to $27\text{ }^{\circ}\text{C}$ and held isothermal for 20 min to observe stability, followed by heating at $3\text{ }^{\circ}\text{C}\cdot\text{min}^{-1}$ to $80\text{ }^{\circ}\text{C}$ for full recovery. (b) Stability of the fixed shape during the isothermal step at $27\text{ }^{\circ}\text{C}$ is reduced for lower deformation temperatures. A composition of 80PCL-20PEG was used for the temperature deformation studies.171

Figure 4-12. Effect of deformation temperature on the recovery behavior of foams during continuous heating. (a) Recovery traces of foams deformed below and above T_m reveal deforming at lower temperatures leads to an earlier onset temperature of recovery; (b) lower temperatures lead to an earlier onset of recover and fully recover at a lower temperature, however a larger range of temperature change is needed to achieve full recovery. A composition of 80PCL-20PEG was used for the temperature deformation studies.172

Figure 4-13. Two-way reversible actuation of SMP foams. (a) An 80PCL–20PEG SMP foam showed reversible two-way actuation of up to 15% when a constant load is applied during crystallization; (b) a maximum actuation strain is observed with a prestrain of 30%, and the actuation strain decreases as the prestrain deviates from 30%.173

Figure 5-1. Scanning electron micrographs show successful incorporation of hydroxyapatite (HA) into 80PCL-20PEG foams. (a) HA nanoparticles (<200 nm according to vendor specifications) aggregate into larger particles; (b) following salt fusion in the presence of HA, cuboidal salt particles are coated with nano HA particles; (c) following foam fabrication and salt extraction, HA nanoparticles cover the pores and struts of the foam. Scale bars are 100 μm for all SEM micrographs.....206

Figure 5-2. Thermal degradation and transition temperature of 80PCL-20PEG-20HA foams. (a) Thermogravimetric analysis (TGA) of HA-incorporated foams show an average of 8% mass remaining following degradation. Dotted black lines represent degradation profiles from different locations of the same foam. (b) DSC 2nd heating traces of dry and wet foams reveal a dry T_m of 40.6 °C that drops to 35.4 °C upon hydration. The sloped baseline in the DSC traces is an artifact from the DSC equipment. A heating rate of 20 °C·min⁻¹ was used for TGA, and a heating/cooling rate of 3 °C·min⁻¹ was used for DSC.....207

Figure 5-3. Temperature dependent dynamic mechanical response (1 Hz, under compression) of the 80PCL-20PEG-20HA foam. Foams have an apparent storage modulus of ~1 MPa below T_m (dry) that drops to ~10 kPa upon heating above T_m . Heating and cooling rates of 3 °C·min⁻¹ were used.208

Figure 5-4. Shape memory behavior of the 80PCL-20PEG-20HA foams. One-way shape memory behavior (compression) of (a) dry and (b) wet foams reveal excellent shape fixing and shape recovery.....209

- Figure 5-5.** Scanning electron micrographs of 80PCL-20PEG-20HA foams during a one-way shape memory cycle. SEM micrographs of foams (top) before fixing, (middle) after fixing a 50% compressive strain, and (c) after recovery reveals the open, porous architecture collapses upon fixing but is restored upon shape recovery. Magnifications of (left) 25x, (middle) 100x, and (right) 1600x show the macroscopic and microscopic effect of shape memory on the foam architecture. Inspection of the 1600x micrographs reveals hydroxyapatite particles remain on the foam surface during all stages of the shape memory cycle. Scale bars are 1 mm, 100 μ m, and 10 μ m for magnifications of 25x, 100x, and 1600x, respectively.210
- Figure 5-6.** Thermal and thermomechanical properties of 92tBA-8BA SMP foams. (a) TGA reveals complete salt extraction upon heating to 600 $^{\circ}$ C; (b) DSC 2nd heating trace reveals a dry T_g of 40 $^{\circ}$ C that drops to 36 $^{\circ}$ C upon hydration; (c) dynamic mechanical analysis (DMA) of dry foam shows an apparent storage modulus of \sim 10 MPa below T_g . Heating rate used for TGA was 20 $^{\circ}$ C \cdot min⁻¹, heating/cooling rate for DSC was 3 $^{\circ}$ C \cdot min⁻¹, and heating rate for DMA was 3 $^{\circ}$ C \cdot min⁻¹.211
- Figure 5-7.** Shape memory behavior of 92tBA-8BA foams. One-way shape memory behavior (compression) of (a) dry and (b) wet foams reveal excellent shape fixing and shape recovery.212
- Figure 5-8.** Optical micrographs and scanning electron micrographs of 92tBA-8BA foams during a one-way shape memory cycle. (left) optical micrographs and (right) SEM micrographs (top) before fixing, (middle) after fixing a 50% compressive strain, and (c) after recovery reveals the open, porous architecture collapses upon fixing but is restored upon shape recovery. Foams have a cuboidal pore morphology with small interconnecting openings between pores. Scale bar is 1 mm.213

Figure 5-9. <i>In situ</i> recovery of a 92tBA-8BA foam in a mouse femoral segmental defect. A compressed foam was triggered to recover by submerging in 45 °C water, simulating intraoperative delivery. The foam expanded to fill the defect within 55 s.....	214
Figure 5-10. Comparison of the stability of soft (80PCL-20PEG-20HA) and stiff (92tBA-8BA) foams implanted <i>in vivo</i> . (a) x-ray radiographs of mice implanted with SMP foams 4 weekspost-surgery show significant limb shortening for 80PCL-20PEG-20HA foam treatment; no shortening occurs for 92tBA-8BA foam treatment. (b) compressive stress v. strain curves for foams hydrated at 37 °C for 24 h reveal compressive elastic moduli of 0.06 MPa and 16 MPa for soft and stiff foams, respectively.....	215
Figure 5-11. Representative radiographs of limbs treated with an SMP graft (92tBA-8BA) and a control allograft at 4, 8, and 12 weeks post-surgery. The SMP graft maintained the length of the segmental defect 12 weeks post-surgery. White arrows indicate bony formations at the margin.....	216
Figure 5-12. Representative reconstructed microcomputed tomography scans of limbs treated with an SMP graft (92tBA-8BA) and a control allograft 12 weeks post-surgery; (a)(top) 3D reconstruction of the entire femur, and (bottom) enlarged cross-sectional view of the defect site sho new bone formation at the margins between the grafts and the native bone. (b) 3D reconstruction of a defect treated with an SMP graft shows bony protrusions (red arrows) that have the same cuboidal morphology and size as the SMP pores. Scale bar in (b) is 300 um.	217

Figure 5-13. Histological analysis of limbs treated with (a) SMP grafts (92tBA-8BA) and (b) an allograft control 12 weeks post-surgery. Granulated tissue and cell infiltration is found into the SMP foam, and the distal native bone marrow appears healthy. Allograft treatment shows remodeling has begun at the margins. Scale bars are 1 mm.	218
Figure 5-14. Example torsional testing output from custom MATLAB algorithm for limbs treated with (a) SMP grafts (92tBA-8BA) and (b) an allograft control 12 weeks post-surgery. Torque-rotation angle curves were generated with real-time testing images overlaid to assess in failure analysis. Torque, energy, and stiffness were determined for each trace.	219
Figure 5-15. Torsional mechanical properties of limbs treated with SMP graft or allograft, and a contralateral intact femur control, 12 weeks post-surgery. (a) Torsional stiffness; (b) peak torque; (c) energy-to-failure. The SMP graft exhibited a trend of lower torsional mechanical properties compared to the allograft group, although not statistically significant. Mechanical properties of both treatment groups were significantly lower than the contralateral intact control.	220
Figure 6-1. Thermal properties of 92tBA-8BA foam scaffolds. (a) TGA degradation profile indicates salt was extracted; (b) DSC 2 nd heat traces show a dry Tg of 47 oC that drops to 43 °C upon hydration. Heating rate for TGA was 20 °C-min ⁻¹ ; heating rate for DSC was 3 °C-min ⁻¹	250

- Figure 6-2.** Shape recovery of 92tBA-8BA scaffolds under simulated *active cell culture* conditions. After sterilization, scaffolds initially recovered 13% of the programmed deformation (25% programmed uniaxial compressive strain). When cultured at 30 °C for 5 d (blue symbols) the scaffold remained stable in its programmed state; upon triggering recovery at 37 °C (red symbols), the scaffold recovers within 24 h. Inset scanning electron micrographs show the architecture remains collapsed during culture at 30 °C and restores its open cuboidal morphology after recovery. Scale bars are 500 µm.....251
- Figure 6-3.** Reconstructed 3D microcomputed tomography of active and static cross-sections during culture. Before transition, *active* scaffolds have a collapsed pore architecture that is restored within the first 2 d after transition. *Static* scaffold pore morphology is open and cuboidal for all time points. Scale bare is 1 mm.....252
- Figure 6-4.** Hoechst nuclear staining for cells seeded in *active* and *static* foam scaffolds. Cell nuclear staining using Hoechst 33342 at three time points show cells attach and proliferate, with cell sheets forming on both *active* and *static* scaffolds after 4 weeks of culture. Cell densities for *active* and *static* foams were comparable. Scale bar is 200 µm.253
- Figure 6-5.** SEM micrographs of active and static foams following culture for 4 weeks. After 4 weeks of culture (5 d at 30 °C + 23 d at 37 °C) a cell sheet formed on the (top) outer surface of both active and static scaffolds; (middle) cross-section SEM micrographs reveal cell significant cell infiltration into the center of the scaffolds, which is further illustrated in (bottom) magnified SEM micrographs showing cells filling the interior pores. Scale bars are 500 µm for (top) and (middle), and 100 µm for (bottom).....254

Figure 6-6. Xylenol orange (XO) staining for calcium deposition on *active* and *static* foam scaffolds. (a) for both *active* and *static* foam scaffolds, no calcium nodules were detectable before transition; following transition at 37 °C for 2 d small calcium nodules were detected (black arrows) but in limited quantity; after 23 d at 37 °C, a significant increase in the size and number of calcium nodules is detected, with no observable different between *active* and *static* groups. (b) Three empty control scaffolds (no cells) that were cultured under the same conditions as the active and static scaffolds show no calcium deposition after 4 weeks, indicating the calcium deposition observed in (a) was deposited by the adhered cells. Scale bars are 200 µm. Histogram stretching was performed on the raw images to allow visualization of calcium nodules.255

Figure 6-7. SEM micrographs of *active* and *static* foam scaffolds reveal mineral deposition. Before transition and 2 d after transition no significant mineral deposition was found on active or static foam scaffolds. After 23 d at 37 °C, scaffolds were covered in mineralized nodules (white specs) for both active and static scaffolds. Scale bar is 20 µm.256

Figure 6-8. Energy dispersive spectroscopy (EDS) of mineral deposition shows minerals contain calcium. (a) SEM images from backscattered electrons of a cell sheet covering the foam scaffold and of a magnified view of a mineralized nodule. (b) EDS traces of the cell sheet and of the mineralized nodule show a significant amount of calcium and phosphorous. Scale bars in (a) are 100 µm for the cell sheet and 10 µm for the mineral nodule.257

Figure 6-9. Microcomputed tomography 3D reconstructions when applying three different thresholds. With an applied threshold of (top) 40, both mineral and foam are included; for a threshold of (middle) 70, the foam is partially removed; for a threshold of (bottom) 100, the mineral is completely isolated from the foam. Using a threshold of 100, the progression of mineral deposition over time was observed. The foam scaffold shown in this figure is a *static* foam. Scale bar is 1 mm.....258

Figure 6-10. Microcomputed tomography 3D reconstructions of active and static foam scaffolds show mineral deposition over time. For both *active* and *static* scaffolds, small quantities of minerals were detected, and mineral size was small before transition and 2 d after transition. Significant increase in mineral volume and size was found on both groups 23 d after transition. A threshold of 100 was used to isolate mineral. Scale bar is 1 mm.259

Figure 6-11. SEM micrographs of independent replicate with cell sheet formation before transition. For the independent replicate where significant mineral deposition was observed before transition, both *active* and *static* scaffolds had a confluent cell sheet covering the (top) outer surface. Inspection of the (bottom) surface of the cell sheet shows large mineral deposits. Scale bars are (top) 500 μm and (bottom) 50 μm261

Figure 6-12. Alkaline phosphatase (ALP) activity for *active* and *static* foam scaffolds before and after transition. No significant difference in ALP activity was found between active and static scaffolds. While a trend of increased ALP activity is seen for after transition (37 °C 2 d and 37 °C 23 d) compared to before transition (30 °C 5 d), no statistically significant difference was found. Horizontal lines indicate averages over 3 independent replicates.262

Figure 6-13. Real-time PCR (qPCR) expression of osteogenic markers Runx2 and osteocalcin (OC) for *active* and *static* foam scaffolds. (a) A trend of increasing (upregulation) Runx2 over time was observed for *active* and *static* scaffolds, although significance was not achieved; (b) a trend of decreasing (downregulation) OC was observed for *active* and *static* scaffolds, but no significance was found. There was no difference between *active* and *static* scaffolds in both markers across all time points. Horizontal lines indicate averages over 3 independent replicates.263

Figure 6-14. Alizarin red staining of *active* and *static* foam scaffolds 4 weeks after culture. Calcium deposition (red stain) was observed throughout the entire scaffold for both *active* and *static* scaffolds. An empty control scaffold (no cells) cultured under the same conditions showed no staining, suggesting calcium deposition is from the adhered cells and not deposition from the medium onto the scaffold. No observable difference was found between *active* and *static* scaffolds.264

Figure A4-1. Functionalization of HA nanoparticles. (a) Fourier transform infrared spectroscopy (FTIR) comparison of functionalized and unmodified HA particles indicate new absorption bands at 1610 cm^{-1} and 1580 cm^{-1} , indicative of successful EG grafting; however, no detectable changes in band absorption were found after grafting with DA. (b) TGA degradation traces show a polymeric degradation for the functionalized HA-EG-DA particles when compared to the unmodified particles, which exhibit minimal weight loss up to $700\text{ }^{\circ}\text{C}$. (c) 80PCL-20PEG-20HA scaffolds had an average of 14% weight remaining, indicating a loading efficiency of 70%, which is better than the 40% from physical HA incorporation in **Chapter 5**.....307

Figure A5-1. Thermal and thermomechanical characterization of thiol-ene mediated PDLLA foams. (a) TGA analysis shows salt was completely extracted from foams; (b) DSC 2nd heat traces reveal a lower T_g for the 3 kDa foam compared to the 16 kDa foam, and hydration plasticizes the T_g causing a drop of $\sim 11\text{ }^\circ\text{C}$ in T_g ; (c) one-way shape memory in compression shows that a sample deformed at $80\text{ }^\circ\text{C}$ had excellent shape fixing upon cooling to $-10\text{ }^\circ\text{C}$, however recovery was very limited (14% recovery).315

Figure A5-2. Thermal and thermomechanical properties of PDLLA TPU foams. (a) DSC 2nd heating trace of both the TPU foam (black) and the TPU before foam fabrication (red) had a dry T_g of $51\text{ }^\circ\text{C}$. This T_g drops to $41\text{ }^\circ\text{C}$ (not shown) due to plasticization when placed in water; (b) one-way shape memory behavior in compression reveals excellent shape fixing and shape recovery of a TPU foam deformed at $60\text{ }^\circ\text{C}$; (c) the effect of deformation temperature during a one-way shape memory cycle shows that deforming near T° ($51\text{ }^\circ\text{C}$) results in the lowest onset of recovery temperature. Higher deformation temperature results in a higher onset of recovery temperature. All deformation temperatures with the exception of $80\text{ }^\circ\text{C}$ result in full recovery of the sample. All heating/cooling rates were $3\text{ }^\circ\text{C}\cdot\text{min}^{-1}$ 316

Figure A6-1. SEM micrographs of SMP foams fabricated using new salt fusion technique. Salt fusion with 6% water mixed in resulted in cuboidal pores with small interconnection openings; with 10% water, pores had larger interconnections sizes and were more open; increasing the water to 15% resulted in highly interconnected pores with a loss in cuboidal morphology. Scale bares are $500\text{ }\mu\text{m}$327

Figure A6-2. Thermal properties of tBA-BA foams with different compositions. (a) TGA analysis reveals salt is completely extracted for all foams; (b) DSC 2nd heat traces show a trend of decreasing T_g with decreasing tBA weight-%. 328

Figure A6-3. Shape memory behavior of tBA-BA foams with different compositions. (a) compressive one-way shape memory traces show all foams have excellent shape fixing and shape recovery; (b) recovery profiles of foams with different compositions shows that as tBA weight-% decreases, the onset of recovery temperature also decreases.....	330
Figure A6-4. Recovery of tBA-BA foams in 37 °C water. As the amount of tBA in the foams decreases, the recovery rate at 37 °C increases; foams with the lowest tBA composition (79-21) recovered most of the programmed strain within one min; foams with the highest tBA composition (95-5) had minimal recovery within the first 9 min.....	331
Figure A6-5. Example cell infiltration micrographs after stitching. The small bright circles in each image are cell nuclei. Qualitatively, an increase in cell infiltration with increasing water-% was observed. Additionally, programmed 79tBA-21BA foams had increased cell infiltration compared to programmed 95tBA-5BA foams.....	332

Chapter One: Introduction

1.1 Tissue Engineering and Cell Mechanobiology: Bridging the Gap

Tissue engineering is an exciting, fast-growing field that combines cells, signals, and scaffolds to regenerate damaged tissues. To date, engineered constructs have found varying degrees of success. For instance, engineered products were first established for skin [1], which, along with bone and bladder, has one of the highest success rates [2]. However, for other tissues, such as the liver, engineered constructs are still in the early stages of development [1]. As researchers continue to develop new functional engineered tissues, it is becoming increasingly important to understand how the underlying cell-material interactions affect the cell mechanobiological response. As such, substantial effort has focused recently on developing complex synthetic materials that can mimic the *in vivo* cell environment. These new materials are of interest for their potential to bridge the gap between cell mechanobiology and tissue engineering, where a better understanding of cell-material interactions would enable researchers to develop functional engineered tissues with properties similar to the native tissues these constructs aim to replace. In a step towards bridging the gap, this dissertation presents the development and application of new 2D substrates and 3D scaffolds that can serve as platforms for studying cell-material interactions in a dynamic environment. This is achieved by employing a special class of stimulus responsive materials, shape memory polymers.

1.2 Cell-Material Interactions

Cells actively probe and respond to the mechanical, electrical, and chemical properties of their surrounding environment. Traditionally, these cell-material interactions have been studied

by performing mammalian cell culture on tissue culture polystyrene or glass slides. These simplistic materials, however, do not mimic the complex environment cells experience *in vivo*, which can result in non-physiological cell responses. In order to develop synthetic materials that more closely mimic the biological environment, researchers may consider a subset of stimuli [3] to which cells respond: chemical, topographical, and mechanical (elasticity).

1.2.1 Surface Chemistry Affects Cell Behavior

In vivo, cell transmembrane receptors known as integrins bind to ligands of the surrounding extracellular matrix (ECM). Cells become anchored to the ECM and can transmit information about the ECM to the interior of the cell, which in turn can instruct the cell to grow, divide, differentiate, migrate, or die [4, 5]. To better understand how integrin-ligand binding complexes direct cell behavior, researchers have developed synthetic materials with different surface chemistries and studied cell response *in vitro*. It has been shown that surface chemistry dictates cell-material adhesion strength, which has a major influence on behaviors such as cell migration and cell morphology. For instance, Palecek et al. coated glass coverslips with various concentrations of fibronectin and measured the velocity of CHO-B2 cells with different levels of integrin expression and binding affinities [6]. It was observed that cell migratory response is biphasic, where at low fibronectin concentrations cell velocity increased with increasing binding affinity and integrin expression. At higher fibronectin concentrations, cell velocity increased with decreasing binding affinity and integrin expression. Likewise, other studies have shown that cell-material adhesive strength is a major regulator of cell migration, with intermediate adhesive strengths resulting in fastest cell velocities [7, 8].

Synthetic substrates with patterned chemistries have also been employed to confine cell attachment and spreading and evaluate the influence of cell shape on cell behavior. For example,

Chen and colleagues microcontact printed adhesive islands of fibronectin ranging in size from 3-50 μm and found that culturing endothelial cells on smaller islands resulted in cells transitioning from a state of growth to a state of apoptosis, demonstrating that cell shape dictates cell function [9]. Similarly, Peng et al. observed cell shape directed stem cell lineage commitment [10]. When seeding rat mesenchymal stem cells on rectangular RGD islands with different aspect ratios, it was observed that optimal adipogenic differentiation was triggered on islands with an aspect ratio of 1, while optimal osteogenic differentiation was triggered on islands with an aspect ratio of 2, and the relationship was non-monotonic. These studies demonstrate that patterned surface chemistries can be employed to direct cell behavior *in vitro*.

1.2.2 Topography Affects Cell Behavior

In vivo, the ECM consists of nano-scale features that direct cell behavior. For instance, surface features of the corneal epithelial and endothelial basement membranes have been found to be on the nanometer scale, with pore and fiber diameters ranging from 30-400 nm [11-13]. Collagen, a component of the ECM, can form fibrils tens of microns long with diameters ranging from 260-410 nm [14]. Cells interact with these topographical structures of the ECM through a phenomenon known as contact guidance, which directs cell migration, adhesion, morphology and orientation. To understand the mechanisms behind contact guidance observed *in vivo*, scientists have developed 2D substrates and 3D scaffolds with nano- and micro- scale topographical features and studied how cell behavior is affected *in vitro*.

One of the primary cell behaviors that is controlled through contact guidance is cell alignment. Synthetic substrates with a nanograting topography have been developed to study the effect of nano-scale topography on many different cell types, and most have shown a dependence of cell alignment on the nanograting topography [15]. For example, Bettinger et al. showed that

endothelial cells atop PDMS nanogratings with a 1.2 μm pitch (distance between gratings) and 600 nm depth elongated and aligned parallel to the nanograting direction [16]. Teixeira and colleagues have shown that human corneal epithelial cells (HCECs) can elongate and align parallel to nanogratings with ridge widths ranging from 70-1900 nm, groove depths of 150 and 600 nm, and pitches (distances between ridges) ranging from 400-4000 nm [17]. Interestingly, cell alignment was found to be more sensitive to groove depth than pitch. In a follow-up study, Teixeira and colleagues found that under different serum conditions, pitch was a major regulator in HCEC alignment, as HCEC aligned perpendicular to nanogratings with nano-scale pitches and transitioned to parallel alignment when the pitch was increased to the micron scale [18]. Nonetheless, these studies demonstrate how nanotopography can be used to direct cell alignment. In **Chapter 2** of this work, we explore how dynamic wrinkle formation can be employed to control mouse fibroblast alignment.

In addition to directing cell alignment, nanotopographies have been employed to influence stem cell differentiation and cell migration *in vitro*. Yim et al. investigated the effect of nanograting topography on human mesenchymal stem cell differentiation and showed that nanotopography alone (in the absence of neurogenic induction medium) promoted upregulation of neurogenic differentiation markers, more so than neurogenic induction medium alone [19]. In combination with the induction medium, a synergistic effect was observed with a significant increase in upregulation of neurogenic differentiation markers. Micro-patterns comparatively resulted in less upregulation, indicating nano-topography had a more significant effect on stem-cell differentiation than micro-topography. Nanogratings have also been employed to study the effect of topography on cell migration, where cells were shown to migrate along the nanogratings [16, 20]. Wang et al. found that rat C6 glioma cells atop periodic surface structures

with a 266 nm wavelength migrated parallel to the surface structures [20]. Additionally preferential cell division was observed along these surface structures. Larger scale micro-groove topographies have also showed preferential epithelial cell migration of a monolayer sheet parallel to the micro-groove direction [21]. Cell migration was more sensitive to micro-groove depth than micro-groove pitch for this study. These studies demonstrate that surface topographies of different length-scales can be employed to direct cell migration *in vitro*. In **Chapter 3** of this work, we explore the effect wrinkle topography and substrate chemistry have on cell migration and discuss a series of physics-based metrics that can be used to describe cell motility.

1.2.3 Elasticity Affects Cell Behavior

In vivo, adhered cells actively probe the mechanics of the ECM through adhesion complexes (e.g. integrin-ligand complexes mentioned above), which cells use to transmit traction forces to the ECM. As cells pull on the ECM, they also respond through cytoskeletal reorganization, which can in-turn elicit different cell behaviors. Pioneering work by Pelham and Wang was the first to demonstrate *in vitro* that cells actively probe and respond to the elasticity of their environment [22]. The authors found that cell adhesion and spreading were dependent on substrate elasticity. Soft substrates ($E \sim 1$ kPa) resulted in less spreading of cells and less stable focal adhesions, while stiff substrates ($E \sim 70$ kPa) resulted in more cell spreading and stable focal adhesions. Substrate elasticity was later found to be a major regulator of cell migration, with 3T3 fibroblasts seeded on a substrate with a modulus gradient preferentially migrating towards the stiff side of the substrate, a term coined “durotaxis” [23]. It was later shown that cell response to elasticity is very cell-type specific and cell-density specific [24]. Neutrophils were found to be insensitive to substrate elasticity, while fibroblasts and endothelial cells required a substrate with an elasticity greater than 2 kPa to form actin stress fibers.

Substrate elasticity has furthermore proven a powerful regulator of stem cell lineage specification. Seminal work by Engler et al. demonstrated that mesenchymal stem cells seeded on polyacrylamide gels with elasticities ranging from 0.1-40 kPa have an elasticity-dependent lineage commitment [25]. Cells seeded on soft substrates (0.1-1 kPa) expressed neurogenic differentiation markers; cells seeded on substrates with intermediate stiffnesses (8-17 kPa) expressed myogenic markers; and cells seeded on stiff substrates (25-40 kPa) expressed osteogenic markers. Additionally, work by Gilbert et al. revealed that the “stemness” of muscle stem cells (MuSCs) cultured *in vitro* was retained on soft substrates that recapitulate skeletal muscle elasticity ($E = 12$ kPa) and not on the much stiffer tissue culture polystyrene ($E \sim 10^6$ kPa)[26]. Furthermore, upon transplantation of cultured MuSCs into the tibialis anterior muscles of mice, only MuSCs cultured on substrates with a modulus comparable to muscle resulted in significant engraftment. These studies demonstrate that substrate elasticity can be employed to direct cell behavior *in vitro*.

1.3 Dynamic Microenvironment During Development and Disease Progression

A major limitation of current synthetic materials developed for studying cell-material interactions is the static nature of these materials, which does not reflect the dynamic environment *in vivo*. *In vivo*, the cell is surrounded by ECM, a complex network comprised primarily of proteins, polysaccharides, and water [27] that directs basic cell functions such as proliferation, migration, adhesion, differentiation, and apoptosis [28]. The ECM is a dynamic network that in many tissues is constantly undergoing degradation and remodeling, and these dynamics play a vital role in developmental processes and disease progression [29]. In this dissertation, we describe a series of shape memory polymer 2D substrates and 3D scaffolds that can be employed as dynamic platforms for studying cell-material response *in vitro*, which is

expected to provide new insights into how the dynamic *in vivo* environment regulates cell function during development and disease progression.

1.3.1 ECM Dynamics During Development

During development, dynamic changes in ECM structure and protein expression are fundamental to many important processes including branching morphogenesis [30, 31], angiogenesis [32] and bone development and remodeling [29]. For example, transient and local expression of fibronectin, a protein of the ECM, has been shown to be a primary regulator in cleft formation and epithelial branching [33]. Additionally, branching morphogenesis is associated with ECM remodeling through proteolytic degradation [31], with localized ECM degradation guiding branching. In bone development, matrix metalloproteinases (MMPs) play a vital role in degrading ECM to promote bone formation and remodeling in both endochondral ossification and intramembranous ossification [34]. MMPs also play a critical role in remodeling the ECM to promote cell invasion and migration during angiogenesis and wound healing [35]. These examples illustrate the dynamic microenvironment that cells experience during development. Substrates and scaffolds that can mimic the *in vivo* ECM dynamics are anticipated to serve as powerful *in vitro* platforms to study developmental cell mechanobiology, and further enhance the development of functional tissue engineered constructs.

1.3.2 ECM Dynamics During Disease Progression

ECM dynamics also play a critical role in disease initiation and progression, particularly in tissue fibrosis and tumor progression. In fibrotic diseases, changes in the ECM composition lead to a stiffening of the ECM and ultimately to organ dysfunction [36]. For example, during pulmonary fibrosis higher concentrations of collagen (stiff component of ECM) relative to

elastin (soft component of ECM) result in progressive dyspnea [36]. In liver fibrosis, stellate cells are activated as a result of liver injury, and the ECM is remodeled with a matrix rich in fibril-forming collagen, ultimately leading to cirrhosis [37]. Likewise, abnormal changes in ECM composition and deposition lead to a stiffening of the ECM and are directly related to tumor formation [36, 38]. Additionally, tumor cells directly remodel collagenous fibers from a random orientation to a radial orientation to promote tumor cell invasion and metastasis [39]. These examples demonstrate how abnormal ECM dynamics, or the loss of homeostasis, lead to disease progression. Substrates and scaffolds that mimic abnormal ECM dynamics can serve as powerful tools to study cell mechanobiology and eventually serve as constructs for screening pharmaceutical treatments. For example, dynamic 3D fibrous scaffolds with the ability to change fiber orientation or stiffness could be used to evaluate the effect of drug treatments on targeted tumor cell death or preventing tumor cell metastasis.

As this section details, ECM dynamics are powerful regulators of cell function *in vivo*, however few *in vitro* platforms can mimic the dynamic ECM. Thus there is a need for 2D substrates and 3D scaffolds that can achieve dynamic changes in material properties (e.g. topography, surface chemistry, elasticity) under cytocompatible conditions to study cell-material interactions in a dynamic *in vitro* environment. We've addressed this need by employing thermal-responsive shape memory polymers.

1.4 Shape Memory Polymers

1.4.1 Overview of SMPs

Shape memory polymers (SMPs) are a class of stimuli-responsive materials that can undergo programmed changes in shape and mechanical properties upon application of an

external stimulus such as heat [40], light [41], electrical current [42, 43], magnetic field [44, 45], pH [46], or solvent [47]. The most common triggering mechanism for SMPs remains direct heating [48]. For a polymer to possess shape memory behavior, two requirements must be satisfied: first, the material must contain chemical or physical crosslinks to “memorize” the permanent shape; second, the material must contain a “mobility switching” mechanism that enables the material to transition between states of low chain mobility and high chain mobility. These mobility switching mechanisms exist in the form of thermal transitions: glass transition temperature (T_g) for amorphous SMPs; crystallization (T_c) and melting transition temperatures (T_m) for semi-crystalline SMPs; and smectic-to-nematic (T_{SN}) or nematic-to-isotropic (T_{NI}) transition temperatures for liquid-crystalline networks.

A traditional one-way shape memory cycle consists of 4 steps (**Figure 1-1a**): (i) At an elevated temperature above its thermal transition temperature ($T > T_{trans}$), an SMP is deformed; (ii) while maintaining the deformation load, the SMP is cooled below its thermal transition temperature, freezing in the temporary shape through chain immobilization (vitrification for amorphous SMPs or crystallization for semi-crystalline SMPs); (iii) the SMP is unloaded to observe shape fixing; (iv) the unloaded SMP is heated back through its thermal transition temperature, affording chain mobility, and recovers back to its permanent shape. This cycle is graphically illustrated in **Figure 1-1b** for poly(cyclooctene), and quantitative descriptions of shape fixing—how much of the programmed deformation is maintained upon unloading—and shape recovery—how much of the programmed deformation is recovered upon heating—can be made.

The shape memory phenomenon is driven by entropic elasticity. At temperatures above its thermal transition temperature, an SMP is in an entropic rubbery state. Deformation of the

SMP serves to lower the entropy of this system, and upon removal of the deformation the SMP returns back to its higher entropic state. However, if the SMP is cooled below its thermal transition temperature while maintaining the deformation, this low-entropy state is “locked” in due to the reduction in chain mobility of individual polymer chains. Upon heating back through the transition temperature, chain mobility is restored and the SMP recovers back to its thermodynamically favored, high-entropy state [48].

1.4.1.1 Surface Shape Memory

While most SMP applications exploit bulk shape memory of polymer films, surface shape memory in the form of topography changing substrates is appealing for cell mechanobiology studies. One of the first demonstrations of surface shape memory was by Nelson and colleagues who showed complete recovery of nano-indentations could be achieved in crosslinked thermoset epoxies [49]. Our lab later developed soft liquid-crystal elastomers that could be reversibly embossed with a temporary micron-scale topography, recovering back to a flat topography upon heating through the transition temperature [50]. Xie et al. later demonstrated that the bulk shape memory effect could be exploited to form nano-topography in the form of wrinkles by fixing a temporary strain into a bulk SMP, coating it with a thin rigid film of “white gold”, and triggering shape recovery of the SMP [51]. Recovery of the SMP substrate induced buckling of the rigid film, forming nano-scale wrinkles. This technique is employed in **Chapters 2-3** to study cell response to nano-wrinkles.

1.4.1.2 Two-Way Shape Memory Polymers

A recent advance in SMP research has led to the development of two-way shape memory polymers, or polymers that can change shape reversibly [52, 53]. This effect has been most

commonly exploited using liquid-crystal elastomers [54], which have been developed with fast thermal- and photo-actuation [55, 56]. Liquid-crystal elastomers have also been reported to exhibit large reversible actuation strains exceeding 300% [57]. A cheaper, alternative class of reversible actuators was recently developed in our lab, where semi-crystalline SMPs were observed to undergo a phenomenon termed “stretch-induced crystallization” [52, 53]. During a typical one-way shape memory cycle, samples are deformed above their thermal transition temperature and cooled to fix in the temporary deformation. For some semi-crystalline SMPs, when cooling through the crystallization temperature under tensile load, a dramatic increase in strain is observed (stretch-induced crystallization) (**Figure 1-2a**). If the SMP is subjected to several heat/cool cycles through T_m/T_c while maintaining this load, reversible actuation can be achieved (**Figure 1-2b**). A schematic comparison of the one-way shape memory cycle and two-way shape memory cycle is shown in **Figure 1-2c**, and it’s important to note that two-way shape memory polymers also intrinsically possess one-way shape memory behavior. This phenomenon was observed in compression for the material system developed in **Chapter 4**, and is expected to be useful for cell mechanobiology studies and developing tissue engineered constructs where reversible actuation can be leveraged (e.g. muscles), as will be discussed in **Chapter 7**.

1.4.1.3 Multi-Shape Memory Polymers

A limitation of traditional one-way shape memory polymers is that they can only be programmed to transition from a prescribed temporary shape back to the permanent shape, where the permanent shape is dictated by the as-fabricated structure and cannot be altered. As such, there is limited control over the permanent shape. Recent developments in SMP chemistry have resulted in the fabrication of multi-shape memory polymers where control over multiple temporary shapes can be achieved [58, 59]. For instance, SMP systems featuring two well-

separated thermal transitions afford the ability to transition between 3 different shapes: 2 programmed shapes and one permanent shape [59, 60]. Thus these materials have been termed “triple-shape memory polymers”. These materials enable scientists to achieve shape change between two controllable, temporary shapes. While the SMP systems discussed in this dissertation do not involve multi-shape memory polymers, the fabrication methods described in **Chapter 4** have directly led to the development of novel triple-shape memory foams [61]. Furthermore, future advances in multi-shape memory polymers are expected to bring added functionality to tissue engineered constructs, as will be discussed in **Chapter 7**.

1.4.2 Applications of SMPs

Shape memory polymers date back as far as 1941, when a US patent was filed for a polymeric dental material possessing “elastic memory” [62]. Widespread commercial application of SMPs occurred in the 1960s with the invention of heat shrink tubing [63, 64]. Since then, SMPs have found use in applications ranging from deployable aerospace structures [65, 66], textiles [67], actuators [43], sensors [68], biomedical devices [69, 70], and tissue engineering constructs [71]. Interested readers are directed to several review articles highlighting these different applications [48, 72-76].

Of particular interest to the work of this dissertation is the use of SMPs for biomedical applications and tissue engineering constructs. Recent efforts in the medical device community have focused on developing medical devices for minimally invasive delivery, applications for which deployable SMPs are well suited. For example, the Maitland group developed an SMP device for mechanically removing blood clots [77]. Here an SMP polyurethane was coupled with an optical fiber that enabled laser triggering of the SMP, going from a temporary straight shape to a memorized corkscrew shape for pulling out the clot. This technology was further developed

to enable electrical triggering by coupling with a shape memory alloy, and in vitro testing conducted in a water-filled silicone neurovascular model [78]. Shape memory polymer foams, a focus of **Chapters 4-6** in this dissertation, have also been developed as deployable minimally invasive constructs such as aneurysm occlusion devices. For instance, Metcalfe and colleagues developed a cold hibernated elastic memory (CHEM) foam that deployed to fill and successfully occlude aneurysms in a dog model [79]. Maitland et al. developed a deployable SMP foam polyurethane for treatment of aneurysms that used a diode laser to photothermally trigger expansion [80]. Other minimally invasive applications of SMPs have included deployable stents [81], self-tightening sutures [69, 82], soft tissue fixation devices [83], and tissue-engineered cell delivery vehicles [84] (an application suitable for the foams developed in **Chapters 4-6**). Developing deployable SMPs for biomedical applications requires tailoring the SMP to deploy under physiological conditions (i.e. heating at body temperature, light activation, water-triggering), tailoring the mechanical properties of the device, and tailoring the chemical properties/degradation rates.

1.5 Active Cell Culture

1.5.1 Cell-Material Interactions in Dynamic Environments

As discussed in **Section 1.2**, cell-material interactions play a vital role in directing cell behaviors. While major advances in materials science have enabled the study of cell-material interactions atop substrates with varying degrees of complexity (e.g. topography, patterned surface chemistry, tailorable elasticity), most studies are still restricted to static substrates that do not mimic the dynamic environment *in vivo*. As highlighted in **Section 1.3**, the ECM is highly dynamic, and those dynamics are responsible for eliciting specific cell phenotypes and behaviors

during development, tissue formation, and repair, and abnormalities in ECM dynamics results in disease initiation and progression. Therefore, a need exists to develop substrates with increasing complexities that can undergo dynamic changes in properties (topography, surface chemistry, and elasticity) under cytocompatible conditions. Such substrates are expected to further our understanding of how cells interact and respond to the dynamic environment *in vivo*.

To address this need, researchers have developed several stimuli-responsive biomaterials. Thermo-responsive poly(N-isopropylacrylamide) materials have been used as cell-releasing substrates capable of triggering cell detachment upon cooling below the lower critical solution temperature (32 °C) [85]. Lam et al. developed a poly(dimethylsiloxane) substrate that, after plasma oxidizing, could form wrinkles with attached and viable cells by applying an external compressive force [86]. Reversible formation of the topography was able to align, unalign, and realign adherent C2C12 mouse myoblasts repeatedly. Dynamic topography changes have also been achieved on soft hydrogels, where an applied magnetic field reversibly induced embedded magnetic nickel microwires to form wrinkles [87]. Acute changes in smooth muscle cell morphology were elicited, but interestingly prolonged exposure to, and dynamic oscillation of, the topography only had a minor effect on morphology. Substrates with dynamic changes in stiffness have also been developed. Frey and Wang developed a polyacrylamide hydrogel that could be softened by up to 30% through UV-triggered crosslink degradation [88]. Surprisingly, these authors observed that softening of the posterior region of polarized cells produced no change in cell response, whereas softening of the anterior region resulted in the cell reversing polarity or becoming trapped in the softened region. These studies illustrate how dynamic changes to substrate properties can lead to new understandings about cell-material interactions.

1.5.2 Shape Memory Polymers as Active Cell Culture Substrates

The ability of SMPs to undergo programmed changes in shape and mechanical properties suits them well for use as dynamic cell culture substrates. Neuss and colleagues were the first to report the use of SMP shape change on cells in culture [71]. Here, cells were seeded on a poly(ϵ -caprolactone) dimethacrylate substrate programmed to contract when heated to 54 °C. As a consequence of this hyperthermic temperature, cell blebbing and death was observed. A primary obstacle preventing SMPs from being further explored for dynamic cell culture substrates was tailoring the recovery temperature to occur in a cell compatible range. Our group was the first to overcome this limitation and report an SMP substrate capable of undergoing a topography change at 37 °C with attached and viable cells [89, 90]. We showed that the shape memory effect could be used to turn on cell alignment as the SMP surface transitioned from a flat to grooved topography[89]. We've termed this application for SMPs as "*Active Cell Culture*" [90].

Subsequent studies have further demonstrated the potential of SMPs as *Active Cell Culture* substrates. Le et al. reported mesenchymal stem cell alignment could be controlled by triggering SMP topography change from 3 μm x 5 μm channels to a flat topography, and this could be achieved using a hyperthermic trigger temperature of 41 °C for a short duration [91]. Later, Ebara and colleagues showed that poly(ϵ -caprolactone) (PCL), which has a T_m of ~60 °C, could be modified to tailor the T_m near 37 °C through combining two-branched and four-branched PCL macromonomers [92]. Using this PCL system, cell alignment on flat-to-nanotopography and nanotopography-to-flat SMPs could be controlled. More recently, an SMP hydrogel was employed to modulate stem cell differentiation through changes in cytoskeletal contractility [93]. Human mesenchymal stem cells were seeded on a hydrogel that was triggered to form a "box". Cells hanging on the walls and on the bottom of the box committed down an

osteogenic lineage while cells on the top of the box committed down an adipogenic lineage. This effect was attributed to contraction in cells grown on different sides of the hydrogel box being dramatically different [93]. These 2D examples illustrate the power of SMPs to modulate cell behavior in *Active Cell Culture* studies. The work in **Chapters 2-3** adds to this field of study by investigating cell alignment and migration atop 2D SMP substrates.

1.5.3 Current Challenges with Active Cell Culture Materials

Use of SMP substrates for *Active Cell Culture* has only been achieved recently, and as a result there are several challenges this dissertation aims to address. First, SMP actuated topography change of current *Active Cell Culture Substrates* is performed by embossing or molding a complex topography [89, 91]. For tunable topographies, this approach requires fabrication of multiple different molds or embossers. We aimed to develop a simple method for developing a dynamic topography with tunable surface features, which we successfully accomplished in **Chapter 2** with a simple wrinkling bilayer system. Additionally, studies involving *Active Cell Culture* SMP substrates have focused primarily on topographical effect on cell alignment. In **Chapter 3**, we developed a method for imaging and tracking cells in real-time to investigate topographical effect on cell motility, a cell behavior that plays an important role during development and tumor metastasis.

While several 2D SMP substrates have been developed for studying cell mechanobiological response *in vitro*, few 3D SMP materials with cytocompatible triggering conditions have been reported. Cui et al. developed 3D porous SMPs that could change pore shape at 37 °C, but no cell studies were performed [94]. Subsequently, we reported the first 3D SMP scaffold with attached and viable cells under body temperature triggering. Cells seeded on an aligned fiber mat showed preferential alignment parallel to the aligned fibers. Upon triggering

fiber reorganization to a random orientation, cells reoriented and lost preferential alignment [95]. This recent advancement, accomplished in thin fiber mats, suggests the potential for further advancements in active 3D scaffolds for tissue engineering, regenerative medicine, and the study of cell mechanobiology. Particularly there is a need to develop 3D scaffolds with increased thickness, larger tunable pore sizes, and the ability to apply large strains to attached cells. We have addressed this need by fabricating highly porous, interconnected SMP foam scaffolds in **Chapters 4-6**, and we demonstrate their applicability in bone tissue engineering and cell mechanobiology.

1.6 Scope of Dissertation

This dissertation examines the use of thermal-responsive shape memory polymers (SMPs) as platforms for studying cell mechanobiology and tissue engineering. The aim of this work is to develop 2D substrates and 3D scaffolds capable of undergoing programmed changes in shape when heated to body temperature, and to explore how these programmed changes in shape can be employed to direct cell behavior *in vitro* and be used to develop functional scaffolds *in vivo*. A chapter-by-chapter outline is presented below.

The current chapter (**Chapter 1**) provides an overview of the importance cell-material interactions play *in vitro* and *in vivo* and how SMPs can be exploited to ascertain the effect dynamic material properties have on cell behavior. **Chapter 2** describes a new SMP bilayer system capable of forming nanoscale wrinkles once heated to body temperature. Here, a pre-strained acrylate-based SMP substrate is coated with a thin layer of gold. Recovery of the pre-strained SMP induces buckling in the gold layer, forming nanoscale wrinkles. Characterization of these wrinkles and the effect wrinkling has on the alignment of adherent cells is investigated. In **Chapter 3** the same bilayer system is employed to study the effect of wrinkles on cell motility

in vitro. A new cell tracking algorithm is developed and used to describe differences in cell motility on substrates with and without wrinkles.

Chapters 4-6 focus on the development and application of 3D SMP scaffolds. In **Chapter 4**, a modified porogen-leaching technique is used to develop highly porous and interconnected scaffolds of poly(ϵ -caprolactone)-co-poly(ethylene glycol) (PCL-co-PEG). Body temperature triggering is achieved by changing the ratio of PCL to PEG and by changing the deformation temperature during shape programming. Characterization of scaffold architecture and shape memory behavior is conducted. In **Chapter 5**, the use of porous SMP scaffolds as expanding synthetic bone grafts is investigated. Semi-crystalline PCL-co-PEG scaffolds and amorphous acrylate-based scaffolds are implanted in a mouse segmental defect model, and the ability of the scaffolds to provide stability to the defect and integrate with the native bone is investigated. **Chapter 6** explores the effect that scaffold expansion has on osteogenic differentiation of adherent stem cells *in vitro*. Stem cells are seeded in compressed SMP scaffolds that are triggered to expand after five days of culture. Protein expression, gene expression, and calcium deposition are assayed to determine if scaffold expansion affects osteogenic differentiation. Finally, **Chapter 7** provides a summary of the findings of this research and suggests future work and directions of using SMP scaffolds for biomedical applications.

1.7 References

- [1] Berthiaume F, Maguire TJ, Yarmush ML. Tissue engineering and regenerative medicine: history, progress, and challenges. Annual review of chemical and biomolecular engineering. 2011;2:403-30.
- [2] O'brien FJ. Biomaterials & scaffolds for tissue engineering. Materials Today. 2011;14:88-95.

- [3] Wong JY, Leach JB, Brown XQ. Balance of chemistry, topography, and mechanics at the cell–biomaterial interface: Issues and challenges for assessing the role of substrate mechanics on cell response. *Surface Science*. 2004;570:119-33.
- [4] Giancotti FG, Ruoslahti E. Integrin signaling. *Science*. 1999;285:1028-33.
- [5] Juliano R, Haskill S. Signal transduction from the extracellular matrix. *Journal of Cell Biology*. 1993;120:577-.
- [6] Palecek SP, Loftus JC, Ginsberg MH, Lauffenburger DA, Horwitz AF. Integrin-ligand binding properties govern cell migration speed through cell-substratum adhesiveness. *Nature*. 1997;385:537-40.
- [7] Maheshwari G, Wells A, Griffith LG, Lauffenburger DA. Biophysical Integration of Effects of Epidermal Growth Factor and Fibronectin on Fibroblast Migration. *Biophysical Journal*. 1999;76:2814-23.
- [8] Huttenlocher A, Ginsberg MH, Horwitz AF. Modulation of cell migration by integrin-mediated cytoskeletal linkages and ligand-binding affinity. *The Journal of Cell Biology*. 1996;134:1551-62.
- [9] Chen CS, Mrksich M, Huang S, Whitesides GM, Ingber DE. Micropatterned surfaces for control of cell shape, position, and function. *Biotechnology Progress*. 1998;14:356-63.
- [10] Peng R, Yao X, Ding J. Effect of cell anisotropy on differentiation of stem cells on micropatterned surfaces through the controlled single cell adhesion. *Biomaterials*. 2011;32:8048-57.
- [11] Abrams G, Goodman S, Nealey P, Franco M, Murphy C. Nanoscale topography of the basement membrane underlying the corneal epithelium of the rhesus macaque. *Cell and tissue research*. 2000;299:39-46.

- [12] Abrams G, Schaus S, Goodman S, Nealey P, Murphy C. Nanoscale topography of the corneal epithelial basement membrane and Descemet's membrane of the human. *Cornea*. 2000;19:57-64.
- [13] Abrams GA, Bentley E, Nealey PF, Murphy CJ. Electron microscopy of the canine corneal basement membranes. *Cells Tissues Organs*. 2002;170:251-7.
- [14] Bozec L, van der Heijden G, Horton M. Collagen fibrils: nanoscale ropes. *Biophysical journal*. 2007;92:70-5.
- [15] Bettinger CJ, Langer R, Borenstein JT. Engineering substrate topography at the micro-and nanoscale to control cell function. *Angewandte Chemie International Edition*. 2009;48:5406-15.
- [16] Bettinger CJ, Zhang Z, Gerecht S, Borenstein JT, Langer R. Enhancement of in vitro capillary tube formation by substrate nanotopography. *Advanced Materials*. 2008;20:99-103.
- [17] Teixeira AI, Abrams GA, Bertics PJ, Murphy CJ, Nealey PF. Epithelial contact guidance on well-defined micro-and nanostructured substrates. *Journal of cell science*. 2003;116:1881-92.
- [18] Teixeira AI, McKie GA, Foley JD, Bertics PJ, Nealey PF, Murphy CJ. The effect of environmental factors on the response of human corneal epithelial cells to nanoscale substrate topography. *Biomaterials*. 2006;27:3945-54.
- [19] Yim EK, Pang SW, Leong KW. Synthetic nanostructures inducing differentiation of human mesenchymal stem cells into neuronal lineage. *Experimental cell research*. 2007;313:1820-9.
- [20] Wang X, Ohlin CA, Lu Q, Hu J. Cell directional migration and oriented division on three-dimensional laser-induced periodic surface structures on polystyrene. *Biomaterials*. 2008;29:2049-59.

- [21] Dalton B, Walboomers XF, Dziegielewski M, Evans MD, Taylor S, Jansen JA, et al. Modulation of epithelial tissue and cell migration by microgrooves. *Journal of biomedical materials research*. 2001;56:195-207.
- [22] Pelham RJ, Wang Y-l. Cell locomotion and focal adhesions are regulated by substrate flexibility. *Proceedings of the National Academy of Sciences*. 1997;94:13661-5.
- [23] Lo C-M, Wang H-B, Dembo M, Wang Y-l. Cell movement is guided by the rigidity of the substrate. *Biophysical journal*. 2000;79:144-52.
- [24] Yeung T, Georges PC, Flanagan LA, Marg B, Ortiz M, Funaki M, et al. Effects of substrate stiffness on cell morphology, cytoskeletal structure, and adhesion. *Cell motility and the cytoskeleton*. 2005;60:24-34.
- [25] Engler AJ, Sen S, Sweeney HL, Discher DE. Matrix elasticity directs stem cell lineage specification. *Cell*. 2006;126:677-89.
- [26] Gilbert PM, Havenstrite KL, Magnusson KE, Sacco A, Leonardi NA, Kraft P, et al. Substrate elasticity regulates skeletal muscle stem cell self-renewal in culture. *Science*. 2010;329:1078-81.
- [27] Frantz C, Stewart KM, Weaver VM. The extracellular matrix at a glance. *Journal of cell science*. 2010;123:4195-200.
- [28] Hynes RO. The extracellular matrix: not just pretty fibrils. *Science*. 2009;326:1216-9.
- [29] Lu P, Takai K, Weaver VM, Werb Z. Extracellular matrix degradation and remodeling in development and disease. *Cold Spring Harbor perspectives in biology*. 2011;3:a005058.
- [30] Fata JE, Werb Z, Bissell MJ. Regulation of mammary gland branching morphogenesis by the extracellular matrix and its remodeling enzymes. *Breast cancer research*. 2003;6:1.

- [31] Daley WP, Peters SB, Larsen M. Extracellular matrix dynamics in development and regenerative medicine. *Journal of cell science*. 2008;121:255-64.
- [32] Li J, Zhang YP, Kirsner RS. Angiogenesis in wound repair: angiogenic growth factors and the extracellular matrix. *Microscopy research and technique*. 2003;60:107-14.
- [33] Sakai T, Larsen M, Yamada KM. Fibronectin requirement in branching morphogenesis. *Nature*. 2003;423:876-81.
- [34] Vu TH, Werb Z. Matrix metalloproteinases: effectors of development and normal physiology. *Genes & development*. 2000;14:2123-33.
- [35] Stupack DG, Chersesh DA. ECM remodeling regulates angiogenesis: endothelial integrins look for new ligands. *Science Signaling*. 2002;2002:pe7.
- [36] Cox TR, Erler JT. Remodeling and homeostasis of the extracellular matrix: implications for fibrotic diseases and cancer. *Disease models & mechanisms*. 2011;4:165-78.
- [37] Friedman SL. Molecular regulation of hepatic fibrosis, an integrated cellular response to tissue injury. *Journal of Biological Chemistry*. 2000;275:2247-50.
- [38] Lu P, Weaver VM, Werb Z. The extracellular matrix: a dynamic niche in cancer progression. *The Journal of cell biology*. 2012;196:395-406.
- [39] Provenzano PP, Eliceiri KW, Campbell JM, Inman DR, White JG, Keely PJ. Collagen reorganization at the tumor-stromal interface facilitates local invasion. *BMC medicine*. 2006;4:38.
- [40] Xie T, Rousseau IA. Facile tailoring of thermal transition temperatures of epoxy shape memory polymers. *Polymer*. 2009;50:1852-6.
- [41] Lendlein A, Jiang H, Jünger O, Langer R. Light-induced shape-memory polymers. *Nature*. 2005;434:879-82.

- [42] Liu Y, Lv H, Lan X, Leng J, Du S. Review of electro-active shape-memory polymer composite. *Composites Science and Technology*. 2009;69:2064-8.
- [43] Luo X, Mather PT. Conductive shape memory nanocomposites for high speed electrical actuation. *Soft Matter*. 2010;6:2146-9.
- [44] Schmidt AM. Electromagnetic activation of shape memory polymer networks containing magnetic nanoparticles. *Macromolecular Rapid Communications*. 2006;27:1168-72.
- [45] Mohr R, Kratz K, Weigel T, Lucka-Gabor M, Moneke M, Lendlein A. Initiation of shape-memory effect by inductive heating of magnetic nanoparticles in thermoplastic polymers. *Proceedings of the National Academy of Sciences of the United States of America*. 2006;103:3540-5.
- [46] Han XJ, Dong ZQ, Fan MM, Liu Y, Wang YF, Yuan QJ, et al. pH-Induced Shape-Memory Polymers. *Macromolecular rapid communications*. 2012;33:1055-60.
- [47] Du H, Zhang J. Solvent induced shape recovery of shape memory polymer based on chemically cross-linked poly (vinyl alcohol). *Soft Matter*. 2010;6:3370-6.
- [48] Mather PT, Luo X, Rousseau IA. Shape memory polymer research. *Annual Review of Materials Research*. 2009;39:445-71.
- [49] Nelson BA, King WP, Gall K. Shape recovery of nanoscale imprints in a thermoset "shape memory" polymer. *Applied Physics Letters*. 2005;86:3108.
- [50] Burke KA, Mather PT. Soft shape memory in main-chain liquid crystalline elastomers. *Journal of Materials Chemistry*. 2010;20:3449-57.
- [51] Xie T, Xiao X, Li J, Wang R. Encoding localized strain history through wrinkle based structural colors. *Advanced Materials*. 2010;22:4390-4.

- [52] Chung T, Romo-Uribe A, Mather PT. Two-way reversible shape memory in a semicrystalline network. *Macromolecules*. 2008;41:184-92.
- [53] Westbrook KK, Mather PT, Parakh V, Dunn ML, Ge Q, Lee BM, et al. Two-way reversible shape memory effects in a free-standing polymer composite. *Smart Materials and Structures*. 2011;20:065010.
- [54] Camacho-Lopez M, Finkelmann H, Palffy-Muhoray P, Shelley M. Fast liquid-crystal elastomer swims into the dark. *Nature materials*. 2004;3:307-10.
- [55] White TJ, Serak SV, Tabiryan NV, Vaia RA, Bunning TJ. Polarization-controlled, photodriven bending in monodomain liquid crystal elastomer cantilevers. *Journal of Materials Chemistry*. 2009;19:1080-5.
- [56] Lee KM, Koerner H, Vaia RA, Bunning TJ, White TJ. Light-activated shape memory of glassy, azobenzene liquid crystalline polymer networks. *Soft Matter*. 2011;7:4318-24.
- [57] Wermter H, Finkelmann H. Liquid crystalline elastomers as artificial muscles. *e-Polymers*. 2001;1:111-23.
- [58] Xie T. Tunable polymer multi-shape memory effect. *Nature*. 2010;464:267-70.
- [59] Luo X, Mather PT. Triple-Shape Polymeric Composites (TSPCs). *Advanced Functional Materials*. 2010;20:2649-56.
- [60] Bellin I, Kelch S, Langer R, Lendlein A. Polymeric triple-shape materials. *Proceedings of the National Academy of Sciences*. 2006;103:18043-7.
- [61] Nejad HB, Baker RM, Mather PT. Preparation and characterization of triple shape memory composite foams. *Soft matter*. 2014;10:8066-74.
- [62] L. B. Vernon H.M.V. Producing Molded Articles such as Dentures from Thermoplastic Synthetic Resins. US Patent. 1941:2234993.

- [63] W. C. Rainer EMR, J. J. Hitov, A. W. Sloan and W.D. Stewart. Heat-shrinkable Polyethylene. US Patent. 1964:3144398.
- [64] Perrone RJ. Heat-shrinkable Articles made from Silicone Rubber-Polyethylene Compositions. US Patent. 1967:3326869.
- [65] Liu Y, Du H, Liu L, Leng J. Shape memory polymers and their composites in aerospace applications: a review. *Smart Materials and Structures*. 2014;23:023001.
- [66] Fabrizio Q, Loredana S, Anna SE. Shape memory epoxy foams for space applications. *Materials Letters*. 2012;69:20-3.
- [67] Vili YYC. Investigating smart textiles based on shape memory materials. *Textile Research Journal*. 2007;77:290-300.
- [68] Kunzelman J, Chung T, Mather PT, Weder C. Shape memory polymers with built-in threshold temperature sensors. *Journal of Materials Chemistry*. 2008;18:1082-6.
- [69] Lendlein A, Langer R. Biodegradable, elastic shape-memory polymers for potential biomedical applications. *Science*. 2002;296:1673-6.
- [70] Singhal P, Small W, Cosgriff-Hernandez E, Maitland DJ, Wilson TS. Low density biodegradable shape memory polyurethane foams for embolic biomedical applications. *Acta biomaterialia*. 2014;10:67-76.
- [71] Neuss S, Blumenkamp I, Stainforth R, Boltersdorf D, Jansen M, Butz N, et al. The use of a shape-memory poly (ϵ -caprolactone) dimethacrylate network as a tissue engineering scaffold. *Biomaterials*. 2009;30:1697-705.
- [72] Sokolowski W, Metcalfe A, Hayashi S, Yahia LH, Raymond J. Medical applications of shape memory polymers. *Biomedical Materials*. 2007;2:S23.

- [73] Ward Small I, Singhal P, Wilson TS, Maitland DJ. Biomedical applications of thermally activated shape memory polymers. *Journal of materials chemistry*. 2010;20:3356-66.
- [74] Meng H, Li G. A review of stimuli-responsive shape memory polymer composites. *Polymer*. 2013;54:2199-221.
- [75] Liu C, Qin H, Mather P. Review of progress in shape-memory polymers. *Journal of Materials Chemistry*. 2007;17:1543-58.
- [76] Leng J, Lan X, Liu Y, Du S. Shape-memory polymers and their composites: stimulus methods and applications. *Progress in Materials Science*. 2011;56:1077-135.
- [77] Maitland DJ, Metzger MF, Schumann D, Lee A, Wilson TS. Photothermal properties of shape memory polymer micro-actuators for treating stroke. *Lasers in Surgery and Medicine*. 2002;30:1-11.
- [78] Small W, Wilson TS, Buckley PR, Benett WJ, Loge JA, Hartman J, et al. Prototype fabrication and preliminary in vitro testing of a shape memory endovascular thrombectomy device. *Ieee Transactions on Biomedical Engineering*. 2007;54:1657-66.
- [79] Metcalfe A, Desfaits AC, Salazkin I, Yahia L, Sokolowski WM, Raymond J. Cold hibernated elastic memory foams for endovascular interventions. *Biomaterials*. 2003;24:491-7.
- [80] Maitland DJ, Small W, Ortega JM, Buckley PR, Rodriguez J, Hartman J, et al. Prototype laser-activated shape memory polymer foam device for embolic treatment of aneurysms. *Journal of Biomedical Optics*. 2007;12:3.
- [81] Yakacki CM, Shandas R, Lanning C, Rech B, Eckstein A, Gall K. Unconstrained recovery characterization of shape-memory polymer networks for cardiovascular applications. *Biomaterials*. 2007;28:2255-63.

- [82] Zhang H, Wang H, Zhong W, Du Q. A novel type of shape memory polymer blend and the shape memory mechanism. *Polymer*. 2009;50:1596-601.
- [83] Yakacki CM, Shandas R, Safranski D, Ortega AM, Sassaman K, Gall K. Strong, Tailored, Biocompatible Shape-Memory Polymer Networks. *Advanced functional materials*. 2008;18:2428-35.
- [84] Thornton AJ, Alsberg E, Albertelli M, Mooney DJ. Shape-defining scaffolds for minimally invasive tissue engineering. *Transplantation*. 2004;77:1798-803.
- [85] Takezawa T, Mori Y, Yoshizato K. Cell culture on a thermo-responsive polymer surface. *Nature Biotechnology*. 1990;8:854-6.
- [86] Lam MT, Clem WC, Takayama S. Reversible on-demand cell alignment using reconfigurable microtopography. *Biomaterials*. 2008;29:1705-12.
- [87] Kiang JD, Wen JH, del Álamo JC, Engler AJ. Dynamic and reversible surface topography influences cell morphology. *Journal of Biomedical Materials Research Part A*. 2013;101:2313-21.
- [88] Frey MT, Wang Y-l. A photo-modulatable material for probing cellular responses to substrate rigidity. *Soft Matter*. 2009;5:1918-24.
- [89] Davis KA, Burke KA, Mather PT, Henderson JH. Dynamic cell behavior on shape memory polymer substrates. *Biomaterials*. 2011;32:2285-93.
- [90] Davis KA, Luo X, Mather PT, Henderson JH. Shape memory polymers for active cell culture. *Journal of visualized experiments: JoVE*. 2011.
- [91] Le DM, Kulangara K, Adler AF, Leong KW, Ashby VS. Dynamic Topographical Control of Mesenchymal Stem Cells by Culture on Responsive Poly(epsilon-caprolactone) Surfaces. *Advanced Materials*. 2011;23:3278-+.

- [92] Ebara M, Uto K, Idota N, Hoffman JM, Aoyagi T. Shape-Memory Surface with Dynamically Tunable Nano-Geometry Activated by Body Heat. *Advanced Materials*. 2012;24:273-8.
- [93] Han Y, Bai T, Liu W. Controlled Heterogeneous Stem Cell Differentiation on a Shape Memory Hydrogel Surface. *Scientific reports*. 2014;4.
- [94] Cui J, Kratz K, Heuchel M, Hiebl B, Lendlein A. Mechanically active scaffolds from radio-opaque shape-memory polymer-based composites. *Polymers for Advanced Technologies*. 2011;22:180-9.
- [95] Tseng L-F, Mather PT, Henderson JH. Shape-memory-actuated change in scaffold fiber alignment directs stem cell morphology. *Acta biomaterialia*. 2013;9:8790-801.

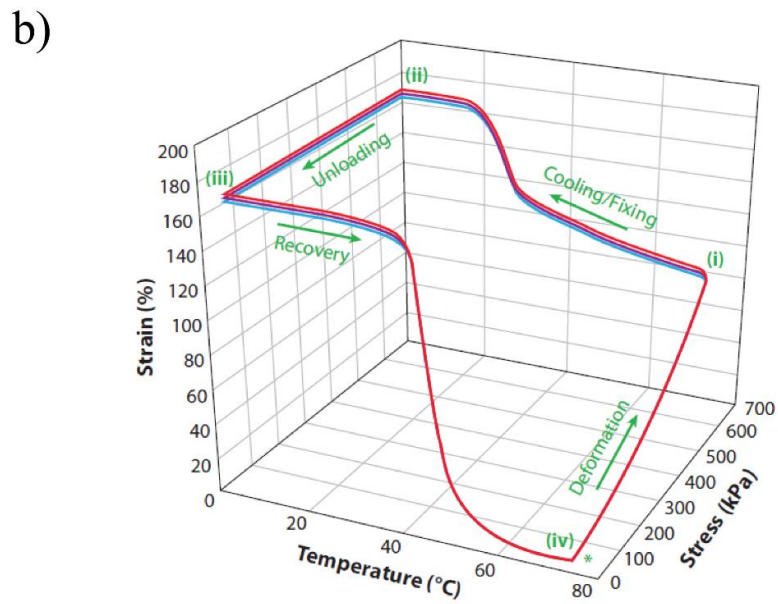
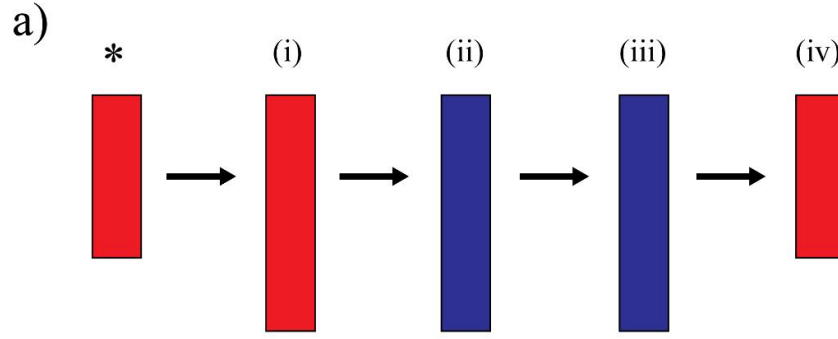
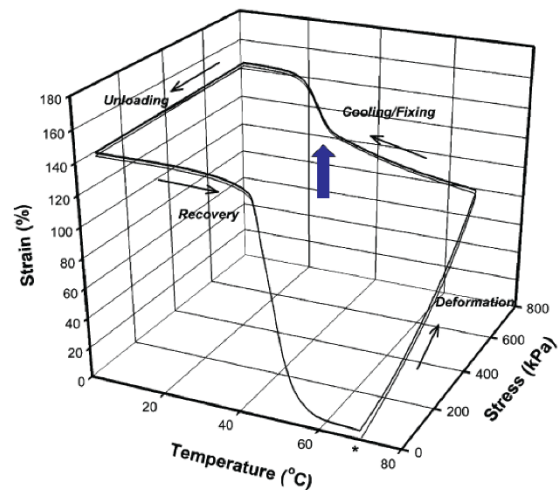
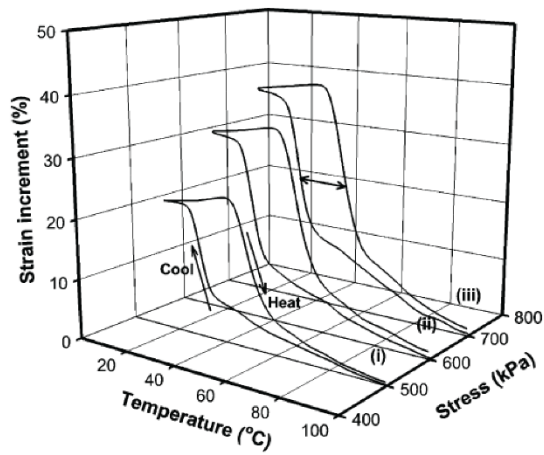


Figure 1-1. One-way shape memory behavior. (a) Schematic depicting a one-way shape memory cycle. Starting at the (*) above the sample's thermal transition temperature, the sample is (i) deformed, (ii) cooled to fix the temporary strain, (iii) unloaded to observe fixing, and (iv) heated to trigger recovery; (b) a corresponding one-way shape memory cycle of crosslinked poly(cyclooctene), with (i-iv) corresponding to the schematic in (a). Figure in (b) is adopted with permission from ref [48].

a)



b)



c)

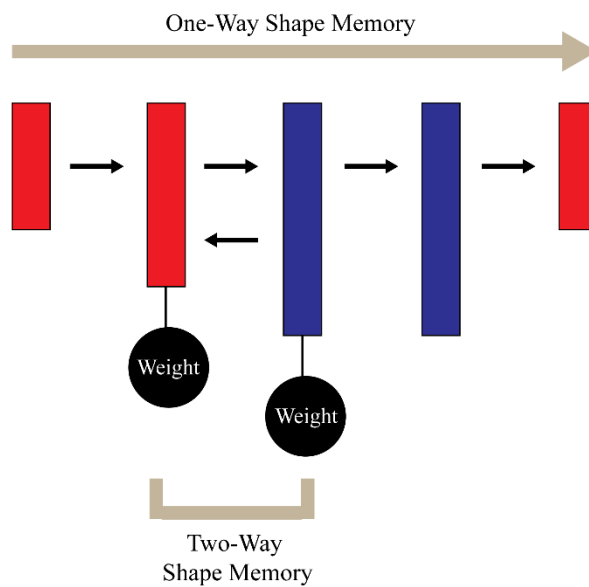


Figure 1-2. Two-way shape memory behavior. (a) The one-way shape memory cycle of poly(cyclooctene) shows a stretch-induced crystallization upon cooling (blue arrow), indicative of two-way shape memory capacity; (b) two-way shape memory behavior of a poly(cyclooctene) sample at different stresses, (i) 500, (ii) 600, and (iii) 700 kPa upon heating/cooling; (c) schematic showing the difference between one-way and two-way shape memory. Two-way shape memory is achieved through repeated heat/cool cycles while maintaining load (weight). Figures in (a) and (b) adapted with permission from ref [52].

Chapter Two: Shape Memory Induced Wrinkle Formation Directs

Cell Alignment In Vitro¹

2.1 Synopsis

This chapter introduces a novel “active cell culture” substrate that can be used to study cell-material interactions atop substrates with actively changing topographies. A tunable shape memory polymer (SMP) bilayer system is programmed to form, under cell compatible conditions, wrinkles with feature sizes on the micron and sub-micron length scale. The ability to control wrinkle wavelength and amplitude through programmed strain in the SMP substrate is investigated, and cell alignment atop substrates with different wrinkle characteristics is assessed. Cell alignment atop previously wrinkled substrates is compared to cell alignment atop actively wrinkling substrates. The tailored and dynamic substrate functionality provided by this approach is expected to enable new investigation and understanding of cell mechanobiology

2.2 Introduction

Ordered patterns with feature sizes on the micron and sub-micron scale play an important role in cell mechanobiology *in vivo*. Cells actively probe and respond to their microenvironment, and the extracellular matrix (ECM) contains proteins with feature sizes in this range that can direct cell function. Cell-matrix interactions have been found to be critical to many biological processes, including angiogenesis [1], embryogenesis [2], and tumorigenesis [3]. While it is known that cell-matrix interactions play a role in biological development, the fundamental

¹Adapted (in part) with permission from P. Yang, R.M. Baker, J.H. Henderson and P.T. Mather, *Soft Matter*, **2013**, 9, 4705-4714. Copyright © Royal Society of Chemistry 2013

mechanisms underlying the cell response largely remain unclear, and technologies exploiting the interactions have remained elusive.

To better understand how cell-matrix interactions direct cell behavior, synthetic substrates of defined topographies on the micro- and nano-scale have been developed and applied *in vitro*. Topographies have included nanofibers [4], nanogratings [5, 6], and nanopillars and nanopits [7]. Studies employing such substrates have shown that cell alignment, migration, proliferation, and cell lineage specification are affected by topography [5, 6, 8, 9]. The structure and size of the topographical features as well as the cell species and cell type determine the nature and extent of the cell response [10].

Surface wrinkling offers an elegant alternative to direct molding of surface topographies for the purpose of controlled cell-material interaction. Surface buckling, or wrinkling, is a natural phenomenon that occurs in daily life. In a bilayer system consisting of a thick compliant substrate and a thin rigid coating undergoing compression, whether by differential thermal contraction [11, 12], externally applied compressive force [13], or differential swelling or shrinkage [14-16], the rigid coating buckles to yield distinct wrinkling patterns ranging from homogenous [17] to hierarchical [18-21] wrinkles, one-dimensional ripple pattern [22] to two-dimensional herringbone [23, 24] and more complex patterns [12, 25, 26]. The Burdick lab has reported interesting studies on swelling-induced wrinkles on hydrogels and their interactions with stem cells.[27, 28] Models describing the mechanics of wrinkle formation provide predictions of the amplitude and wavelength within the frameworks of small [29, 30] and large [31] strain deformation, giving promise for the control of such features to the extent that compressive strain can be manipulated. For small deformations, wrinkle formation is well

modeled by minimizing the total elastic energy [29, 32] in a uniaxial bilayer wrinkle system whose wavelength, λ , and amplitude, A , are given as follows:

$$\lambda = 2\pi h_f \left(\frac{\bar{E}_f}{3\bar{E}_s} \right)^{\frac{1}{3}} \quad (\text{Eq 2-1})$$

$$A = h_f \left(\frac{\varepsilon}{\varepsilon_c} - 1 \right)^{\frac{1}{2}} \quad (\text{Eq 2-2})$$

$$\varepsilon_c = \frac{1}{4} \left(\frac{3\bar{E}_s}{\bar{E}_f} \right)^{\frac{2}{3}} \quad (\text{Eq 2-3})$$

Here, $\bar{E} = E/(1 - \nu^2)$, ε_c is the critical or minimum strain that is necessary for buckling to occur, h_f is the film thickness, ν is Poisson's ratio, and \bar{E}_f and \bar{E}_s are the plane-strain moduli of the film and substrate, respectively.

While polydimethylsiloxane (PDMS) is the most popular compliant substrate used for wrinkle formation [11, 18, 22, 23, 33], recent attention has turned to the use of shape memory polymers (SMPs) as “active” wrinkling substrates that can apply compression to a coating upon triggering a return from a temporarily strained state to the equilibrium, unstrained state [34, 35]. While the first reported use of an SMP as a substrate for wrinkle formation [36] involved a polystyrene SMP that yielded nano-scale, hierarchical wrinkles of a gold coating, subsequent diversified approaches have included the IPH (Indentation-Polishing-Heating) process [37], and the creation of localized structural colors [38]. Intended applications range from optical devices [39], to electronics [17, 40, 41], to controlled surface wettability [16, 42] and biosensors [36, 43]. Interested readers are referred to a recently published review article highlighting current work on wrinkle formation via the shape memory effect in polymers and metal alloys [44].

In this study, our goal was to prepare a coated SMP bilayer system for the study of cell mechanobiology on previously wrinkled (static) and actively wrinkling (dynamic) substrates, recognizing the need to develop a “tunable” SMP that was compatible with cell culture. We hypothesized that by changing the amount of deformation fixed (and later recovered) in the new SMP substrate we could control the resulting wrinkle characteristics and the resulting degree of cellular alignment. In addition to studying cells cultured on previously wrinkled, static substrates, study of the response of cells to wrinkle formation during “active” cell culture is enabled for the first time. For active cell culture, cell seeding is performed at a cell-compatible temperature below body temperature and below the temperature at which wrinkles form, followed by a thermal activation at body temperature, forming wrinkles. In this manner, wrinkles form on a time scale comparable to both cell motility and cell division, yielding an opportunity to study dynamic interactions among these phenomena.

2.3 Methods and Materials

2.3.1 Materials

Tert-butyl acrylate (tBA), butyl acrylate (BA), tetraethylene glycol dimethacrylate (TEGDMA), and 2,2-dimethoxy-2-phenyl acetophenone (DMPA) were purchased from Sigma Aldrich. Prior to use, tBA and BA were purified by passing through inhibitor removal columns (SDHR-4, Scientific Polymer). TEGDMA and DMPA were used as received.

2.3.2 Substrate Preparation

A copolymerization technique was employed to synthesize a substrate with a tunable glass transition temperature (T_g). Two monomers, tBA and BA, were mixed with a crosslinker,

TEGDMA, and a photoinitiator, DMPA (**Scheme 1**), and injected between two glass slides with a 1 mm thick Teflon spacer. Glass slides were treated with Rain-X™ (Rain-X) to prevent adhesion with the cured SMP films. After injection, the mold was placed in a UV box (Black Ray, 365 nm, 2.0 mW/cm²) featuring symmetric illumination from both sides of each specimen and allowed to cure for 1 h. To determine the effect of comonomer composition on the T_g , five formulations of tBA-BA were prepared (100tBA-0BA, 75tBA-25BA, 50tBA-50BA, 25tBA-75BA, and 0tBA-100BA), where each number corresponds to the wt-% of tBA-BA in the copolymer film (e.g. 75tBA-25BA refers to 75 wt-% of tBA and 25 wt-% of BA in the comonomer solution). The wt-% of crosslinker, TEGDMA, was kept constant at 5 wt-% relative to the comonomer weight, and a constant 0.5 wt-% of DMPA photoinitiator, relative to the comonomer weight, was used. By tuning the T_g of the system, control over the activation temperature for wrinkle formation could be achieved since the shape memory effect for amorphous-based SMPs is driven by the T_g .

For active cell culture experiments conducted in this study, a composition of 95tBA-5BA was used as this composition enabled wrinkle formation at 37 °C. An example formulation for preparing this substrate is as follows: tBA (1.5 g), BA (78.9 mg), TEGDMA (61.5 mg), and DMPA (8.2 mg). Following photocure the polymer films were placed in methanol for 6 h to extract unreacted monomers and free linear chains and dried overnight.

2.3.3 Substrate Characterization

2.3.3.1 Thermal Characterization

Differential scanning calorimetry (DSC) was employed to determine the T_g of each composition. DSC experiments were conducted using a Q200 (TA Instruments) equipped with a

refrigerated cooling system. Samples with a mass of 3-5 mg were placed in Tzero aluminum pans (TA Instruments) and were heated from -10 °C to 80 °C (first heat), cooled back to -10 °C (first cool), and finally heated back to 80 °C (second heat). All heating and cooling rates were 3 °C-min⁻¹. The T_g of each sample was determined using Universal Analysis Software (TA Instruments) to calculate the inflection point of the step transition in heat flow from the second heating trace.

2.3.3.2 Thermomechanical Characterization

Linear viscoelastic thermomechanical properties of the SMP substrate were determined using a dynamic mechanical analyzer (DMA) (TA Instruments Q800). A rectangular bar of the copolymer film was cut and placed in the tensile grips of the DMA and loaded in multi-frequency strain mode with an oscillation amplitude of 10 µm and an oscillation frequency of 1 Hz. The sample was heated to 70 °C to erase all thermal history and then cooled to -90 °C at 3 °C-min⁻¹. Once thermally equilibrated, the sample was heated to 100 °C at 3 °C-min⁻¹. The second heating trace was recorded and used to determine storage modulus as a function of temperature.

To determine the shape memory characteristics of the SMP substrate, a rectangular bar was first loaded in the DMA at room temperature. In controlled force mode, the sample was heated to 70 °C, deformed to 50% strain, and then cooled to 10 °C to fix the deformation through vitrification of the amorphous network chains. To recover the deformation, the sample was heated to 70 °C, completing the shape memory cycle. Three cycles were repeated to investigate shape memory reproducibility of the substrate. The fixing ratio (R_f), or the degree of fixing, and the recovery ratio (R_r) were calculated as [45]:

$$R_f(N) = \frac{\varepsilon_u(N)}{\varepsilon_m(N)} \times 100\% \quad (\text{Eq 2-4})$$

$$R_r(N) = \frac{\varepsilon_u(N) - \varepsilon_p(N)}{\varepsilon_u(N) - \varepsilon_p(N-1)} \times 100\% \quad (\text{Eq 2-5})$$

Here N , ε_u , ε_m , and ε_p represent the cycle number, strain after unloading, strain before unloading, and the final strain after heating under no applied load, respectively. Shape memory characterization of hydrated samples was also performed using the submersion tension clamp of the DMA, and the same procedure was followed.

To determine the thermomechanical properties of the substrate in the hydrated state, a rectangular bar of the sample was first equilibrated in water for 24 h. The sample was then loaded at room temperature into the DMA submersion clamp and heated to 70 °C at 2 °C-min⁻¹ while measuring the linear viscoelastic properties as a function of temperature at a frequency of 1 Hz.

2.3.3.3 Hydrated Recovery at 37 °C

The ability of the SMP substrate to recover a fixed strain under cell compatible conditions (hydrated at 37 °C) was assessed by measuring the time-dependent recovery profile using a DMA submersion tension clamp. A dogbone-cut sample with a 6.25 mm gauge length was loaded in the tension submersion clamp, heated to 70 °C, and uniaxially strained 14%. While maintaining the load, the sample was cooled to 10 °C at 10 °C-min⁻¹ and held isothermally for 5 min to fix the deformation. The sample was unloaded and the recovery kinetics assessed by heating the sample to 37 °C in a two-stage method. First the sample was heated at 5 °C-min⁻¹ to 30 °C and held isothermally for 5 min. Then the sample was heated at 5 °C-min⁻¹ to 37 °C and held isothermally for 360 min. This two-stage heating was performed to prevent significantly overshooting the set temperature of 37 °C. A heater PID of P:4.0, I:0.0, and D:0.2 was used.

2.3.4 Wrinkle Formation[‡]

2.3.4.1 Wrinkle Formation in Dry State

Wrinkle formation was enabled by compressive bulking of a gold coating that was first applied to an SMP that had been fixed with a temporary uniaxial strain and then recovered thermally (**Scheme 2**). To fix a strain into the substrate, uniaxial stretching was conducted using the DMA. Samples were first heated to 80 °C and subsequently loaded until a prescribed strain was achieved. Upon reaching the prescribed strain the load was held constant and the samples were cooled to fix the prestrain into the substrate. Uniaxial prestrains of 2, 7, 12, 17, and 23% were investigated to ascertain the effect of prestrain on wrinkle characteristics. Next, a gold coating was applied to the substrate via sputtering. A total sputter time of 100 s was used to yield a 33 nm thick layer, measured using a method developed by Bowden et. al [11]. Gold-coated substrates were placed in an isothermal oven at 55 °C for 30 min to allow the substrates to completely recover, resulting in wrinkle formation.

2.3.4.2 Wrinkle Formation in Hydrated State

Wrinkle formation experiments were conducted in water to simulate active cell culture conditions. Bilayers were prepared following the method described above (**Section 2.3.4.1**) with a prestrain of 12% fixed in the SMP substrate. After applying a thin gold layer to the substrate, the bilayer was placed in water at 30 °C for 5 h and then at 37 °C for 24 h. A control experiment was conducted with a bilayer submerged in water at 30 °C for 5 h and then for an additional 24 h at 30 °C, which was expected not to yield wrinkles. Characteristics of wrinkles formed in the

[‡] This work was performed by Dr. Pine Yang

hydrated state were compared to those formed in the dry state to determine if hydration influences wrinkling behavior.

2.3.5 Wrinkle Characterization[‡]

Atomic force microscopy (AFM; Nano R-2 from Pacific Nanotechnology) with tapping mode was employed to characterize the resulting wrinkle morphologies. Two dimensional Fast Fourier Transforms (2D FFT) were performed to analyze the wrinkle wavelength distributions. The wavelength was calculated as the inverse of wavenumber. A custom MatLab program (**Appendix 1**) was written and used to calculate the wrinkle amplitude using AFM profiles. Wrinkle alignment analysis based on the 2D FFT images was conducted by ImageJ software using the “Oval plot” function. The full width at half maximum value was chosen to represent the relative degree of wrinkle alignment. Optical microscopy (OM) was utilized to image cracks that form during wrinkling and the crack density (CD) calculated as the inverse of the average crack spacing measured directly from the optical micrographs.

2.3.6 Cell Culture

Prior to static and active cell culture experiments, human adipose derived stem cells (hASCs; Invitrogen) from a single donor were expanded in complete growth medium (MesenPro RS, 2% Growth Serum, 1% penicillin/streptomycin, 1% GlutaMAX). Cells were plated on T175 flasks at a seeding density of 5,000 cells-cm⁻² and expanded in a 37 °C humidified incubator with 5% CO₂. Growth medium was changed every 3 d and cells were passaged at 70% confluence using TrypLE. Cells at passages 6 and 7 were collected for the static and active cell experiments.

[‡] This work was performed by Dr. Pine Yang

2.3.6.1 Cell Culture on Previously Wrinkled Substrates

To evaluate the extent to which cell alignment could be controlled by wrinkle properties, hASCs were seeded on substrates after wrinkle formation had occurred and cell nuclear alignment was quantified. Following the procedure for wrinkle formation, SMPs with fixed uniaxial prestrains of 2, 7, 12, 17 and 23% were coated with gold and recovered for 2.5 h at 45 °C. A gold coated SMP with no prestrain was used as the control group. Samples from each group were cut into 6 mm x 6 mm squares and exposed to UV light for 10 h for sterilization. Samples were then equilibrated in complete medium for 5 h at room temperature to allow wetting of the surface. The samples were then placed in wells of a 48 well plate and seeded with a 20 μ L droplet of cell solution at a concentration of 87,500 cells- mL^{-1} . The plate was placed in a 37 °C incubator for 2 h to allow for cell attachment. After 2 h, 250 μ L of additional medium was placed in each well and the plate was placed in a 37 °C incubator for an additional 22 h, after which point the cells were fixed and stained. For each group an n of 5 independent samples was used, where an independent sample was defined as being prepared from a separate cure of the SMP substrate.

2.3.6.2 Cell Culture on Actively Wrinkling Substrates

To investigate the effect of wrinkle formation on adherent-cell behavior, hASCs were plated on prestrained, gold-coated SMPs and cell behavior before and after triggering wrinkle formation was analyzed. Prestrained, gold-coated samples were cut into 6 mm x 6 mm squares and exposed to UV light for 1 h for sterilization. Samples were equilibrated in complete medium at room temperature for 5 h, after which they were placed in a 48 well plate and seeded with a 20 μ L droplet of cell solution at a concentration of 87,500 cells mL^{-1} . The samples were placed in an incubator at 30 °C for 2 h to allow for cell attachment without triggering wrinkle formation.

After 2 h, 250 μ L of additional medium pre-warmed to 30 °C was added to each well and the plate was placed in a 30 °C incubator for 3 h to allow cells to spread. After 3 h, cells on one set of samples were fixed, stained, and imaged to determine cell alignment before wrinkle formation. A second set of samples was left in the 30 °C incubator for an additional 24 h to serve as the control, and the third set, the experimental group, was placed in a 37 °C incubator for an additional 24 h, triggering wrinkle formation. These groups were fixed, stained, and imaged to evaluate cell alignment. For each group, an *n* of 5 independent samples was used.

2.3.7 Cell Staining and Imaging

Both the cell nucleus and the actin cytoskeleton were stained to quantitatively and qualitatively assess cell alignment. Alexa Fluor 647 conjugated phalloidin (Invitrogen) was used to stain the actin cytoskeleton, and DAPI was used to stain the nucleus. After incubation, cells were fixed in 3.75% paraformaldehyde for 10 min, permeabilized with 0.1% Triton X-100 for 5 min, and blocked with 1% bovine serum albumin for 30 min. Cells were then stained with phalloidin for 30 min, followed by staining with DAPI for 5 min. All steps were performed at room temperature. After staining, samples were mounted in Prolong Gold Antifade Mounting Medium (Invitrogen).

Cells stained with phalloidin and DAPI were imaged using a Leica DMI 4000B inverted microscope. Images were captured with a Leica DFC 340FX camera using a 10x/0.22 NA objective. Pseudocolor was applied to the micrographs using Leica Application Suites software, and histogram stretching was used to increase contrast for the images.

2.3.8 Determining Cell Alignment

2.3.8.1 Cell Nuclear Alignment Determination

To quantify cell alignment of DAPI-stained samples, the nuclear angle for each cell was determined using ImageJ, and the standard deviation of the angular distribution was determined. In ImageJ, a threshold was applied to each image to isolate cell nuclei and a binary image was created. The Analyze Particles function was then used to fit an ellipse to each nucleus and determine the corresponding angle, ranging from 0° to 180° . These angles correspond to an arbitrary reference angle of 0° , which is subsequently refined as described below. A value of 90° was subtracted from each cell angle to adjust the range of angles to -90° to $+90^\circ$, centered around 0° . The truncated standard deviation [46] of nuclear angles about 0° was then calculated, yielding the angular spread. The reference angle was then incremented by 1° and the resulting truncated standard deviation calculated for all angles up to a reference angle of 180° . To normalize between wrinkled and non-wrinkled substrates, the reference angle that yielded the minimum standard deviation, or highest degree of alignment, was the angle used for statistical comparison. The reference angle yielding the minimum standard deviation was compared to the angle of wrinkle direction for wrinkled substrates and was always within $\pm 3^\circ$ of the wrinkle direction, meaning the angle of orientation was well aligned with the wrinkle direction. Statistical analyses were then performed on the truncated standard deviations, or angular spread, for the different groups. The truncated standard deviation was used to determine the degree of orientation, as it has been shown to be a simple means of determining degree of alignment [46]; randomly distributed nuclear angles would produce a standard deviation of 52° , whereas perfectly aligned nuclear angles would produce a standard deviation of 0° . Cells with a nuclear aspect ratio less than 1.2 were excluded from analysis.

2.3.8.2 Cell Cytoskeleton Alignment Determination

To quantify cell cytoskeleton alignment during active wrinkling, the cytoskeleton angle for each cell was determined using ImageJ and compared to the corresponding nuclear angle for the same cell (**Scheme 2-3**). Only cells whose cytoskeleton was not overlapping with another cell's cytoskeleton were analyzed. In ImageJ, each cell cytoskeleton was manually traced and the outlines of each cell filled. After all non-overlapping cells were traced and filled, a threshold was applied to the image to isolate the cell traces. The Analyze Particles function was then used to fit an ellipse to each cytoskeleton trace and determine the corresponding angle, ranging from 0° to 180°. After determining the cytoskeleton angle for each cell, the same process was repeated for the corresponding nuclear angle. Cell cytoskeleton and cell nuclear angles were then refined as described in **Section 2.3.8.1**, and the resulting angular histograms for cell nuclear orientation and cell cytoskeleton orientation were compared.

2.3.9 Statistics

Statistical analysis was performed using a similar method as reported in our previous study[47]. Resampling statistics were used rather than parametric statistics since sample size was small. One factor ANOVA was used to compare all groups in a given experiment using the Design5 Excel Macro [48]. For the previously wrinkled substrate experiment, the one factor was substrate prestrain with 6 groups (0%, 2%, 7%, 12%, 17%, and 23%), and for the actively wrinkling substrate experiment the one factor was topography with 3 groups (flat, wrinkled, and flat control). Each group was then compared to every other group using permutation testing on the raw data of angular spread for each replicate in a group. This was performed using the Design5a Excel Macro [48]. Significance was determined on the $P < 0.05$ level, and p-values were corrected for multiple comparisons.

2.4 Results

2.4.1 Substrate Material Properties

2.4.1.1 Tuning the Glass Transition Temperature (T_g)

A copolymer network with a tunable T_g was developed to serve as an active substrate in a coated SMP bilayer system. Control over the T_g , and therefore the shape recovery temperature, was achieved through systematically varying the weight ratio of tBA and BA comonomers while keeping the crosslinking density constant (**Figure 2-1a**). Using this comonomer system, T_g could be tuned from -44 °C (100% BA) to 48 °C (100% tBA), a range that includes the target T_g near 37 °C. Further optimization of the comonomer ratio led to a composition of 95 wt-% tBA and 5 wt-% BA (hereafter referred to as “95tBA-5BA”) yielding a dry T_g of 45 °C, which is lowered to 40 °C once hydrated due to water plasticization (**Figure 2-1b**). While this value of T_g is higher than 37 °C, this composition allowed the SMP bilayer system to remain stable at 30 °C and form wrinkles upon heating to 37 °C, as is discussed later in **Section 2.3.4**.

2.4.1.2 Thermomechanical Properties

Thermomechanical analysis showed the temperature-dependence of storage modulus for both dry and wet substrates (**Figure 2-2a**). Below T_g , the substrate tensile storage modulus was on the order of 1 GPa. Heating above T_g resulted in a rapid drop in the storage modulus, which decreased up to 3 orders of magnitude upon heating into the rubbery plateau. When hydrated, the onset of the modulus drop shifted to a lower temperature; however, modulus plateaus below and above T_g remained similar between the dry and hydrated states. Isothermal experiments of the dry substrate at 55 °C and the wet substrate at 37 °C, temperatures used to form wrinkles,

revealed modulus values of 5 MPa and 515 MPa, respectively (**Figure 2-2b**). Interestingly, small fluctuations in temperature had a significant impact on the tensile storage modulus for the hydrated state.

Shape memory characterization of substrates in the dry and wet states revealed excellent shape fixing and shape recovery ratios (**Figure 2-3**). The dry substrate was subjected to three subsequent one-way shape memory cycles, revealing excellent shape fixing and recovery ratios with values greater than 97% for each. The substrate also showed excellent reproducibility, as there was no detectable loss in fixing or recovery between the three consecutive shape memory cycles. Furthermore, fixing and recovery ratios for the wet substrate were also greater than 97%. Hydrated recovery experiments showed that upon exposure to 37 °C water, fixed substrates with a 95tBA-5BA composition recovered 50% of the programmed strain within the first 30 min, and 98% within the first 6 h (**Figure 2-4**). Small changes to the copolymer composition significantly slowed the recovery kinetics, as substrates with compositions of 98tBA-2BA and 100tBA-0BA only recovered 34% and 7%, respectively, within the first 6 h.

2.4.2 Strain Effect on Wrinkle-Crack Properties[‡]

Wrinkles formed by recovery of prestrains ranging from 2% to 23% were investigated to reveal any strain-dependence on wrinkle characteristics. From the AFM scans (**Figure 2-5, left**) it is qualitatively clear that increasing prestrain tends to increase wrinkle amplitude, while the wrinkle wavelength decreases. This effect was further supported by the 2D FFT analysis which showed a shift of the entire wrinkle wavelength distribution toward smaller wavelength (larger wavenumber) with increasing prestrain (**Figure 2-6**). The wrinkle wavelength was found to decrease with prestrain (**Figure 2-7a**), whereas the wrinkle amplitude appeared to increase with

[‡] This work was performed by Dr. Pine Yang

prestrain (**Figure 2-7b**). It was also found that increasing prestrain led to the appearance of two or more characteristic wrinkle wavelength peaks in response to substrate recovery. Qualitative inspection of 2D FFT azimuthal scans (**Figure 2-6c**) suggests that the degree of alignment is similar for all wrinkled samples, independent of prestrain. Quantitatively, however, the full-width-at-half-maximum plots of the same data sets (**Figure 2-7c**) reveal that orientation increased with increasing prestrain. Cracks (**Figure 2-5, right**) showed a strong dependence on prestrain. In particular, cracks formed for prestrains larger than 7%, beyond which crack density increased with prestrain.

2.4.3 Cell Culture on Previously Wrinkled Substrates

Cell alignment on wrinkled samples prepared from prestrains of 2, 7, 12, 17, and 23% was compared to cell alignment on a non-wrinkled sample by staining and imaging cell nuclei and f-actin 24 h after seeding. Cell viability analysis revealed that cells adhered and remained viable atop all substrates, with a cell viability greater than 95% (**Figure 2-8**). Additionally, from the LIVE/DEAD stain, qualitative cell alignment parallel to the wrinkle direction (as noted by the double-headed arrows) was observed. Alignment atop wrinkled substrates was also confirmed from the f-actin and nuclei staining (**Figure 2-9**). On the non-wrinkled substrate (**Figure 2-9a**), the cell cytoskeleton appears spread and elongated in all directions, showing no preferential angle of orientation. However, on wrinkled substrates of all prestrains (**Figure 2-9 b-f**), the cell cytoskeleton appears spread and elongated parallel to the wrinkle direction.

The degree of cell alignment was quantified by fitting ellipses to cell nuclei and calculating the standard deviation of the resulting cell nuclear angles. A large distribution of nuclear angles was found on the non-wrinkled sample (**Figure 2-10a**), whereas a narrow

distribution of nuclear angles was found on all wrinkled samples (**Figure 2-10 b-f**). For each angular histogram, the wrinkle direction was chosen as a reference orientation set at 90° .

For the wrinkled samples, each distribution is centered about this angle, demonstrating that the preferential angle of orientation is parallel to the wrinkle direction. The resulting standard deviation of the nuclear angles was calculated for each group and plotted as a function of prestrain (**Figure 2-11**). For the non-wrinkled sample (0% prestrain), a standard deviation of $51.0 \pm 0.7^\circ$ was found, consistent with a random distribution of nuclear angles. As the prestrain increased, the resulting angular standard deviation decreased until saturating beyond 7% prestrain. Comparing this trend to the trends of wrinkle amplitude and wavelength with increasing prestrain (**Figure 2-7 a-b**), we find significant correlation but are unable to determine which wrinkle characteristic dictates nuclear alignment. Noticeably, crack density (**Figure 2-11**) showed a gradual and nearly linear increase with prestrain that apparently saturates wrinkle refinement with strain and thus saturates the degree of cell alignment. Inspection of **Figure 2-11** reveals roughly four regions of behavior. In region I, where prestrain is lower than 7%, cell nuclear alignment increased with increasing prestrain as shown by a decrease in angular spread. Meanwhile, cracks were observed with prestrain larger than 4.5%. In region II, where prestrain is higher than 7%, cell nuclear orientation plateaued while crack density increased. Thus, increasing SMP prestrain increases the degree of nuclear orientation, a phenomenon that offers quite interesting potential for future studies, but methods that suppress crack formation may be needed to extend the control of nuclear alignment to higher extents.

2.4.4 Wrinkle Formation in Simulated Cell-Culture Conditions[‡]

Wrinkle formation in the hydrated state - here termed “active wrinkling” - was investigated to determine whether or not the bilayer system was stable at 30 °C (cell seeding temperature) and whether or not it would fully recover at 37 °C (activation temperature for active cell experiment). Gratifyingly, no wrinkle formation occurred in water at room temperature and 30 °C for 5 h (**Figure 2-12**) but wrinkles formed when the water temperature was elevated to 37 °C, which was expected, as the SMP substrate demonstrates bulk recovery at 37 °C when hydrated (**Figure 2-4**). Wrinkles formed in state. Wavelengths ranging from 2 to 6 μm , comparable to those observed in the dry state, were observed for the water-triggered wrinkle experiment using 2D FFT analysis (**Figure 2-7**). Notably, the wrinkle amplitude began to saturate at the highest prestrains examined. No significant differences in wrinkle alignment and amplitude were observed when comparing wrinkles formed under dry (static in cell culture) and wet (active in cell culture) conditions (**Figure 2-7b and 2-7c**).

2.4.5 Cell Culture on Actively Wrinkling Substrates

Cellular response to actively wrinkling substrates was assessed by imaging cell nuclei and f-actin first on cells cultured on a wrinkle-free, prestrained (and coated) substrate at a sub-trigger temperature ($T = 30\text{ }^{\circ}\text{C}$) and then at a higher temperature ($T = 37\text{ }^{\circ}\text{C}$) capable of triggering wrinkle formation. Seeding cells at the sub-trigger temperature did not affect cell viability (**Figure 2-13**), as cells remained viable at 30 °C for 5 h and an additional 24 h. Cells remained viable after triggering wrinkle formation at 37 °C (**Figure 2-13c**), indicating that neither dynamic topography change nor temperature change negatively affected cell viability. Prior to wrinkle formation no obvious cytoskeleton orientation was observed (**Figure 2-14a**);

[‡] This work was performed by Dr. Pine Yang

however, as a result of wrinkle formation the cytoskeleton elongated parallel to the wrinkle direction (**Figure 2-14b**). Similar results were found for cell nuclear orientation, assessed by fitting ellipses to cell nuclei and determining the spread of nuclear angles, as was done described above for cells cultured on previously wrinkled substrates. Interestingly, while a broad distribution of nuclear angles was observed before wrinkling (**Figure 2-15a**), this distribution significantly narrowed upon wrinkle formation (**Figure 2-15c**). A control group of cells left at 30 °C for 29 h showed no preferential orientation (**Figure 2-15b**). Comparison of the two types of experiments (cellular response to previously wrinkled versus actively wrinkling substrates) is seen in **Figure 2-11**. In the latter case, an average angular standard deviation of $50.1^{\circ} \pm 0.5^{\circ}$ was found prior to triggering, whereas an average angular standard deviation of $32.7^{\circ} \pm 2.5^{\circ}$ was found after triggering wrinkle formation – close to the value for nuclear alignment of cells cultured on previously wrinkled substrates ($34.8^{\circ} \pm 1.7^{\circ}$).

2.4.6 Comparing Cell Nuclear and Cell Cytoskeleton Alignment

Correlation between cell nuclear alignment and cell cytoskeletal alignment was assessed by comparing the nuclear and cytoskeletal angles of isolated cells during active wrinkling. Both nuclear and cytoskeleton distributions showed similar results (**Figure 2-16**), where a broad distribution of angles was observed prior to wrinkling (**Figure 2-16a**), while a narrow distribution of angles was observed after wrinkling (**Figure 2-16c**) indicating a transition from random alignment to increased alignment parallel to the wrinkle direction. A control group of cells left at 30 °C for the 29 h showed no preferential orientation (**Figure 2-16b**). When comparing the average angular spread values (**Table 2-1**), both nuclear and cytoskeleton alignment were in agreement. Interestingly, the angular spread for the isolated cells studied here showed a much stronger alignment compared to the angular spread of all cells regardless of

isolation or overlap, as noted by the angular spread value of 20.8° for isolated cells compared to 32.7° for all cells. This indicates that cell packing may also influence cell-topography interactions; however, this may also be an artifact attributed to a small number of isolated cells (average of 15 isolated cells per sample compared to an average of 400 total cells per sample). Comparing the difference between measured nuclear angle and the corresponding measured cytoskeleton angle (**Figure 2-17**) also revealed that prior to wrinkling, large differences between the measured angles may exist (**Figure 2-17a**); however upon wrinkling nuclear and cytoskeleton angles are identical, as shown by over 50% of the cells having measured angles being within $\pm 5^\circ$ of each other.

2.5 Discussion

In this study we developed a coated SMP bilayer system capable of forming tunable wrinkles under conditions amenable to cell culture, namely, in aqueous media at temperatures near and including 37°C . More importantly, cell culture on both previously wrinkled and actively wrinkling substrates was proven to result in clear orientation of both f-actin and ellipsoidal cell nuclei. Prior to wrinkle formation, no preferential angle of orientation was observed; however, as a result of wrinkle formation whose amplitude increased and wavelength decreased with increasing recovered strain, clear cell orientation was observed with orientation along the wrinkle direction and with a degree that increased with wrinkle amplitude.

Considering wrinkle formation results alone, we observed that our bilayer wrinkle system agreed well with the prestrain dependence for both wavelength and amplitude described by Jiang et. al [49]. In contrast, a report by Xie et. al. showed that while wrinkle wavelength decreased with increasing recovered strain, no dependence of amplitude on strain was observed [38]. We are currently unable to explain the difference between this result and our results reported in **Figure**

2-7. A salient feature of the SMP-triggered wrinkles reported in **Figure 2-6** is the broad distribution of wrinkle wavelengths observed. Such hierarchical wrinkling has been reported before and found to be associated with large compressive stress [18]. It is understood that the origin of this phenomenon is the saturation of first generation wrinkles at a small amplitude which forms an effective film that can undergo a similar wrinkling process. This hierarchical buckled pattern forms with further application of a compressive strain. However, the mechanism for our bilayer wrinkle system is different. Heating the SMP above its glass transition temperature induces the transition from the glassy to the rubbery state during which the modulus decreases several orders of magnitude as shown in **Figure 2-2**. In particular, while the surface buckling process at lower temperatures favors smaller wavelengths, larger wavelengths are favored at higher temperatures. Thus, the evolving modulus change with continued increase in temperature during heat-triggered shape-recovery resulted in a distribution of wrinkle wavelengths. Further, while the linear buckling theory [29, 30] has proven to work well for elastic substrates, our system is viscoelastic [50-52] and thus features significant time-dependence that our group is currently exploring. Using linear theory, we did a simple calculation to compare our results to the predicted theoretical values with the following parameters. For gold (f) and substrate (s), $E_f = 82 \text{ GPa}$, $\nu_f = 0.33$, $E_s (\text{dry } 55^\circ\text{C}) = 5 \text{ MPa}$, $E_s (\text{wet } 37^\circ\text{C}) = 515 \text{ MPa}$, $\nu_s = 0.44$ (assumed). In the case where wrinkles were formed under dry conditions, the predicted wavelength is $3.5 \mu\text{m}$, which is in the range of our experimental result. However, for the wrinkles formed in water at 37°C , the predicted wavelength is $0.75 \mu\text{m}$, at least 4 times lower than our experimental value. We are unable to explain this discrepancy, but tentatively point to a viscoelastic effect. Clearly, an SMP wrinkle model will need to be developed in the future.

Cracks (**Figure 2-5, right**) were also observed to form for samples that were prestrained 7% and higher, with an increase in crack density with increasing prestrain (**Figures 2-5, 2-11**). By comparison, the crack spacing is much larger than the wrinkle wavelength for all conditions explored. We attribute the formation of cracks to the SMP's lateral elongation [13] that occurs during recovery, which induces a tensile stress in the gold in the direction perpendicular to the direction of recovery. Interestingly, the onset prestrain of crack formation corresponded to the beginning of saturation in both wrinkle characteristics and degree of cell alignment (**Figures 2-7 and 2-11**). The crack density data in **Figure 2-11** were fitted into a power-law function [53]

$$CD = c \left(\varepsilon - \varepsilon^* \right)^\beta \quad (\text{Eq 2-6})$$

where c is a constant, ε^* is the critical strain for cracking, and β is an exponent governing the rate of fragmentation. Our fitting equation yielded an ε^* of 2.6% and $\beta \sim 1.0$. For still higher strains, it is likely that the fragmentation process will also saturate to yield $\beta < 1$.

We observed without exception that the wrinkles formed on our SMP, whether before or during cell culture, remained stable following prolonged exposure to cell culture conditions. Gratifyingly, we did not observe delamination between the gold coating and SMP substrate, neither during wrinkle formation nor cell culture. This suggests a robust interface despite not using an adhesion interlayer that is sometimes required [11, 54, 55]. However, an additional interlayer such as titanium (Ti) could improve the adhesion and further suppress crack formation when submerged in medium for longer culture periods. Nano-sized gold coatings are known to be plastic with a very low yield strain. The strain applied on the gold from the substrate was irreversible and the gold thickness could have potentially changed due to plastic deformation. Whether the gold thickness and stiffness were changed during wrinkling is still unknown. Further studies can be conducted to investigate the effect of this mechanical loading on the thin

gold film properties. For the present study, we focused on cell behavior far from cracks; however, the interaction of cells with cracks may be an interesting area for future study due to large tensile strains that could be applied to cells spanning a crack. To clarify the role of wrinkle wavelength distribution, we must first learn how to control this distribution width, average wavelength, and amplitude independently, an endeavour of great interest to us.

While the complex topography associated with hierarchical wrinkles is thought useful for microfluidic sieves [18], antifouling marine coatings [56], and substrates for cell mechanosensitivity studies [21], its relevance, per se, to cell culture substrates has not yet been revealed. Here, we were able to control the degree of cell alignment by variation in wrinkle characteristics. By increasing the prestrain in the SMP we were able to increase the degree of wrinkle orientation as well as increase the wrinkle amplitude. This resulted in increasing degrees of cell alignment until saturation occurred after 7% prestrain. The increase in cell alignment can be attributed to both the increase in orientation of the wrinkles and the increase in wrinkle amplitude. Which of these two is the prominent cause is unknown, and further studies would need to be conducted to isolate each effect and determine which played a more significant role. Prior studies have found that atop grating patterns cell alignment increases with grating depth [5, 6, 57]. Cell alignment (**Figure 2-11**) showed an exponential decay that followed the following form:

$$y = 36.49 + 14.48e^{-0.494x} \quad (\text{Eq 2-7})$$

where x is the prestrain (%) and y is the angular spread of nuclear orientation in degrees. The saturation of cell alignment at prestrains above 7% is strongly correlated with the onset of crack density growth as noted above. This dynamic approach also proved to be a viable way of turning on cell alignment. Prior to topography change, cells had shown a random orientation, whereas

shortly after activating the topography change cells re-oriented parallel to the wrinkle direction. This effect was observed previously in the work by Lam et. al, who used an external force to compress a PDMS substrate that had a thin oxidized film resting atop, forming wrinkles while cells were attached [58]. Our system expands on the work by Lam and colleagues because here we have a material intrinsically capable of forming wrinkles in culture without the need for an external compression mechanism and with the potential for control over the time scale of their formation, as demonstrated by the ability to tune the recovery kinetics by varying the copolymer composition (**Figure 2-4**).

The present work contributes to recent progress in SMPs designed for application in cell culture. Here we have shown that a wrinkled topography can be controlled simply by changing the prestrain in the SMP, and with this system we are able to trigger wrinkle formation at 37 °C. It is important to note that the cell alignment observed on the actively wrinkling substrate was similar to that observed on its previously wrinkled counterpart. Further studies into the dynamics of cell alignment through time-lapse microscopy may reveal transient cell alignment during active wrinkling that may differ from the equilibrium state. Developing a method to observe cells in time-lapse microscopy is the focus of the work in **Chapter 3**. Also of interest to our group is the effect of wrinkling kinetics on cell behavior, recognizing the possibility of distinct regimes for strain rates [59, 60] applied to adherent cells. One advantage of this system is that the composition can be tuned to obtain a range of T_g 's, which can be used to study how the dynamics of topography change elicit different effects from cells. This extension of the present work should improve our fundamental understanding of the mechanisms behind cell-material interactions in a dynamic state. Studies employing actively changing topography on a timescale slower than, similar to, or faster than that of cell cytoskeleton reorganization will provide

unprecedented new insight into cell cytoskeleton reorganization and cell mechanobiology. I speculate there may exist a critical timescale for topographical reorganization where faster topography changes may induce cell detachment or apoptosis.

2.6 Conclusion

We have developed a cytocompatible coated SMP bilayer system with tunable wrinkle formation that can be used to direct cell alignment in static and active culture experiments. An increase in prestrain of the SMP led to an increase in wrinkle amplitude and orientation and a decrease in wrinkle wavelength. Subsequently, the degree of cell alignment in static cultures increased with increasing SMP prestrain until saturation occurred. Furthermore, this system showed that cell alignment can be turned on through triggering wrinkle formation during active cell culture. Both nuclear and cytoskeleton angles were in agreement, indicating that either could be used to assess cell orientation. The ease of which the transition temperature of this system can be tuned should enable the study of the kinetic effects of topography change on cellular response.

2.7 Acknowledgements

This work was performed in collaboration with Dr. Pine Yang, a former graduate student in Dr. Patrick Mather's lab. All wrinkle formation and characterization studies performed in this chapter were conducted by Dr. Yang, and a more detailed discussion and analysis of wrinkling SMP bilayers can be found in her dissertation [61].

2.8 References

[1] Ingber DE. Mechanical signalling and the cellular response to extracellular matrix in angiogenesis and cardiovascular physiology. *CircRes*. 2002;91:877-87.

- [2] Wozniak MA, Chen CS. Mechanotransduction in development: a growing role for contractility. *Nat Rev Mol Cell Biol.* 2009;10:34-43.
- [3] Suresh S. Biomechanics and biophysics of cancer cells. *Acta Biomater.* 2007;3:413-38.
- [4] Bhattarai SR, Bhattarai N, Yi HK, Hwang PH, Cha DI, Kim HY. Novel biodegradable electrospun membrane: scaffold for tissue engineering. *Biomaterials.* 2004;25:2595-602.
- [5] Teixeira AI, Nealey PF, Murphy CJ. Responses of human keratocytes to micro- and nanostructured substrates. *J Biomed Mater Res Part A.* 2004;71A:369-76.
- [6] Hu W, Yim EKF, Reano RM, Leong KW, Pang SW. Effects of nanoimprinted patterns in tissue-culture polystyrene on cell behavior. *J Vac Sci Technol B.* 2005;23:2984-9.
- [7] Curtis ASG, Casey B, Gallagher JO, Pasqui D, Wood MA, Wilkinson CDW. Substratum nanotopography and the adhesion of biological cells. Are symmetry or regularity of nanotopography important? *Biophys Chem.* 2001;94:275-83.
- [8] Berry CC, Campbell G, Spadiccino A, Robertson M, Curtis ASG. The influence of microscale topography on fibroblast attachment and motility. *Biomaterials.* 2004;25:5781-8.
- [9] Dalby MJ, Gadegaard N, Tare R, Andar A, Riehle MO, Herzyk P, et al. The control of human mesenchymal cell differentiation using nanoscale symmetry and disorder. *Nat Mater.* 2007;6:997-1003.
- [10] Bettinger CJ, Langer R, Borenstein JT. Engineering substrate topography at the micro- and nanoscale to control cell function. *Angew Chem-Int Edit.* 2009;48:5406-15.
- [11] Bowden N, Brittain S, Evans AG, Hutchinson JW, Whitesides GM. Spontaneous formation of ordered structures in thin films of metals supported on an elastomeric polymer. *Nature.* 1998;393:146-9.

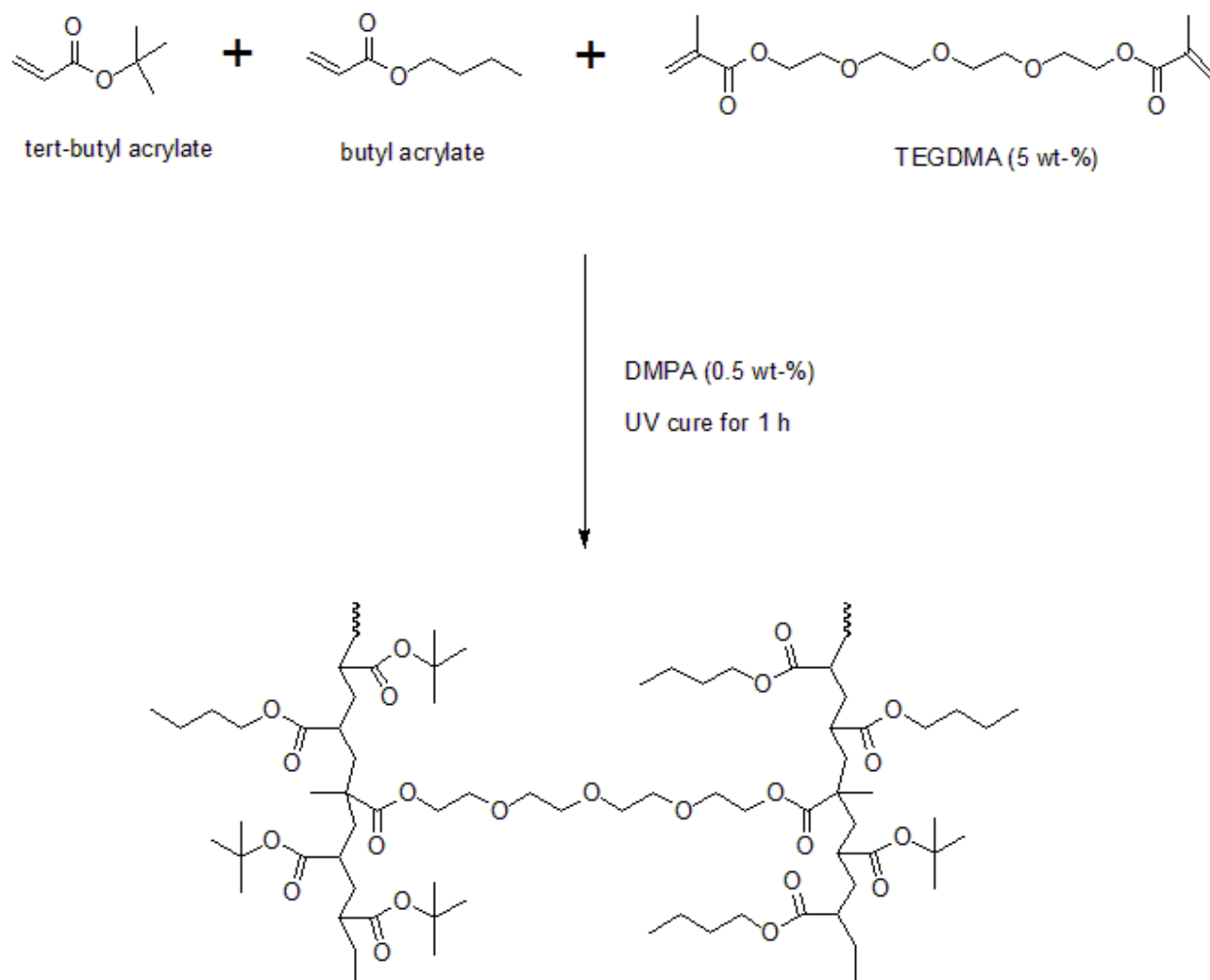
- [12] Huck WTS, Bowden N, Onck P, Pardoën T, Hutchinson JW, Whitesides GM. Ordering of spontaneously formed buckles on planar surfaces. *Langmuir*. 2000;16:3497-501.
- [13] Volynskii AL, Bazhenov S, Lebedeva OV, Bakeev NF. Mechanical buckling instability of thin coatings deposited on soft polymer substrates. *Journal of Materials Science*. 2000;35:547-54.
- [14] DuPont SJ, Cates RS, Stroot PG, Toomey R. Swelling-induced instabilities in microscale, surface-confined poly(N-isopropylacryamide) hydrogels. *Soft Matter*. 2010;6:3876-82.
- [15] Tanaka T, Sun ST, Hirokawa Y, Katayama S, Kucera J, Hirose Y, et al. Mechanical instability of gels at the phase-transition *Nature*. 1987;325:796-8.
- [16] Yang S, Khare K, Lin PC. Harnessing surface wrinkle patterns in soft matter. *Advanced Functional Materials*. 2010;20:2550-64.
- [17] Khang DY, Rogers JA, Lee HH. Mechanical buckling: Mechanics, metrology, and stretchable electronics. *Advanced Functional Materials*. 2009;19:1526-36.
- [18] Efimenko K, Rackaitis M, Manias E, Vaziri A, Mahadevan L, Genzer J. Nested self-similar wrinkling patterns in skins. *Nat Mater*. 2005;4:293-7.
- [19] Moon MW, Vaziri A. Surface modification of polymers using a multi-step plasma treatment. *Scripta Materialia*. 2009;60:44-7.
- [20] Wang M, Comrie JE, Bai YP, He XM, Guo SY, Huck WTS. Formation of hierarchically structured thin films. *Advanced Functional Materials*. 2009;19:2236-43.
- [21] Vandeparre H, Gabriele S, Brau F, Gay C, Parker KK, Damman P. Hierarchical wrinkling patterns. *Soft Matter*. 2010;6:5751-6.
- [22] Hyun DC, Jeong U. Substrate thickness: An effective control parameter for polymer thin film buckling on PDMS substrates. *Journal of Applied Polymer Science*. 2009;112:2683-90.

- [23] Lin PC, Yang S. Spontaneous formation of one-dimensional ripples in transit to highly ordered two-dimensional herringbone structures through sequential and unequal biaxial mechanical stretching. *Applied Physics Letters*. 2007;90.
- [24] Chiche A, Stafford CM, Cabral JT. Complex micropatterning of periodic structures on elastomeric surfaces. *Soft Matter*. 2008;4:2360-4.
- [25] Chen X, Hutchinson JW. Herringbone buckling patterns of compressed thin films on compliant substrates. *J Appl Mech-Trans ASME*. 2004;71:597-603.
- [26] Jiang C, Singamaneni S, Merrick E, Tsukruk VV. Complex buckling instability patterns of nanomembranes with encapsulated gold nanoparticle arrays. *Nano Letters*. 2006;6:2254-9.
- [27] Guvendiren M, Burdick JA, Yang S. Solvent induced transition from wrinkles to creases in thin film gels with depth-wise crosslinking gradients. *Soft Matter*. 2010;6:5795-801.
- [28] Guvendiren M, Burdick JA. The control of stem cell morphology and differentiation by hydrogel surface wrinkles. *Biomaterials*. 2010;31:6511-8.
- [29] Chung JY, Nolte AJ, Stafford CM. Surface wrinkling: A versatile platform for measuring thin-film properties. *Adv Mater*. 2011;23:349-68.
- [30] Huang R, Suo Z. Wrinkling of a compressed elastic film on a viscous layer. *J Appl Phys*. 2002;91:1135-42.
- [31] Song J, Jiang H, Liu ZJ, Khang DY, Huang Y, Rogers JA, et al. Buckling of a stiff thin film on a compliant substrate in large deformation. *International Journal of Solids and Structures*. 2008;45:3107-21.
- [32] Chung JY, Chastek TQ, Fasolka MJ, Ro HW, Stafford CM. Quantifying residual stress in nanoscale thin polymer films via surface wrinkling. *ACS Nano*. 2009;3:844-52.

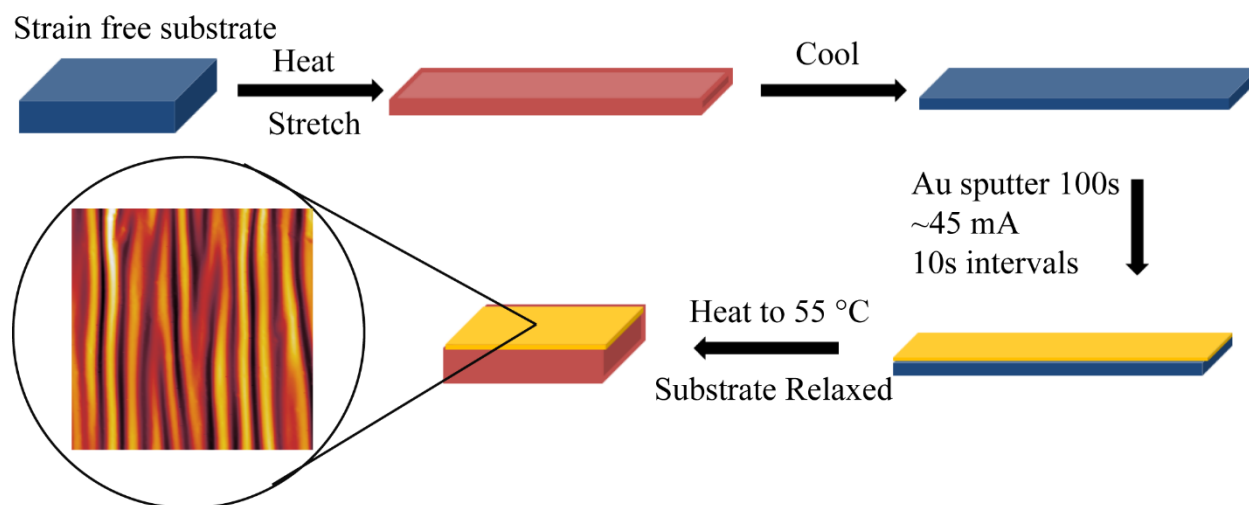
- [33] Bukowsky C, Torres JM, Vogt BD. Slip-stick wetting and large contact angle hysteresis on wrinkled surfaces. *J Colloid Interface Sci.* 2011;354:825-31.
- [34] Mather PT, Luo XF, Rousseau IA. Shape memory polymer research. *Annual Review of Materials Research.* 2009;39:445-71.
- [35] Behl M, Razzaq MY, Lendlein A. Multifunctional shape-memory polymers. *Adv Mater.* 2010;22:3388-410.
- [36] Fu CC, Grimes A, Long M, Ferri CGL, Rich BD, Ghosh S, et al. Tunable nanowrinkles on shape memory polymer sheets. *Adv Mater.* 2009;21:4472-+.
- [37] Sun L, Zhao Y, Huang WM, Tong TH. Formation of combined surface features of protrusion array and wrinkles atop shape -memory polymer *Surface Review and Letters.* 2009;16:929-33.
- [38] Xie T, Xiao XC, Li JJ, Wang RM. Encoding localized strain history through wrinkle based structural colors. *Adv Mater.* 2010;22:4390.
- [39] Robert M.Braun, Ravi Sharma. *Silicone contact lenses with wrinkled surface.* US: Bausch&Lomb incorporated, Rochester, NY 2008. p. 6.
- [40] Khang DY, Jiang HQ, Huang Y, Rogers JA. A stretchable form of single-crystal silicon for high-performance electronics on rubber substrates. *Science.* 2006;311:208-12.
- [41] Sun YG, Choi WM, Jiang HQ, Huang YGY, Rogers JA. Controlled buckling of semiconductor nanoribbons for stretchable electronics. *Nat Nanotechnol.* 2006;1:201-7.
- [42] Chung JY, Youngblood JP, Stafford CM. Anisotropic wetting on tunable micro-wrinkled surfaces. *Soft Matter.* 2007;3:1163-9.
- [43] Zhang L, Lang XY, Hirata A, Chen MW. Wrinkled nanoporous gold films with ultrahigh surface-enhanced raman scattering enhancement. *ACS Nano.* 2011;5:4407-13.

- [44] Sun L, Zhao Y, Huang WM, Purnawali H, Fu YQ. Wrinkling atop shape memory materials. *Surface Review and Letters*. 2012;19.
- [45] Luo XF, Mather PT. Preparation and characterization of shape memory elastomeric composites. *Macromolecules*. 2009;42:7251-3.
- [46] Davidson P, Bigerelle M, Bounichane B, Giazson M, Anselme K. Definition of a simple statistical parameter for the quantification of orientation in two dimensions: Application to cells on grooves of nanometric depths. *Acta Biomater*. 2010;6:2590-8.
- [47] Davis KA, Burke KA, Mather PT, Henderson JH. Dynamic cell behavior on shape memory polymer substrates. *Biomaterials*. 2011;32:2285-93.
- [48] Todman JB, Dugard P. Single-case and small-n experimental designs: A practical guide to randomization tests: Lawrence Erlbaum Associates; 2001.
- [49] Jiang HQ, Khang DY, Song JZ, Sun YG, Huang YG, Rogers JA. Finite deformation mechanics in buckled thin films on compliant supports. *Proceedings of the National Academy of Sciences of the United States of America*. 2007;104:15607-12.
- [50] Yoo PJ, Lee HH. Morphological diagram for metal/polymer bilayer wrinkling: Influence of thermomechanical properties of polymer layer. *Macromolecules*. 2005;38:2820-31.
- [51] Chan EP, Kundu S, Lin QH, Stafford CM. Quantifying the stress relaxation modulus of polymer thin films via thermal wrinkling. *ACS Appl Mater Interfaces*. 2011;3:331-8.
- [52] Yoo PJ, Lee HH. Evolution of a stress-driven pattern in thin bilayer films: Spinodal wrinkling. *Physical Review Letters*. 2003;91:154502.
- [53] Chung JY, Lee JH, Beers KL, Stafford CM. Stiffness, strength, and ductility of nanoscale thin films and membranes: A combined wrinkling-cracking methodology. *Nano Letters*. 2011;11:3361-5.

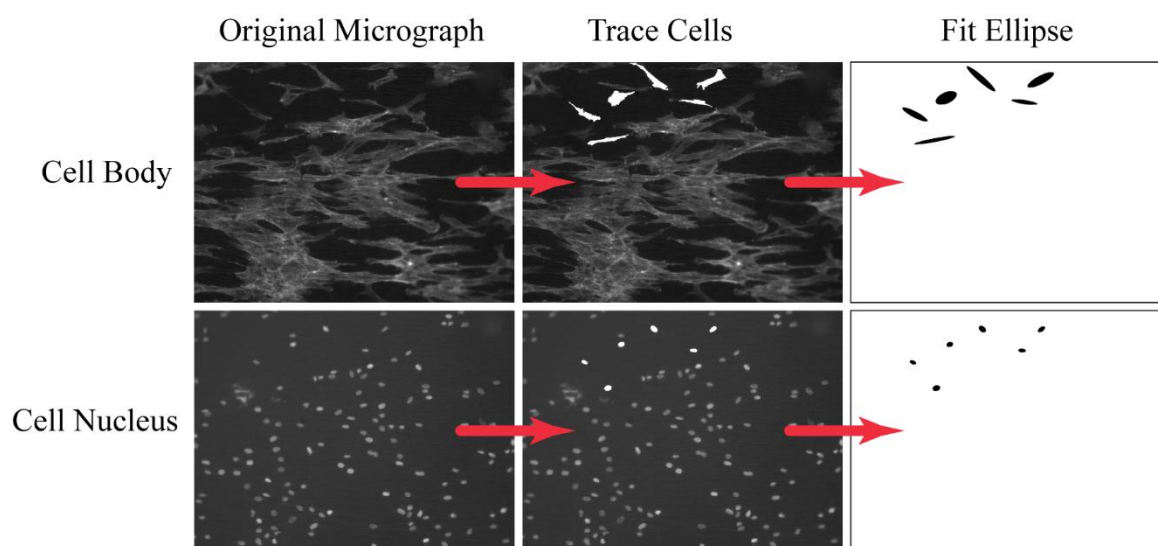
- [54] Volynskii AL, Panchuk DA, Moiseeva SV, Kechek'yan AS, Dement'ev AI, Yarysheva LM, et al. New approach to evaluation of the stress-strain properties of nanolayers of solid materials. *Russ Chem Bull.* 2009;58:865-82.
- [55] Hurley DC, Kopycinska-Muller M, Langlois ED, Kos AB, Barbosa N. Mapping substrate/film adhesion with contact-resonance-frequency atomic force microscopy. *Applied Physics Letters.* 2006;89.
- [56] Efimenko K, Finlay J, Callow ME, Callow JA, Genzer J. Development and testing of hierarchically wrinkled coatings for marine antifouling. *ACS Appl Mater Interfaces.* 2009;1:1031-40.
- [57] Sun JR, Ding YF, Lin NJ, Zhou J, Ro H, Soles CL, et al. Exploring cellular contact guidance using gradient nanogratings. *Biomacromolecules.* 2010;11:3067-72.
- [58] Lam MT, Clem WC, Takayama S. Reversible on-demand cell alignment using reconfigurable microtopography. *Biomaterials.* 2008;29:1705-12.
- [59] Hoffman BD, Crocker JC. Cell mechanics: Dissecting the physical responses of cells to force. *Annual Review of Biomedical Engineering.* Palo Alto: Annual Reviews; 2009. p. 259-88.
- [60] Janmey PA, McCulloch CA. Cell mechanics: Integrating cell responses to mechanical stimuli. *Annual Review of Biomedical Engineering.* Palo Alto: Annual Reviews; 2007. p. 1-34.
- [61] Yang P. New Surface and Bulk Shape Memory Effects in Polymers for Biomedical Applications: Syracuse University; 2014.



Scheme 2-1. Chemical structure of synthesized substrate; tert-butyl acrylate (tBA) and butyl acrylate (BA) monomers are crosslinked with tetraethylene glycol dimethacrylate (TEGDMA) and photo-polymerized using DMPA as a photoinitiator.



Scheme 2-2. Using an SMP bilayer system to form nano-scale wrinkles. A uniaxial tensile strain is fixed in the SMP substrate by heating, deforming, and subsequently cooling. Following fixing, a thin film of gold is deposited on the surface of the SMP substrate. Upon heating the substrate recovers and induces surface buckling into the gold film.



Scheme 2-3. Process for determining cell body and nuclear orientation. Fluorescent micrographs of the cell body (actin cytoskeleton) and cell nucleus were manually traced using ImageJ software. Traced cell bodies and nuclei were then thresholded and fitted with an ellipse. The angle of the major axis of the fit ellipse was used to describe cell orientation.

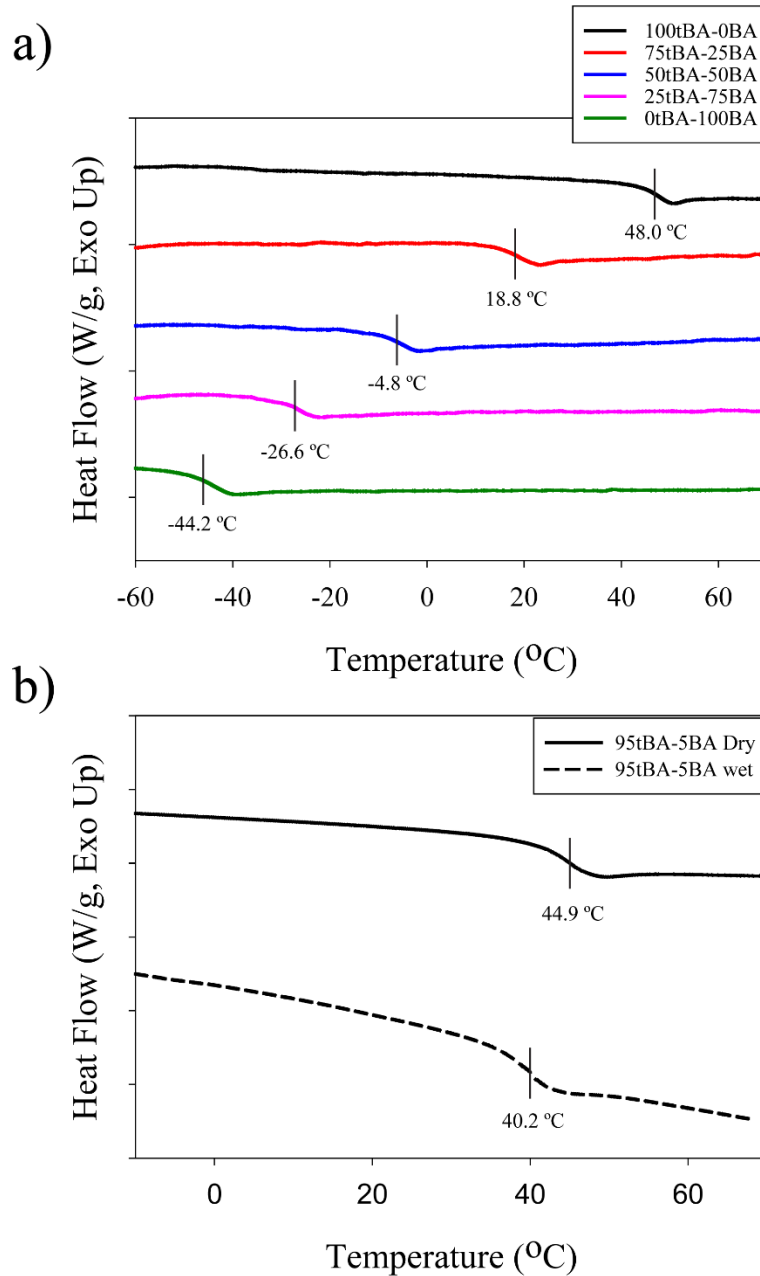


Figure 2-1. Copolymer glass transition temperature (T_g) is tuned through composition control; (a) DSC thermograms of copolymers with different compositions of tBA-BA show that T_g increases as the amount of tBA increases. (b) DSC thermograms of samples before methanol extraction, after methanol extraction, and after hydration show that methanol extraction increases T_g , while water plasticization decreases T_g . All DSC thermograms are from the second heat.

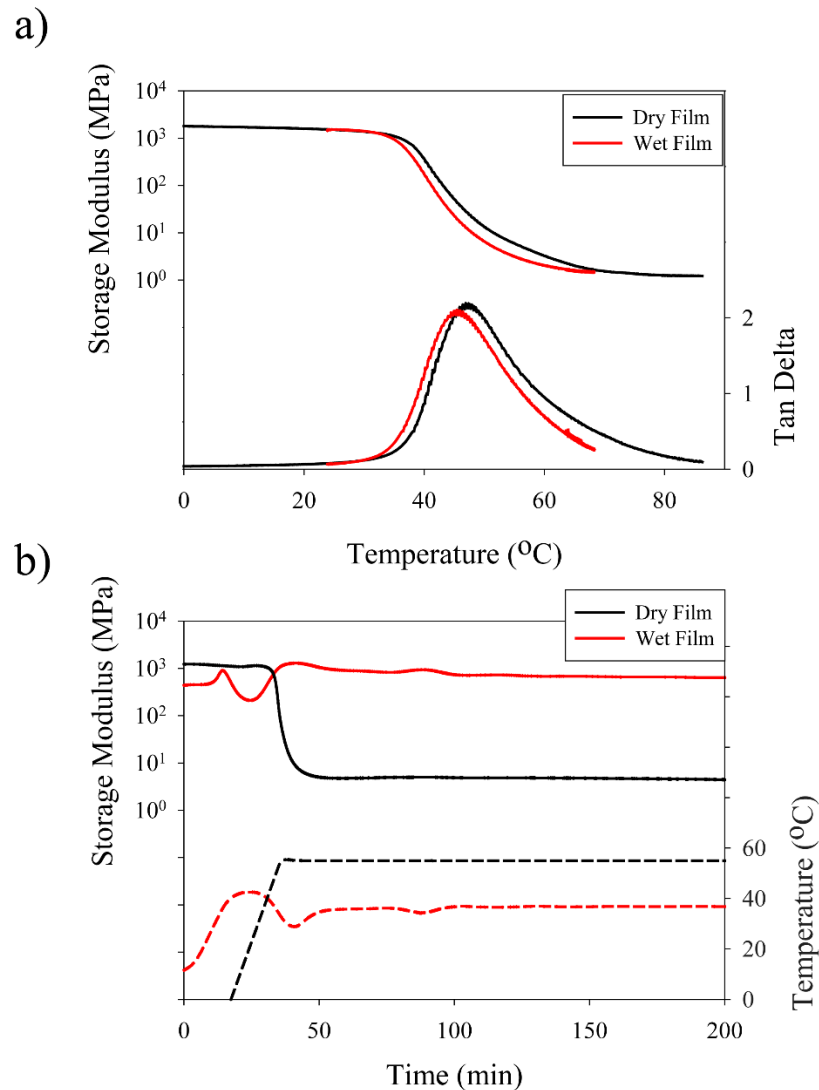


Figure 2-2. Temperature dependent dynamic mechanical response (1 Hz, under tension) of the 95tBA-5BA substrate. (a) Effect of temperature on the tensile storage modulus for dry and wet films shows a drop in modulus of 3 orders of magnitude upon heating through the glass transition temperature. (b) Isothermal storage modulus of a dry film heated to 55 °C and a wet film heated to 37 °C, temperatures used for forming wrinkles in the dry and wet state, respectively.

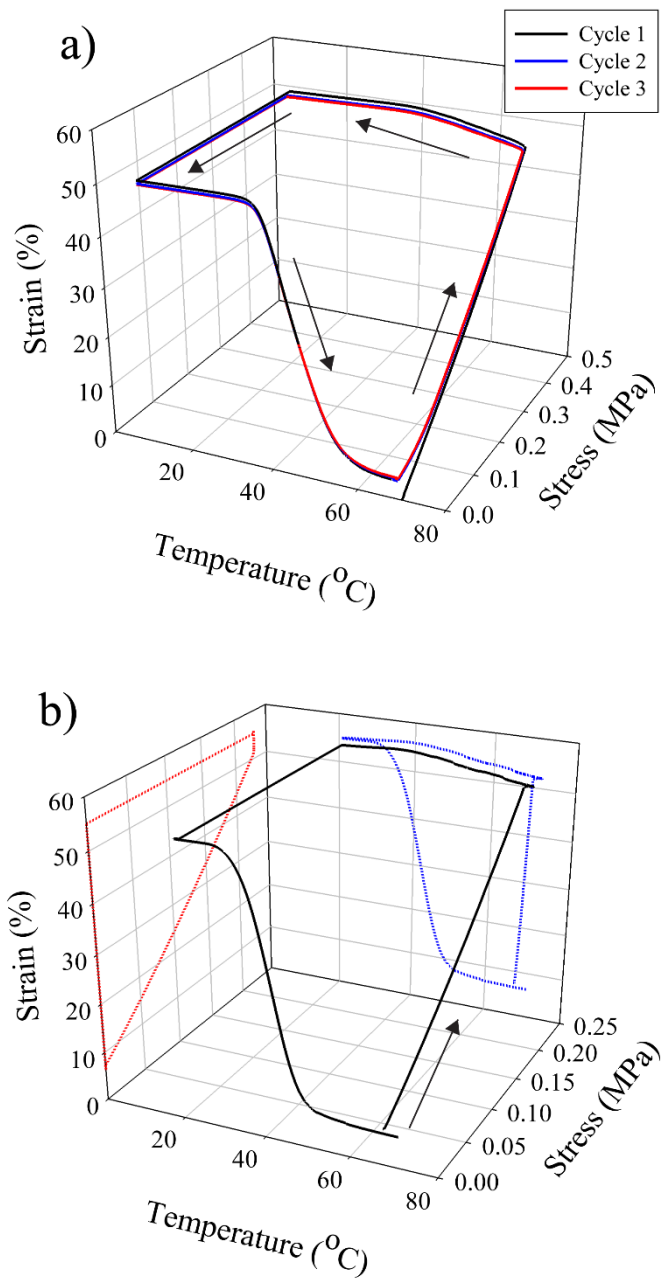


Figure 2-3. Shape memory characterization of the 95tBA-5BA substrate (a) dry and (b) wet show excellent shape fixing and shape recovery.

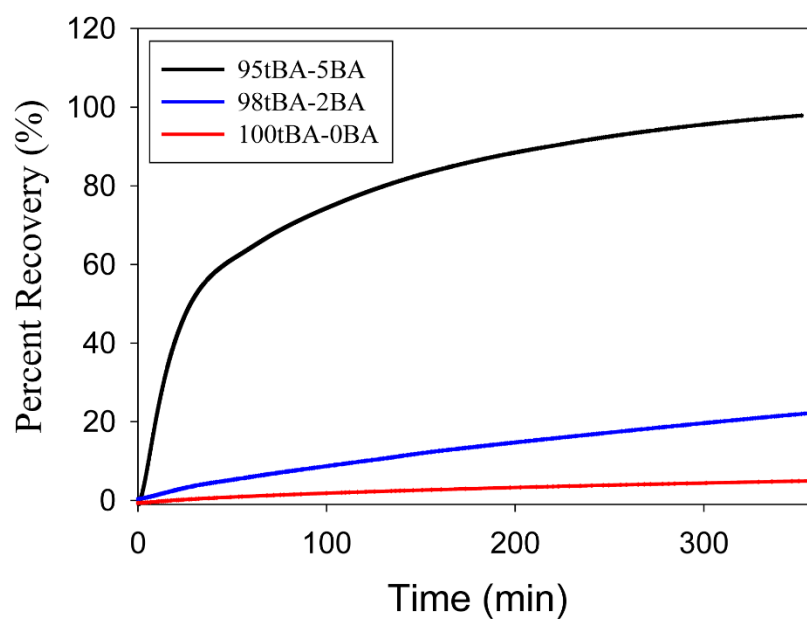


Figure 2-4. Effect of composition on recovery kinetics in 37 °C water. Increased amounts of tBA in the SMP substrate result in slower recovery once hydrated at 37 °C.

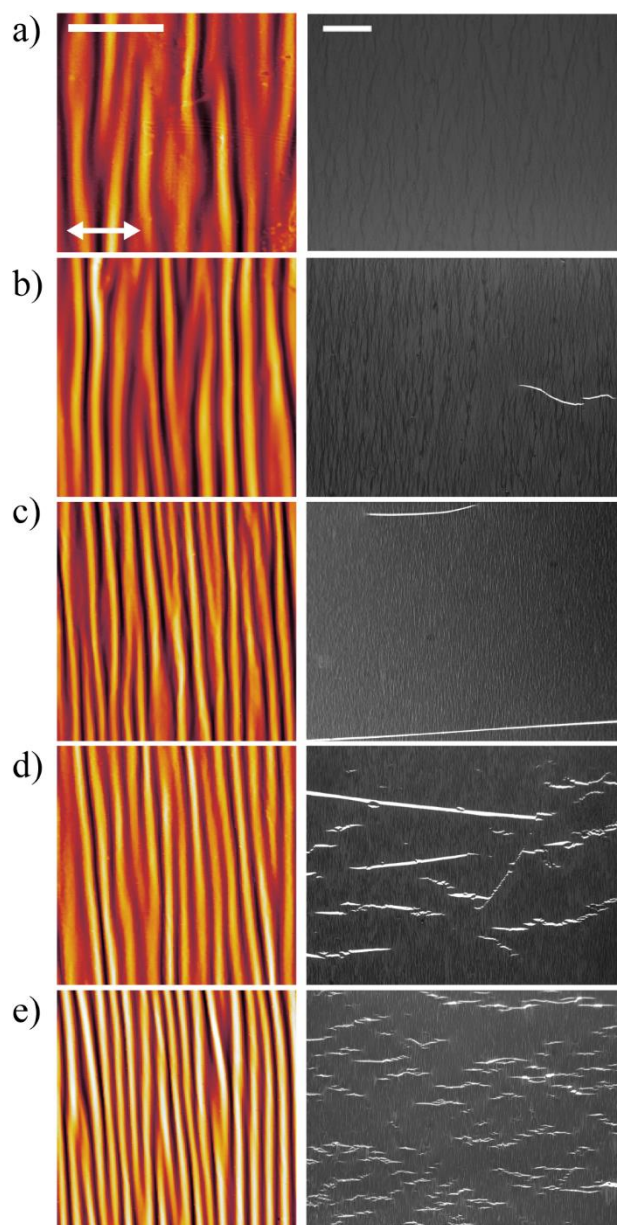


Figure 2-5. Fixed SMP prestrain affects wrinkle and crack formation. (left) AFM wrinkle images and (right) optical micrograph crack images with prestrain values of (a) 2%, (b) 7%, (c) 12%, (d) 17%, (e) 23%. Increasing prestrain increases wrinkle amplitude and crack density. Heights in the AFM images are given in color scale and range from $z=0$ nm black pixels to $z=700$ nm bright pixels. Scale bar is $20\text{ }\mu\text{m}$ for AFM images and $200\text{ }\mu\text{m}$ for optical micrographs. Arrow indicates the strain direction

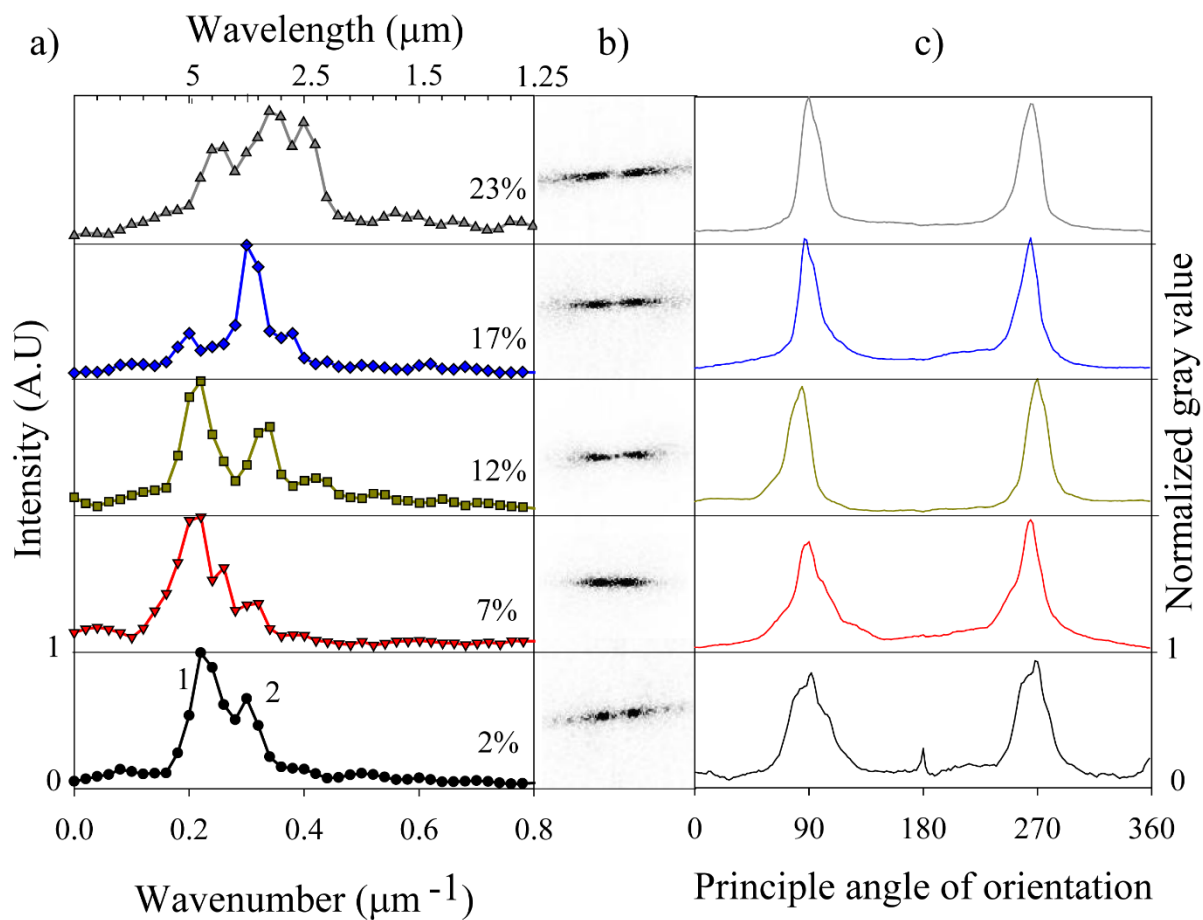


Figure 2-6. Characterization of wrinkles using 2D FFT. (a) Wavelength distributions of uniaxial wrinkles with controlled thickness of gold at varying prestrain; (b) 2D FFT pattern of wrinkled surfaces; (c) relative degree of alignment characterization using 2D FFT pattern. “1” and “2” in the left frame indicate the first and second populations of uniaxial wrinkle wavelengths.

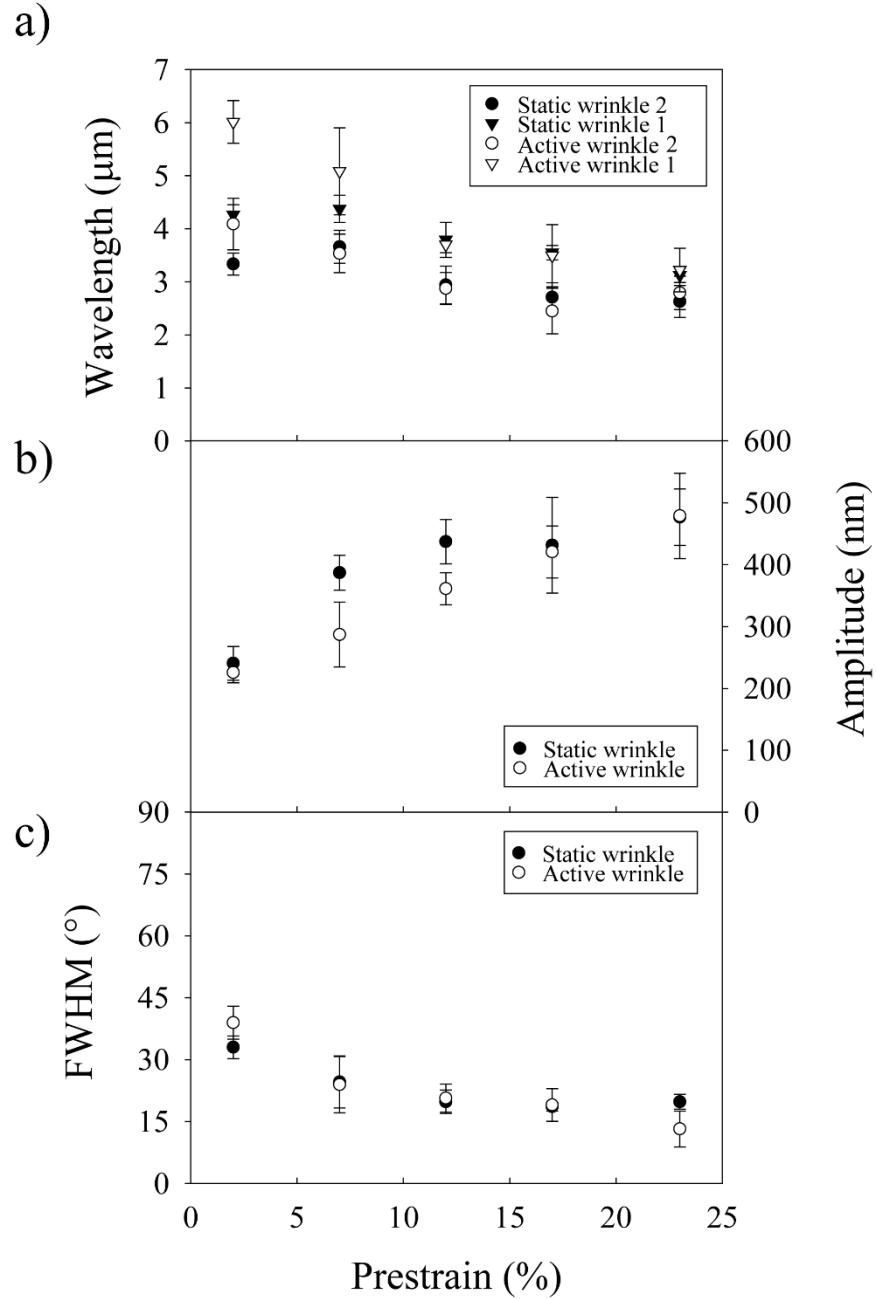


Figure 2-7. Characterization of static and active wrinkles. (a) Wavelength change with respect to the prestrain, (b) amplitude dependence of wrinkle prestrain, (c) relative degree of alignment as a function of prestrain. The controlled gold thickness in (a), (b), and (c) is 33 nm. “1” and “2” in (a) indicate the first and second populations of uniaxial wrinkle wavelengths.

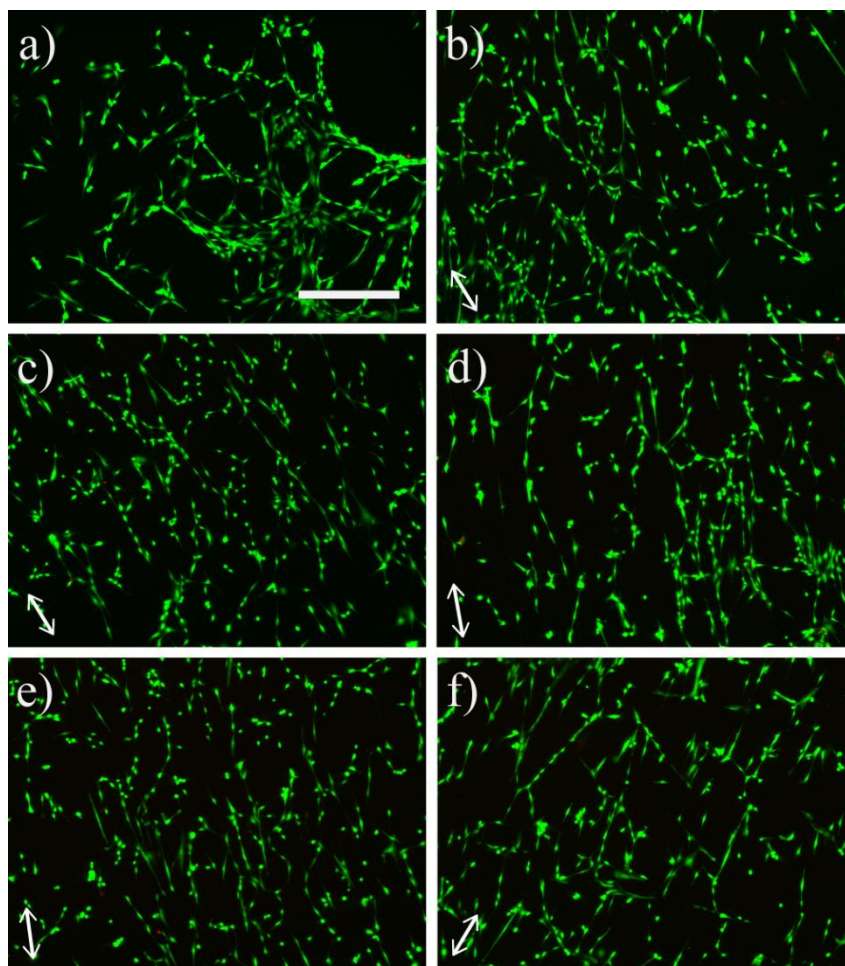


Figure 2-8. Cell viability on wrinkled substrates. LIVE/DEAD assay performed on cells seeded on (a) non-wrinkled, (b) 2%, (c) 7%, (d) 12%, (e) 17%, and (f) 23% prestrain. Scale bar is 200 μm . Green cells represent live cells while red cells represent dead cells. Cells showed >95% viability for all samples.

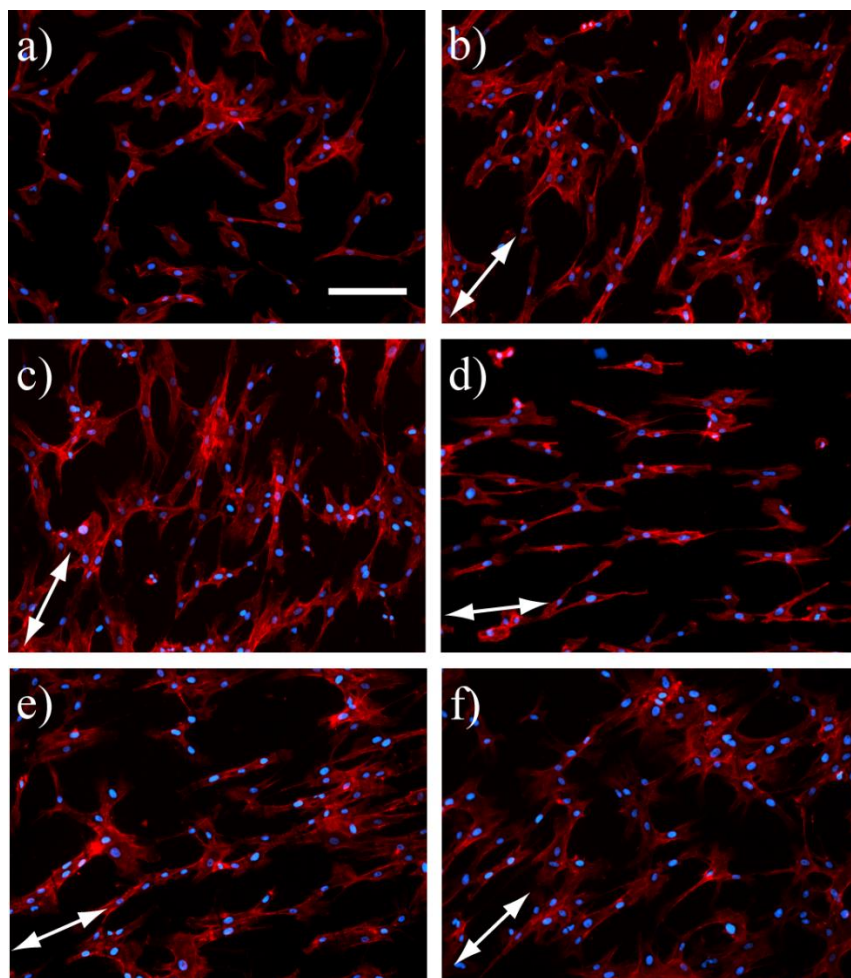


Figure 2-9. Wrinkle effect on cell alignment. Phalloidin (cytoskeleton) and DAPI (nuclear) assays performed on cells seeded on (a) non-wrinkled, (b) 2%, (c) 7%, (d) 12%, (e) 17%, and (f) 23% prestrain. Scale bar is 200 μm . Cytoskeleton stain is shown in red and nuclear stain in blue. Cells on the non-wrinkled sample appear randomly distributed whereas cells on all wrinkled samples how alignment parallel to the wrinkle direction.

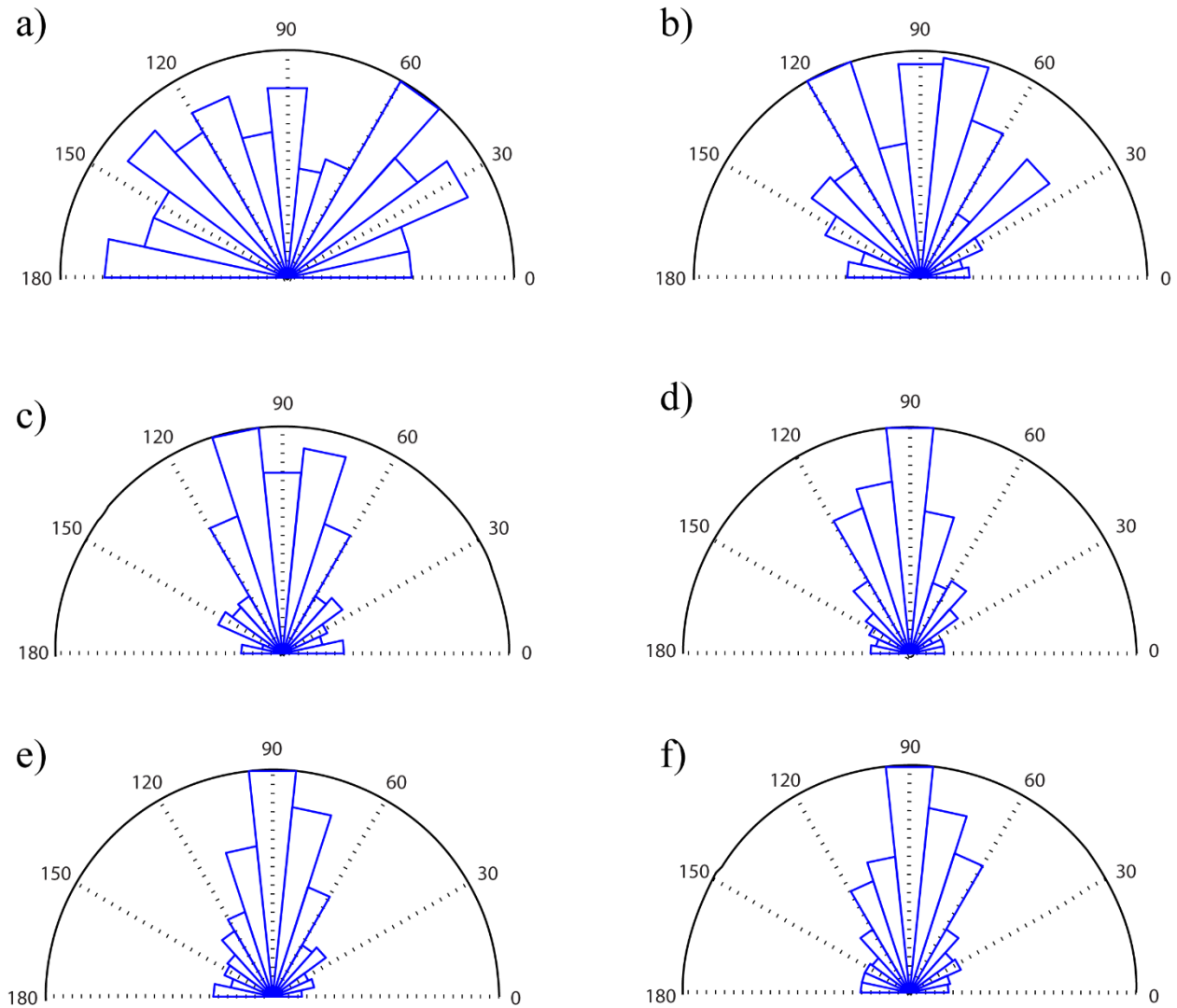


Figure 2-10. Wrinkle effect on cell nuclear distribution. Angular histograms of cells seeded on (a) non-wrinkled, (b) 2%, (c) 7%, (d) 12%, (e) 17%, and (f) 23% prestrained wrinkled substrates show the distribution of cell nuclear angles, with a broad distribution of angles representing no alignment and a narrow distribution representing a high degree of alignment. Increased prestrain results in a narrowing of the cell nuclear angle distribution, indicating increased cell alignment. The 90° angle in the angular histogram represents the angle parallel to the wrinkles.

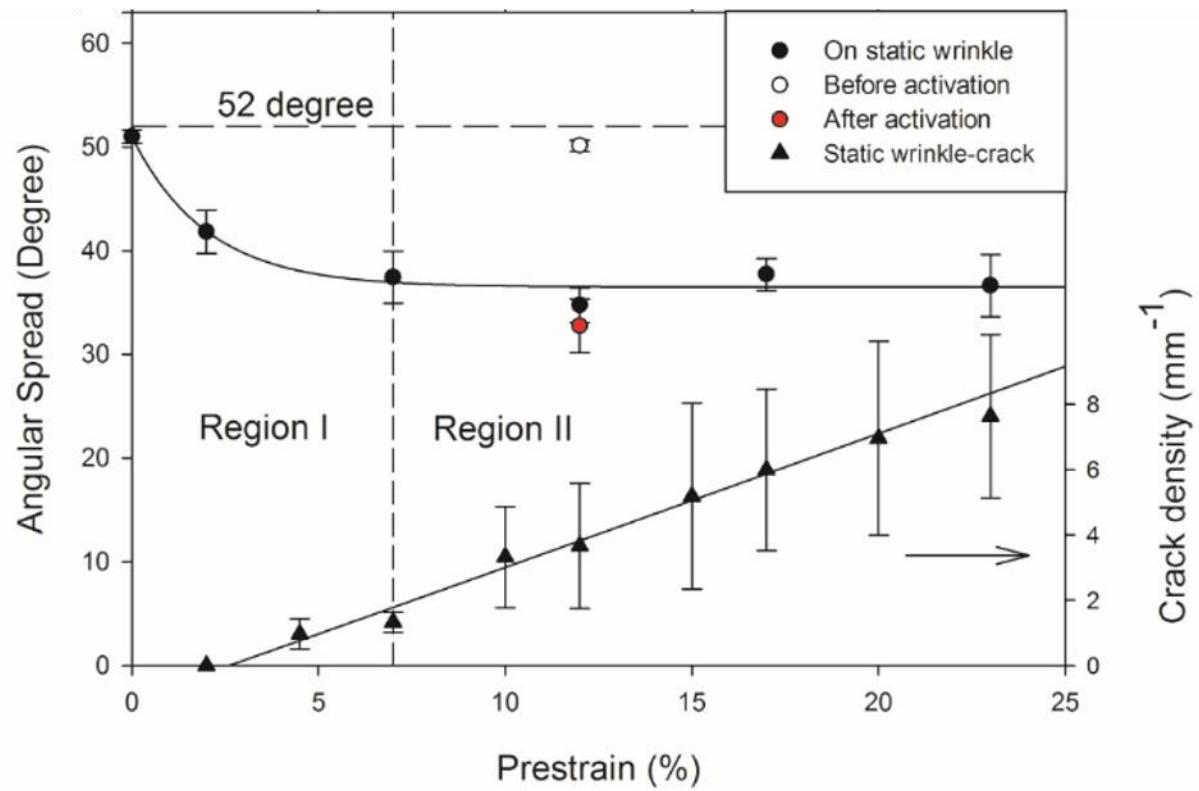


Figure 2-11. Effect of prestrain on cell orientation and crack density. With increasing prestrain, a decrease in angular spread is observed, indicating increased cell orientation. Crack density increases with increasing prestrain, with a critical prestrain of 2.6% required for crack formation.

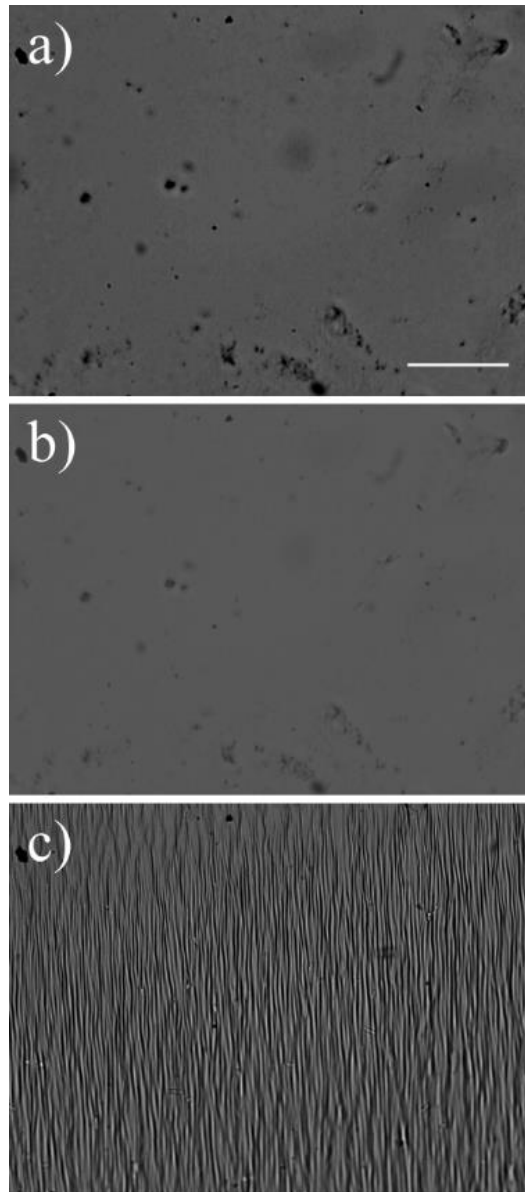


Figure 2-12. Optical micrographs of water triggered wrinkle formation with 100 s gold coating and 12% prestrain. Prestrained samples are soaked in water (a) at 30 °C for 5 h, (b) at 30 °C for 29 h, and (c) at 30 °C for 5 h and 37 °C for 24 h, simulating conditions for cell culture. Scale bar is 50 μm .

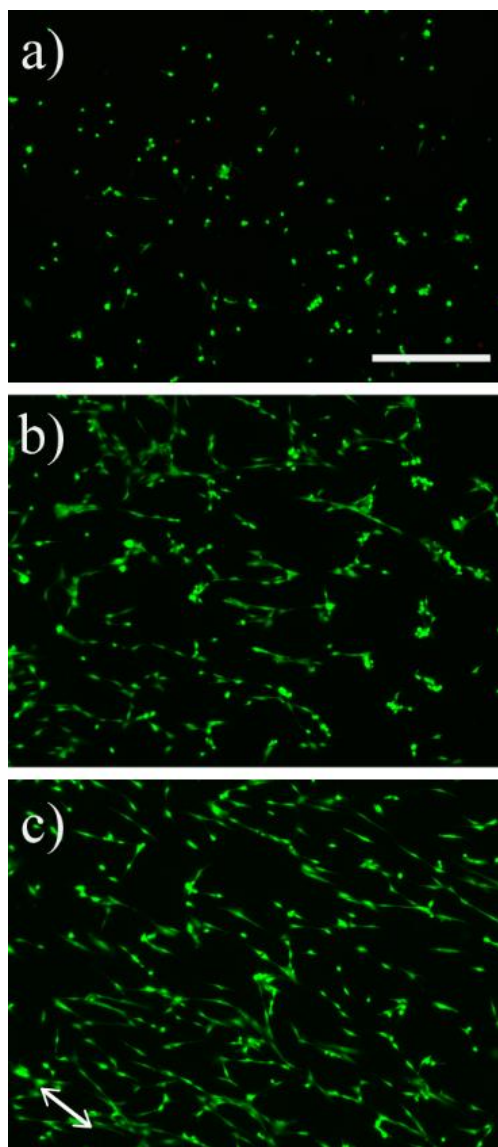


Figure 2-13. Cells remain viable following wrinkle formation. LIVE/DEAD assay performed on cells seeded (a) at 30 °C for 5 h, (b) at 30 ° C for 29 h, and (c) at 30 ° C for 5 h and 37 °C for 24 h. (Scale bar is 200 μ m). Green cells represent live cells while red cells represent dead cells. Cells showed >95% viability for all samples.

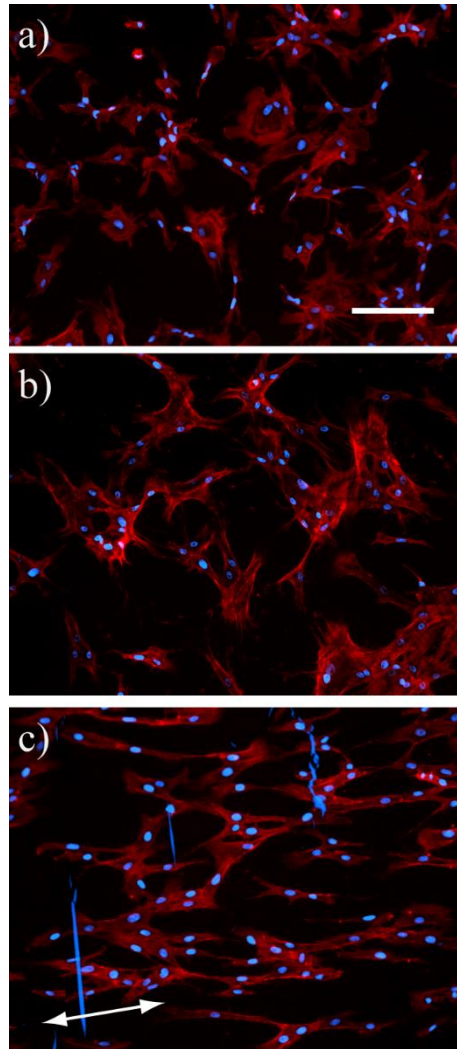


Figure 2-14. Cell morphology is affected by active wrinkle formation. Phalloidin (cytoskeleton) and DAPI (nuclear) assays were performed on cells seeded (a) at 30 °C for 5 h, (b) at 30 °C for 29 h, and (c) at 30 °C for 5 h followed by 37 °C for 24 h. For conditions (a) and (b), the substrate is flat as wrinkle formation has not been triggered. In condition (c) wrinkle formation is triggered while cells are attached. Scale bar is 200 μm . Cells show no orientation prior to wrinkle formation and subsequently align parallel to the wrinkle direction (denoted by arrow) after wrinkle formation is triggered.

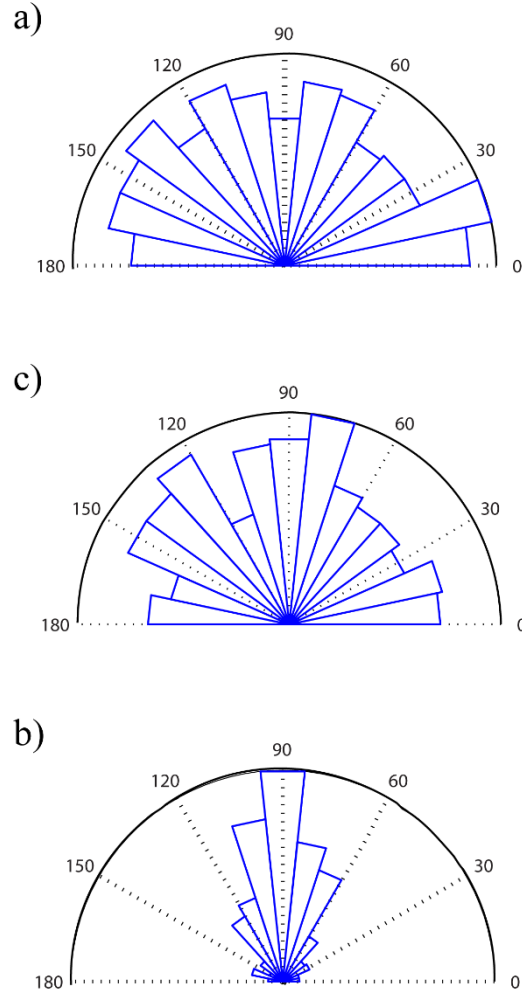


Figure 2-15. Active wrinkling results in narrowed nuclear angle distribution. Angular histograms of cells seeded (a) at 30 °C for 5 h, (b) at 30 °C for 29 h, and (c) at 30 °C for 5 h followed by 37 °C for 24 h show that before wrinkling (condition (a)) cell nuclear angle has a broad distribution that narrows upon active wrinkling.(condition (c)). The 90° angle in the angular histogram represents the angle parallel to the wrinkles for condition (c).

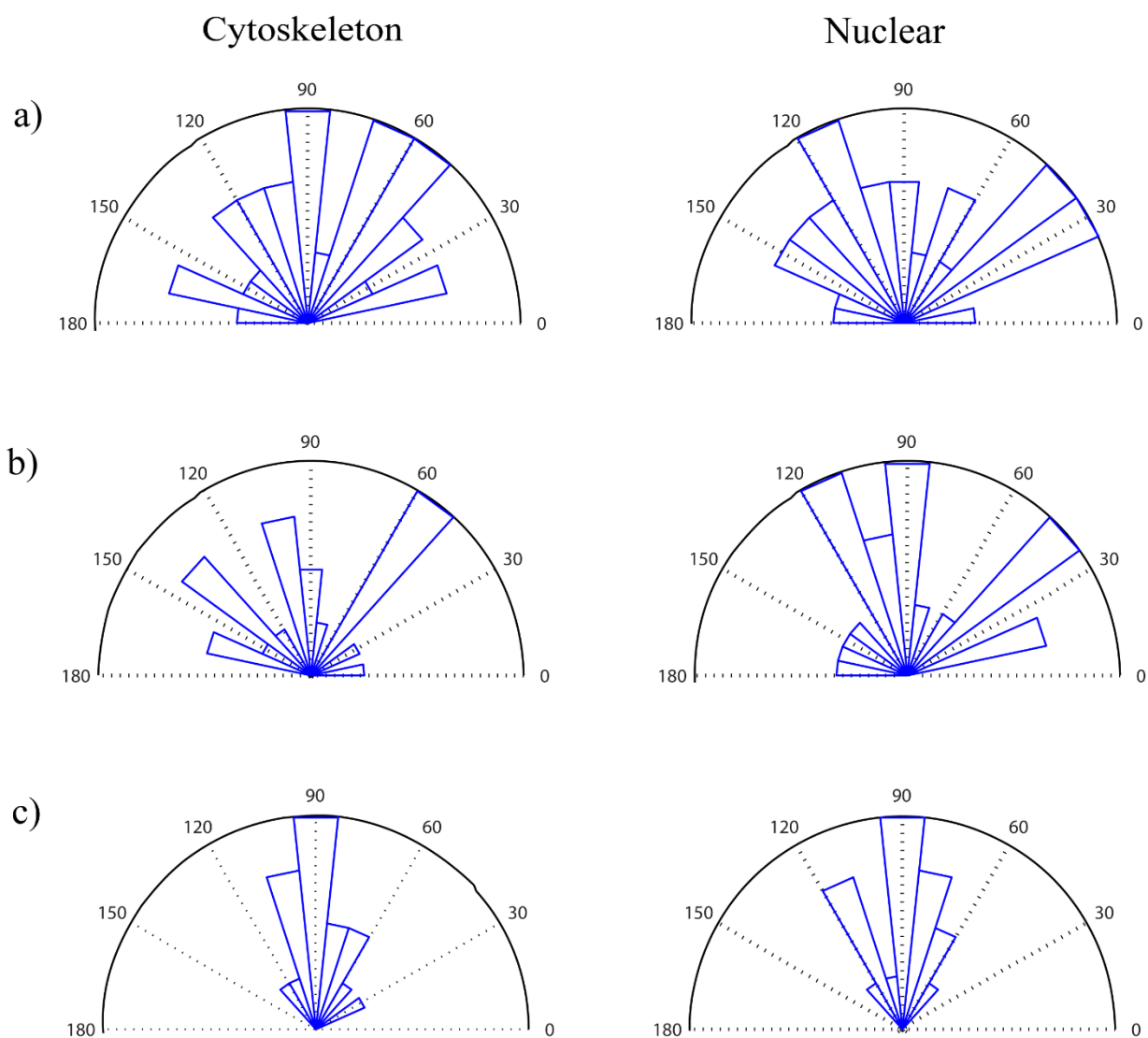


Figure 2-16. Representative cell cytoskeleton and cell nuclear angular distributions during active wrinkling. Angular histograms of cells seeded (a) at 30 °C for 5 h, (b) at 30 °C for 29 h, and (c) at 30 °C for 5 h followed by 37 °C for 24 h show that both cytoskeleton and nuclear angular distributions are broad before wrinkling (condition (a)) and narrow upon wrinkling (condition (c)). The 90° angle in the angular histogram represents the angle parallel to the wrinkles for condition (c).

Table 2-1. Comparing cell nuclear angular spread to cell cytoskeletal angular spread. Values for the average nuclear spread are comparable to values obtained from the cytoskeletal spread for all time points. Prior to triggering wrinkle formation (30 °C 5 h) cell nuclear and cytoskeletal alignment is random, as noted by the large spread values (52 ° being completely random). Upon wrinkle formation, cell nuclei and cytoskeleton become highly oriented as shown by the low angular spreads. Averages were calculated from 6 samples for the before and after wrinkling groups, and 5 samples for the control group.

Condition	Nuclear Spread (Degree)	Cytoskeletal Spread (Degree)	Avg. Cells per sample
30 °C 5 h	44.8	44.5	30
30 °C 29 h	47.3	46.5	19
30 °C 5 h + 37 °C 24 h	20.8	18.6	14

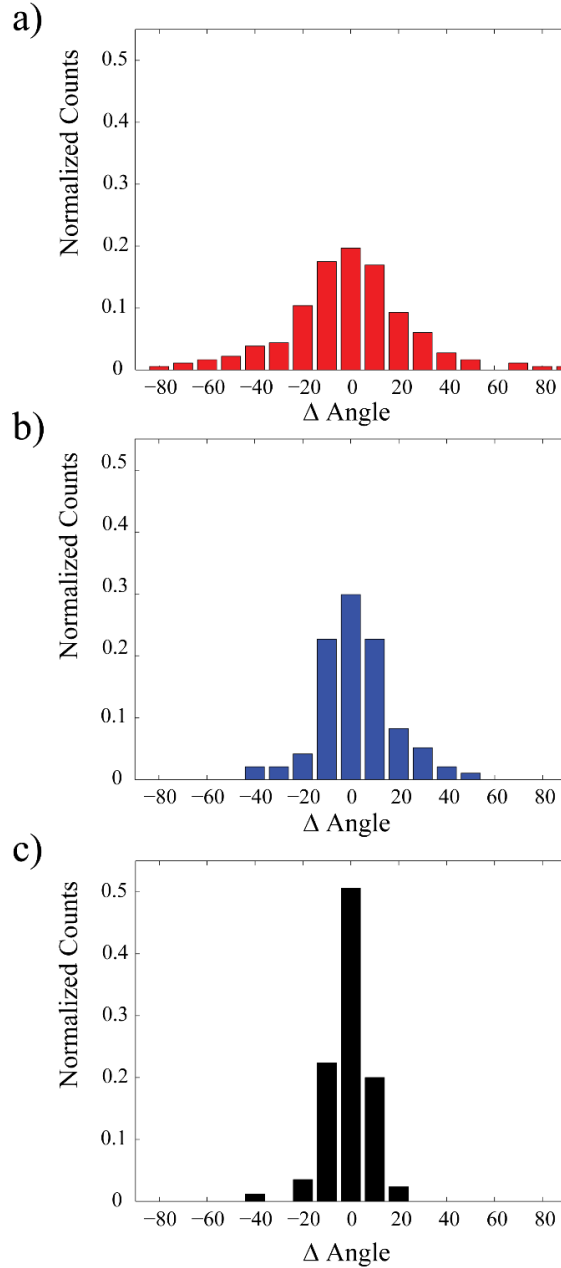


Figure 2-17. Histograms showing the difference between measured cell nuclear angle and the corresponding cell cytoskeletal angle for cells seeded (a) at 30 °C for 5 h, (b) at 30 °C for 29 h, and (c) at 30 °C for 5 h followed by 37 °C for 24 h. Prior to wrinkling angles between cell nuclei and cell cytoskeleton can vary significantly, however upon wrinkling nuclei and cytoskeletal angles are identical, as noted by over 50% of the measured angles being within $\pm 5^\circ$. Δ Angle is the difference in nuclear and cytoskeletal angle, measured cell-by-cell.

Chapter Three: Effect of Surface Topography and Surface

Chemistry on Cell Motility *In Vitro*[†]

3.1 Synopsis

This chapter explores the use of the bilayer system described in **Chapter 2** to study how surface topography and chemistry affect cell motility *in vitro*. To elucidate subtle differences in cell motility atop various substrates, a cell tracking algorithm was developed. This algorithm, termed automated contour-based tracking for *in vitro* environments (ACTIVE), was designed for adherent cell populations subject to nuclear staining or transfection. ACTIVE is employed here to compare cell motility atop wrinkled substrates, flat gold-coated substrates, and flat tissue-culture polystyrene substrates. We expect ACTIVE to be a powerful approach for tracking adherent cell motion over long time scales in complex environments, advancing the fundamental understanding of the effect of cell–cell interactions, coupled with cell–material interactions, on cell motility. Combined with quantitative statistical metrics, this should enable new insights into cancer biology, mechanobiology and morphogenesis.

3.2 Introduction

The innovative application of cell tracking techniques in complex *in vitro* model environments often enables and precipitates important new insights in biology, biomedical science, and biophysics. *In vitro* environments have recently been tailored to have specific biophysical and biochemical properties, including patterned stiffness [1], patterned surface chemistries [2], and ordered topographies [3, 4]. These increasingly complex environments are

[†] Adapted (in part) with permission from R.M. Baker, M.E. Brasch, M.L. Manning, and J.H. Henderson, *Journal of The Royal Society Interface*, **2014**, 11, 20140386. Copyright © The Royal Society 2014

now broadly employed in research on morphogenesis[5, 6], cancer cell biology[7, 8], cell biomechanics [9], and cell mechanobiology [10].

Although *in vitro* model environments have traditionally been static, recent advances in synthetic biomaterials have led to the development of environments with programmable functionality during cell culture. These *in vitro* environments can better mimic dynamic processes that exist *in vivo*, such as morphogenetic deformations [11-17] and extracellular matrix remodeling [18-20]. For example, materials with mechanically or magnetically actuated surface topography or altered stiffness can change cell morphology [21-23] and lineage specification [24]. Recently, we [25-29] and others [30, 31] developed 2D substrates and 3D scaffolds based on shape memory polymers (SMPs) that can undergo programmed thermally-triggered changes in topography or architecture with attached and viable cells.

Accurate and efficient tracking of cells in these and other architecturally and temporally complex environments has become increasingly challenging. Manual tracking of cells remains widely used, largely due to the reliability of the technique and the modest computational resources and operator training required [32, 33]. Manual tracking is, however, time intensive and therefore typically performed only for small or sparse cell populations and/or short timescales. To overcome limitations associated with manual tracking, many semi- or fully-automated computational techniques have been developed to identify (segment) and associate (link) cells in consecutive images [34, 35]. Active contour methods have been successfully used to trace cells [36, 37], cellular components [38], and animals [37], in high-contrast images, but because these methods search for compartment boundaries, they are less useful in noisy, low contrast images and situations where cells often change direction [37]. Another commonly used segmentation method is a noise threshold, in which a specific intensity value is chosen and all

intensities falling below this threshold value are deemed background noise [39, 40]. There is often high variability in cell fluorescence, however, which can render thresholding methods ineffective.

The challenges associated with long-term tracking are amplified by the growing need to track and analyze more than a few cells at a time. Due to the large variability observed in cell behavior [41], it will be necessary to collect statistically large data sets detailing cell motions and develop appropriate metrics for analyzing them if tracking-based research is to tease apart subtle differences in behavior. Improved automated tracking can aid in data collection, and the field of statistical physics provides metrics that have been successfully adapted to extract patterns and characterize collective behaviors in large data sets from several types of biological systems, including bacterial colonies [42] and schools of fish [43], at large timescales [44]. If widely adopted, the adaptation and application of displacement, velocity, and diffusion metrics from statistical physics could be used to standardize comparison of cell motility across studies and fields. Yet use of these tools in tracking research has remained limited and has generally been performed in conjunction with manual tracking or semi-automated techniques [8].

Therefore, the goal of this work was to accurately and efficiently track adherent cell populations subject to nuclear staining or transfection in complex *in vitro* environments over sufficiently long timescales to enable statistical-physics-based analyses of cell motility. To do so, we have developed, validated, and applied a new automated computational algorithm, *ACTIVE* (Automated Contour-based Tracking for *In Vitro* Environments), that identifies cell nuclei of variable staining intensities in low-contrast images, segments and links the nuclei over long periods of time (large image stacks), and processes multi-cell interactions that have traditionally limited the accuracy of automated systems. We applied *ACTIVE* to carefully quantify subtle

differences in 2D cell motility behavior on various static topographies and at different cell densities, studied using adherent mouse fibroblasts stained with nuclear fluorescent dye. Using several physics-based statistical metrics, including mean-squared displacement, velocity autocorrelation, and asphericity, we analyzed the cell tracks and tested for motility differences in the different environments.

3.3 Methods and Materials

3.3.1 Overview of the Cell Tracking Algorithm (ACTIVE)[‡]

To accurately track large cell populations over long timescales, a custom tracking algorithm, ACTIVE (Automated Contour-based Tracking for *In Vitro* Environments), was developed using MATLAB. ACTIVE was designed to track stained cell nuclei by accomplishing four main tasks (**Scheme 3-1**). First, ACTIVE segments cells by employing a contour-based approach based on nuclear stain intensity, and fits an ellipse to each cell nuclei. The contour-based approach enables detection of dividing cells and merging cells used for post-processing to improve track accuracy. Second, ACTIVE links cell nuclei between consecutive frames, using a previously published approach [45]. Third, post-processing of cell tracks is performed using a fingerprint method to correct inaccuracies that arise from merging cells. Fourth, cell tracks are analyzed by applying a series of physics-based metrics including mean squared displacement, velocity autocorrelation, diffusion analysis, and cell track asphericity. This chapter focuses on application of the tracking algorithm to describe cell motility on substrates with different chemistries, topographies, and cell seeding densities. For a detailed description of how ACTIVE works and the steps taken to validate it, readers are referred to our publication on this work [46].

[‡] Development, validation, and benchmarking of the ACTIVE tracking algorithm was performed by Megan Brasch.

Sample data and the fully functional tracking code used to generate the data presented herein are available for download at: <http://henderson.syr.edu/downloads/>, and a user manual for the tracking code can be found in **Appendix 2**.

3.3.2 Substrate Preparation

To study the effects of topography and surface chemistry on cell motility *in vitro*, three different substrates were prepared: a gold-coated wrinkled substrate; a gold-coated flat substrate; and a tissue culture polystyrene substrate (TCPS).

3.3.2.1 Gold-Coated Wrinkled Substrate Preparation

Substrates with an anisotropic topography were fabricated following the procedure described in **Chapter 2 (Sections 2.3.2 and 2.3.4)**. Briefly, an acrylate-based SMP substrate with the composition of 95tBA-5BA was prepared through photoinitiated polymerization (**Section 2.3.2**). The SMP substrate was fixed with a uniaxial tensile strain of 7% and subsequently coated with a 33 nm layer of gold (**Section 2.3.4**). Wrinkle formation was triggered by heating at 55 °C for 30 min. A prestrain of 7% was chosen because it was the saturation point for increased cell alignment, as discussed in **Chapter 2**, and resulted in a low density of crack formation. Prior to cell culture, 6 mm x 6 mm samples were cut and UV sterilized for 10 h on the gold side and 1 h on the non-gold side.

3.3.2.2 Gold-Coated Flat Substrate

As a flat control with the same surface chemistry as the anisotropic wrinkled substrates, gold-coated non-wrinkle substrates were prepared. An SMP substrate with a 95tBA-5BA composition was coated with a 33 nm layer of gold. The gold-coated substrate was heated at 55 °C for 30 min to undergo the same thermal treatment as the wrinkled substrates. No wrinkles

formed on these bilayers since there was no prestrain in the SMP substrate. Prior to cell culture, 6 mm x 6 mm samples were cut and UV sterilized for 10 h on the gold side and 1 h on the non-gold side.

3.3.2.3 TCPS Substrate

As a flat control with a different surface chemistry, tissue culture polystyrene (TCPS) samples were prepared. Samples with a 6 mm x 6 mm dimension were cut from TCPS petri dishes (Falcon™, Fischer Scientific). TCPS substrates were UV sterilized for 1 h on each side prior to use in cell culture.

3.3.3 Cell Culture

For cell experiments, C3H10T1/2 mouse fibroblasts (ATCC) were first expanded in complete growth medium (BME, 10 % FBS, 1 % penicillin/streptomycin, 1 % GlutaMAX) on T75 flasks, with initial seeding at 5,000 cells-cm⁻². Expansion was conducted in a humidified incubator with 5% CO₂ at 37 °C. Medium was changed after 3 d, and cells were passaged at 80% confluence using 0.25% Trypsin. Cells at passage 13-15 were used for experiments. Samples were prepared for cell tracking experiments by seeding cells on wrinkled, non-wrinkled, and TCPS substrates. To study the effects of varying density, cells were seeded onto 6 mm × 6 mm substrates using a droplet of cell solution at 5,000, 10,000 or 20,000 cells-cm⁻². In each case, a 20 µL droplet of cell solution was seeded onto the substrates with cell concentrations of 87,500, 175,000, and 350,000 cells-mL⁻¹, respectively, and samples were then placed in a 37 °C incubator for 2 h to allow for cell attachment. After 2 h, complete growth medium was added and the samples were placed in a 37 °C incubator for an additional 22 h, at which point the cells were stained and prepared for live cell imaging.

3.3.4 Nuclear Staining and Imaging

To image cell nuclei for tracking analysis, cells were stained with Hoechst 33342 nuclear dye (Invitrogen) and imaged over 24 h. Hoechst dye was added to complete growth medium at a concentration of $0.01 \mu\text{g}\cdot\text{mL}^{-1}$. A concentration significantly lower than the recommended staining concentration was deliberately selected to ensure cell divisions throughout the 24 h time period (as Hoechst dye at the recommended concentration significantly suppressed cell division). Using a low staining concentration also enabled live cell imaging over a longer period of time due to reduced phototoxicity when compared to higher concentrations. Substrates with attached cells were placed in LabTek glass-bottom chamber slides and $800 \mu\text{L}$ of staining solution was added to each chamber. The chamber slide was then placed in a 37°C incubator for 20 min to allow for cell nuclei to be stained. Substrates were then inverted in the chamber slide and a hemocytometer glass coverslip was placed on top of each sample for stabilization. The glass chamber slide was placed in a live cell microscope stage incubator (INC-2000, 20-20 Technology Inc.) and imaged on a Leica DMI 6000B inverted microscope. Live cell imaging was conducted at 37°C for 24 h under 5% CO_2 , with images captured every 3 min using an Andor Luca R camera with a 10x/0.30 NA objective. An A4 filter cube with an excitation filter of 360/40 nm was used for imaging.

3.3.5 Quantification of Cell Motility

3.3.5.1 Mean Squared Displacement (MSD)

One method to describe how a particle or group of particles moves is by calculating the mean squared displacement (MSD). MSD is a measure of the average distance a particle travels, and is defined as:

$$MSD(\Delta t) = \sum_{i=1}^N \frac{[r(t + \Delta t) - r(t)]^2}{N} \quad (\text{Eq 3-1})$$

where Δt is the time interval change, r is the $[x,y]$ distance at a specific time, and N is the total number of cells [47].

The MSD was calculated for each Δt and a plot of $\log_{10} \text{MSD}$ vs. $\log_{10} \Delta t$ was generated for each substrate and cell density studied. Decomposition of the MSD into the x- and y-directions was also performed, with the x-direction representing the direction parallel to the wrinkle direction. Wrinkle direction was determined from phase contrast images using ImageJ (National Institutes of Health). Quantification of cell motility was achieved through comparison of MSD slopes at short and long timescales, as well as comparison of a mobility parameter, δ , which uses the y-intercept of a line fit to the long timescale MSD data to describe how fast cells displace. Diffusive migration, or migration via a “random walk,” generates a slope equal to unity in the $\log_{10} \text{MSD}$ vs. $\log_{10} \Delta t$ plot. In these plots, superdiffusive trajectories have a slope greater than one, and ballistic migration, where cells move in a constant direction with a constant velocity, corresponds to a slope equal to two. The mobility parameter, δ , is defined as the y-intercept of a line fit to the long timescale behavior of $\log_{10} \text{MSD}$ vs. $\log_{10} \Delta t$. With this definition, 10^δ is equal to the square of the average cell velocity if motion is purely ballistic, and equal to $1/4^{\text{th}}$ of the diffusion constant if the motion is purely diffusive. For the cell motions in the present work, which were found to be intermediate between ballistic and diffusive, 10^δ is a quantitative measure of how fast cells displace.

3.3.5.2 Velocity Autocorrelation

A second metric employed to describe cell motility is the cell velocity autocorrelation function, given by:

$$C_v(t) = \langle v_i(0) \cdot v_i(t) \rangle \quad (\text{Eq 3-2})$$

2)

where $C_v(t)$ is the velocity autocorrelation for a time-step t , $v_i(0)$ is the initial velocity and $v_i(t)$ is the velocity at time t [47]. A plot of $C_v(t)$ v. Δt illustrates the persistence (opposite of randomness) of cell migration. For calculation of the velocity autocorrelation function, cell velocities were estimated using the central finite difference approximation [48], with decomposition of the velocity into x- and y-directions. For wrinkled substrates, the coordinate system was rotated so the x-direction was parallel to the wrinkle direction. Plots of velocity autocorrelation as a function of time were generated for each group, and each curve was fit with an exponential decay to extract a velocity decorrelation rate constant, which was compared between all groups. This rate constant quantifies how long a single cell tends to move in the same direction.

3.3.5.3 Cell Track Asphericity

A third metric used to describe cell motility was the cell track asphericity, which described the degree of directed cell migration. The track asphericity was measured by first calculating the gyration tensor (S) for each complete cell track (after 24 h migration):

$$S_{mn} = \frac{1}{2N^2} \sum_{i=1}^N \sum_{j=1}^N (m_i - m_j)(n_i - n_j) \quad (\text{Eq 3-3})$$

3)

where m and n refer to the Cartesian coordinates (x or y), N is the total number of track positions, and i and j are given track positions [49]. We then extracted the largest and smallest eigenvalues for the gyration tensor, λ_1^2 and λ_2^2 , respectively, and calculated the track asphericity (A) [50-52]:

$$A = \frac{(\lambda_2^2 - \lambda_1^2)}{(\lambda_2^2 + \lambda_1^2)} \quad (\text{Eq 3-4})$$

Cell track asphericity was calculated for each group and the average asphericity for each substrate and density was compared. Asphericities range from 0 to 1, with a larger asphericity indicative of more directed cell migration. Cell motility was further qualitatively assessed through the construction of diffusion plots, in which the final position for each cell was plotted after the starting location was renormalized to the plot origin.

3.3.6 Assessing Division Directionality

To determine the influence of topography on division directionality—the direction in which the daughter cells pull apart—cell divisions tracked by *ACTIVE* were analyzed. In the first frame the daughter cells pull apart, the angle made between the two centroids and the horizontal axis was calculated. The spread of these division angles was calculated following the protocol described in **Chapter 2 (Section 2.3.8)** to determine angular spread of cell nuclei [28]. Division angles were adjusted so all angles fell in the range of -90° to $+90^\circ$, centered around 0° . The truncated standard deviation [53] of the divisions was then calculated, yielding the angular spread. For statistical comparisons and to normalize between isotropic and anisotropic substrates, division angles were systematically rotated by 1° from 0° to 180° and the corresponding angular spreads calculated. For each substrate, the reference angle resulting in the minimum angular spread was used. For histogram plotting, division angles atop wrinkled substrates were rotated so that the wrinkle direction was 90° .

3.3.7 Statistics

3.3.7.1 Statistics for Effect of Density on Cell Motility Parameters

Statistical analyses for comparison of MSD exponents, velocity auto-correlation rate constants, and asphericity parameters within and between substrates and cell seeding densities were performed using non-parametric statistics due to deviations from the assumption of normality as revealed by Shapiro-Wilks testing. Spearman rank correlation testing was used to evaluate the effect of density on motility parameters, and significance testing performed on the resulting correlation coefficients using a 95% confidence level (alpha value of 0.05). An $n=12$ was used for statistical comparison.

3.3.7.2 Statistics for Effect of Substrate on Cell Motility Parameters

Kruskal-Wallis one-way analysis of variance was conducted to reveal statistical significance between substrates, followed by Wilcoxon rank-sum testing for individual comparisons. Multiple comparison testing was then performed using the Holms-Sidak correction for familywise error. Comparison of the changes in slopes as well as the difference in velocity autocorrelation rate constants within groups was conducted using a paired t-test. All testing was conducted using 95% confidence levels (alpha value of 0.05). For each of the three substrate combinations, an n of 4 technical replicates was used. Therefore, substrate comparisons used an $n=12$, whereas for paired testing within a group $n=4$.

3.3.7.3 Statistics for Cell Division Directionality

Statistical analyses were conducted on the angular spread values for each substrate. One factor ANOVA was used to compare all substrates (wrinkled, non-wrinkled, and TCPS) with an $n=12$ for each substrate. Individual comparison testing was conducted using a student's t-test,

with the Holms-Sidak correction applied to correct for multiple comparisons (3 comparisons). Significance was determined at the 95% confidence level.

3.4 Results

3.4.1 ACTIVE Tracking

By employing the ACTIVE tracking algorithm, we were able to track large populations of cells over long timescales (**Table 3-1**). As expected, the average number of cells identified by ACTIVE increased with increasing seeding density, with a total number of cells tracked ranging from 760-2670 cells over the course of 24 h of imaging. This was coupled with a higher standard deviation of cell number for higher density experimental groups, indicating larger attachment and/or proliferation variation as seeding density increased. Representative fluorescent micrographs of cells seeded on wrinkled substrates at different densities (**Figure 3-1a**) showed a clear increase in attached cells as cell seeding density increased. When measuring the average number of cells segmented following seeding (**Figure 3-1b**), each type of substrate showed a continuous range of cell numbers in the first frame, which was unexpected. Rather, we expected three distinct groupings of cell numbers corresponding to low, medium and high density seeding. Because of this, correlation analyses were conducted to compare the effects of density rather than comparing between low, medium and high density (discussed later in **Section 3.4.3.4**). The lack of three distinct groupings suggests there were large variations in the droplet seeding technique used in this study. Nonetheless, ACTIVE was able to identify and construct accurate tracks of cells, as qualitatively demonstrated by the comparison of raw images to tracked images shown in **Figure 3-2**.

3.4.2 Cell Trajectory Analysis

Cell trajectories for all cells tracked over the course of 24 h were compiled to qualitatively assess patterns in cell migration direction. Analysis of cell tracks indicated that cell migratory behavior was influenced by substrate topography (**Figure 3-3**). Cells on the wrinkled substrates moved preferentially parallel to the wrinkle direction, indicative of cell migration along the wrinkles (indicated with black arrows). This behavior was not observed on the non-wrinkled and TCPS substrates, as cell tracks showed a random orientation indicative of more random migratory behavior. Cell density had no observable effect on cell trajectories, as directed migration was found atop wrinkled substrates regardless of seeding density; likewise cell trajectories appeared to be random on all flat substrates regardless of cell seeding density.

3.4.3 Cell Motility Analysis

3.4.3.1 Mean Squared Displacement (MSD)

The MSD behavior of cells atop wrinkled, non-wrinkled and TCPS substrates was compared to see the effect of topography and substrate chemistry on cell motility. Analysis of the slope of decomposed \log_{10} MSD vs. $\log_{10} \Delta t$ showed differences between substrates (**Figure 3-4 and Table 3-2**). Atop wrinkled substrates, the short timescale slope was significantly higher than the short timescale slope for both the non-wrinkled and TCPS substrates. This indicates that cell migration is more ballistic atop wrinkled substrates and in the direction along the wrinkles. Additionally, from the MSD plots in **Figure 3-4** it is apparent cell migration is direction-dependent atop the wrinkled substrates, but not atop the flat non-wrinkled or TCPS substrates. A clear separation of the MSD traces exists between the parallel (x) and perpendicular (y) directions, with the parallel direction always having higher \log_{10} MSD for a given Δt . This shows

that cells migrate preferentially parallel to the wrinkle direction. For flat substrates, no direction-dependence was observed, as shown by the overlapping (x) and (y) traces. Furthermore, these trends held true regardless of initial seeding density.

ACTIVE also allowed the study of accurate cell tracks over longer timescales. The slope on the \log_{10} - \log_{10} plots decreased significantly at the longest timescales across all substrates, indicating that cell motion becomes more diffusive over time. When decomposing the MSD and analyzing the y-intercept of a line fit to the long timescale slope, which we have termed the mobility parameter (δ), we find significant difference between the mobility parameter for wrinkled substrates when comparing the mobility parallel (x) and perpendicular (y) to the wrinkles (**Table 3-2**), with higher mobility in the wrinkled direction. No significant difference between mobility parameters was observed atop the flat substrates.

3.4.3.2 Velocity Autocorrelation

Temporal velocity autocorrelation analysis was performed to compare the persistence of cell migration between substrates. Representative plots of the velocity autocorrelation for different substrates seeded at different densities (**Figure 3-5**) agreed with the MSD results, showing direction-dependent migration atop wrinkled substrates but not atop flat substrates. Velocity autocorrelation traces parallel (x) and perpendicular (y) to wrinkle direction are separated for the wrinkled substrates. Comparing decay constants between the (x) and (y) directions show a significantly slower decay in the (x) direction, indicating cells persistently migrate parallel to the wrinkle direction. Overlapping traces for the (x) and (y) directions for flat substrates demonstrate no direction-dependent migration, as was expected. These trends were consistent across all cell seeding densities.

Comparing the decay constants between substrates also revealed significant effects of substrate properties on the cell motility (**Table 3-3**). For the anisotropic wrinkled substrates, a statistically significant difference between the time relaxation constants for the x-velocity autocorrelation functions was observed when compared to the TCPS substrates. The relaxation time for the wrinkled samples was less than the relaxation time for the non-wrinkled substrates, though the difference was not statistically significant. These results show that cell migration atop wrinkled substrates is more persistent than atop non-wrinkled and TCPS substrates, and in a direction parallel to the wrinkle direction.

3.4.3.3 Cell Diffusion and Track Asphericity

Qualitative assessment of motility behavior was performed by generating diffusion plots for each group. After renormalization for the starting position, it was observed that cell migration on anisotropic substrates was greatest parallel to the wrinkle direction (**Figure 3-6**), as noted by the majority of final cell positions resting along the x-axis. This directed migration was not observed atop the isotropic substrates, noted by the radial distribution of final cell positions.

Cell track asphericity revealed statistically significant differences between all substrates (**Table 3-3**). Track asphericities for wrinkled substrates were higher than those for both non-wrinkled and TCPS substrates. When rotating each cell track so the largest gyration tensor eigenvector (or direction of greatest cell migration) is parallel to the x-axis, this difference is qualitatively observed (**Figure 3-7**). A difference between the two isotropic substrates was also observed, with cell track asphericity atop non-wrinkled substrates being significantly higher than atop TCPS substrates.

3.4.3.4 Motility Parameters and Effect of Cell Density

ACTIVE also revealed significant correlation between average cell density and cell motility behavior. Atop the flat substrates, a strong trend of decreasing short timescale slope with increasing cell density was observed (**Figure 3-8a**), whereas atop the wrinkled substrate this correlation was weak, as noted by the Spearman rank correlation coefficients, r_s ($r_s = -0.551$, -0.592 , and -0.189 for non-wrinkled, TCPS, and wrinkled substrates, respectively). For long timescale slopes, however, no correlation was observed (**Figure 3-8b**). Interestingly, cell track asphericity had a strong positive correlation with cell density atop the anisotropic and isotropic TCPS substrates ($r_s = 0.762$ and 0.524 for wrinkled and TCPS, respectively; **Figure 3-8c**), but a weak positive correlation atop the isotropic gold substrate ($r_s = 0.259$). This suggests that atop wrinkled substrates, increased cell packing may further restrict cells to migrating parallel to the wrinkle direction.

3.4.4 Division Angle Analysis

In addition to investigating how surface topography and chemistry affected cell motility, we also investigated how these substrate properties influenced cell division directionality. One benefit of the ACTIVE tracking algorithm compared to other tracking algorithms is its ability to identify and track dividing cells. The directionality of cell division was determined based on the angle made between the two centroids of the daughter cells and the horizontal axis (**Figure 3-9**). Interestingly, we found that cell divisions were highly oriented atop wrinkled substrates and random atop both flat substrates (**Figure 3-10**), as noted by the narrow distribution of division angles centered around 90° (parallel to wrinkle direction) for wrinkled substrates at all densities, and the broad distribution of division angles for the flat substrates at all densities. Average angular spread values (**Table 3-4**) showed that wrinkled divisions were significantly more

oriented (41.0°) than both non-wrinkled (47.3°) and TCPS (48.5°). No significant difference was found between the non-wrinkled and TCPS substrates. The reference angle yielding the minimum angular spread was typically within $\pm 10^\circ$ of the wrinkle angle for the wrinkled substrates, meaning the division angle occurred parallel to the wrinkles. An angular spread of 52° represents a completely random spread—no preferential division directionality—and a decrease in the angular spread represents an increase in the preferential division directionality.

3.5 Discussion

Here we have demonstrated statistically significant differences between motility behavior on wrinkled and non-wrinkled substrates at cell seeding densities ranging from 5,000 to 20,000 cells-cm⁻². The motility differences included differences in the velocity decorrelation time and track asphericity between wrinkled and flat substrates, and a more surprising difference between cell track asphericity on the flat “control” substrates, which have different material compositions. We also found differences in the short timescale motility behavior as a function of cell density—at low densities cells move more ballistically, while at high densities they move more diffusively. These results suggest that a careful analysis of statistically large data sets can provide new insights into how cells behave as a function of their environment.

Analysis of cell behavior revealed interesting similarities and differences in the motility of cells on different substrates. One surprising similarity is that the mean squared displacement of cell tracks has the same functional form as a function of time, independent of density, substrate, or topography. In other words, the slopes of the MSD vs. time on a log₁₀-log₁₀ plot are indistinguishable. This is very different from what is seen in non-active materials (such as colloids) as a function of density, and suggests that direct cell-cell interactions (which occur

more often at higher densities) do not strongly impact the trajectories of this cell type, or at least at the density range investigated here.

This analysis identifies several different metrics that can be used to distinguish cell motility on wrinkled vs. non-wrinkled substrates. We show quantitatively that cell tracks have significantly larger asphericity (anisotropy), longer velocity decorrelation times, and more short-timescale ballistic motion on wrinkled substrates compared to non-wrinkled substrates. Furthermore, we demonstrate, unsurprisingly, that the anisotropy is in the direction of the wrinkles. This agrees with previously published studies on small numbers of manually tracked cells in anisotropic environments [3, 54, 55], but the analysis included in the present study achieved tracking of more than 200 times the number of cells segmented in the previous manual analysis [55]. It is anticipated that ACTIVE will facilitate this type of quantitative analysis of large cell track data sets, standardizing comparison of results across studies and fields and leading to new insights about how cell environments influence cell motility.

We also observed that cell tracks atop both of the flat substrates (gold coated and TCPS) had asphericities much larger than that expected for a 2D random walk (0.57) [52]. This is not surprising, since we know from the MSD data that our cell tracks are much more directed or ballistic than that for a random walk. Furthermore and as mentioned previously, we found that cell tracks exhibited larger asphericities atop the flat gold-coated substrates than atop the flat TCPS substrates. One potential explanation, based on our manual observations, is that individual cells tend to follow the track of a previous cell. Such “repeat” tracks, which could be assumed to involve cell-derived matrix deposition on the substrates, might be more anisotropic, and also might occur more often on materials where cells adhere less strongly to the pristine substrate.

This hypothesis could be tested in future work by analyzing cells atop substrates with varying adhesion strength.

Furthermore, analysis of cell divisions atop anisotropic and isotropic substrates revealed cell division orientation is highly dependent on substrate topography. Atop anisotropic wrinkled substrates, cells divided parallel to the wrinkle direction (the cleavage plane was perpendicular to wrinkle direction). This result is comparable to previous work, where rat C6 glioma cells divided parallel to a sub-micrometer laser-irradiated periodic surface structure with a wavelength of 266 nm [56], which is approximately $1/5^{\text{th}}$ the wavelength of our wrinkles. Oriented divisions parallel to the wrinkle direction is attributed to the anisotropy of the cell body and nucleus (as was found atop wrinkled substrates in **Chapter 2**), and follows the “long axis rule” [57] proposed by Hertwig over 130 years ago which suggests cells divide along their long axis. Cell shape is a strong regulator of oriented cell division [58], and oriented cell divisions play a critical role in many systems during development, serving to organize and shape tissues as well as create cellular diversity [59]. The ability to “turn-on” oriented cell divisions could be a powerful tool for controlling tissue development and assaying cell-material responses during development. While the work in this chapter only focused on assaying cell motility and division directionality on static samples, these substrates have the capacity to transition from flat to wrinkled topographies for active experiments, a research endeavor we are actively pursuing. As we move from tracking in static environments to tracking in active environments, additional tracking challenges will arise. As topography change occurs, substrates may translate, rotate, or shift out of focus, which must be minimized experimentally and accounted for during tracking. Analysis of cell motility in these environments also requires tracking of cells over longer periods of time to study the dynamic cell-material interactions on these non-equilibrium substrates.

Application of ACTIVE to tracking of cells in complex *in vitro* environments, such as shape changing SMPs, is anticipated to provide new insights in diverse fields. For example, it is known that breast cancer cells can exhibit mesenchymal motility or amoeboid motility depending on several factors, including the extracellular matrix (ECM) stiffness and pore size and the ability of the cells to generate matrix metalloproteases [60]. Cells exhibiting mesenchymal motility degrade the ECM and leave behind a path that serves as a migration track for other invasive cells to follow [61]. Accurate tracking of large cell populations over long time scales may reveal important correlations of invasive cell migration, both at the individual and collective cell levels, as cells follow proteolytically generated paths. Tumor cell migration can also exhibit a mesenchymal-amoeboid transition (MAT) [62], which may be caused by changes in cell-ECM adhesion, inhibition of RHO signaling pathways, and inhibition of proteolysis [63]. SMP fibrous scaffolds capable of undergoing architecture and stiffness changes under cytocompatible conditions may serve as platforms for activating the MAT. Accurate tracking of cells through SMP scaffold change may uncover new findings about the single cell and collective MAT behavior and whether this effect is reversible. Application of ACTIVE with SMPs may also be used to study the effects of mechanical loading of cells on wound healing. Application of mechanical forces through vacuum-assisted closure of implanted scaffolds has shown to promote closure of skin wounds [64], where it is hypothesized that elongation of cells at the wound site enhances proliferation [65]. SMPs could be used to apply programmed strains to cells during wound healing assays. The effect of these programmed strains on the individual and collective cell migration behavior could be analyzed with ACTIVE, potentially revealing new insights into the individual and collective cell motility responsible for improved wound healing under programmed elongation.

3.6 Conclusion

Quantitative, statistical-physics-based analyses of cell motility atop anisotropic and isotropic substrates revealed more diffusive (less ballistic) cell motility for increasing timescales, more persistent motility along wrinkles than perpendicular to wrinkles, and a subtle difference in cell motility between our two flat “controls”. Our new tracking tool, termed Automated Contour-based Tracking for *In Vitro* Environments (ACTIVE), enabled this analysis of cell motility. We expect ACTIVE to be a powerful approach for tracking adherent cell motion over long timescales in complex environments, advancing the fundamental understanding of the effect of cell-cell interactions, coupled with cell-material interactions, on cell motility. Combined with quantitative statistical metrics, this should enable new insights into cancer biology, mechanobiology, and morphogenesis.

3.7 Acknowledgements

This work was conducted in collaboration with Megan Brasch, a graduate student in Dr. James Henderson’s lab, and Dr. Lisa Manning, a Professor in Physics at Syracuse University. Megan helped with developing, benchmarking, and applying the ACTIVE tracking algorithm, and detailed description and testing of the ACTIVE code is discussed in her thesis. Dr. Manning was paramount to guiding the development of the ACTIVE code, providing expertise in coding and using physics metrics to describe cell motility.

3.8 References

[1] Gray DS, Tien J, Chen CS. Repositioning of cells by mechanotaxis on surfaces with micropatterned Young's modulus. *Journal of Biomedical Materials Research Part A*. 2003;66A:605-14.

- [2] Magnani A, Priamo A, Pasqui D, Barbucci R. Cell behaviour on chemically microstructured surfaces. *Materials Science & Engineering C-Biomimetic and Supramolecular Systems*. 2003;23:315-28.
- [3] Dalton BA, Walboomers XF, Dziegielewski M, Evans MDM, Taylor S, Jansen JA, et al. Modulation of epithelial tissue and cell migration by microgrooves. *Journal of Biomedical Materials Research*. 2001;56:195-207.
- [4] Yim EKF, Reano RM, Pang SW, Yee AF, Chen CS, Leong KW. Nanopattern-induced changes in morphology and motility of smooth muscle cells. *Biomaterials*. 2005;26:5405-13.
- [5] Nelson CM, VanDuijn MM, Inman JL, Fletcher DA, Bissell MJ. Tissue geometry determines sites of mammary branching morphogenesis in organotypic cultures. *Science Signaling*. 2006;314:298.
- [6] Aman A, Piotrowski T. Cell migration during morphogenesis. *Developmental biology*. 2010;341:20-33.
- [7] Lu P, Weaver VM, Werb Z. The extracellular matrix: a dynamic niche in cancer progression. *The Journal of cell biology*. 2012;196:395-406.
- [8] Tzvetkova-Chevolleau T, Stéphanou A, Fuard D, Ohayon J, Schiavone P, Tracqui P. The motility of normal and cancer cells in response to the combined influence of the substrate rigidity and anisotropic microstructure. *Biomaterials*. 2008;29:1541-51.
- [9] Tan JL, Tien J, Pirone DM, Gray DS, Bhadriraju K, Chen CS. Cells lying on a bed of microneedles: an approach to isolate mechanical force. *Proceedings of the National Academy of Sciences*. 2003;100:1484-9.

- [10] Plotnikov SV, Pasapera AM, Sabass B, Waterman CM. Force Fluctuations within Focal Adhesions Mediate ECM-Rigidity Sensing to Guide Directed Cell Migration. *Cell*. 2012;151:1513-27.
- [11] Fong KD, Nacamuli RP, Loba EG, Henderson JH, Fang TD, Song HM, et al. Equibiaxial tensile strain affects calvarial osteoblast biology. *Journal of Craniofacial Surgery*. 2003;14:348-55.
- [12] Fong KD, Warren SM, Loba EG, Henderson JH, Fang TD, Cowan CM, et al. Mechanical strain affects dura mater biological processes: implications for immature calvarial healing. *Plastic and reconstructive surgery*. 2003;112:1312-27.
- [13] Henderson J, De la Fuente L, Romero D, Colnot C, Huang S, Carter D, et al. Rapid growth of cartilage rudiments may generate perichondrial structures by mechanical induction. *Biomechanics and modeling in mechanobiology*. 2007;6:127-37.
- [14] Henderson JH, Chang LY, Song HM, Longaker MT, Carter DR. Age-dependent properties and quasi-static strain in the rat sagittal suture. *Journal of biomechanics*. 2005;38:2294-301.
- [15] Henderson JH, Nacamuli RP, Zhao B, Longaker MT, Carter DR. Age-dependent residual tensile strains are present in the dura mater of rats. *Journal of The Royal Society Interface*. 2005;2:159-67.
- [16] Henderson JH, Longaker MT, Carter DR. Sutural bone deposition rate and strain magnitude during cranial development. *Bone*. 2004;34:271-80.
- [17] Henderson J, Carter D. Mechanical induction in limb morphogenesis: the role of growth-generated strains and pressures. *Bone*. 2002;31:645-53.
- [18] Rozario T, DeSimone DW. The extracellular matrix in development and morphogenesis: a dynamic view. *Developmental biology*. 2010;341:126-40.

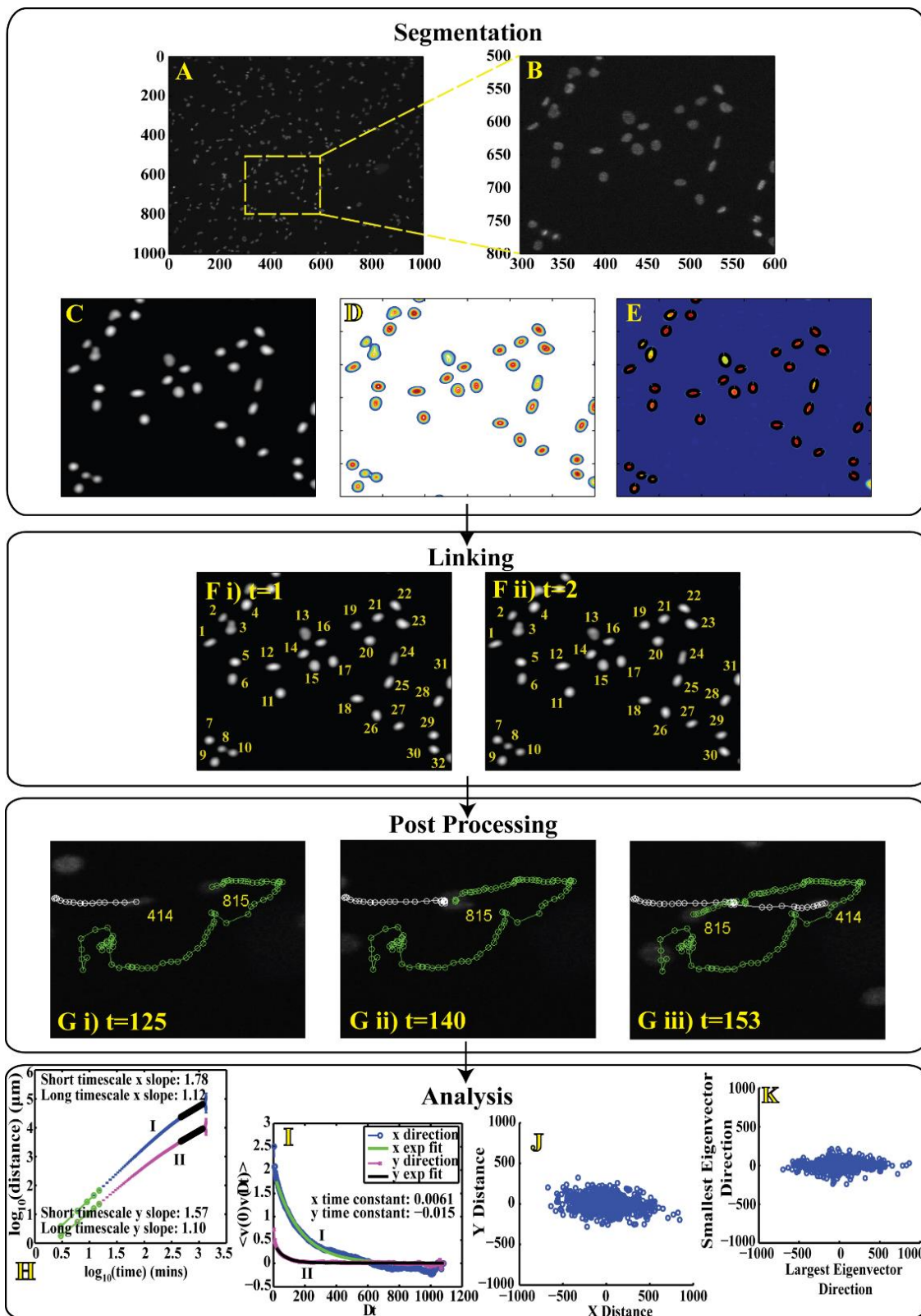
- [19] Mammoto T, Ingber DE. Mechanical control of tissue and organ development. *Development*. 2010;137:1407-20.
- [20] Park H, Guo X, Temenoff JS, Tabata Y, Caplan AI, Kasper FK, et al. Effect of swelling ratio of injectable hydrogel composites on chondrogenic differentiation of encapsulated rabbit marrow mesenchymal stem cells in vitro. *Biomacromolecules*. 2009;10:541-6.
- [21] Tibbitt MW, Kloxin AM, Dyamenahalli KU, Anseth KS. Controlled two-photon photodegradation of PEG hydrogels to study and manipulate subcellular interactions on soft materials. *Soft Matter*. 2010;6:5100-8.
- [22] Guvendiren M, Burdick JA. Stem Cell Response to Spatially and Temporally Displayed and Reversible Surface Topography. *Advanced healthcare materials*. 2013;2:155-64.
- [23] Kiang JD, Wen JH, del Álamo JC, Engler AJ. Dynamic and reversible surface topography influences cell morphology. *Journal of Biomedical Materials Research Part A*. 2013.
- [24] Guvendiren M, Burdick JA. Stiffening hydrogels to probe short- and long-term cellular responses to dynamic mechanics. *Nat Commun*. 2012;3:792.
- [25] Davis KA, Burke KA, Mather PT, Henderson JH. Dynamic cell behavior on shape memory polymer substrates. *Biomaterials*. 2011;32:2285-93.
- [26] Davis KA, Luo X, Mather PT, Henderson JH. Shape Memory Polymers for Active Cell Culture. *J Vis Exp*. 2011:e2903.
- [27] Xu X, Davis KA, Yang P, Gu X, Henderson JH, Mather PT. Shape Memory RGD-Containing Networks: Synthesis, Characterization, and Application in Cell Culture. *Macromolecular Symposia*. 2011;309-310:162-72.
- [28] Yang P, Baker RM, Henderson JH, Mather PT. In vitro wrinkle formation via shape memory dynamically aligns adherent cells. *Soft Matter*. 2013;9:4705-14.

- [29] Tseng L-F, Mather PT, Henderson JH. Shape-memory actuated change in scaffold fiber alignment directs stem cell morphology. *Acta Biomaterialia*.
- [30] Le DM, Kulangara K, Adler AF, Leong KW, Ashby VS. Dynamic Topographical Control of Mesenchymal Stem Cells by Culture on Responsive Poly (ϵ -caprolactone) Surfaces. *Advanced Materials*. 2011;23:3278-83.
- [31] Neuss S, Blumenkamp I, Stainforth R, Boltersdorf D, Jansen M, Butz N, et al. The use of a shape-memory poly(ϵ -caprolactone)dimethacrylate network as a tissue engineering scaffold. *Biomaterials*. 2009;30:1697-705.
- [32] Eilken HM, Nishikawa SI, Schroeder T. Continuous single-cell imaging of blood generation from haemogenic endothelium. *Nature*. 2009;457:896-900.
- [33] Boldajipour B, Mahabaleshwar H, Kardash E, Reichman-Fried M, Blaser H, Minina S, et al. Control of chemokine-guided cell migration by ligand sequestration. *Cell*. 2008;132:463-73.
- [34] Beltman JB, Maree AFM, de Boer RJ. Analysing immune cell migration. *Nature Reviews Immunology*. 2009;9:789-98.
- [35] Meijering E, Dzyubachyk O, Smal I. Methods for cell and particle tracking. *Imaging and Spectroscopic Analysis of Living Cells: Optical and Spectroscopic Techniques*. 2012;504:183-200.
- [36] Vasilkoski Z, Stepanyants A. Detection of the optimal neuron traces in confocal microscopy images. *Journal of neuroscience methods*. 2009;178:197-204.
- [37] Deng Y, Coen P, Sun M, Shaevitz JW. Efficient Multiple Object Tracking Using Mutually Repulsive Active Membranes. *PloS one*. 2013;8:e65769.

- [38] Xu T, Li H, Shen T, Ojic N, Vavylonis D, Huang X. Extraction and analysis of actin networks based on open active contour models. *Biomedical Imaging: From Nano to Macro*, 2011 IEEE International Symposium on: IEEE; 2011. p. 1334-40.
- [39] Tonkin JA, Rees P, Brown MR, Errington RJ, Smith PJ, Chappell SC, et al. Automated Cell Identification and Tracking Using Nanoparticle Moving-Light-Displays. *Plos One*. 2012;7.
- [40] Becker T, Madany A. Morphology-based Features for Adaptive Mitosis Detection of In Vitro Stem Cell Tracking Data. *Methods of Information in Medicine*. 2012;51:449-56.
- [41] Elowitz MB, Levine AJ, Siggia ED, Swain PS. Stochastic gene expression in a single cell. *Science*. 2002;297:1183-6.
- [42] Zhang H-P, Be'er A, Florin E-L, Swinney HL. Collective motion and density fluctuations in bacterial colonies. *Proceedings of the National Academy of Sciences*. 2010;107:13626-30.
- [43] Katz Y, Tunstrøm K, Ioannou CC, Huepe C, Couzin ID. Inferring the structure and dynamics of interactions in schooling fish. *Proceedings of the National Academy of Sciences*. 2011;108:18720-5.
- [44] Othmer HG, Dunbar SR, Alt W. Models of dispersal in biological systems. *Journal of mathematical biology*. 1988;26:263-98.
- [45] Gao YX, Kilfoil ML. Accurate detection and complete tracking of large populations of features in three dimensions. *Optics Express*. 2009;17:4685-704.
- [46] Baker RM, Brasch ME, Manning ML, Henderson JH. Automated, contour-based tracking and analysis of cell behaviour over long time scales in environments of varying complexity and cell density. *Journal of The Royal Society Interface*. 2014;11:20140386.
- [47] McQuarrie DA. *Statistical Mechanics*: Viva Books Private Limited; 2003.
- [48] Levy H, Lessman F. *Finite Difference Equations*: DOVER PUBN Incorporated; 1992.

- [49] Šolc K. Shape of a Random-Flight Chain. *The Journal of Chemical Physics*. 1971;55:335.
- [50] Aronovitz J, Nelson D. Universal features of polymer shapes. *Journal de Physique*. 1986;47:1445-56.
- [51] Theodorou DN, Suter UW. Shape of unperturbed linear polymers: polypropylene. *Macromolecules*. 1985;18:1206-14.
- [52] Rudnick J, Gaspari G. The aspharity of random walks. *Journal of Physics A: Mathematical and General*. 1986;19:L191.
- [53] Davidson P, Bigerelle M, Bounichane B, Giazzon M, Anselme K. Definition of a simple statistical parameter for the quantification of orientation in two dimensions: Application to cells on grooves of nanometric depths. *Acta biomaterialia*. 2010;6:2590-8.
- [54] Bettinger CJ, Zhang Z, Gerecht S, Borenstein JT, Langer R. Enhancement of in vitro capillary tube formation by substrate nanotopography. *Advanced Materials*. 2008;20:99-103.
- [55] Mitchel JA, Hoffman-Kim D. Cellular scale anisotropic topography guides Schwann cell motility. *PloS one*. 2011;6:e24316.
- [56] Wang X, Ohlin CA, Lu Q, Hu J. Cell directional migration and oriented division on three-dimensional laser-induced periodic surface structures on polystyrene. *Biomaterials*. 2008;29:2049-59.
- [57] Hertwig O. Das problem der befruchtung und der isotophie des eies. eine theorie der vererbun. *Jenaische Zeitschrift für Naturwissenschaft*. 1884;18:276-318.
- [58] Minc N, Burgess D, Chang F. Influence of cell geometry on division-plane positioning. *Cell*. 2011;144:414-26.
- [59] Gillies TE, Cabernard C. Cell division orientation in animals. *Current Biology*. 2011;21:R599-R609.

- [60] Pathak A, Kumar S. Biophysical regulation of tumor cell invasion: moving beyond matrix stiffness. *Integrative Biology*. 2011;3:267-78.
- [61] Wolf K, Wu YI, Liu Y, Geiger J, Tam E, Overall C, et al. Multi-step pericellular proteolysis controls the transition from individual to collective cancer cell invasion. *Nature Cell Biology*. 2007;9:893-904.
- [62] Wolf K, Mazo I, Leung H, Engelke K, Von Andrian UH, Deryugina EI, et al. Compensation mechanism in tumor cell migration mesenchymal–amoeboid transition after blocking of pericellular proteolysis. *The Journal of cell biology*. 2003;160:267-77.
- [63] Friedl P, Wolf K. Tumour-cell invasion and migration: diversity and escape mechanisms. *Nature Reviews Cancer*. 2003;3:362-74.
- [64] Argenta LC, Morykwas MJ, Marks MW, DeFranzo AJ, Molnar JA, David LR. Vacuum-assisted closure: state of clinic art. *Plastic and reconstructive surgery*. 2006;117:127S-42S.
- [65] Saxena V, Hwang C-W, Huang S, Eichbaum Q, Ingber D, Orgill DP. Vacuum-assisted closure: microdeformations of wounds and cell proliferation. *Plastic and Reconstructive Surgery*. 2004;114:1086-96.



Scheme 3-1. Overview of ACTIVE tracking algorithm. The tracking algorithm accomplishes 4 main tasks: segmentation, linking, post-processing, and analysis. (a-b) Cells are stained with Hoechst 33342 dye and imaged for 24 h. (c) Images are initially processed using a bandpass filter and (d) contour profiles are established based on nuclear intensity fluctuations. (e) For single peak contours, cells are fit with a representative ellipse, while multi-peak instances are tagged as two separate ellipses for division and merging event cases. (f-i) Cell identification tags (IDs) are established and (f-ii) IDs are linked between consecutive frames. (g-i) Post-tracking, interaction events are identified, (ii) processed using a customized cost function and (iii) cell track information is updated for more complete and accurate complex interaction event analysis. To characterize the diffusivity and velocity dynamics of cell behavior, cell motility behavior is then quantified using (h) MSD (I and II for x and y data, respectively), (i) velocity-autocorrelation analyses (I and II for x and y data, respectively), (j) diffusion plots of cell tracks in which the final position for each cell was plotted after the starting location was renormalized to the plot origin and (k) final cell locations rotated by the principal axis of the gyration tensor.

Table 3-1. Average number of cells identified by ACTIVE for various frames at each density and substrate type.

Density (cells/cm²)	Material Type	Avg # of Cells Segmented in First Frame	Avg # of Cells Segmented in Last Frame	Avg # of Cells Identified by ACTIVE Over All Frames
5,000	Wrinkled	327 ± 118	344 ± 171	760 ± 347
	Non-Wrinkled	278 ± 61	308 ± 56	716 ± 112
	TCPS	405 ± 260	348 ± 213	956 ± 650
10,000	Wrinkled	611 ± 145	597 ± 152	1196 ± 465
	Non-Wrinkled	662 ± 130	590 ± 88	1519 ± 480
	TCPS	725 ± 239	636 ± 217	1558 ± 586
20,000	Wrinkled	898 ± 389	746 ± 234	1627 ± 729
	Non-Wrinkled	869 ± 316	652 ± 150	1943 ± 1164
	TCPS	1097 ± 347	780 ± 137	2670 ± 989

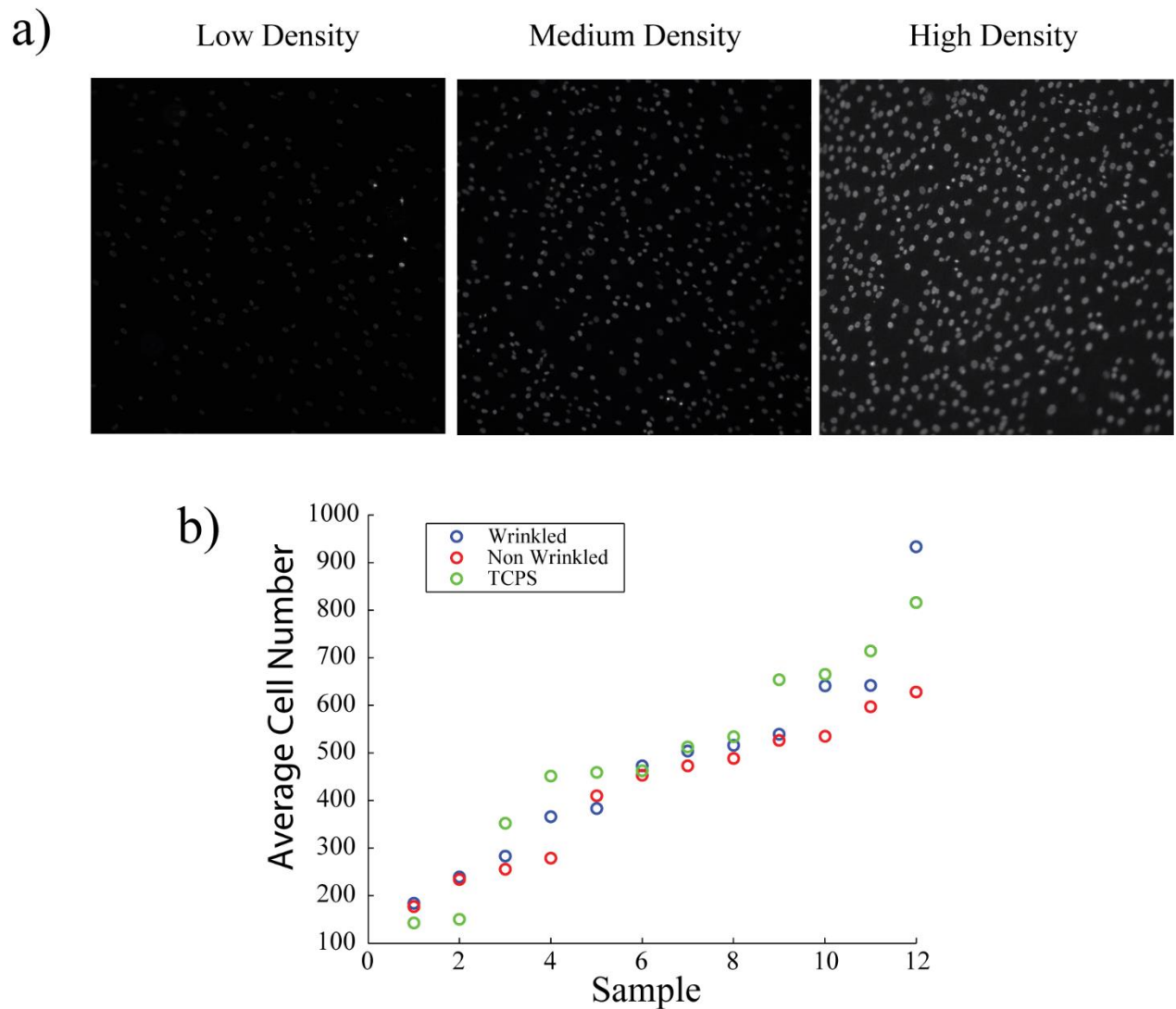


Figure 3-1. Representative fluorescent micrographs of stained nuclei seeded at different densities. (a) Cells were stained with Hoechst 33342 nuclear dye after seeding on a wrinkled substrate at three different densities: low density (5,000 cells/cm²); medium density (10,000 cells/cm²); and high density (20,000 cells/cm²). (b) Cells segmented in the first frame for each sample image on wrinkled, non-wrinkled and TCPS substrates (n=12 samples per substrate; samples ordered first by cell number).

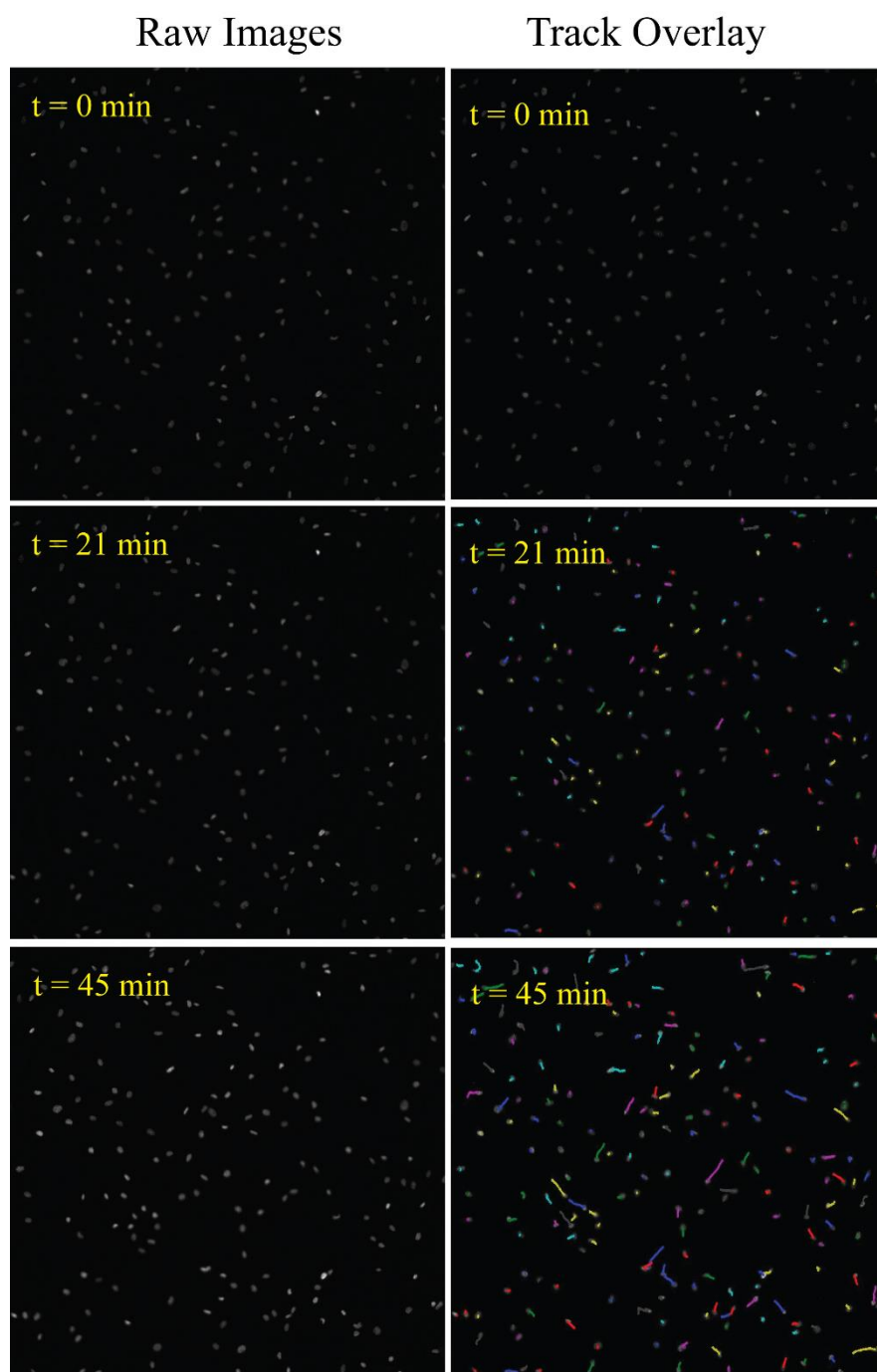


Figure 3-2. Raw fluorescent images and the corresponding tracked images with overlaid tracks. Time progression of cell nuclei with overlaid tracks shows accurate full tracks are constructed. Only the first 45 min are shown for ease of visualizing all cell tracks.

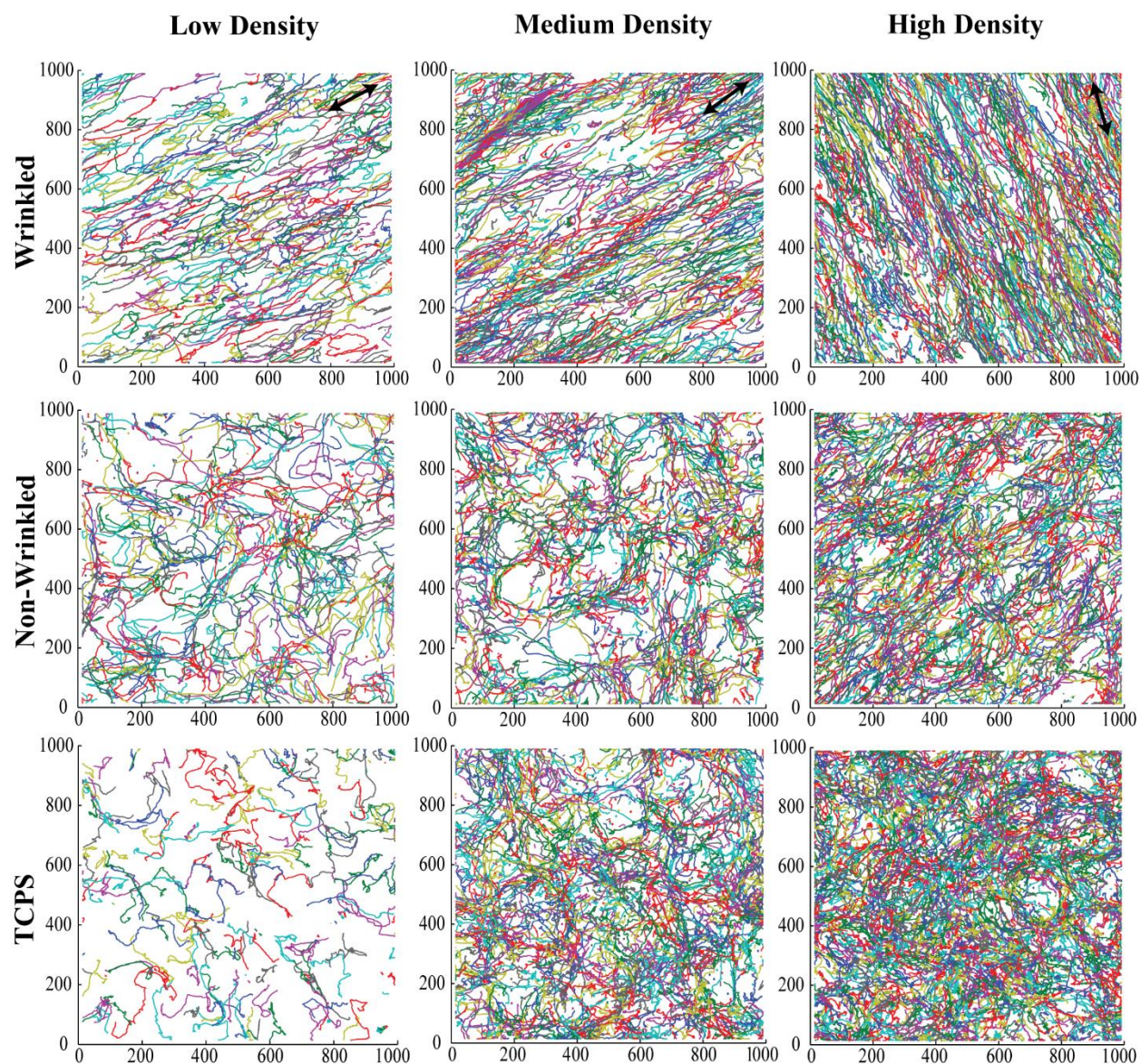


Figure 3-3. Representative cell trajectories for cells seeded on (top) wrinkled, (middle) non-wrinkled, and (bottom) TCPS substrates at (left) low, (middle) medium and (right) high densities. The resulting trajectory information qualitatively shows that wrinkled samples yield directional migration of C3H10T1/2 mouse fibroblast cells. Representative tracks for non-wrinkled and TCPS isotropic substrates qualitatively show no preferential directional migration. For the wrinkled images, black double headed arrows indicate wrinkle direction.

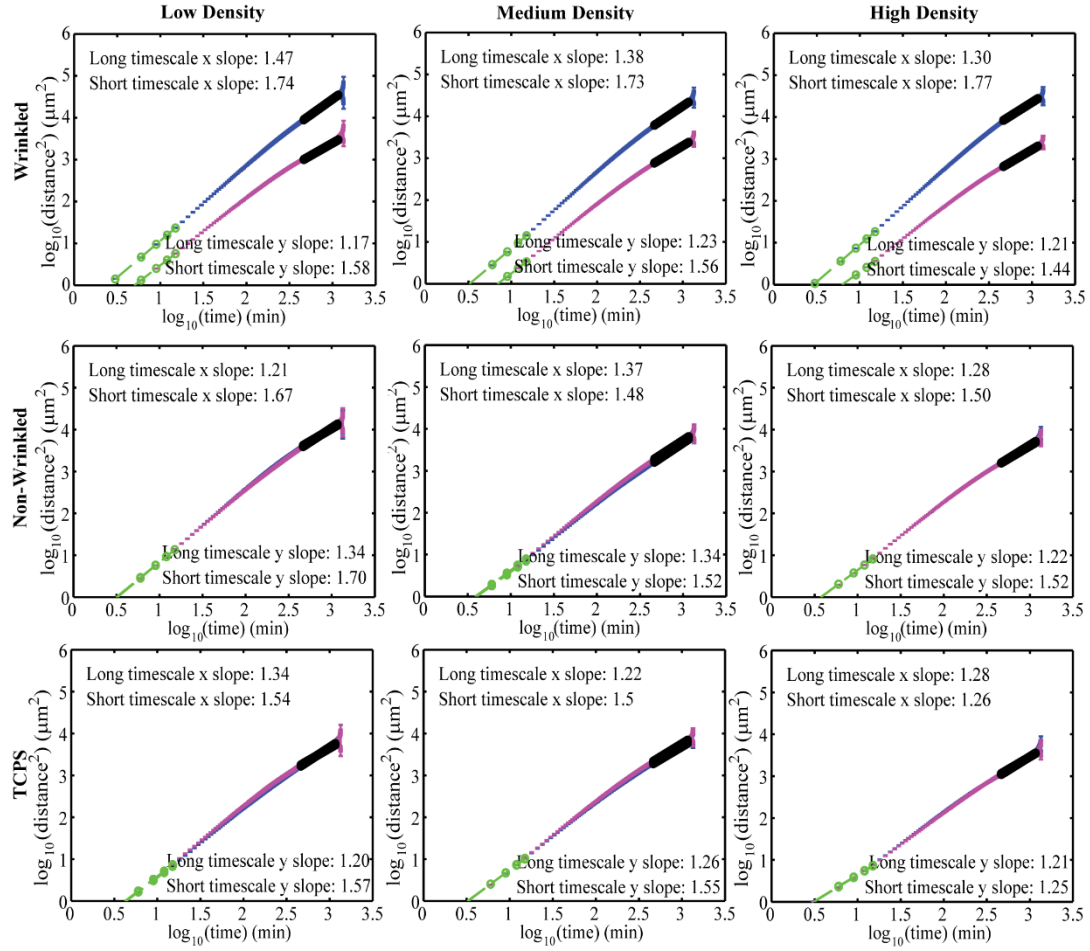


Figure 3-4. Representative MSD plots for cells seeded on anisotropic and flat substrates at various densities. Cells seeded on (top) wrinkled, (middle) non-wrinkled, and (bottom) TCPS at (left) 5,000, (middle) 10,000 and (right) 20,000 cells/cm² were analyzed using a mean squared displacement correlation analysis. Slopes of the MSD plots were calculated at small timescales and large timescales to determine the diffusive nature of migration. Linear regression was used on the first 5 data points for short timescale slopes and a range of 60 data points for the long timescale slope, using the same range for each sample. Blue lines depict MSD traces of the x-direction (parallel to wrinkle direction for wrinkled samples) and magenta lines depict MSD traces of the y-direction (perpendicular to wrinkle direction for wrinkled samples).

Table 3-2. Average slopes and mobility parameters are reported for the non-decomposed and decomposed MSD profiles. Standard deviations are in parentheses. For substrates, wrinkled = W, non-wrinkled = NW, and tissue culture polystyrene = TCPS. For a given metric (column), statistical comparisons were made between substrate type (W vs. NW vs. TCPS). For each metric, substrates sharing a label are statistically different. Substrates that do not share a label are not statistically different.

		Non-decomposed MSD			Decomposed MSD					
		Short Timescale Slope	Long Timescale Slope	δ	X-Short Timescale Slope	X-Long Timescale Slope	X- δ	Y-Short Timescale Slope	Y-Long Timescale Slope	Y- δ
Substrate	W	1.67 ^a (0.09)	1.32 ^a (0.13)	0.45 (0.52)	1.71 ^{a,b} (0.09)	1.33 (0.13)	0.37 (0.54)	1.52 (0.11)	1.23 (0.09)	-0.25 (0.42)
	NW	1.53 ^a (0.13)	1.32 ^b (0.11)	0.18 (0.51)	1.53 ^a (0.12)	1.34 ^a (0.12)	-0.16 (0.55)	1.53 (0.14)	1.28 (0.12)	-0.07 (0.48)
	TCPS	1.56 (0.16)	1.21 ^{a,b} (0.12)	0.58 (0.59)	1.56 ^b (0.16)	1.21 ^a (0.15)	0.27 (0.60)	1.56 (0.16)	1.20 (0.12)	0.31 (0.65)

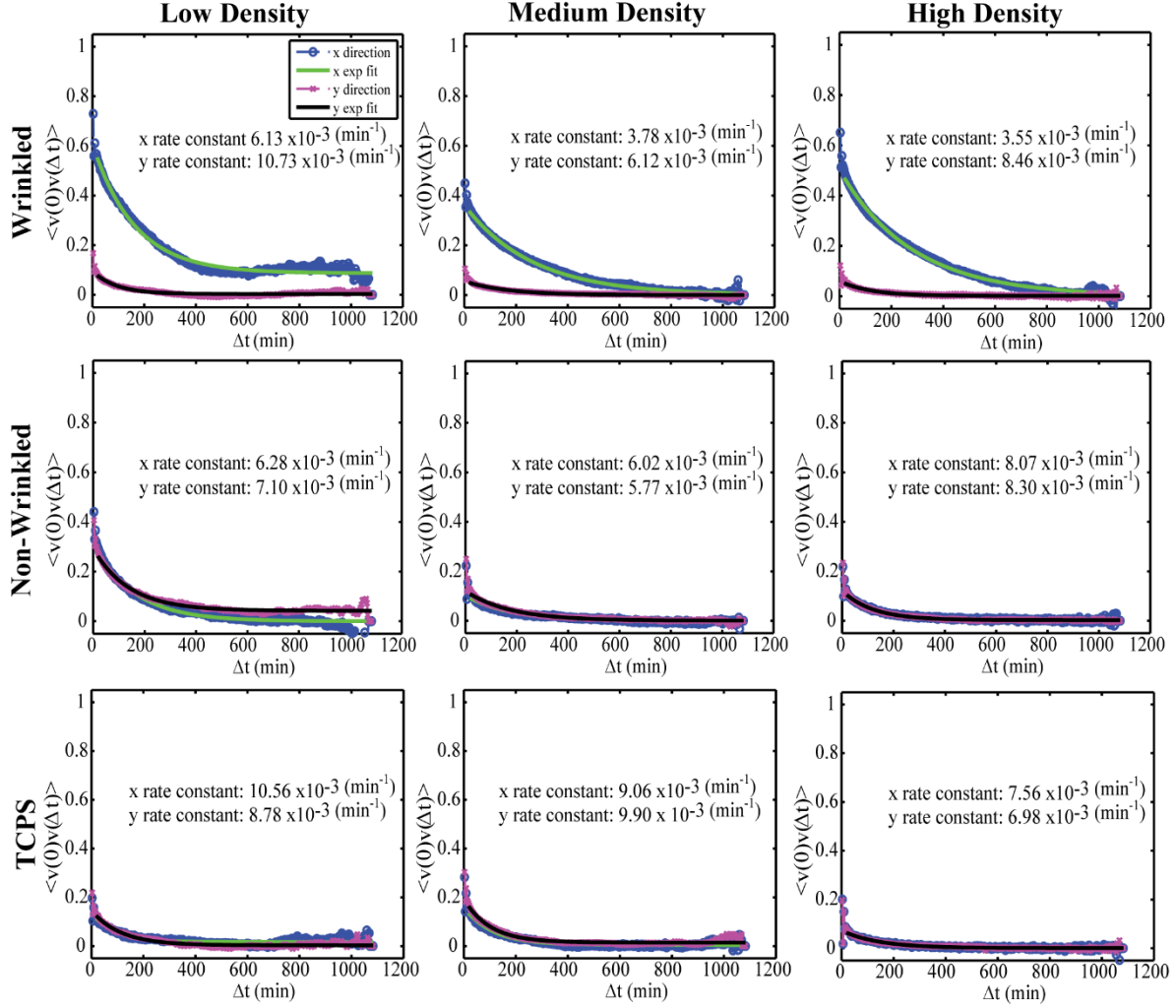


Figure 3-5. Representative velocity autocorrelation plots for cells seeded on anisotropic and flat substrates at various densities. Cells seeded on (top) wrinkled, (middle) non-wrinkled, and (bottom) TCPS at (left) 5,000, (middle) 10,000 and (right) 20,000 cells/cm² were analyzed using a velocity autocorrelation function. Anisotropic substrates showed distinct preferential migration along the grooved direction, while non-wrinkled and TCPS controls demonstrated no statistically significant difference in their x- and y-velocity autocorrelation components. An exponential decay was fit to each profile after removing the first 5 points due to noise. A decay constant was extracted and compared amongst all samples.

Table 3-3. Velocity auto-correlation and track asphericity for different substrates. Average track asphericity and the decay constants fit to the velocity autocorrelation function, where x is the direction parallel to the wrinkles for the wrinkled substrate, are reported. Standard deviations are in parentheses. For a given metric (column), statistical comparisons were made between substrate type (W vs. NW vs. TCPS). For each metric, substrates sharing a label are statistically different. Substrates that do not share a label are not statistically different.

		Velocity Auto-correlation		Asphericity
		X-Rate Constant x 10 ⁻³ (min ⁻¹)	Y-Rate Constant x 10 ⁻³ (min ⁻¹)	Track Asphericity
Substrate	Wrinkle	4.85 (1.29) ^a	9.99 (3.24) ^{a,b}	0.85 (0.02) ^{a,b}
	Non-Wrinkle	5.79 (1.31) ^b	6.49 (1.94) ^a	0.81 (0.02) ^{a,c}
	TCPS	8.35 (2.04) ^{a,b}	7.88 (2.35) ^b	0.77 (0.02) ^{b,c}

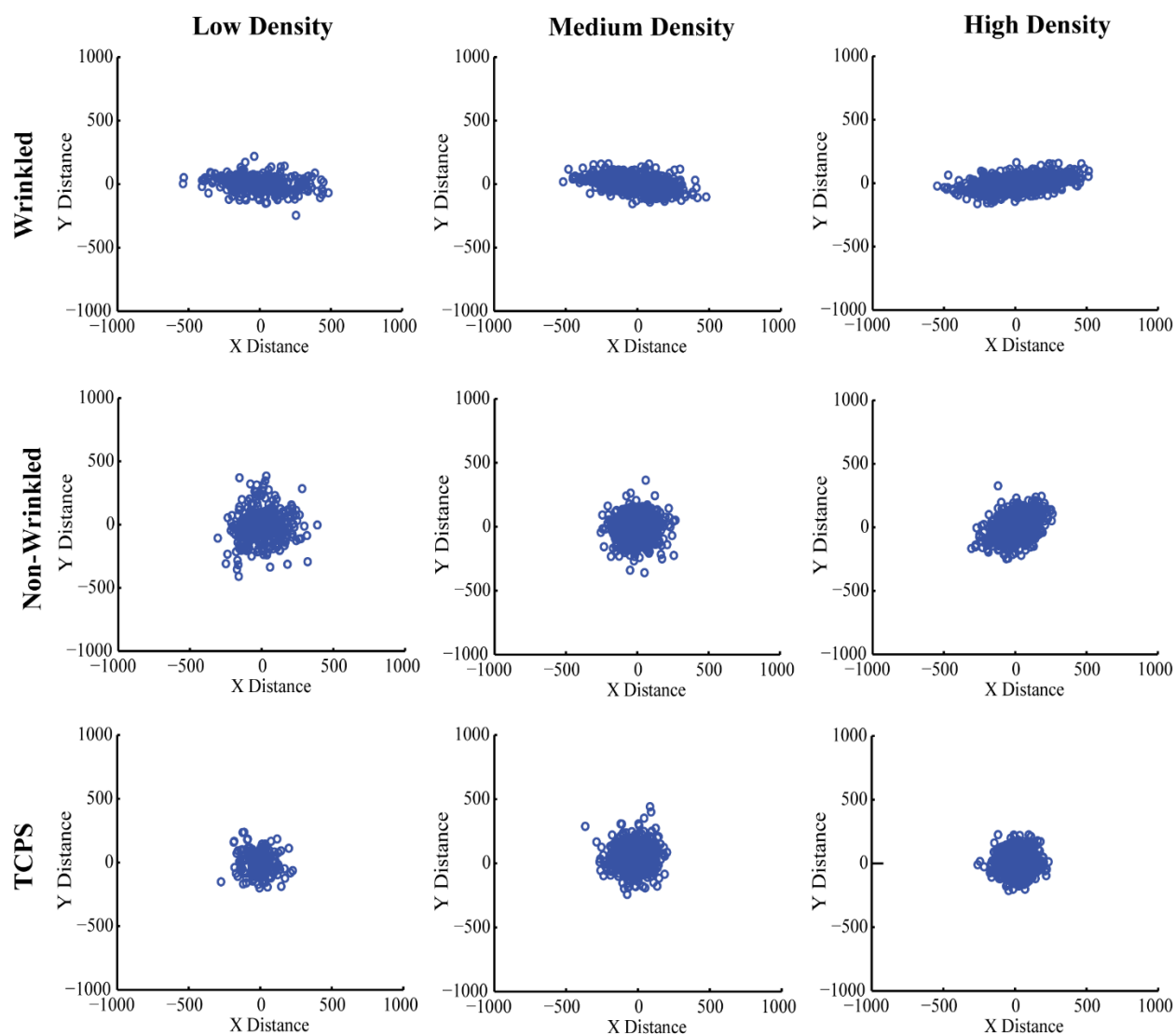


Figure 3-6. Representative cell diffusion plots for cells seeded on anisotropic and flat substrates at various densities. Cells seeded on (top) wrinkled, (middle) non-wrinkled, and (bottom) TCPS at (left) 5,000, (middle) 10,000 and (right) 20,000 cells/cm² were analyzed when the final position for each cell was plotted after renormalizing the starting location to the plot origin. Anisotropic substrates showed directed cell migration as noted by the location of most cells along the x-axis (parallel to the wrinkle direction). In contrast, cells atop both isotropic substrates showed no preferential migration as noted by the radial distribution of cells from the origin.

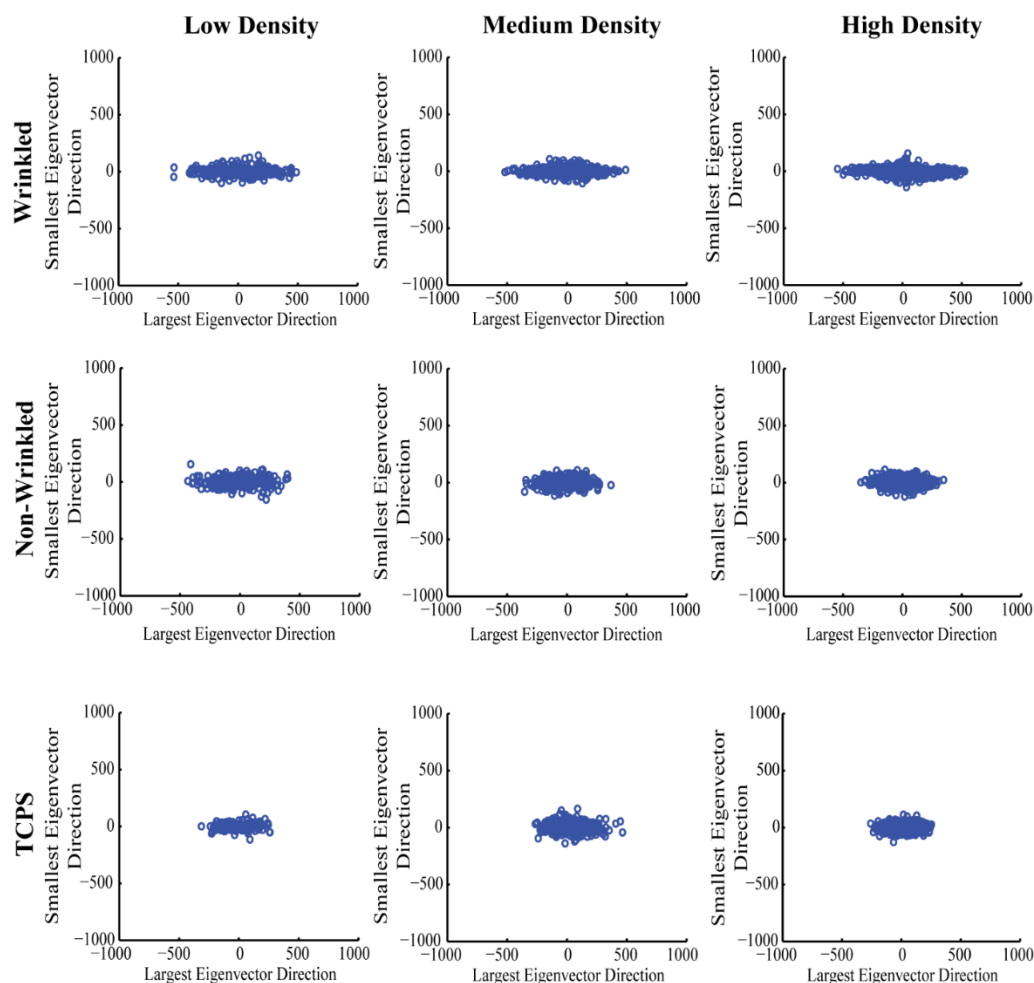


Figure 3-7. Representative cell track terminal points for cells seeded on anisotropic and flat substrates at various densities. Terminal points for cell tracks are shown for cells seeded on (top) wrinkled, (middle) non-wrinkled, and (bottom) TCPS at (left) 5,000, (middle) 10,000 and (right) 20,000 cells/cm². Terminal points were rotated so that the largest eigenvector of the gyration tensor (**Eq. 3-3** in the main text) lies along the x-axis. Therefore, the anisotropy of the points is a visualization of average track asphericity. Surprisingly, cell track asphericity was significantly higher atop flat gold substrates when compared to flat TCPS substrates, indicative of a dependence of cell motility on surface chemistry.

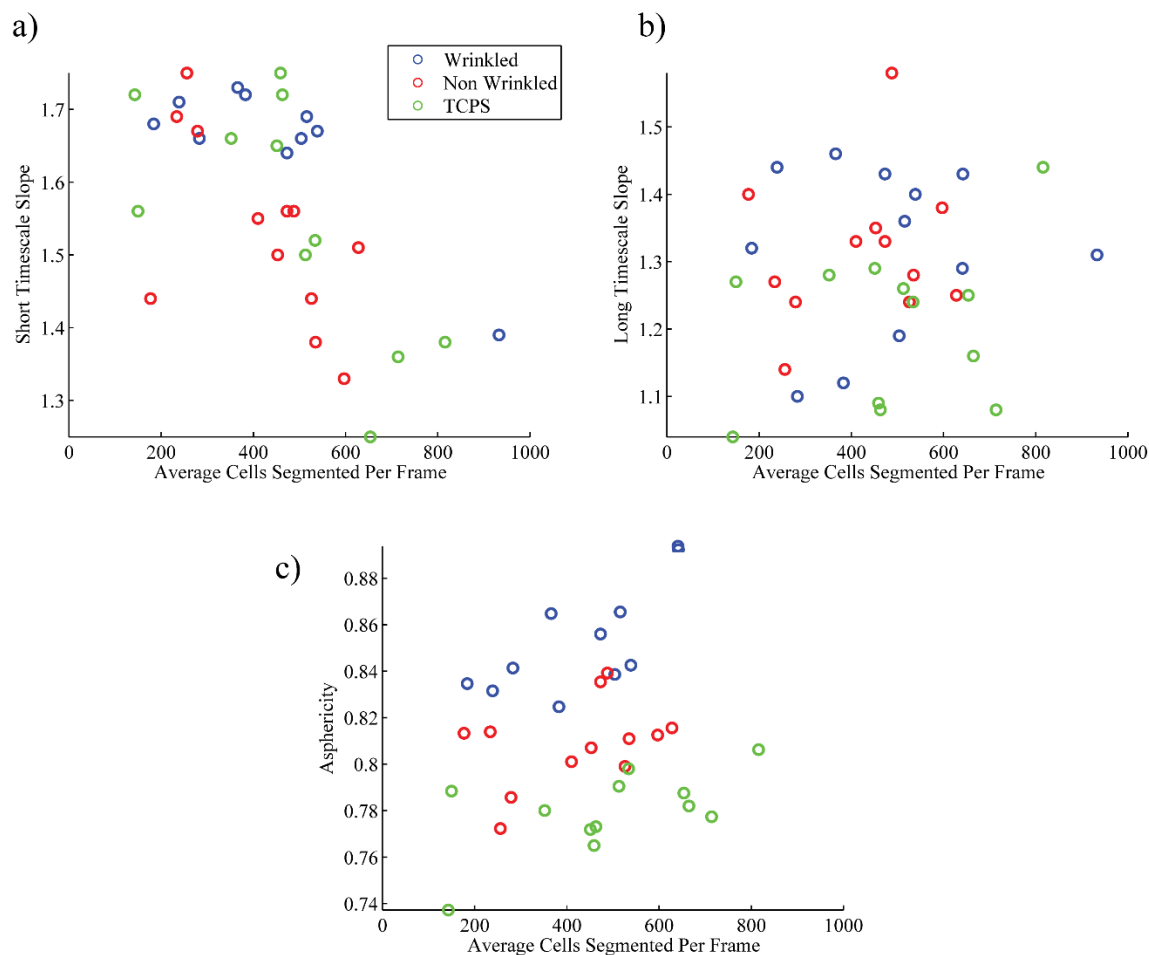


Figure 3-8. Cell motility behavior correlation with average cell density. (a) Short timescale slopes extracted from the non-decomposed MSD, (b) long timescale slopes extracted from the non-decomposed MSD, and (c) cell track asphericity are plotted as a function of the average cell density for a given sample. Short timescale slopes exhibit a negative correlation with cell density, while long timescale slopes have no correlation with cell density. Cell track asphericity is positively correlated with cell density particularly atop the anisotropic wrinkled substrate. Average cell density is determined as the average number of particles segmented in the beginning and ending frames.

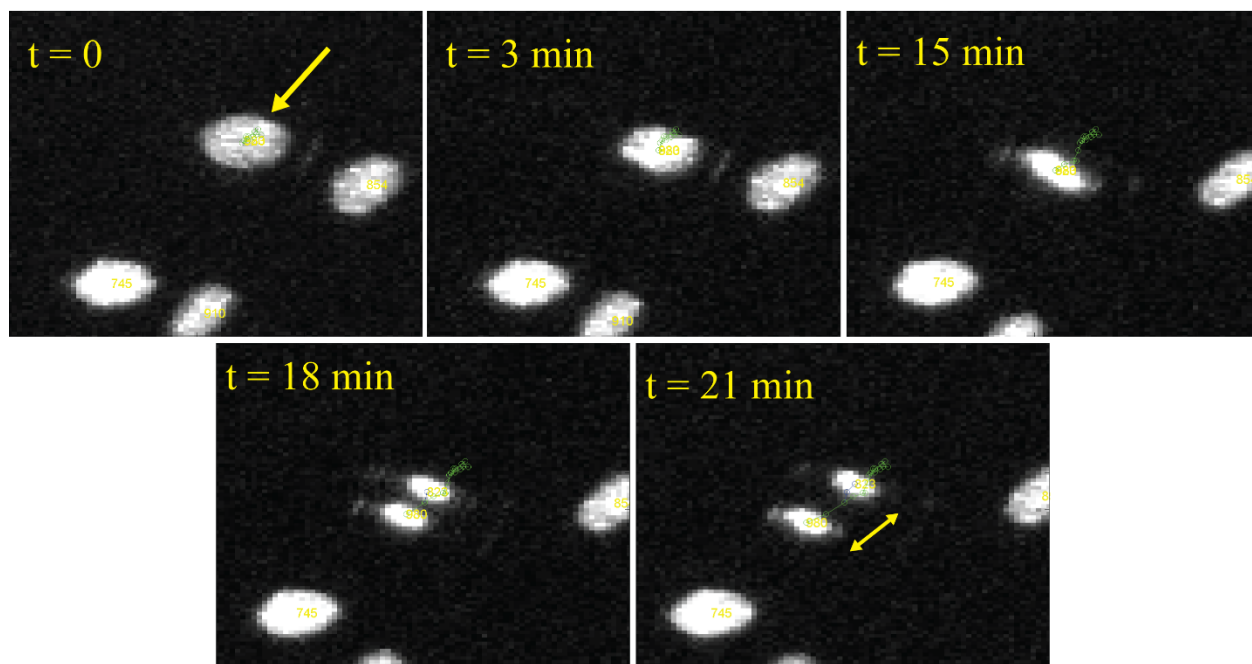


Figure 3-9. Cell divisions and determining cell division orientation. A timelapse sequence of a dividing cell (yellow arrow in $t=0$ frame) shows a cell condensing its nucleus and dividing into two daughter cells. For cell division orientation, a line is drawn between the two nuclei centroids, and the angle of that line is used as the cell division angle (noted by double headed arrow).

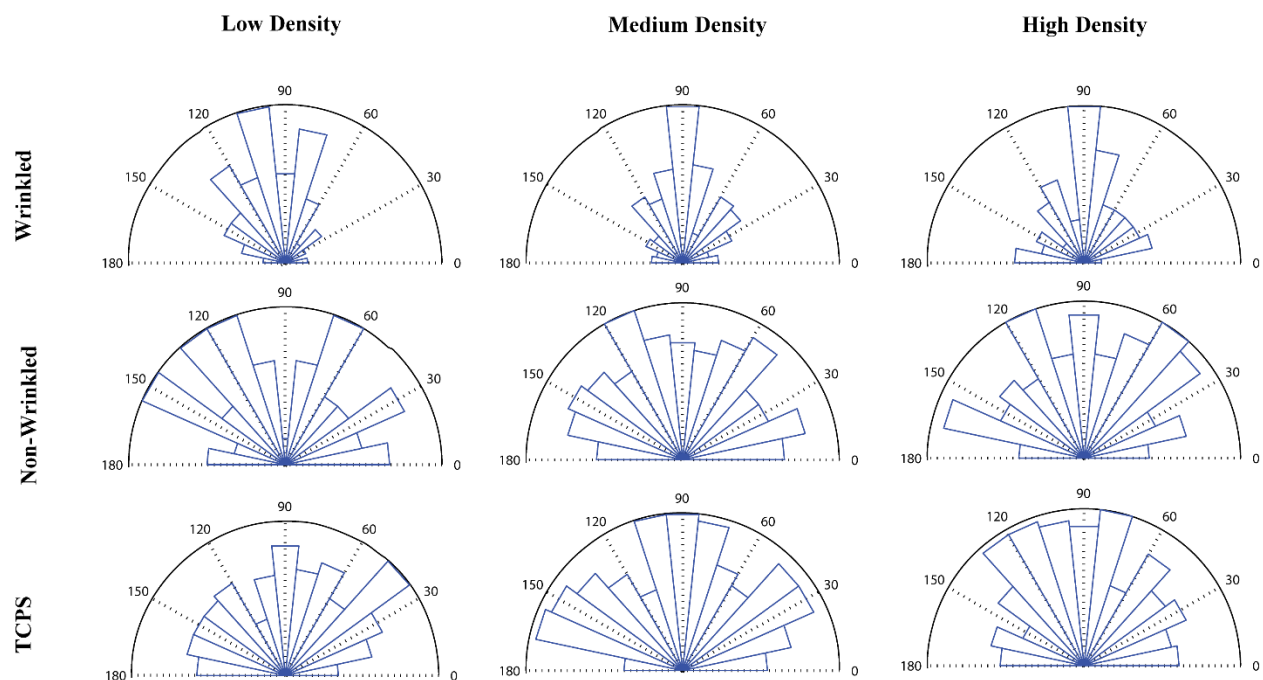


Figure 3-10. Representative angular histograms of the division angles of cells seeded on anisotropic and flat substrates at various densities. Angular histograms of cell division angles are shown for cells seeded on (top) wrinkled, (middle) non-wrinkled, and (bottom) TCPS at (left) 5,000, (middle) 10,000 and (right) 20,000 cells/cm². Histograms show a narrow distribution of division angles for the wrinkled substrates, centered around 90° (parallel to the wrinkle direction), and broad distributions of division angles for both the non-wrinkled and TCPS substrates, independent of seeding density.

Table 3-4. Angular spread of division angles atop anisotropic and isotropic substrates. Average angular spread for the wrinkled substrate is lower than the non-wrinkled and TCPS substrates, indicative of more directed division atop the wrinkled topography.

	Wrinkled	Non-wrinkled	TCPS
Angular Spread	41.0 (3.7)	47.3 (3.1)	48.5 (2.9)

Chapter Four: Shape Memory Poly(ϵ -caprolactone)-co-Poly(ethylene glycol) Foams with Body Temperature Actuation[†]

4.1 Synopsis

Chapters 2-3 described the fabrication and application of a shape memory polymer (SMP) 2D substrate for studying cell-material interactions in a dynamic environment. **Chapters 4-6** focus on the development of SMP 3D scaffolds and their application in regenerative medicine and cell mechanobiology. In this chapter, the fabrication and characterization of a porous SMP scaffold is described. Here, a modified porogen leaching technique was employed to fabricate a poly(ϵ -caprolactone)-co-poly(ethylene glycol) SMP foam with a tunable triggering temperature. Two mechanisms for tuning the recovery temperature were explored, and these foams surprisingly exhibited reversible actuation in compression, a first for SMP scaffolds. Scaffolds with dynamic programmability are anticipated to become powerful tools for the study of cell mechanobiology, providing new understanding of how cells respond to biophysical stimuli as well as deployable tissue-engineered constructs.

4.2 Introduction

While **Chapters 2-3** describe the development and application of shape memory polymer (SMP) 2D substrates for *Active Cell Culture*, efforts in this chapter focus on expanding this work to 3D scaffolds. Developing 3D SMP scaffolds capable of dynamically changing shape, porosity, and architecture under physiological conditions is of particular interest for application of

[†] Adapted (in part) from R.M. Baker, J.H. Henderson, and P.T. Mather. *J. Mater. Chem. B*, **2013**, 1, 4916-4920. Copyright © Royal Society of Chemistry 2013

scaffolds in tissue engineering and regenerative medicine [1, 2]. Scaffolds with dynamic programmability are anticipated to become powerful tools for the study of cell mechanobiology, providing new understanding of how cells respond to biophysical stimuli. For example, scaffolds that better mimic the dynamic nature of *in vivo* microenvironments, such as extracellular reorganization, could provide new insights for studies of tissue development and disease progression [3, 4]. Only recently has the application of 3D SMP scaffolds for *Active Cell Culture* been realized. Our group reported the first application of a 3D SMP scaffold where cells remained attached and viable through scaffold architecture reorganization [5]. Cell alignment was controlled by seeding cells on an aligned fiber mat that was programmed to transition to random fiber orientation; as a result cell alignment was turned off following SMP activation [5]. This recent advancement, accomplished in thin fiber mats, suggests the potential for further advancements in active 3D scaffolds for tissue engineering, regenerative medicine, and study of cell mechanobiology. These fiber mats, however, are limited in thickness and not adaptable to applications requiring large scaffold volumes or large volume changes. Furthermore, control over pore morphology and size is limited to the small spacing between nanofibers. As such, there is a need to develop large-volume SMP scaffolds with controllable pore morphology.

Recently, shape memory functionality has been integrated with the high compressibility and low density of porous foams to develop 3D SMP foams [6-8]. SMP foams are versatile and can be fabricated via multiple techniques, including emulsion templating [9], salt leaching [10], and chemical foaming [11, 12]. The advantage of SMP foams which can be used for *Active Cell Culture* substrates is they can have controllable pore shape and sizes, with pores ranging from sub-micron to several mm, depending on the fabrication method [13]. Additionally, SMP foams can undergo large expansion ratios, attributed to high achievable porosities, with porosities as

high as 98% achieved [14]. As a result, foams can be programmed to expand up to 50 times their programmed shape (if compressed 98%). This large expansion ratio suits foams well for applications requiring large volume changes, as discussed below.

Most studies to-date have reported SMP foams based on thermoplastic polyurethane (PU) [15-17] or epoxy [18] chemistries and have found wide use in applications ranging from deployable space aircraft structures [17, 19] to devices for treating aneurysms [20]. Most recently, SMP foams have received increased attention for use in biomedical applications where large volume expansions are desired [7]. For instance, Metcalfe et al. reported the use of cold-hibernated elastic memory (CHEM) polyurethane-based foams as an occlusive material for embolization of aneurysms [20]. It was found that CHEM foams were able to successfully occlude internal maxillary arteries in a dog model, although some residual aneurysm necks and recurrences were reported. Maitland and colleagues developed a laser-triggered SMP foam as an aneurysm occlusion device [21]. There, an SMP comprised of hexamethylene diisocyanate, N,N,N',N'-tetrakis(2-hydroxypropyl)ethylenediamine, and triethanolamine was placed in a PDMS basilar-necked aneurysm model and deployed by photothermal laser activation. The SMP foam, with a glass transition temperature (T_g) of 45 °C, was able to fully expand within 60 s of activation [21]. Such applications demonstrate the applicability of porous SMP foams as minimally invasive medical devices.

SMP foams show potential as deployable, minimally invasive medical devices and as *Active Cell Culture* scaffolds. Both applications require deployability under physiological temperatures, while *Active Cell Culture* also requires the deploying temperature be cytocompatible (37 °C). As such, the goal of this study was to develop highly porous SMP foam scaffolds capable of changing pore size and morphology under body temperature triggering.

Here, we present the fabrication and characterization of poly(ϵ -caprolactone)-co-poly(ethylene glycol) (PCL-PEG) foams with excellent shape memory behavior. Control over the recovery temperature is achieved through scaffold composition and programming conditions.

4.3 Methods and Materials

4.3.1 Materials

Poly(ϵ -caprolactone) diol (PCL) ($M_n = 3000$ g/mol) was purchased from Scientific Polymer and used as received. Poly(ethylene glycol) diol (PEG) ($M_w = 4000$ g/mol), acryloyl chloride, allyl isocyanate, triethylamine, dibutyltin dilaurate, pentaerythritol tetrakis(3-mercaptopropionate) (tetrathiol), and 2, 2-dimethoxy-2-phenylacetophenone (DMPA) were purchased from Sigma Aldrich and used as received.

4.3.1.1 PCL Macromer Functionalization

PCL diol was end-capped with acryloyl chloride to enable crosslinking through thiol-ene chemistry (**Scheme 4-1**). PCL diol was dissolved in anhydrous benzene at room temperature under nitrogen purge. After the PCL was completely dissolved, triethylamine was added in a 2.5 times molar ratio to PCL. Acryloyl chloride at 2.5 times the molar ratio of PCL was then added dropwise, and the reaction was carried out at 80 °C for 3 h under nitrogen purge. The salt products were filtered and the end-capped PCL precipitated in cold hexanes. This functionalized PCL macromer was then dried in a vacuum oven at room temperature for 48 h.

4.3.1.2 PEG Macromer Functionalization

PEG diol was end-capped with allyl isocyanate to enable crosslinking through thiol-ene chemistry (**Scheme 4-2**). PEG diol was dissolved in distilled toluene at 60 °C under nitrogen

purge. Two drops of dibutyltin dilaurate were added to the solution for catalysis. Allyl isocyanate was added dropwise to the solution at 2.5 time the molar ratio of PEG. The reaction was carried out at 90 °C for 4 h, followed by precipitation in cold hexanes.

4.3.2 Scaffold Preparation

Highly porous and interconnected scaffolds were prepared via end-linking of telechelic macromers with thiol-ene chemistry[22, 23], combined with a modified porogen-leaching technique, similar to a method established by Zhang and colleagues for PCL-block-polydimethylsiloxane SMP foams[24]. Functionalized PCL and PEG macromers were dissolved in dichloromethane (DCM), combined with tetrathiol crosslinker and DMPA photoinitiator, and UV cured to form a covalently crosslinked network (**Scheme 4-3**). To fabricate porous scaffolds, this polymerization was performed in a fused sacrificial salt template, as discussed below.

4.3.2.1 Salt Fusion

Salt particles (NaCl) were first sieved to obtain particles with diameters ranging from 150-300 μm and particles with diameters ranging from 300-500 μm . A simple method was developed to fuse salt particles prior to foam fabrication, as previous studies have shown salt fusion improves pore interconnectivity[25]. Here, salt was fused by exposure to a humid environment, where water vapor was used to form salt bridges between adjacent particles. Salt was added to a 20 mL glass vial which was subsequently placed in a Styrofoam box (9.25 x 6.25 x 8.25 in.) with the lid off. A 2 L beaker with 2 L of water at approximately 37 °C (hot water from faucet) was placed in the Styrofoam box, and the lid was sealed. After 24 h, vials were removed from the Styrofoam box and dried in a vacuum oven overnight.

4.3.2.2 Scaffold Fabrication

Foam scaffold synthesis was carried out in the 20 mL glass vial containing fused salt (**Scheme 4-4**). Added to the salt template were PCL and PEG (in a 9:1 salt:polymer weight ratio), tetrathiol crosslinker (in a 2:1 polymer:tetrathiol molar ratio), and DMPA photoinitiator (at 1 wt-% of the polymer weight) dissolved in DCM. The solution was next UV cured for 1.5 - 2 h (Black Ray, 365 nm, 2.0 mW/cm²). Following curing, glass vials were broken and samples removed. A thin skin was present on all surfaces of the scaffold and removed by cutting with a razor blade. Scaffolds were dried in a vacuum oven at 50 °C overnight to remove residual DCM. Next, salt was extracted by soaking samples in water at 37 °C and placing in a shaker for 48 h. Water was changed after the first 24 h. After salt extraction and prior to characterization, scaffolds were rinsed with running deionized water and dried.

In this study, five foams with different weight ratios of PCL-PEG (100-0, 90-10, 80-20, 70-30, and 60-40) were fabricated to investigate the effect of composition on the melt transition temperature (T_m) of the semi-crystalline copolymer. We hypothesized that incorporation of the hydrophilic PEG chains would enable tuning of the T_m , particularly in the hydrated state.

4.3.2.3 Example Formulation

For an 80PCL-20PEG sample cured in 2.5 g of salt, the following example protocol was used: 222 mg of functionalized PCL and 55.6 mg of functionalized PEG were added to a 20 mL glass vial. Added to that same vial was 202 μ L of tetrathiol dissolved in DCM (0.1 g of tetrathiol per mL of DCM) yielding a molar ratio of 2:1 polymer:tetrathiol. Next, 2.8 mg of DMPA photoinitiator was added. Extra DCM was added to bring the total solution volume to 625 μ L.

After mixing, the solution was added dropwise to the fused salt and UV cured for 2 h. Unless noted otherwise, all experiments in this study used a foam composition of 80PCL-20PEG.

4.3.3 Thermal Characterization

4.3.3.1 Thermogravimetric Analysis

Thermogravimetric analysis (TGA) was used to verify complete extraction of the sacrificial salt template. Samples weighing 5-10 mg of the foam scaffold were loaded in a Q500 (TA Instruments) thermogravimetric analyzer and heated to 600 °C at a rate of 20 °C-min⁻¹ under nitrogen purge. The mass of each sample was recorded as a function of temperature to construct the thermal degradation profile.

4.3.3.2 Differential Scanning Calorimetry

Differential scanning calorimetry (DSC) was employed to determine the T_m of each composition. DSC experiments were conducted using a Q200 (TA Instruments) equipped with a refrigerated cooling system. Samples with a mass ranging from 3-6 mg were placed in Tzero aluminum pans (TA Instruments) and were heated from -10 °C to 80 °C (first heat), cooled back to -10 °C (first cool), and finally heated back to 80 °C (second heat). All heating and cooling rates were 3 °C-min⁻¹. The T_m of each sample was determined from the endothermic peak of the second heating cycle, and crystallization temperatures (T_c) were determined from the exothermic peak from the cooling cycle. Hydrated samples were soaked in water 24 h prior to performing DSC analysis and were placed in Tzero hermetic pans (TA Instruments) to prevent water evaporation. Similar heating and cooling protocols were used for wet and dry samples.

4.3.4 Thermomechanical Characterization

4.3.4.1 One-Way Shape Memory

One-way shape memory testing was performed in a dynamic mechanical analyzer (TA Q800) using compression platens to determine the shape memory characteristics of the SMP foam. Circular discs of 7 mm diameter and 3 mm thickness were tested. Using the force controlled method in the Q800, a preload force of 0.01 N was applied. Samples were heated to 80 °C and loaded with a force rate of 0.5 N·min⁻¹ until reaching the force limit of the Q800 of 18 N. Next, samples were cooled at a rate of 3 °C·min⁻¹ to -10 °C and held isothermal for 5 min to fix the temporary state through crystallization. Samples were then unloaded at a rate of 0.5 N·min⁻¹ to the preload force of 0.01 N to observe shape fixing. To observe recovery, samples were heated at 3 °C·min⁻¹ to 80 °C. Shape fixing and recovery ratios were calculated using equations **Eq 2-4** and **Eq 2-5** discussed in **Chapter 2**.

4.3.4.2 Two-Way Shape Memory

Evident in some crosslinked semi-crystalline SMPs is the capacity to undergo two-way reversible shape memory as discussed in **Chapter 1 (Section 1.4.1.2)**. To determine if the semicrystalline PCL-PEG foams possessed this capability in compression, two-way compressive shape memory tests were carried out using a Q800 dynamic mechanical analyzer. Discs of 7 mm diameter and 3 mm thickness were tested in the compression platens of the Q800. Samples were equilibrated to 80 °C and held isothermal for 2 min. Next, samples were loaded at 0.5 N·min⁻¹ until reaching a predetermined compressive strain (10, 20, 30, 40, 50, or 60%) and then cooled at 3 °C·min⁻¹ to -20 °C, while the stress was held constant, and held isothermal for 5 min. During the cooling and isothermal step at -20 °C, samples experienced compression-induced

crystallization. While holding the stress constant, samples were then heated at $3\text{ }^{\circ}\text{C}\cdot\text{min}^{-1}$ to $80\text{ }^{\circ}\text{C}$, where samples recovered the compression-induced crystallization. Three heat-cool cycles were performed for each compressive strain, and the resulting actuation strain—or the amount of elongation/compression achieved through heating/cooling—was measured. A foam composition of 80PCL-20PEG was used to study the two-way shape memory effect.

4.3.4.3 Varying Deformation Temperature to Control Recovery

In addition to controlling the T_m of the PCL-PEG foams through systematically varying the composition, we hypothesized that the functional recovery temperature of the foams could be tuned through varying the programming conditions, particularly deforming at different temperatures with respect to the T_m . Deformation temperature studies were conducted using circular discs of 7 mm diameter and 3 mm thickness in the compression platens. For each run, thermal history of the sample was removed by equilibrating to $80\text{ }^{\circ}\text{C}$, holding isothermal for 5 min, cooling to $-10\text{ }^{\circ}\text{C}$ at a rate of $3\text{ }^{\circ}\text{C}\cdot\text{min}^{-1}$ and holding isothermal for 5 min. This allowed the same crystallization kinetics to occur for testing at each deformation temperature. Next, samples were heated at $3\text{ }^{\circ}\text{C}\cdot\text{min}^{-1}$ to a specified deformation temperature (T_m+30 , T_m+10 , T_m , T_m-5 , T_m-10 , and $T_m-15\text{ }^{\circ}\text{C}$) and deformed at $0.5\text{ N}\cdot\text{min}^{-1}$ until reaching 30% strain. While holding the stress constant, samples were then cooled at $3\text{ }^{\circ}\text{C}\cdot\text{min}^{-1}$ to $-10\text{ }^{\circ}\text{C}$ and held isothermal for 5 min to allow crystallization. Next, samples were unloaded at $0.5\text{ N}\cdot\text{min}^{-1}$ to the preload force of 0.01 N to observe shape fixing. After unloading, samples were heated at $3\text{ }^{\circ}\text{C}\cdot\text{min}^{-1}$ to $27\text{ }^{\circ}\text{C}$ and held isothermal for 20 min. This step allowed for determination of the stability of the fixed shape at room temperature. Samples were then heated at $3\text{ }^{\circ}\text{C}\cdot\text{min}^{-1}$ to $80\text{ }^{\circ}\text{C}$ to observe the recovery profile and percent recovery of the samples.

The effect of deformation temperature on the recovery profile of foams during continuous heating was also investigated. The same procedure was followed as described above, with only the recovery protocol modified. Rather than holding isothermal at 27 °C, samples were heated continuously from -10 °C to 80 °C at a rate of 3 °C-min⁻¹. An 80PCL-PEG with a dry T_m of 41 °C was used, and the same sample was tested at different T_{def} for this study. The resulting onset temperature of recovery and temperature required to recover 95% of the programmed deformation were measured and compared.

4.3.5 Architecture Characterization

Qualitative and quantitative analysis of porosity, interconnectivity, and pore morphology were assessed using scanning electron microscopy (SEM) and microcomputed tomography (μCT).

4.3.5.1 Scanning Electron Microscopy (SEM)

To visualize pore morphology of SMP foams following salt extraction, a JEOL JSM-5600 Scanning Electron Microscope was used. Foam bars were freeze-fractured using liquid nitrogen and sputter-coated with gold for 60 s prior to SEM analysis. SEM images of foam cross-sections were acquired. SEM analysis was also used to qualitatively show the effect of shape fixing and shape recovery on the SMP foams. Foams were subjected to a one-way shape memory cycle (described in **Section 4.3.4.1**) with a programmed strain of 50%. SEM images were taken before programming, after programming, and after recovery to ascertain the effect of shape memory on the foam architecture.

4.3.5.2 Microcomputed Tomography (μ CT)

Three-dimensional analysis of SMP foam architecture was performed by microcomputed tomography (Micro-CT 40; Scanco Medical). Circular discs with a 10.2 mm diameter and 3 mm thickness were scanned. A nominal voxel resolution of 12 μ m and a 45 kV and 177 μ A beam with a 200 ms integration time were used for scanning. Average porosity of SMP foams was calculated from analyzing the 3D reconstructions of 5 foam samples prepared with 150- 300 μ m diameter fused salt. Images of the 3D reconstructed foam cross-sections were prepared using Scanco's built-in software.

4.4 Results

4.4.1 Scaffold Fabrication

A modified porogen-leaching technique was employed to fabricate porous SMP foams. Salt particles used in this study had a cuboidal morphology (**Figure 4-1a**) that in turn dictated the pore morphology of the SMP foam. Upon exposure to a humid environment for 24 h, salt particles maintained their cuboidal morphology but formed salt bridges between adjacent particles (**Figure 4-1b and 1c**). These salt bridges resulted in an interconnected porous structure of the SMP foam after salt extraction. Fusion of salt particles also resulted in complete extraction of the salt upon soaking in water for 48 h, as shown by thermogravimetric analysis (**Figure 4-2**). Salt particles are thermally stable through 600 $^{\circ}$ C, whereas the PCL-PEG foam nearly completely degraded at 600 $^{\circ}$ C. This indicates that no salt particles remained in the porous foam. Following this modified porogen-leaching technique, we were able to fabricate foams with a diameter of 2.5 cm (**Scheme 4-4b**) and thicknesses up to 7 mm. Foam thickness was directly

proportional to the amount of salt used for the template, with approximately a 1:1 thickness(mm):salt(g) ratio after skin removal and densification.

4.4.2 Scaffold Architecture

Microcomputed tomography (μ CT) and SEM were used to quantitatively and qualitatively assess foam architecture. 3D reconstructions of SMP foams showed an open pore morphology that was highly interconnected (**Figure 4-3**). Circular discs punched from salt-extracted foam showed high porosity from all surfaces including the periphery (**Figure 4-3a**). Inspection of the foam cross-section (**Figure 4-3b**) revealed that high pore interconnectivity was achieved, as can be seen by the open pore morphology and the ability to see through the scaffold when a thin slice is made (**Figure 4-3b, right**). SMP foams fabricated using a salt size of 150-300 μ m had an average porosity of $79 \pm 5\%$ and an average pore size of 134 μ m. Interestingly, this pore size is lower than the expected range of 150-300 μ m dictated by the salt particles. This lower pore size is attributed to densification that occurs upon first heat of the foam (shrinking up to 20%) and as the result of having an interconnected pore structure, where the opening between pores is much smaller than the pore itself. This effect is clear from the SEM cross-section of a foam fabricated with salt of 300-500 μ m diameter (**Figure 4-4**). Larger, cuboidal pores are evident with smaller, round openings connecting the pores. The larger cuboidal pores are similar in size to the salt used for the template. Nonetheless, it is clear from the μ CT and SEM analysis that highly porous and interconnected foams were achieved.

4.4.3 Controlling Melt Transition Temperature Through Chemical Composition

DSC was employed to determine the effect of composition on PCL-PEG foam thermal properties. Five compositions ranging from 60PCL-40PEG to 100PCL-0PEG showed a trend of

decreasing T_m with increasing PEG content (**Figure 4-5**), most notably in the hydrated state (**Figures 4-5b and 4-5c**). Furthermore, increasing the PEG content resulted in a larger drop in T_m upon hydration (**Figure 4-5c**). This was coupled with an increase in the amount of water uptake (**Figure 4-6**) as the amount of PEG increased, due to the hydrophilic nature of PEG. This effect was observed for both foams and films with varying compositions of PCL-PEG. Through systematic control of the ratio of PCL to PEG, we were able to achieve a range of T_m 's near body temperature, with a composition of 80PCL-20PEG yielding a hydrated T_m of 37 °C. This composition was selected for further testing.

4.4.4 One-Way Shape Memory Behavior

One-way shape memory behavior of 80PCL-20PEG foams tested in compression was conducted to determine the shape fixing and shape recovery behavior. Foams tested in the dry and hydrated state showed excellent shape memory behavior, with shape fixing ratios >97% and shape recovery ratios >97% (**Figure 4-7**). When deformed above T_m , foams in the dry and wet state were able to be compressed up to 78% before reaching the force limit (18 N) of the Q800 DMA. This strain was comparable to the average porosity of the foams, and we expect that the achieved compression ratio for porous foams is proportional to the foam's porosity. Gratifyingly, the SMP foams were able to fix 97% of the deformation, even with such large compression ratios. SEM imaging was performed to determine the effect of shape memory programming on the pore architecture of SMP foams (**Figure 4-8**). Prior to fixing, an open pore morphology was observed (**Figure 4-8, top**). Following fixing a 50% compressive strain, the pore struts buckled and pores closed (**Figure 4-8, middle**); upon shape recovery, however, the open pore morphology was restored (**Figure 4-8, bottom**). No observable differences were found between the architecture of foams before and after programming, both in SEM analysis and in mechanical

behavior from repeated shape memory cycles. This suggests that struts do not break during programming, but rather bend/fold. Shape recovery ratios of >97% also support this finding, as lower recovery ratios would be expected if strut integrity was compromised.

To demonstrate the ability of programmed SMP foams to be triggered under physiological conditions, an 80PCL-20PEG foam programmed in a compact state was submerged in 37 °C water (**Figure 4-9**). Recovery of the foam was rapid with complete expansion occurring within 5 s.

4.4.5 Controlling Shape Recovery Temperature Through Deformation Temperature

We hypothesized that an alternative approach to tuning the functional T_m , or here the shape recovery temperature, was to control the programming conditions during a one-way shape memory cycle. To test this hypothesis, 80PCL-20PEG foams with a dry T_m of 41 °C were deformed at different temperatures and their shape memory behavior investigated (**Figure 4-10**). During the recovery step, foams were held isothermal at 27 °C for 20 min to assess stability near room temperature. When deforming above T_m , shape fixing and shape recovery ratios were both >99.5% (**Figure 4-10a and 4-10b; Table 4-1**). Additionally, foams maintained their temporary shape at 27 °C with no significant recovery after 20 min (**Figure 4-11a and 4-11b**). No difference between the shape memory behavior was observed for foams deformed above T_m . However, when deforming at or below T_m several trends appeared. First, as T_{def} decreased a decrease in the fixing ratio was observed (**Figure 4-10c through 4-10f; Table 4-1**). Samples deformed at T_m fixed 98.8% of the deformation, while samples deformed 15 °C below T_m only fixed 79% of the deformation. Furthermore, as T_{def} decreased the stability of the temporary shape also decreased when held isothermal at 27 °C for 20 min, as shown from the vertical drop in strain at 27 °C in **Figure 4-11a**. Premature recovery for deformation temperatures below T_m

stabilized after 5 min (**Figure 4-11b**). While the fixing and stability of foams deformed below T_m were reduced, all foams regardless of deformation temperature had excellent shape recovery ratios of >99% (**Table 4-1**). For samples deformed below T_m recovery ratios greater than 100% were calculated. This is due to the temperature difference between the deformation temperature and the higher recovery temperature of 80 °C, where thermal expansion resulted in additional foam expansion.

The effect of deformation temperature on the recovery profile of foams during continuous heating was also investigated (**Figure 4-12**). Similar to the interrupted heating discussed above, no difference between recovery traces was observed for samples deformed above T_m . When deforming at or below T_m , a decrease in the onset of recovery temperature was observed as the deformation temperature decreased. Deforming 15 °C below T_m resulted in an onset recovery temperature of 25.6 °C, whereas deforming above T_m resulted in an onset of recovery temperature of 55.3 °C. Also, as deformation temperature decreased the temperature to completely recover decreased (**Figure 4-12b**). When deforming 15 °C below T_m , 95% recovery occurred at 58.8 °C, while a temperature of 64.4 °C was required to reach 95% recovery when deforming above T_m . As a consequence, however, deforming at lower temperatures resulted in a broad recovery requiring a larger temperature range to achieve complete recovery. For *Active Cell Culture* applications where quick, complete recovery over a small temperature range is desired, using this approach to tune recovery is not ideal. However, for applications where a staged shape recovery over a wider temperature range is desired (e.g. incremental strain recovery with increasing temperature), this approach can be employed.

4.4.6 Two-Way Shape Memory Behavior

Analysis of the one-way shape memory profile of 80PCL-20PEG foams deformed above T_m (**Figure 4-10a and 4-10b**) revealed crystallization-induced compression upon cooling, indicating this semi-crystalline foam possessed two-way shape memory behavior. To evaluate the two-way shape memory behavior in compression, foams were loaded to 10, 20, 30, 40, 50 or 60% strain and subsequently subjected to 3 cool-heat cycles while maintaining a constant force. Surprisingly, foams showed excellent two-way reversible actuation for all loads applied (**Figure 4-13a**). During cooling, foams experienced a crystallization-induced compression that was recovered upon heating through T_m . This compression/expansion during cooling/heating was reproducible over multiple cycles. A maximum actuation strain of 15% was achieved when the initial strain loading was 30% (**Figure 13-b**), and deviations from this initial strain resulted in lower actuation strains.

4.5 Discussion

In this chapter, we have developed a simple modified-porogen leaching technique to fabricate highly porous SMP foams capable of changing pore size and morphology under body temperature triggering. Here, semi-crystalline PCL-PEG foams with tunable recovery temperatures were developed and characterized. These SMP foams exhibited excellent shape memory behavior in the dry and hydrated states and, surprisingly, possessed reversible two-way actuation in compression.

Large compression ratios of up to 78% (**Figure 4-7**) were achieved, which is desirable for tissue engineering strategies, such as minimally invasive delivery, or mechanobiological study of large tensile strains on cells seeded in fixed scaffolds. For example, in adult cardiac fibroblasts it has been shown that a 10% uniaxial tensile strain can stimulate extracellular matrix

mRNA levels and transform growth factor- β (TGF- β), whereas a 20% strain decreases extracellular matrix mRNA expression while stimulating TGF- β to a lesser extent [26]. Low porosity in the fixed state may inhibit cell infiltration into the scaffold when seeding in the temporary state. As a result, tissue engineering applications or cell mechanobiology studies for which large strain triggering is desired necessitate balancing of the desired strain with the ability to achieve cell seeding in the fixed, low porosity state. Therefore, to enable studies on increasing levels of strain recovery, increasing porosity in the permanent state will be required. SMP scaffolds fabricated via the alternative method of gas foaming have been developed with permanent porosities of 98% [14], but with gas foaming pore interconnectivity is typically low [27], which would limit cell infiltration into such scaffolds. For the salt leaching approach employed in the present work, pore size, porosity and interconnectivity can be tuned by control over salt particle size, degree of salt fusion, and macromer concentration [24]. Control over the porous structure is important for cell mechanobiology studies, as previous studies on static scaffolds have shown that cell behavior is dependent on pore morphology and size [28, 29].

Shape-changing scaffolds that can change shape under cell compatible conditions, particularly at or near body temperature, require control over the triggering mechanism. Shape recovery of semi-crystalline SMPs occurs at their melting transition temperature (T_m), and the T_m of PCL is $\sim 60^\circ\text{C}$, which is much higher than body temperature. Therefore, lowering of T_m is necessary to fabricate a shape-changing PCL-based construct. Here we have achieved lowering of T_m via two mechanisms. The first mechanism utilized copolymerization of macromers of PCL with PEG, a hydrophilic polymer. We previously reported a PCL-PEG hydrogel with a T_m of 31°C , where tuning of the T_m was achieved through control over the molecular weight of the PCL[30]. Here we kept the molecular weight of the macromers constant and varied the weight

ratios of each to control the T_m . DSC revealed that the T_m of the scaffold in both the dry and wet states decreased with increasing PEG content (**Figure 4-5**). Employing this design strategy, a range of T_m 's around body temperature was achieved, with a composition of 80 wt-% PCL and 20 wt-% PEG yielding a hydrated T_m of 37 °C.

In addition to copolymerizing the PCL scaffolds with PEG for melting point modulation, we also varied the programming temperature of the SMP foam to lower the apparent T_m , or onset temperature for shape recovery. We were able to lower the onset of recovery temperature by decreasing the deformation temperature (**Figure 4-12b**), but at the expense of reduced fixing and reduced stability at room temperature. Such a “temperature memory” phenomenon has previously been reported by Xie et al. for a Nafion-based SMP, where a large alpha transition related to the ionic cluster phase is largely responsible for this effect [31]. A related phenomenon has been exploited in amorphous systems to tune the recovery temperature and recovery kinetics [32, 33], where deforming at or below the glass transition temperature led to lower recovery temperatures. Kratz and colleagues also reported this phenomenon in semi-crystalline polymers with a broad T_m where recovery temperatures spanning a range of 100 °C were achieved [34]. The temperature memory effect observed in the semi-crystalline PCL-PEG foams is not attributed to a broad T_m , but rather to the lower thermal energy required to recover the inelastic deformation of the crystalline phase. The present work is the first report of semi-crystalline SMP foams exhibiting a temperature memory effect.

Although deforming near T_m results in a lowering of the onset temperature for strain recovery to within a physiological range, two undesirable consequences of this approach were found. First, deforming below T_m resulted in a reduction in the shape fixing upon cooling. This is attributed to a difference in the fixing mechanisms when deforming above compared to below

T_m . When deforming above T_m , shape fixing is achieved through crystallization of the PCL and PEG chains, which is robust. Strains fixed by deforming at or below T_m did so through inelastic deformation of the crystalline phase that is recoverable upon subsequent heating through T_m [35, 36]. Second, there was a reduction in the stability of the temporary shape at room temperature, examined by dwelling at that temperature during the heating step of the shape memory cycle (**Figure 4-11a and 4-11b**). We attribute the reduction in fixed strain stability at room temperature to relaxation of internal stresses between the high melting fraction of the material, which is elastically deformed at the lower temperature and thus under compressive stress, and the lower melting fraction that is subject to tensile stress from the high-melting fraction. Despite these complexities, the temperature memory effect offers a useful tool to control the recovery temperature of this SMP foam. Used in combination with composition-variation to tune equilibrium T_m , this approach will yield adequate design flexibility for biological experiments, we anticipate.

Surprisingly, the new shape memory foams also exhibited two-way reversible shape memory (**Figure 4-13**) under the bias of a compressive load, consisting of dramatic cooling-induced compression and heating-induced expansion. By inspection, neither effect is due to ordinary thermal expansion effects; rather, crystallization of the foams under a compressive load results in additional contraction that is reversed upon heating through T_m , with thermal hysteresis of ca. 50 °C when a heating rate of 3 °C-min⁻¹ is used. This effect is repeatable through several cool-heat cycles and represents a new example of reversible, soft actuation. For these samples, a compressive actuation strain of ca. 15% (**Figure 4-13b**) was achieved through contraction upon crystallization. Interestingly, the actuation magnitude (strain) was found to be non-monotonic in the initial strain applied, indicating competing effects of strain that drives crystallization-induced

actuation, and an upper bound of compressive strain for the foams. The observed compressive two-way shape memory is not explicitly due to the materials porous structure, as solid cylinders of the material in compression also were found to exhibit a similar effect. However the actuation strain achieved with the porous structure is much larger than that achieved in the solid, non-porous structure, a finding likely related to the complex distribution of stress within compressed open-cell foams [37]. We have previously reported two-way shape memory in a cross-linked poly(cyclooctene) film under tensile loading [38]. Other studies have also reported the use of the two-way shape memory effect in shape memory elastomers [39], glass-forming nematic networks [40], and triple-shape SMPs [41], all of which use tensile loading. To our knowledge, this is the first demonstration of an SMP scaffold with two-way reversible shape memory in compression. Two-way reversible actuation has been studied in other material systems, such as shape memory alloys, for application in reversible actuators [42]. Incorporating this functionality in a cytocompatible scaffold creates the possibility for generating cyclic loading on attached cells by simply switching the incubation temperature. This would enable studies into the effects of low frequency cyclic loading on cell behavior without the need of complex bioreactors or specialized loading devices. Further optimization is needed to decrease the thermal hysteresis of actuation, affording cytocompatibility for both compression and expansion.

The new PCL-PEG foam reported here shows promise as a tool for studying cell mechanobiology in 3D, and potential to enable minimally invasive delivery of scaffold constructs. As a scaffold, the foams could enable filling of critical-size bone defects, as is the focus of **Chapter 5**. SMPs have also previously been proposed for deployable medical devices including aneurysm occlusion devices [43-45], ischemic stroke devices [46], and stents [32, 47]. For minimally invasive delivery in any of these applications, SMP scaffolds must have high

compression ratios with high stability of the fixed shape. The foam presented here exhibited a high compression ratio of 78% and was able to recover 97% of the programmed deformation. Recovery at body temperature is also rapid, as demonstrated by a functional recovery experiment in which the foam is submerged in body temperature water (**Figure 4-9**). Large volume expansions suit this SMP foam well for space-filling applications where large volume expansions are desired.

4.6 Conclusion

We have employed a modified porogen-leaching technique to fabricate PCL-PEG scaffolds with shape memory capability. We have shown that recovery at body temperature can be achieved through control of the composition of the scaffolds. Recovery at body temperature may also be achieved through control of the deformation temperature during programming. In addition, we have shown that these scaffolds possess two-way reversible shape actuation. More generally, SMP foams such as these are promising candidates for functional tissue engineering constructs that can be delivered minimally invasively, due to high compression ratios and stable temporary shapes, and as platforms to study cell mechanobiology in active 3D environments, where shape change under cytocompatible conditions is required.

4.7 References

- [1] Shastri VP. Future of regenerative medicine: challenges and hurdles. *Artificial organs*. 2006;30:828-34.
- [2] Chan G, Mooney DJ. New materials for tissue engineering: towards greater control over the biological response. *Trends in biotechnology*. 2008;26:382-92.

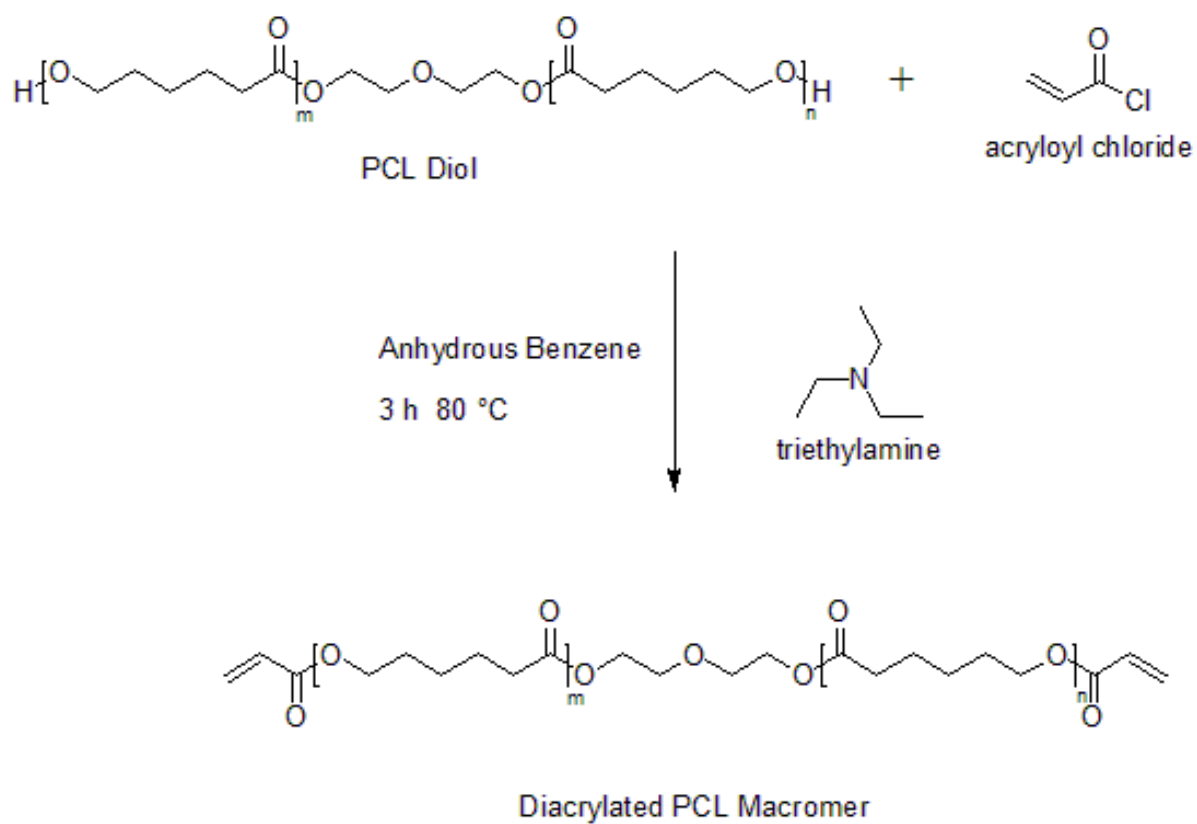
- [3] Davis KA, Burke KA, Mather PT, Henderson JH. Dynamic cell behavior on shape memory polymer substrates. *Biomaterials*. 2011;32:2285-93.
- [4] Shastri VP, Lendlein A. Materials in regenerative medicine. *Advanced Materials*. 2009;21:3231-4.
- [5] Tseng L-F, Mather PT, Henderson JH. A programmable shape-changing scaffold for regenerative medicine. *Bioengineering Conference (NEBEC)*, 2012 38th Annual Northeast: IEEE; 2012. p. 227-8.
- [6] Fujimura H, Hayashi S. Shape memory polymer foam. *Google Patents*; 1991.
- [7] Sokolowski W, Metcalfe A, Hayashi S, Yahia LH, Raymond J. Medical applications of shape memory polymers. *Biomedical Materials*. 2007;2:S23.
- [8] Tey S, Huang W, Sokolowski W. Influence of long-term storage in cold hibernation on strain recovery and recovery stress of polyurethane shape memory polymer foam. *Smart materials and structures*. 2001;10:321.
- [9] Gurevitch I, Silverstein MS. Shape memory polymer foams from emulsion templating. *Soft Matter*. 2012;8:10378-87.
- [10] Chung SE, Park CH. The thermoresponsive shape memory characteristics of polyurethane foam. *Journal of applied polymer science*. 2010;117:2265-71.
- [11] Squeo E, Quadrini F. Shape memory epoxy foams by solid-state foaming. *Smart Materials and Structures*. 2010;19:105002.
- [12] Lee SH, Jang MK, Kim SH, Kim BK. Shape memory effects of molded flexible polyurethane foam. *Smart Materials and Structures*. 2007;16:2486.

- [13] Chevalier E, Chulia D, Pouget C, Viana M. Fabrication of porous substrates: a review of processes using pore forming agents in the biomaterial field. *Journal of pharmaceutical sciences*. 2008;97:1135-54.
- [14] Singhal P, Rodriguez JN, Small W, Eagleston S, Van de Water J, Maitland DJ, et al. Ultra low density and highly crosslinked biocompatible shape memory polyurethane foams. *Journal of Polymer Science Part B: Polymer Physics*. 2012;50:724-37.
- [15] Sokolowski WM, Chmielewski AB, Hayashi S, Yamada T. Cold hibernated elastic memory (CHEM) self-deployable structures. 1999 Symposium on Smart Structures and Materials: International Society for Optics and Photonics; 1999. p. 179-85.
- [16] Sokolowski WM, Tan SC. Advanced self-deployable structures for space applications. *Journal of Spacecraft and Rockets*. 2007;44:750-4.
- [17] Huang W, Lee C, Teo H. Thermomechanical behavior of a polyurethane shape memory polymer foam. *Journal of intelligent material systems and structures*. 2006;17:753-60.
- [18] Tobushi H, Matsui R, Hayashi S, Shimada D. The influence of shape-holding conditions on shape recovery of polyurethane-shape memory polymer foams. *Smart materials and structures*. 2004;13:881.
- [19] Di Prima M, Lesniewski M, Gall K, McDowell D, Sanderson T, Campbell D. Thermo-mechanical behavior of epoxy shape memory polymer foams. *Smart materials and Structures*. 2007;16:2330.
- [20] Metcalfe A, Desfaits A-C, Salazkin I, Yahia LH, Sokolowski WM, Raymond J. Cold hibernated elastic memory foams for endovascular interventions. *Biomaterials*. 2003;24:491-7.

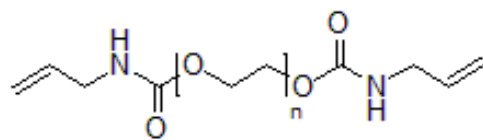
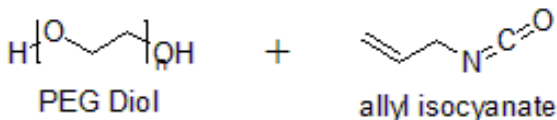
- [21] Maitland DJ, Small W, Ortega JM, Buckley PR, Rodriguez J, Hartman J, et al. Prototype laser-activated shape memory polymer foam device for embolic treatment of aneurysms. *Journal of biomedical optics*. 2007;12:030504--3.
- [22] Knight PT, Lee KM, Chung T, Mather PT. PLGA– POSS End-Linked Networks with Tailored Degradation and Shape Memory Behavior. *Macromolecules*. 2009;42:6596-605.
- [23] Lee KM, Knight PT, Chung T, Mather PT. Polycaprolactone– POSS Chemical/Physical Double Networks. *Macromolecules*. 2008;41:4730-8.
- [24] Zhang D, Petersen KM, Grunlan MA. Inorganic–Organic Shape Memory Polymer (SMP) Foams with Highly Tunable Properties. *ACS applied materials & interfaces*. 2012;5:186-91.
- [25] Murphy WL, Dennis RG, Kileny JL, Mooney DJ. Salt fusion: an approach to improve pore interconnectivity within tissue engineering scaffolds. *Tissue engineering*. 2002;8:43-52.
- [26] Lee AA, Delhaas T, McCulloch AD, Villarreal FJ. Differential Responses of Adult Cardiac Fibroblasts to in vitro Biaxial Strain Patterns. *Journal of Molecular and Cellular Cardiology*. 1999;31:1833-43.
- [27] Liu X, Ma PX. Polymeric scaffolds for bone tissue engineering. *Annals of biomedical engineering*. 2004;32:477-86.
- [28] Murphy CM, Haugh MG, O'Brien FJ. The effect of mean pore size on cell attachment, proliferation and migration in collagen–glycosaminoglycan scaffolds for bone tissue engineering. *Biomaterials*. 2010;31:461-6.
- [29] Zeltinger J, Sherwood JK, Graham DA, Müller R, Griffith LG. Effect of pore size and void fraction on cellular adhesion, proliferation, and matrix deposition. *Tissue Engineering*. 2001;7:557-72.

- [30] Xu X, Davis KA, Yang P, Gu X, Henderson JH, Mather PT. Shape Memory RGD-Containing Networks: Synthesis, Characterization, and Application in Cell Culture. *Macromolecular Symposia*. 2011;309:162-72.
- [31] Xie T, Page KA, Eastman SA. Strain-Based Temperature Memory Effect for Nafion and Its Molecular Origins. *Advanced Functional Materials*. 2011;21:2057-66.
- [32] Yakacki CM, Shandas R, Lanning C, Rech B, Eckstein A, Gall K. Unconstrained recovery characterization of shape-memory polymer networks for cardiovascular applications. *Biomaterials*. 2007;28:2255-63.
- [33] Cui J, Kratz K, Heuchel M, Hiebl B, Lendlein A. Mechanically active scaffolds from radio-opaque shape-memory polymer-based composites. *Polym Adv Technol*. 2011;22:180-9.
- [34] Kratz K, Madbouly SA, Wagermaier W, Lendlein A. Temperature-Memory Polymer Networks with Crystallizable Controlling Units. *Advanced Materials*. 2011;23:4058-62.
- [35] Rodriguez ED, Luo X, Mather PT. Linear/Network Poly(ϵ -caprolactone) Blends Exhibiting Shape Memory Assisted Self-Healing (SMASH). *ACS Applied Materials & Interfaces*. 2011;3:152-61.
- [36] Gu X, Mather PT. Entanglement-based shape memory polyurethanes: Synthesis and characterization. *Polymer*. 2012;53:5924-34.
- [37] Zhu HX, Windle AH. Effects of cell irregularity on the high strain compression of open-cell foams. *Acta Materialia*. 2002;50:1041-52.
- [38] Chung T, Romo-Uribe A, Mather PT. Two-way reversible shape memory in a semicrystalline network. *Macromolecules*. 2008;41:184-92.
- [39] Li J, Rodgers WR, Xie T. Semi-crystalline two-way shape memory elastomer. *Polymer*. 2011;52:5320-5.

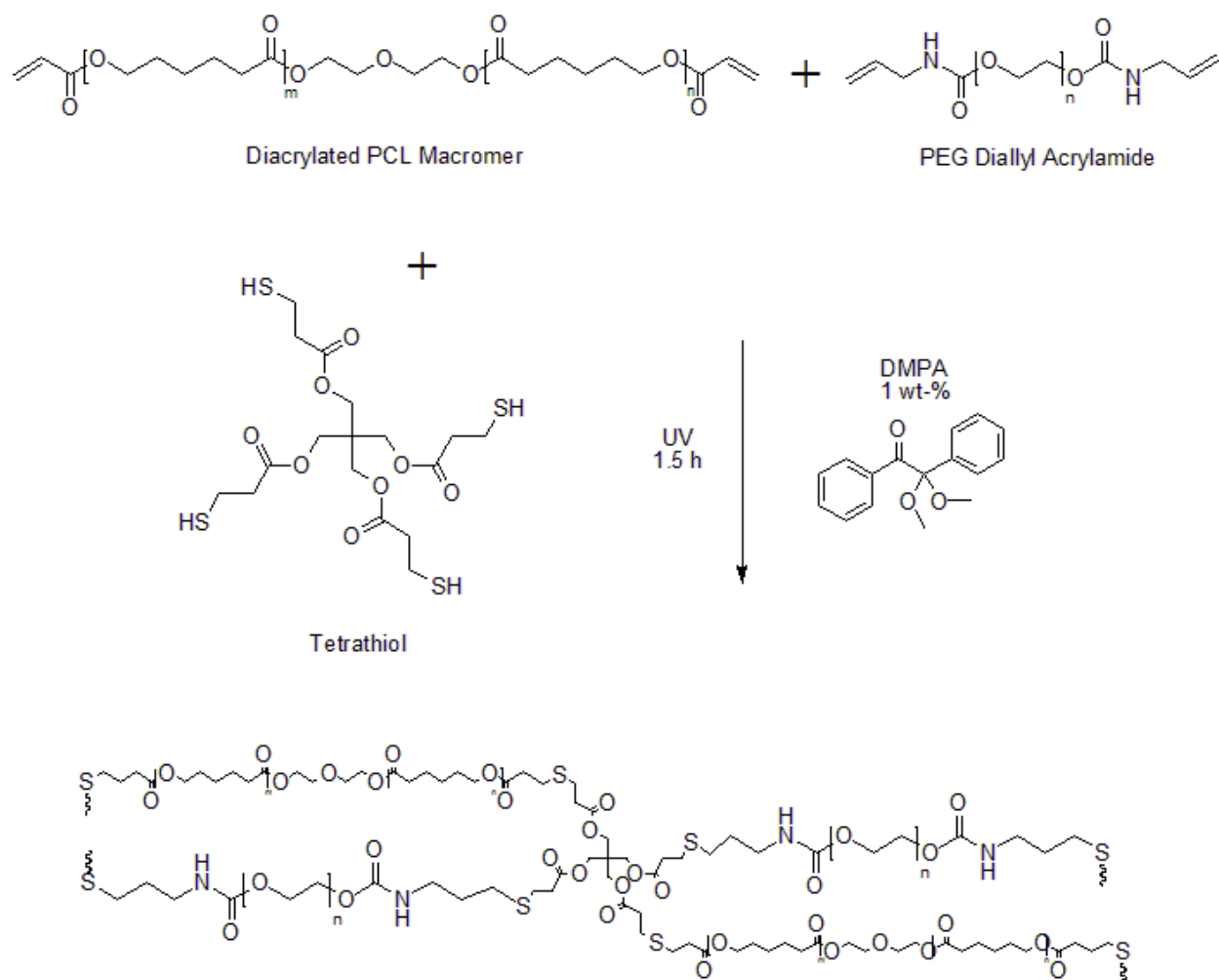
- [40] Qin H, Mather PT. Combined one-way and two-way shape memory in a glass-forming nematic network. *Macromolecules*. 2008;42:273-80.
- [41] Zotzmann J, Behl M, Hofmann D, Lendlein A. Reversible Triple-Shape Effect of Polymer Networks Containing Polypentadecalactone- and Poly(ϵ -caprolactone)-Segments. *Advanced Materials*. 2010;22:3424-9.
- [42] De Blonk BJ, Lagoudas DC. Actuation of elastomeric rods with embedded two-way shape memory alloy actuators. *Smart Materials and Structures*. 1998;7:771-83.
- [43] Metcalfe A, Desfaits AC, Salazkin I, Yahia L, Sokolowski WM, Raymond J. Cold hibernated elastic memory foams for endovascular interventions. *Biomaterials*. 2003;24:491-7.
- [44] Maitland DJ, Small W, Ortega JM, Buckley PR, Rodriguez J, Hartman J, et al. Prototype laser-activated shape memory polymer foam device for embolic treatment of aneurysms. *Journal of biomedical optics*. 2007;12:Art. No. 030504.
- [45] Singhal P, Boyle A, Brooks ML, Infanger S, Letts S, Small W, et al. Controlling the Actuation Rate of Low-Density Shape-Memory Polymer Foams in Water. *Macromolecular Chemistry and Physics*. 2013;214:1204-14.
- [46] Maitland DJ, Metzger MF, Schumann D, Lee A, Wilson TS. Photothermal properties of shape memory polymer micro-actuators for treating stroke*. *Lasers in surgery and medicine*. 2002;30:1-11.
- [47] Wache HM, Tartakowska DJ, Hentrich A, Wagner MH. Development of a polymer stent with shape memory effect as a drug delivery system. *J Mater Sci-Mater Med*. 2003;14:109-12.



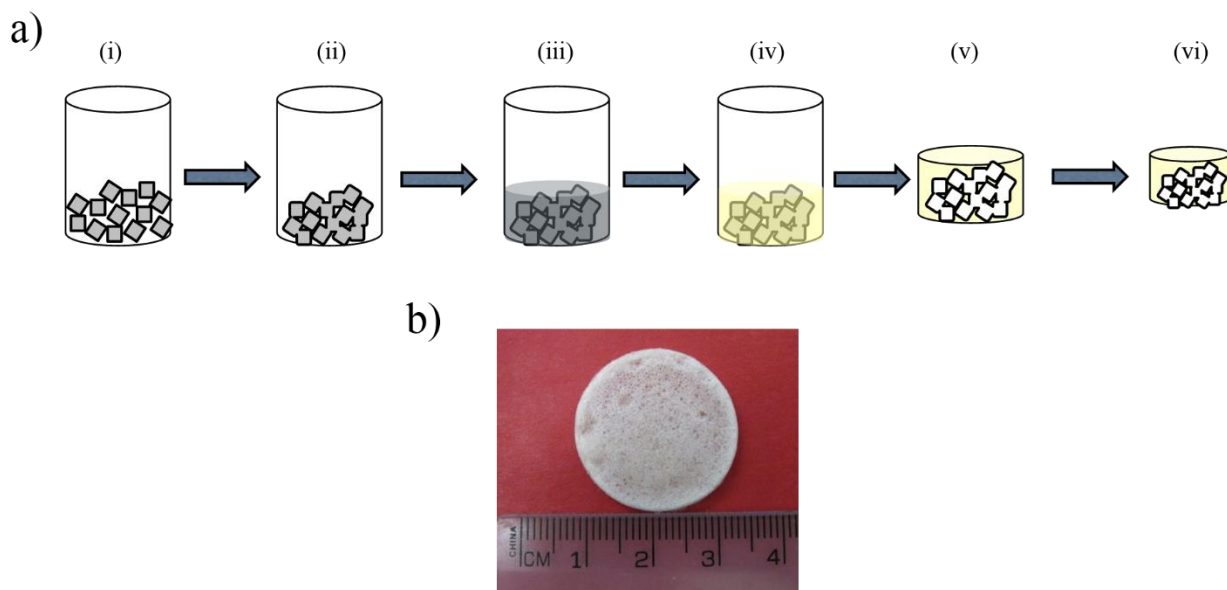
Scheme 4-1. PCL functionalization through end-capping with acryloyl chloride.



155



Scheme 4-3. SMP network formation using photo-initiated addition reactions between oligomeric macromers and the shown tetrathiol.



Scheme 4-4. Fabricating foams using a modified porogen-leaching technique. (a)(i) Salt particles with the desired diameter are sieved and added to a 20 mL glass vial; (ii)salt particles are fused in a humidity chamber for 24 h; (iii) a prepolymer solution consisting of PCL, PEG, tetrathiol crosslinker, and DMPA photoinitiator are added to the salt template; (iv) the solution is UV cured for 2 h; (v) foams are removed from the glass vials, surface skins are cut off, and salt is extracted by soaking in water for 48 h; (vi) upon first heating, densification occurs. (b) A picture of a foam following salt extraction.

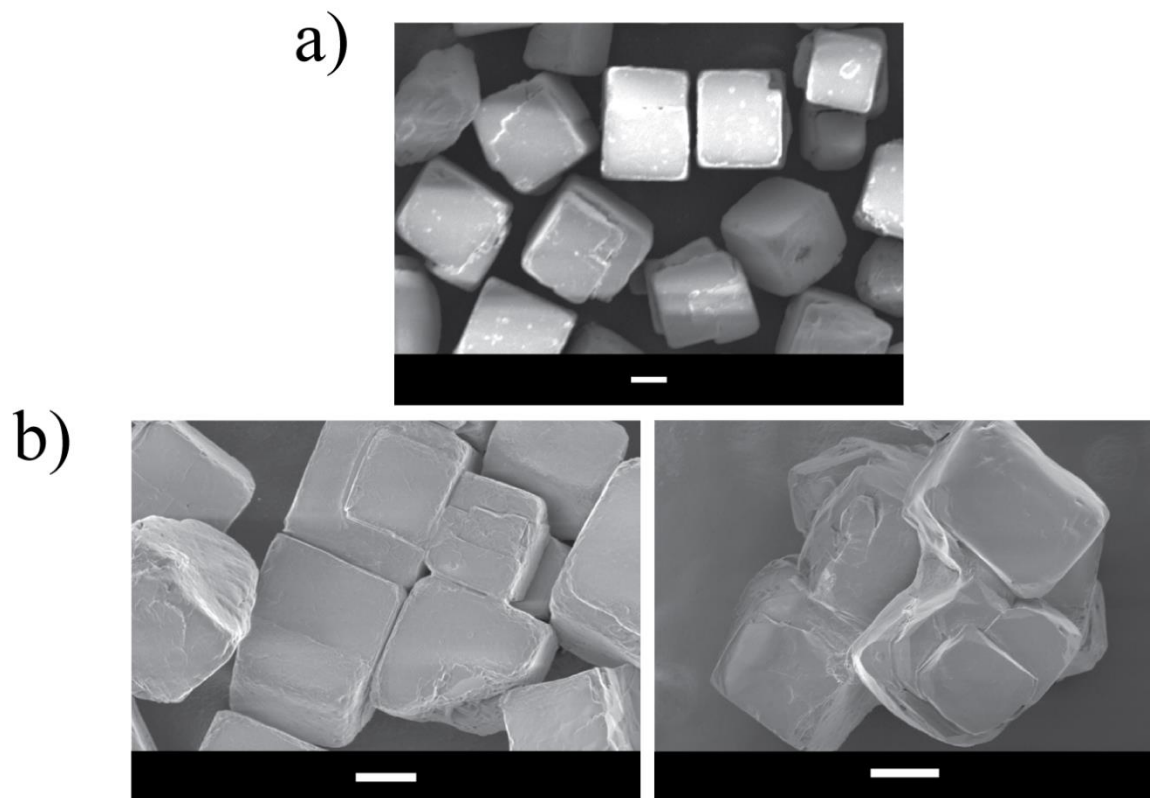


Figure 4-1. Salt fusion forms thick salt bridges between salt particles. SEM micrographs of salt particles (a) before fusion and (b) after fusion reveal that upon exposure to a humid atmosphere for 24 h, salt particles form thick salt bridges at contact sites. Scale bars are 100 μm for all SEM micrographs.

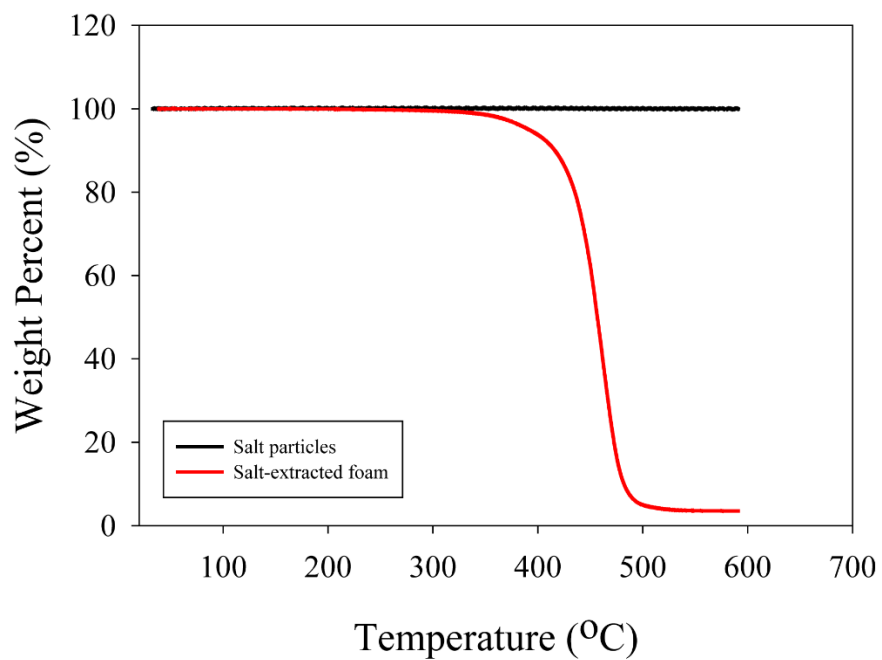


Figure 4-2. Thermal degradation profile of a salt-extracted foam. Following salt extraction the foam nearly completely degrades when heated to 600 °C. Salt crystals are thermally stable to this temperature, indicating salt was successfully extracted from the foam. Samples were heated at 20 °C-min⁻¹.

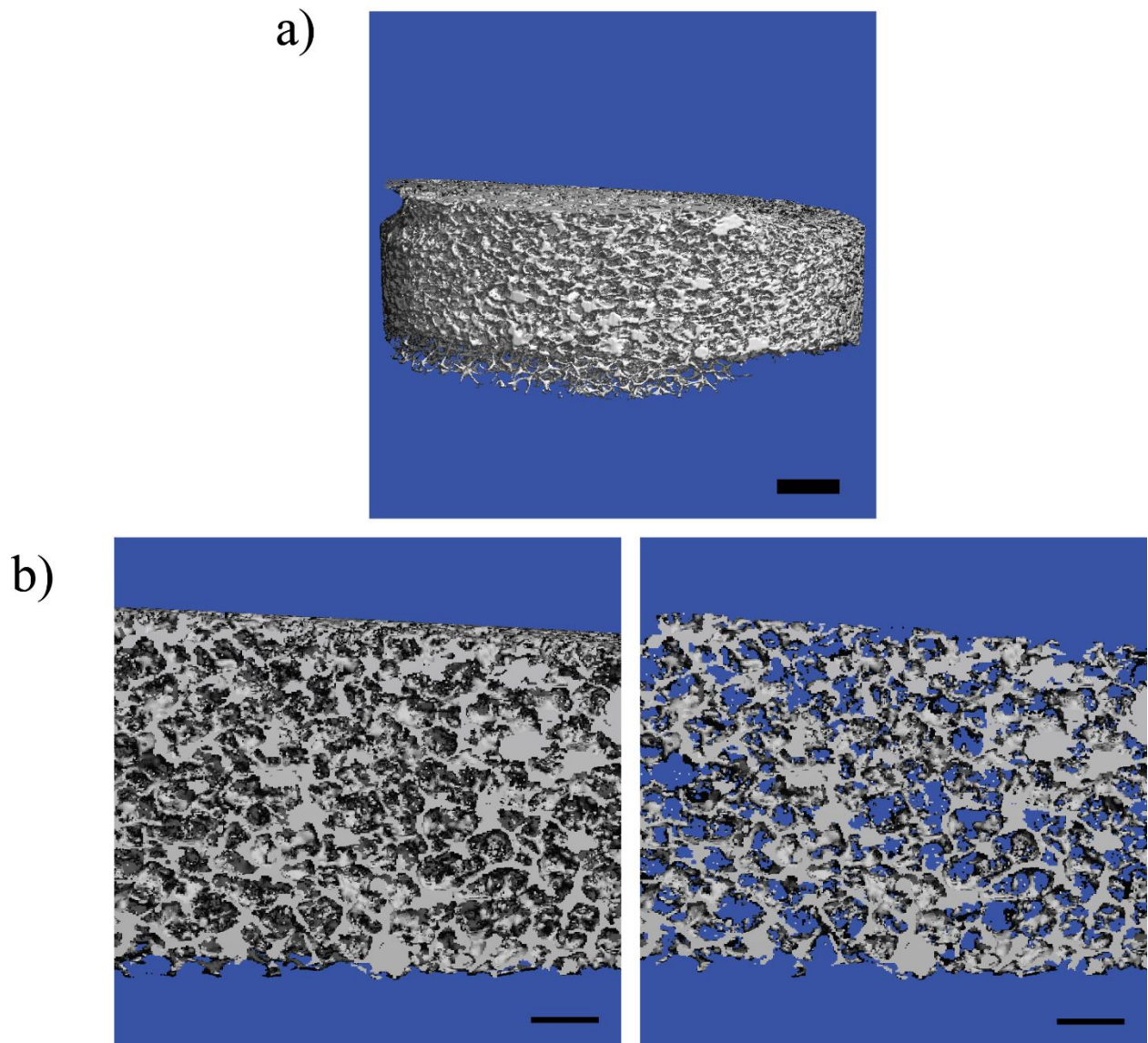


Figure 4-3. Microcomputed tomography 3D reconstructions of an SMP foam. (a) 3D reconstruction of a circular disc with 3 mm thickness and 10.2 mm diameter; (b) cross-sectional views. In (b), the image on the right is a thin slice of the cross-section shown in the image on the left. Scaffolds appear highly porous with interconnected pores. Scale bars are 1 mm for (a) and 400 μm for (b).

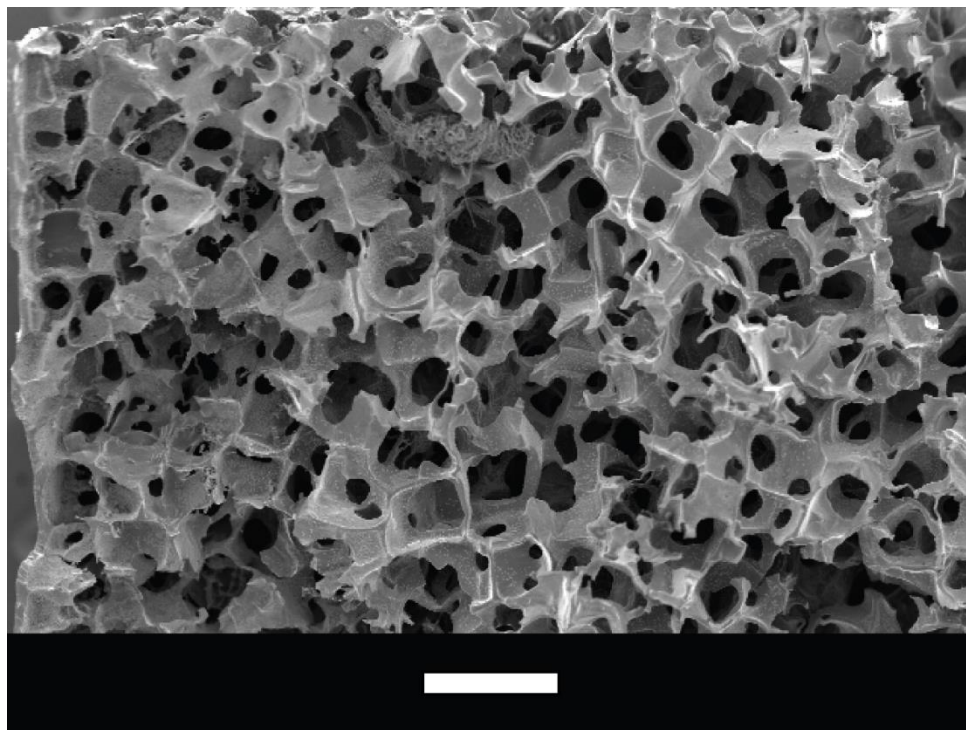


Figure 4-4. SEM micrograph of SMP foam. A freeze-fractured cross-section of an 80PCL-20PEG foam shows large cuboidal pores with small round interconnections. Scaffolds appear highly porous and interconnected. Scale bar is 500 μm .

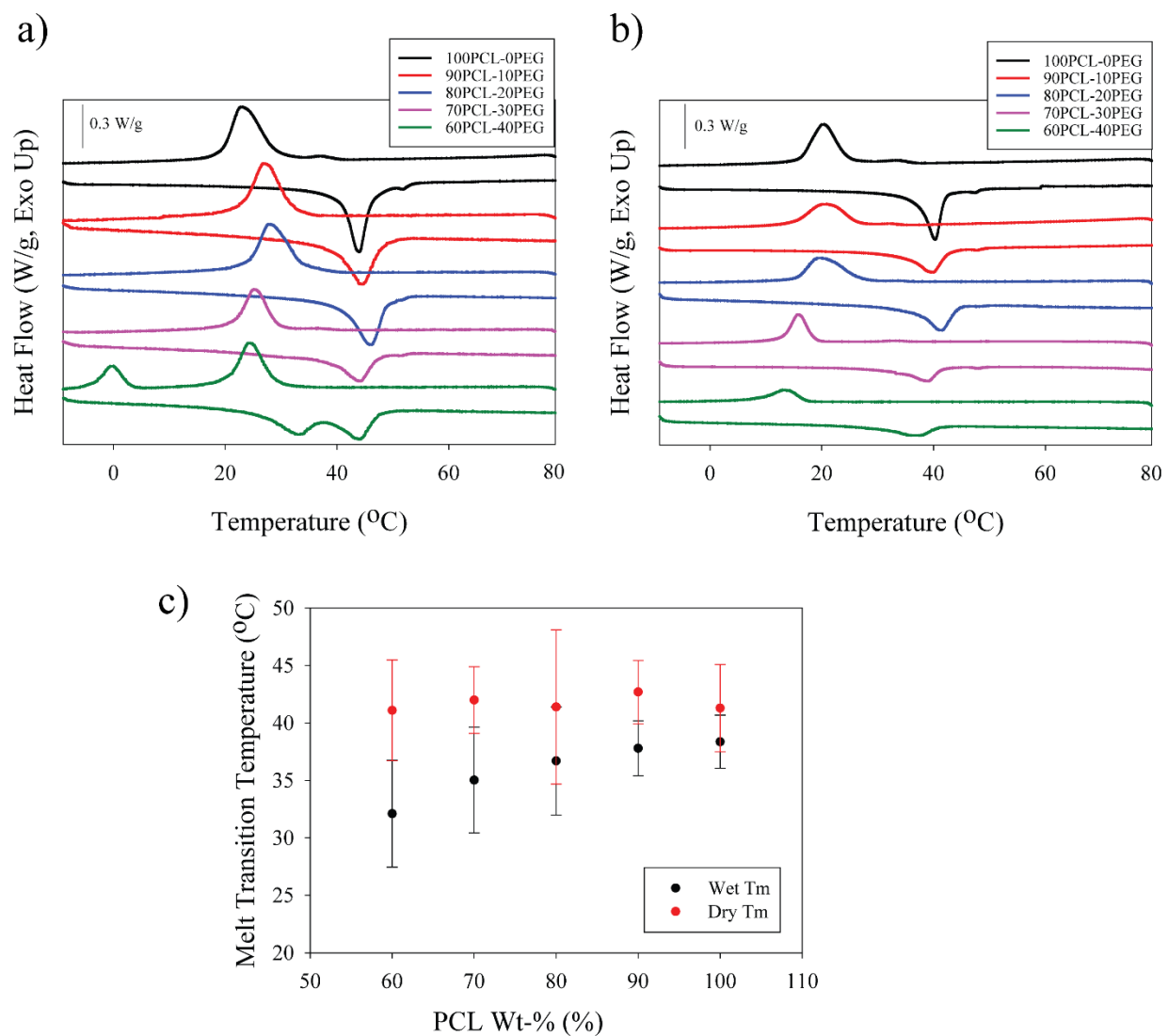


Figure 4-5. Effect of PCL-PEG composition on thermal properties of SMP foams. DSC 2nd heat traces of foams with weight ratios of PCL-PEG ranging from 100PCL-0PEG to 60PCL-40PEG in the (a) dry and (b) wet state show T_m decreases with increasing PEG content. This effect is more prominent in the wet state. (c) Hydration lowers the T_m of each composition.

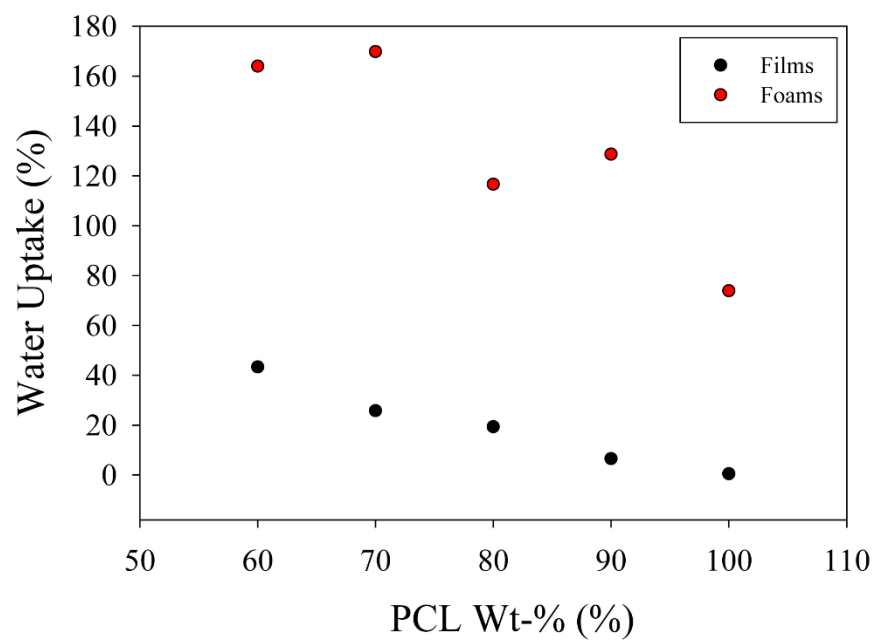


Figure 4-6. Effect of PCL-PEG composition on water uptake. As the weight percent of hydrophilic PEG increases, the amount of water uptake increases for both foams and films.

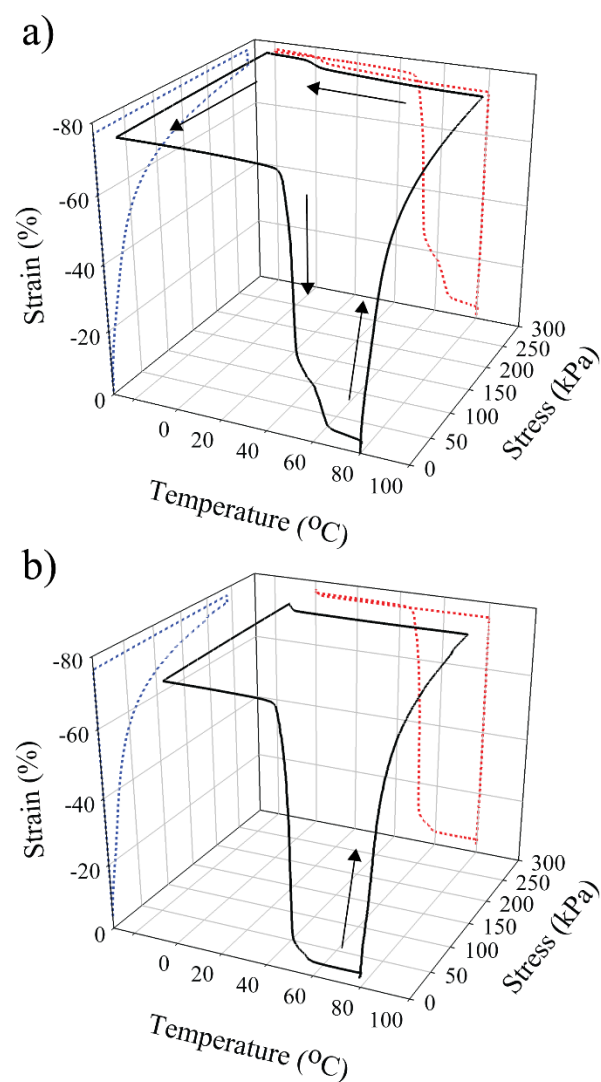


Figure 4-7. Shape memory behavior of SMP foams. (a) Dry one-way shape memory testing of 80PCL-20PEG in compression reveals excellent shape fixing and recovery; (b) wet one-way shape memory testing of 80PCL-20PEG in compression also shows excellent shape fixing and recovery.

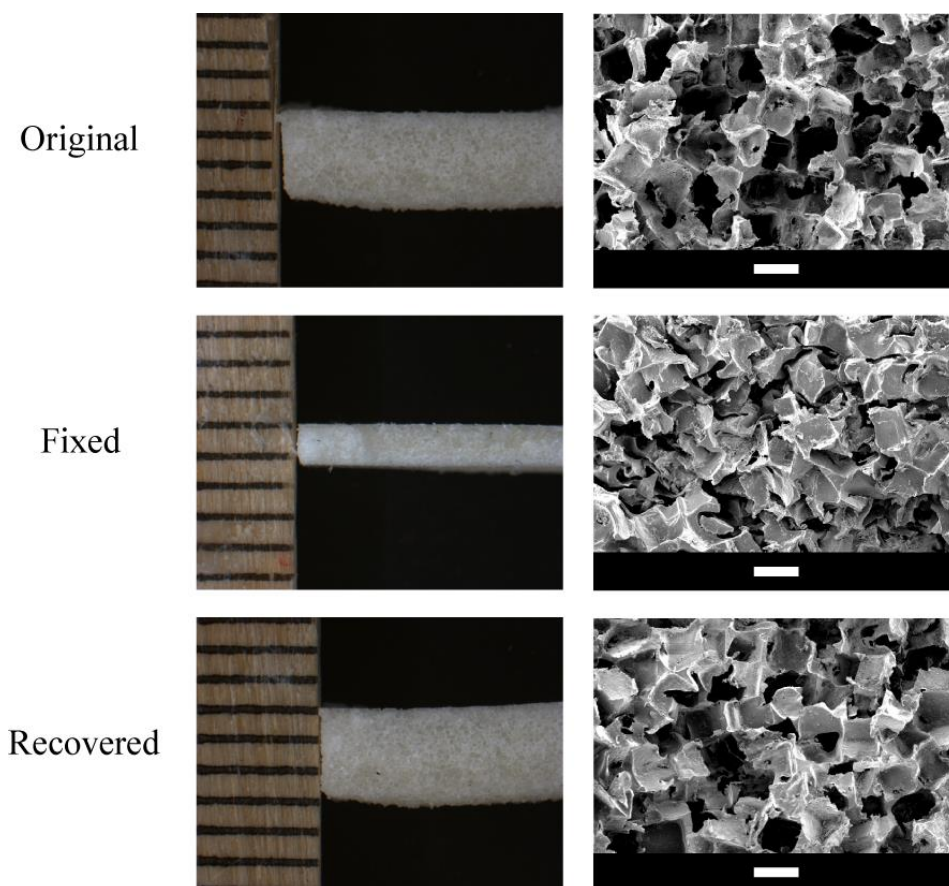


Figure 4-8. Shape memory effect on SMP foam architecture. (left) Optical micrographs and (right) SEM images of foam cross-sections prior to compressing 50% (top), after compressing 50% (middle), and after triggering recovery (bottom) reveal the porous architecture collapses upon fixing but is subsequently restored following shape recovery. Scale bars are 200 μm .

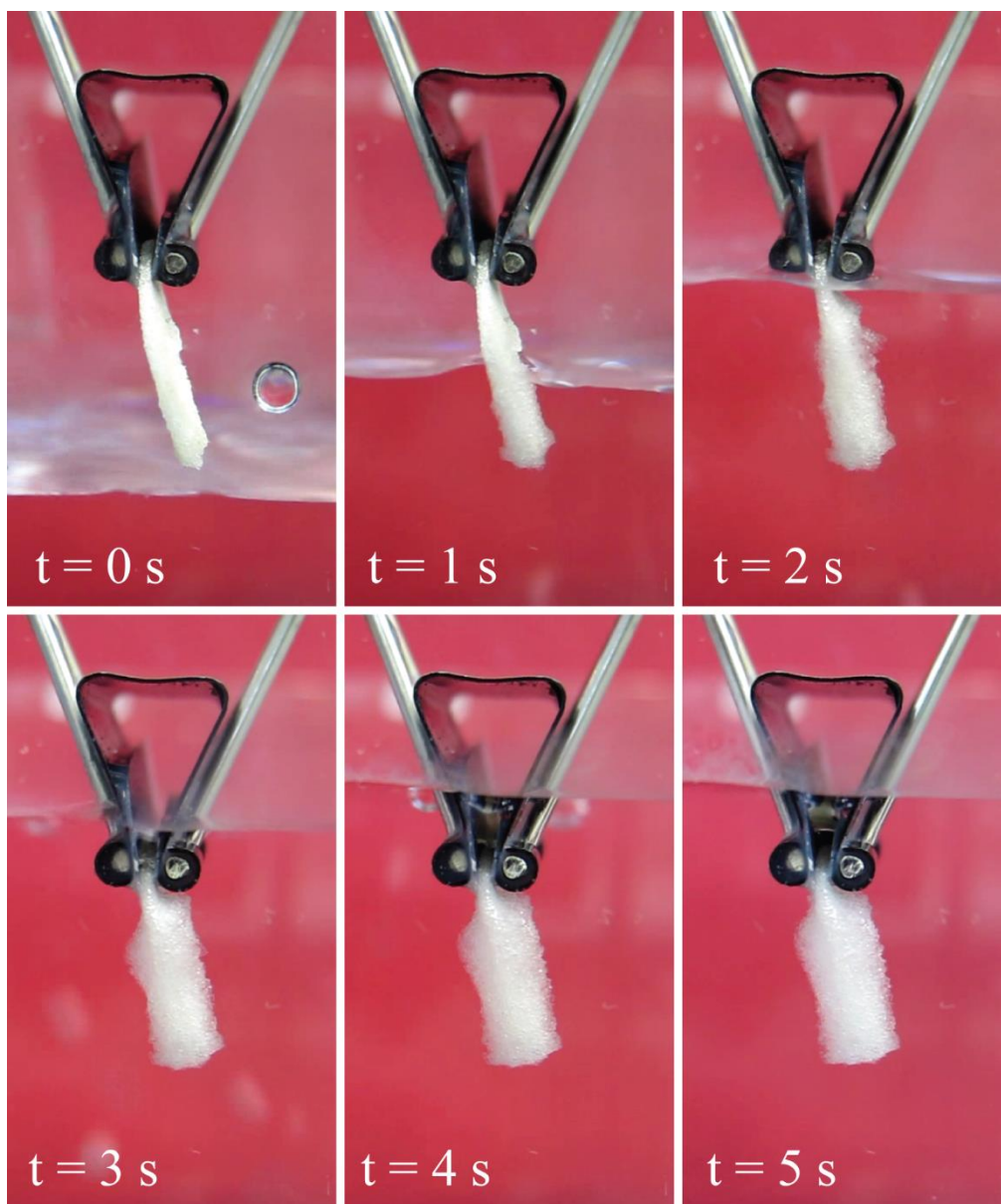
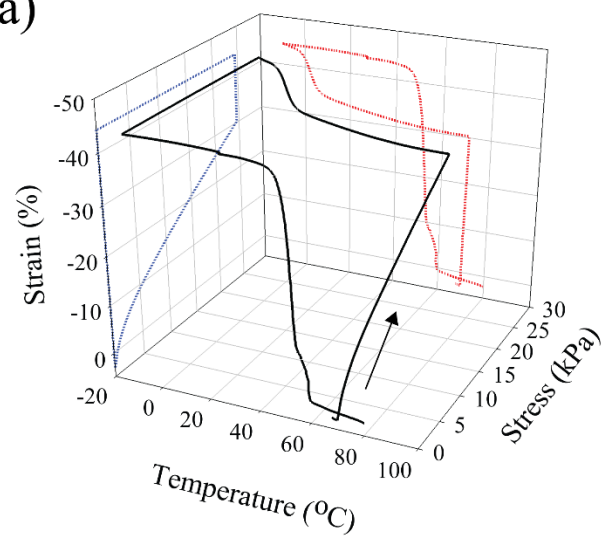
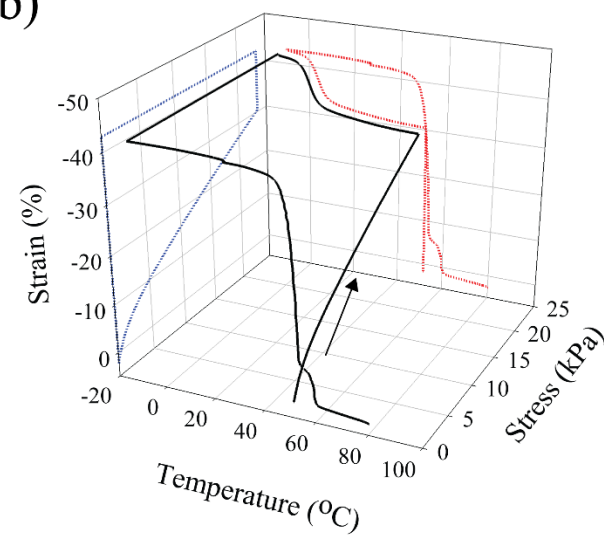


Figure 4-9. Hydrated recovery of 80PCL-20PEG foam at 37 °C. A sample with a hydrated T_m of 36 °C is triggered to fully expand within seconds of being exposed to 37 °C water. Prior to the addition of the water, the foam was heated to 80 °C, compressed between two steel plates, and fixed in a -4 °C freezer for 10 min.

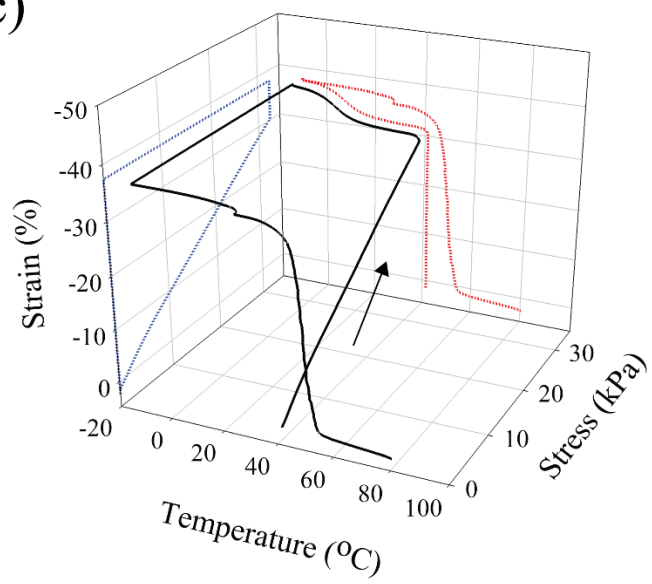
a)



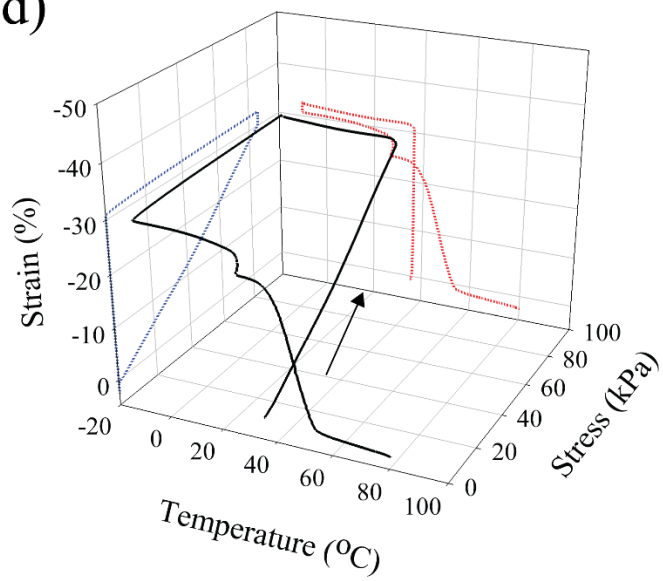
b)



c)



d)



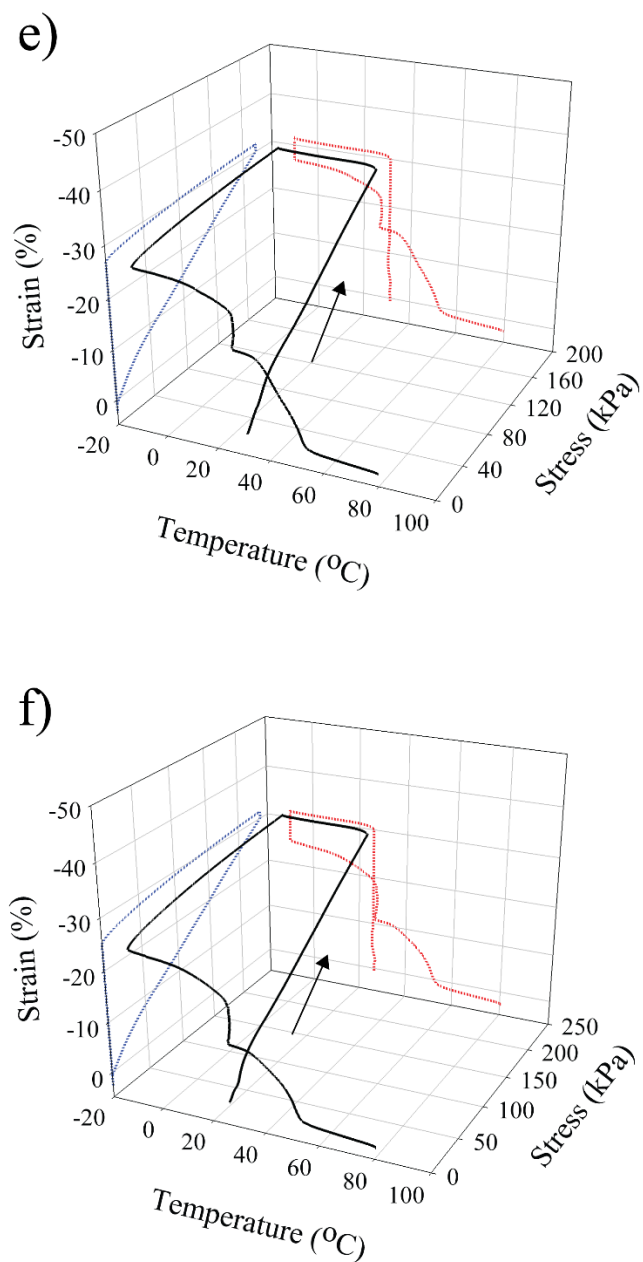


Figure 4-10. Shape memory behavior of 80PCL-20PEG foams deformed at different temperatures. Deformation temperatures (T_{def}) at (a) $T_m + 30\text{ }^{\circ}\text{C}$, (b) $T_m + 10\text{ }^{\circ}\text{C}$, (c) T_m , (d) $T_m - 5\text{ }^{\circ}\text{C}$, (e) $T_m - 10\text{ }^{\circ}\text{C}$, and (f) $T_m - 15\text{ }^{\circ}\text{C}$, reveal that foams fully recover regardless of T_{def} , however shape fixing decreases as T_{def} decreases below T_m .

Table 4-1. Summary of fixing (R_f) and recovery (R_r) ratios for 80PCL-20PEG foams deformed at different temperatures. All samples show excellent recovery, but fixing ratios decrease as deformation temperature decreases. R_f and R_r were calculated according to equations **Eq 2-4** and **Eq 2-5**, respectively, discussed in **Chapter 2**.

$T_{\text{def}} (^{\circ}\text{C})$	ϵ_m	ϵ_u	$\epsilon_p(\text{N-1})$	$\epsilon_p(\text{N})$	$R_f (\%)$	$R_r (\%)$
$T_m + 30$	-44.4	-44.4	2.8	2.4	99.9	99.2
$T_m + 10$	-43.1	-42.9	1.7	2.7	99.7	102.2
T_m	-37.9	-37.5	1.5	2.7	98.8	102.9
$T_m - 5$	-32.8	-30.7	0.7	2.7	93.7	106.4
$T_m - 10$	-31.5	-26.6	0.7	2.5	84.4	106.8
$T_m - 15$	-31.4	-24.8	0.5	2.7	79.0	109.0

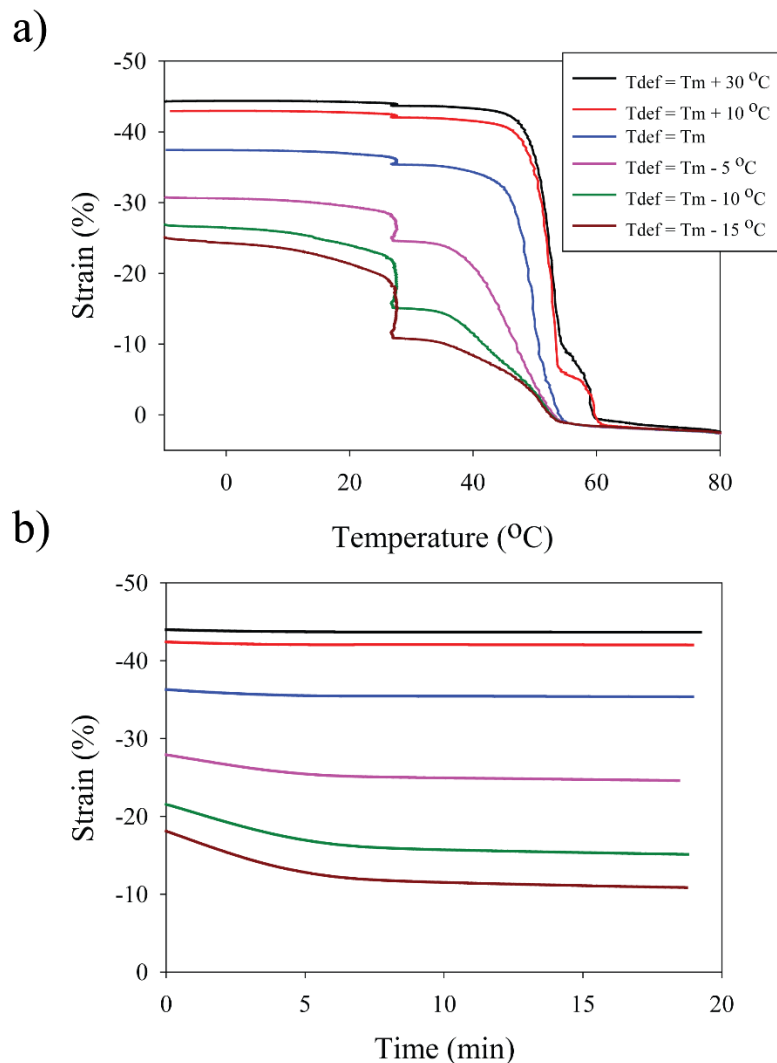


Figure 4-11. Effect of deformation temperature on the stability of fixed foams at room temperature. (a) Recovery traces of foams deformed below and above T_m reveal deforming at lower temperatures leads to a decrease in stability near room temperature. Fixed samples were heated at $3\text{ }^{\circ}\text{C}\cdot\text{min}^{-1}$ to $27\text{ }^{\circ}\text{C}$ and held isothermal for 20 min to observe stability, followed by heating at $3\text{ }^{\circ}\text{C}\cdot\text{min}^{-1}$ to $80\text{ }^{\circ}\text{C}$ for full recovery. (b) Stability of the fixed shape during the isothermal step at $27\text{ }^{\circ}\text{C}$ is reduced for lower deformation temperatures. A composition of 80PCL-20PEG was used for the temperature deformation studies.

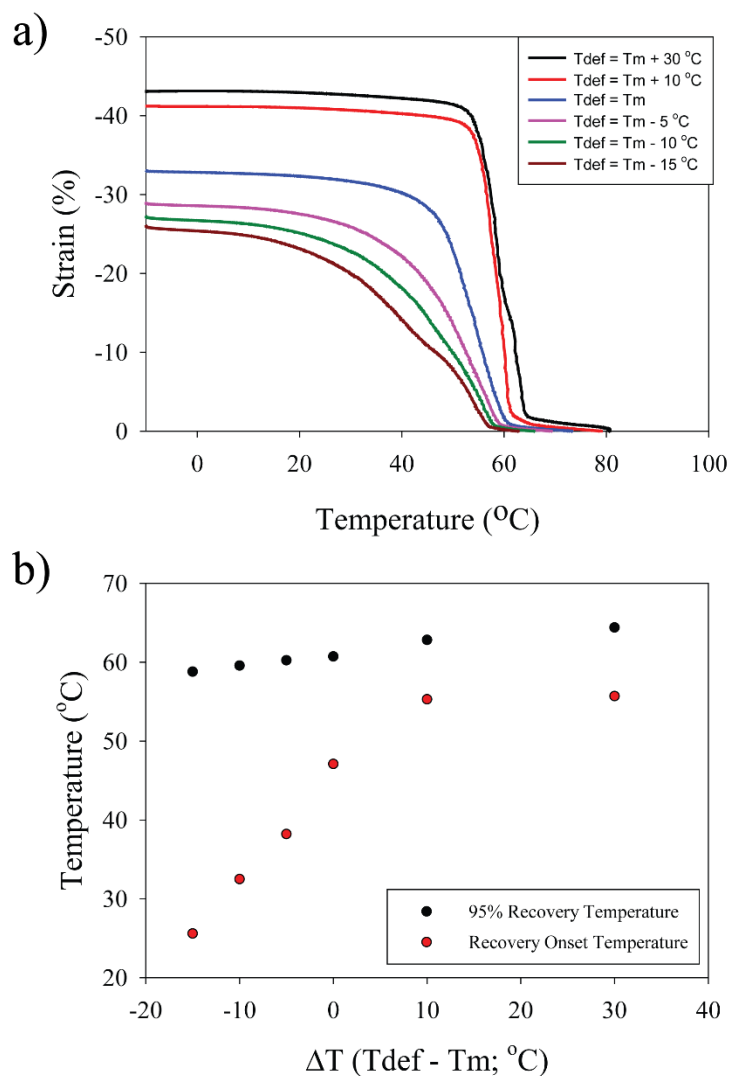


Figure 4-12. Effect of deformation temperature on the recovery behavior of foams during continuous heating. (a) Recovery traces of foams deformed below and above T_m reveal deforming at lower temperatures leads to an earlier onset temperature of recovery; (b) lower temperatures lead to an earlier onset of recover and fully recover at a lower temperature, however a larger range of temperature change is needed to achieve full recovery. A composition of 80PCL-20PEG was used for the temperature deformation studies.

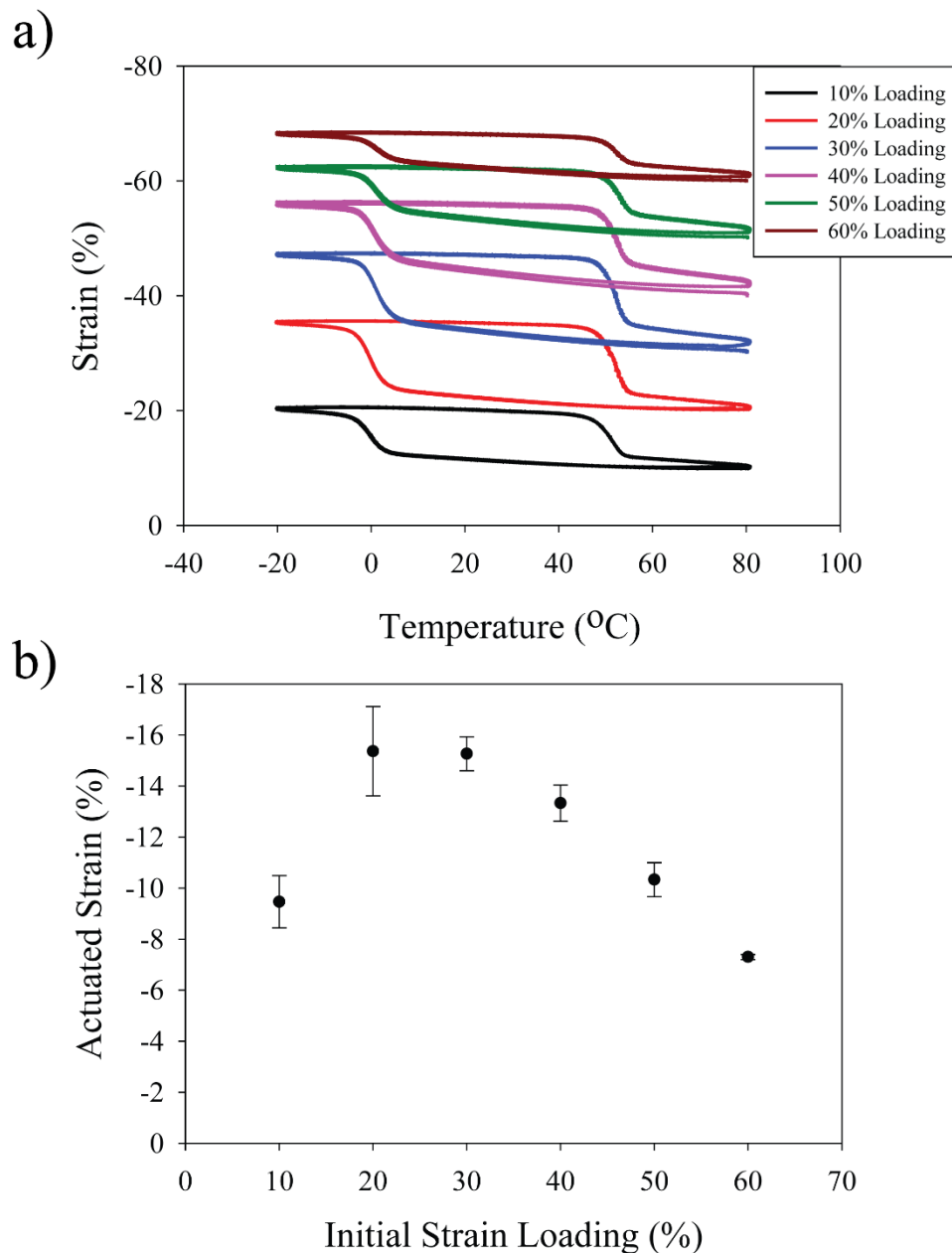


Figure 4-13. Two-way reversible actuation of SMP foams. (a) An 80PCL–20PEG SMP foam showed reversible two-way actuation of up to 15% when a constant load is applied during crystallization; (b) a maximum actuation strain is observed with a prestrain of 30%, and the actuation strain decreases as the prestrain deviates from 30%.

Chapter Five: Shape Memory Scaffolds for Treating Critical Size

Defects[†]

5.1 Synopsis

This chapter explores the application of the poly(ϵ -caprolactone)-co-poly(ethylene glycol) shape memory polymer (SMP) scaffold described in **Chapter 4** as a space-filling construct for treatment of critical size bone defects. In addition, this chapter describes the fabrication of a stiffer SMP scaffold that combines the chemistry in **Chapter 2** with the porogen-leaching technique from **Chapter 4**. The ability of each SMP scaffold to serve as a space-filling construct is investigated via implantation in a mouse femoral segmental defect model. Bone remodeling and integration is assessed through imaging and biomechanical testing 12 weeks post-implantation.

5.2 Introduction

Critical size bone defects, or defects that are too large for bone repair to occur without intervention, pose a significant burden to the US veteran and civilian healthcare systems. Improvements to combat armor provided to warfighters has led to an increase in survivability, but has resulted in a corresponding increase in the number of orthopedic reconstructions needed for extremity injuries. During Operation Iraqi Freedom and Operation Enduring Freedom, 54% of combat casualties involved extremity injuries [1, 2], with 26% of these injuries involving complex fractures. Additionally, complex fractures resulting from trauma, primary bone malignancies, benign tumors, and revision surgery [3] are common among veterans and civilians

[†] Adapted (in part) from R.M. Baker, L.F. Tseng, M.T. Iannolo, M.E. Oest, and J.H. Henderson, **2015**, (*submitted*)

[4] and often result in critical size defects. The current gold standard for treating critical size defects is autologous bone grafts [5], however several limitations exist with this treatment option including limited donor site availability, donor site pain [6], and added operation time for graft harvest. Allografting is the standard of care, but often achieves limited osseointegration with a failure rate of 60% at 10 years [7].

To address limitations associated with auto- and allografting, researchers have focused on developing synthetic bone grafts as alternative bone repair strategies. Synthetic grafts have been fabricated from different materials including metals [8], ceramics [9, 10], polymers [11], and ceramic/polymer composites [10], with the latter three being the most often used. Ceramics such as hydroxyapatite and tricalcium phosphate show good osseointegration and osteoconductivity [12] due to their similar mineral structure to native bone, but are brittle and not easily processed. Several injectable ceramic-based cements and putties [13] have been developed for non load-bearing applications, but their brittleness and poor fatigue behavior suits them poorly for load-bearing applications. Polymeric scaffolds [14] such as poly(lactic acid) and poly(ϵ -caprolactone) can be readily processed with tunable degradation kinetics, however their elastic modulus is often significantly lower than that of native bone. Treatment of bone defects can be further complicated among healing-compromised individuals, such as smokers and diabetics.

Due to these factors and the challenges and limitation of current approaches cited above, 3.6% of trauma admissions for U.S. service members between 2001 and 2011 resulted in major amputation [15]. Reflecting limitations of current treatments, 10% of amputations occur more than 90 days after injury [15]. Therefore, a clinical need exists for space-filling synthetic bone grafts that can be easily processed, readily conform to the defect fracture surface, maintain stability of the defect site, and promote bone remodeling.

Recent advances in shape-memory polymer (SMP) science provide the potential for polymeric devices that include mechanical programmability to be employed in orthopedic applications. For instance, Yakacki and colleagues demonstrated the potential benefits of SMPs in orthopedic applications by developing a soft-tissue fixation device, in which an SMP tube can be inserted between tendon and bone and radially expand to anchor the tendon, providing sufficient anchoring to prevent tendon pullout [16, 17]. Recently porous SMPs (such as the SMP foam described in **Chapter 4**) have been proposed for use as deployable synthetic bone graft substitutes [18-21] (**Scheme 5-1**). Zhang et al. developed a porous PCL SMP foam coated with polydopamine that could be programmed to fit an irregular model bone defect[20]. This scaffold exhibited excellent bioactivity *in vitro*, supporting osteoblast adhesion, proliferation, and osteogenic gene expression; however, no *in vivo* studies were reported. Liu and colleagues developed a porous chemically crosslinked PCL SMP foam coated with hydroxyapatite and used as a synthetic bone substitute in an *in vivo* non-load bearing rabbit mandibular critical-size defect model [21]. The results showed that the foam could be triggered at a physiologically relevant temperature and promoted bone formation compared to sham (no graft) control. These studies demonstrate the potential of employing deployable SMP scaffolds as synthetic bone grafts, but questions remain regarding the application of SMPs in load-bearing applications.

For treatment of load-bearing defects, it must be determined whether an SMP suitable for intraoperative deployment can possess mechanical properties sufficient to withstand loading post-op and during healing. The work in this chapter aims to address this question and evaluate the feasibility of intraoperative delivery and load-bearing of SMP grafts for treatment of segmental defects. To achieve this, we evaluated *in vitro* and *in vivo* two expanding porous SMP scaffolds as synthetic load-bearing bone grafts. A semi-crystalline poly(ϵ -caprolactone)-co-

poly(ethylene glycol) SMP foam (**Chapter 4**) and an acrylate-based (chemistry employed in **Chapters 2-3**) SMP foam with significantly differing mechanical properties were tested. Intraoperative delivery, deployment, and healing were studied in the treatment of a mouse segmental defect model and evaluated after 12 weeks to determine the feasibility of SMP synthetic bone grafts.

5.3 Methods and Materials

5.3.1 Materials

Poly(ϵ -caprolactone) diol (PCL) ($M_n = 3000$ g/mol) was purchased from Scientific Polymer and used as received. Poly(ethylene glycol) diol (PEG) ($M_w = 4000$ g/mol), acryloyl chloride, allyl isocyanate, triethylamine, dibutyltin dilaurate, pentaerythritol tetrakis(3-mercaptopropionate) (tetrathiol), tetraethylene glycol dimethacrylate (TEGDMA), 2, 2-dimethoxy-2-phenylacetophenone (DMPA), and dopamine hydrochloride were purchased from Sigma Aldrich and used as received. Tert-butyl acrylate (tBA) and butyl acrylate (BA) were purchased from Sigma Aldrich and purified by passing through inhibitor removal columns (SDHR-4, Scientific Polymer) prior to use.

5.3.2 Scaffold Fabrication

For this study, SMP foams were fabricated following the porogen-leaching method described in **Chapter 4 (Section 4.3.2)**. Two classes of foams were explored as potential expanding grafts for the treatment of segmental bone defects: “soft” semi-crystalline SMP foams and “stiff” amorphous SMP foams.

5.3.2.1 Semi-crystalline SMP Foams

Semi-crystalline SMP foams were fabricated following the same chemistry and procedures outlined in **Chapter 4 (Sections 4.3.1 and 4.3.2)**, and a composition of 80PCL-20PEG was used as its hydrated melt transition temperature (T_m) was 37 °C. One modification was made during fabrication for this study. Prior to salt fusion, hydroxyapatite (HA, <200 nm particle size) (Sigma) at a weight fraction of 20% of the polymer weight (PCL+PEG) was added to the salt and manually mixed with a stir rod. This was performed to physically incorporate HA nanoparticles onto the surface of the SMP foam, as HA has been shown to improve osteoconductivity when used in polymer scaffolds for bone repair strategies [22-24]. Foams with a nominal pore size of 300-500 μm were used for this study. A sample name of 80PCL-20PEG-20HA is used to denote the foams containing 20% HA.

5.3.2.2 Amorphous SMP Foams

Amorphous SMP foams were fabricated as a stiffer alternative to the semi-crystalline SMP foams. Amorphous SMPs undergo programmed changes in shape upon heating above their glass transition temperature (T_g). Below T_g , amorphous SMPs are glassy with a tensile modulus on the order of 1 GPa. Above T_g , this modulus can drop several orders of magnitude, often on the order of 1 MPa. In contrast, semi-crystalline SMPs undergo shape change when heated above the melt transition temperature (T_m). When below T_m (but above T_g), semi-crystalline SMPs typically have a modulus on the order of 100 MPa, a value that is dependent on the degree of crystallinity. Above T_m , this modulus can drop several orders of magnitude and is comparable to the modulus amorphous SMPs above their T_g . As a result, amorphous SMPs are stiffer than semi-crystalline SMPs below their respective thermal transition temperatures.

Stiffer amorphous SMP foams were fabricated by combining the acrylate-based chemistry from **Chapter 2** and the porogen-leaching technique from **Chapter 4 (Scheme 5-2a)**. tBA and BA monomers were mixed in a 92-8 (tBA-BA) wt-% ratio. To the solution was added TEGDMA at 5 wt-% of the monomer weight and DMPA photoinitiator at 1 wt% of the monomer weight. This solution was added to a fused salt template and photo cured with UV light for 2 h. After curing, salt was extracted by soaking in deionized water and unreacted monomers were extracted by soaking in methanol for 6 h. To prepare 92tBA-8BA foams for characterization and implantation *in vivo*, cylindrical plugs with a 3 mm diameter and 4.5 mm height were punched using a biopsy punch and coated with polydopamine (**Scheme 5-2b and 2c**). Coating with polydopamine was performed because it has been shown to improve cell attachment and bioactivity [20, 25], and could serve as an alternative to incorporation of HA that was done for the semi-crystalline SMP foams.

To coat samples with polydopamine, foams were rinsed in deionized water 3 times, followed by a 1 h submersion in dopamine solution. The dopamine solution consisted of dopamine hydrochloride at a concentration of 2 mg·ml⁻¹ in 10 mM Tris buffer with a pH of 8.5. Submersion of the foams led to polymerization of the dopamine on the foams (**Scheme 5-2b**), as observed from the darkening of the dopamine solution over time. After soaking for 1 h, foams were vigorously rinsed in deionized water 3 times to remove non-attached polydopamine. Foams were dried and prepared for sterilization. Following polydopamine coating, foams turned from white to a dark brown/black color (**Scheme 5-2c**), indicating coating was successful.

5.3.3 Thermal Characterization

Thermogravimetric analysis (TGA) was employed to determine the loading efficiency of HA into 80PCL-20PEG-20HA foams, as well as confirm complete salt extraction of 92tBA-8BA

foams. Samples weighing 5-10 mg of the foam scaffold were loaded in a Q500 (TA Instruments) thermogravimetric analyzer and heated to 600 °C at a rate of 20 °C-min⁻¹ under nitrogen purge. The mass of each sample was recorded as a function of temperature to construct the thermal degradation profile.

Differential scanning calorimetry (DSC) was employed to determine the T_m of the 80PCL-20PEG-20HA foams and the glass transition temperature (T_g) of the 92tBA-8BA foams. DSC experiments were conducted using a Q200 (TA Instruments) equipped with a refrigerated cooling system. Samples with a mass of 3-5 mg were placed in Tzero aluminum pans (TA Instruments) and were heated from -10 °C to 80 °C (first heat), cooled back to -10 °C (first cool), and finally heated back to 80 °C (second heat). All heating and cooling rates were 3 °C-min⁻¹. The T_m or T_g of each sample was determined using Universal Analysis Software (TA Instruments).

5.3.4 Thermomechanical Characterization

Thermomechanical testing of semi-crystalline and amorphous SMP foams was conducted using a Q800 dynamic mechanical analyzer (TA Instruments). Cylindrical discs of SMP foams were placed in the compression platens of the Q800 and tested under multi-frequency strain mode. A preload force of 0.5 N (Dry) and 0.1 N (wet) was applied to each sample to ensure conformal contact of the entire foam. An oscillatory strain of 5% was applied and the scaffolds were equilibrated at 80 °C for 2 min, followed by cooling to -20 °C at a rate of 3 °C-min⁻¹. After holding isothermal at -20 °C for 2 min, samples were heated to 80 °C at a rate of 3 °C-min⁻¹, and the storage modulus as a function of temperature was recorded.

The compressive elastic modulus of foams hydrated at 37 °C was also measured using the Q800. Cylindrical discs were soaked in deionized water at 37 °C for 24 h then loaded in the

compression platens of the Q800. Samples were kept hydrated at 37 °C by placing a 30 mm diameter petri dish lid on the bottom platen and filling it with 37 °C water. Samples were tested submerged during testing. Samples were uniaxially compressed at a strain rate of 10%-min⁻¹ to 60% strain or until reaching the force limit of the Q800 (18 N). The compressive elastic modulus was measured from the slope of the linear portion of the stress v. strain graph.

Shape memory characterization of semi-crystalline and amorphous foams was also conducted using the Q800 in compression. Cylindrical discs were heated to 80 °C, uniaxially compressed at a rate of 0.5 N-min⁻¹ until reaching 60% strain, cooled at 3 °C-min⁻¹ to -10 °C and held isothermal for 5 min to fix the deformation, unloaded to the preload force of 0.01 N to observe shape fixing, and finally heated at 3 °C-min⁻¹ to 80 °C to observe shape recovery. Both dry and hydrated foams were tested.

5.3.5 Scanning Electron Microscopy

Scanning electron microscopy (SEM) was employed to qualitatively assess pore morphology and foam architecture during shape memory testing. A JEOL JSM-5600 Scanning Electron Microscope was used. Rectangular bars of each foam were freeze-fractured and sputter-coated with gold for 60 s prior to SEM analysis. To assess the effect of shape memory cycling on foam architecture, foams were subjected to a one-way shape memory cycle with a programmed strain of 50%. SEM images of foam cross-sections were taken before programming, after programming, and after recovery.

5.3.6 Preparing Foams for *In Vivo* Testing

To prepare programmed foams for in vivo testing, cylindrical plugs with a 3 mm diameter and 4.5 mm height were punched using a biopsy punch. A hole was made in the center

of each foam using a 22 G needle to allow for easy insertion on the intramedullary nail during surgery. Semi-crystalline foams were programmed in a temporary compressed state by first heating in 45 °C water and uniaxially compressing to a thickness of 2 mm using calipers. To fix the temporary deformation, the foams, still compressed in the calipers, were dipped in ice water for 1 min. Foams were then dried and prepared for sterilization. Amorphous foams were programmed in a temporary compressed state at room temperature by uniaxially compressing the samples to a thickness of 2 mm using calipers. Once programmed, smart grafts were ready for sterilization and implantation *in vivo*.

5.3.7 Scaffold Sterilization

Traditional sterilization approaches for biomaterials employ heat to achieve sterilization (e.g. autoclaving). This approach, however, is not compatible with programmed SMPs designed to undergo shape changes upon heating to body temperature. An alternative sterilization technique that employs nitric oxide (NO_x) at room temperature has been developed in our labs. A schematic of the sterilization setup is shown in **Scheme 5-3**. Programmed foams were sealed in Tyvek/PET sterilization pouches (SPS Medical), and pouches were put in a closed glass chamber. NO gas was injected into the glass chamber. After 1 h, approximately 120 ml of humid air was injected into the glass chamber at room temperature under atmospheric pressure. At this stage, NO reacts with O₂ and forms NO₂. NO₂ further reacts with water and results in nitric acid (HNO₃), which enhances the antimicrobial capacity of this NO_x sterilization technique [26]. Pouches were removed from the glass chamber after 18 h and kept in a chemical fume hood to aerate residual NO_x gas. The day before scheduled mouse surgeries, NO_x-sterilized foams were fully infiltrated and immersed in Penicillin-Streptomycin solution (P4333, Sigma Aldrich) overnight.

5.3.8 Surgical Procedure[‡]

The ability of expanding SMP foams to be used as deployable synthetic bone grafts was tested using a mouse femoral segmental defect model. A schematic of the surgical procedure is shown in **Scheme 5-4**. A critically-sized defect was surgically created using an oscillating saw by removing a 4-mm segment in the left femora in 12-week-old C57BL/6J female mice (The Jackson Laboratory) under isoflurane anesthesia with 0.2 L·min⁻¹ of O₂. The operated femora were stabilized by blunt-tipped 25 G needles used as intramedullary nails. Defects were treated with programmed SMP foams and allografts as a control. Programmed SMP foams were placed on the intramedullary nail, and the intramedullary nail was inserted into the proximal end of the femur. To prevent the intramedullary nail from penetrating through the proximal end of the femur, approximately 50 µl of bone cement (Surgical Simplex P, Stryker) was injected in the medullary canal. SMP foams were triggered to expand by irrigating with 45 °C saline during surgery. Following irrigation with 45 °C saline, SMP foams were irrigated with room temperature saline to increase foam stiffness by inducing crystallization in 80PCL-20PEG-20HA foams and by cooling 92tBA-8BA foams below their T_g. Next, the distal needle ends were bent, and the bent region was positioned between the distal condyles. Surgical wounds were closed using bioresorbable sutures (5-0 Vicryl, Ethicon) and wound clips (7 mm Reflex wound clips, Harvard Apparatus). A thin layer of New-Skin liquid bandage and metronidazole mixture (M3761, Sigma-Aldrich) was painted on the wound clips to prevent mice from chewing off wound clips prematurely. Mice were given subcutaneous injections of 0.03 mg/kg buprenorphine every 12 h for the first 72 h post-surgery. Animals were euthanized 12 weeks post-surgery and operated limbs were harvested for evaluation and testing. The contralateral intact femurs of 5

[‡] Surgical implantations of SMP grafts and allografts were conducted by Dr. Megan Oest

mice were also harvested and used as controls for mechanical testing. A total of $n = 7$ mice for each treatment group was used for this study. All procedures were reviewed and approved by SUNY Upstate Medical University Institutional Animal Care and Use Committee.

5.3.9 X-ray Radiography

To provide qualitative assessment of graft stability and bridging between the defect and graft, two-dimensional x-ray survival radiographs (Faxitron MX-20; Faxitron X-ray Corp.) were taken of the operated limbs at 4, 8, and 12 weeks post-surgery under ketamine anesthesia.

5.3.10 Histology[‡]

Histology was performed on harvested limbs 12 weeks post-surgery to assess bone formation. Harvested femurs with surrounding muscles were dissected for histological analyses, and the intramedullary nails were forcefully removed. Femurs were fixed in 10% neutral buffered formalin at 4 °C for 48 h with mild agitation, and then decalcified using RDO-Gold (Apex Engineering Products Corp.) solution at room temperature for 30 ~ 60 min. Femurs were ethanol-dehydrated, embedded in paraffin and cut at 3 µm thick sections. Sections were treated with hematoxylin and eosin stain (H&E stain; a stain for basophilic and acidophilic substances such as DNA and proteins, respectively) and examined using optical microscopy.

5.3.11 Microtomography

Three-dimensional analysis of foam integration and stability was performed by microcomputed tomography (Micro-CT 40; Scanco Medical) of harvested limbs 12 weeks post-surgery. A nominal voxel resolution of 12 µm and a 55 kV and 144 µA beam with a 200 ms integration time were used for scanning. Scans of the entire femur were performed, and

[‡] Histology sectioning and staining was performed by the Histology Core Lab at SUNY Upstate Medical University

intramedullary nails were not removed, as preliminary attempts to remove the nails were found to compromise the integrity of the remodeled bone. The resulting 3D reconstructed files were imported into ImageJ software and a threshold applied to isolate the bone. Three-dimensional images were rendered using the 3D viewer in ImageJ.

5.3.12 Torsional Testing and Analysis

At 12 weeks post-surgery, mice were euthanized and the operative limbs were harvested for mechanical testing. Two specimens were excluded in this assay due to compromised integration between foam and native bone upon limb harvesting ($n = 7$ for allograft group and $n = 5$ for foam and contralateral control groups). A test protocol was adapted from Arrington et al. [27] (**Scheme 5-5**). Prior to testing, soft tissue was stripped off the femurs using surgical scalpels to expose the foam and bare bone. The intramedullary nails were not removed from the marrow cavity to avoid compromising bony bridging between the foams and the native bone. The proximal femur and tibia of each sample were potted at 90° flexion in molds using dental cement (COE Tray Plastic, GC America). The tibia was internally rotated at a constant rate of 180°-min⁻¹ and the applied torque and rotation angle were recorded by a materials testing unit (QTest, MTS Corporation). Torque-at-failure (N-mm) was defined as a 20% drop of applied torque from a previous peak or a maximum rotation angle of 70°. Energy-to-failure (N-mm-degree) was measured as the area under the torque-rotation angle curve. Torsional stiffness (N-mm-degree⁻¹) was calculated as the slope of the linear portion of the torque-displacement curve. Analyses were performed using a custom developed algorithm in MATLAB (**Appendix 3**), and real-time loading images were overlaid with the loading curve to aid in analysis. All mechanical tests were conducted at room temperature, and all specimens were prepared and tested under moist conditions using saline-soaked gauze and saline irrigation.

5.3.13 Statistics

Statistical analyses were performed on the torsional mechanical results to compare defects treated with SMP foams to those treated with allograft controls. One-way analysis of variance (ANOVA) with Tukey-Kramer post hoc testing was performed using the built-in functions in a MATLAB for all measurements of torsional mechanical testing. Statistical analysis was performed with unequal sample sizes ($n = 7$ for allograft group and $n = 5$ for SMP foam and contralateral control groups). Statistical significance was set at $p < 0.05$.

5.4 Results

5.4.1 Scaffold Characterization

5.4.1.1 Semi-crystalline SMP Foams (80PCL-20PEG-20HA)

Semi-crystalline SMP foams with a hydrated T_m of 37 °C were fabricated using a modified porogen-leaching technique. Foams with a composition of 80PCL-20PEG were enhanced by physically incorporating HA during scaffold fabrication. HA nanoparticles with a nominal size of <200 nm according to the vendor showed a tendency to aggregate into larger particles (**Figure 5-1a**). When physically mixed with salt and fused in a humidity chamber, HA particles formed a thin coating on the cuboidal salt particles (**Figure 5-1b**). Following foam fabrication and salt extraction, HA nanoparticles were physically bound to the pore struts of the SMP foam (**Figure 5-1c**). While SEM analysis showed that HA particles were successfully incorporated into the SMP foams, TGA analysis revealed that loading efficiencies were low (**Figure 5-2a**). HA particles were thermally stable through 600 °C, and foams with 20% HA were expected to have 20% weight remaining following heating to 600 °C. However, when 4

different locations of the foam were tested, an average of 8.0% mass remained, indicating a loading efficiency of approximately 40%. We speculate this is due to not all of the HA being physically trapped in the polymer during polymerization, with a large amount being washed away during salt extraction.

Thermal analysis using DSC showed that a composition of 80PCL-20PEG-20HA had a T_m of 40.6 °C in the dry state that dropped to 35.4 °C in the hydrated state (**Figure 5-2b**). These values agree with values observed for 80PCL-20PEG in **Chapter 4**.

Linear viscoelastic characterization was employed to determine the thermomechanical response of both dry and hydrated foams. When fully crystallized and below T_m , dry foams had an apparent storage modulus on the order of 1 MPa that dropped 2 orders of magnitude upon heating (**Figure 5-3**). Hydrated foams by comparison had a lower apparent storage modulus which may be attributed to swelling from water uptake and incomplete crystallization during cooling. Also, the apparent onset of modulus drop occurs at a higher temperature, but this is likely an artifact of temperature lag between the furnace temperature and the water temperature. Shape memory characterization of both dry and hydrated foams showed excellent shape fixing and shape recovery (**Figure 5-4**), with fixing and recovery ratios >99%. SEM analysis of foams before fixing, after fixing, and after recovery illustrated the effect of the one-way shape memory cycle on pore architecture and HA incorporation (**Figure 5-5**). Prior to fixing, pores were open and interconnected (**Figure 5-5, top**). Upon fixing a 50% compressive strain, the pore architecture collapsed with layers of struts folding (**Figure 5-5, middle**). The porous structure is gratifyingly restored upon triggering recovery (**Figure 5-5, bottom**). Further investigation of the pore surfaced revealed that HA remained on the surface following a one-way shape memory cycle with no qualitative difference in attached HA content before and after recovery (**Figure 5-**

5, right). This indicates that HA on the surface of the pores after salt extraction was well-bound to the surface.

5.4.1.2 Amorphous SMP Foams (92tBA-8BA)

As a stiffer alternative to the semi-crystalline SMP foams, amorphous SMP foams were fabricated by combining the acrylate-based chemistry from **Chapter 2** and the porogen-leaching technique from **Chapter 4**. Salt extraction from the 92tBA-8BA foams was complete, as demonstrated by the thermal degradation profile of a salt-extracted foam where the foam had degraded by 600 °C (**Figure 5-6a**). Thermal analysis employing DSC showed a composition of 92tBA-8BA yielded a dry T_g of 40 °C that was plasticized upon hydration and dropped to 35 °C (**Figure 5-6b**), near body temperature. Thermomechanical characterization using a Q800 DMA showed that the apparent storage modulus of amorphous foam below its T_g (**Figure 5-6c**) was an order of magnitude higher than the semi-crystalline foam below its T_m . Due to the large drop in modulus upon heating through the T_g , modulus data through the thermal transition was unobtainable. It is evident, however, that the amorphous foam is significantly stiffer than the semi-crystalline foam.

Shape memory characterization in compression was conducted to determine the shape fixing and shape recovery behavior of dry and hydrated foams. The 92tBA-8BA foams showed excellent shape memory behavior (**Figure 5-7**) with fixing ratios >99% and recovery ratios >98%, as was expected based on the results of films of this system from **Chapter 2**. Optical micrographs and SEM analysis of foam cross-sections before fixing, after fixing, and after recovery (**Figure 5-8**) showed that prior to fixing foams had an open, cuboidal pore morphology with a diameter of approximately 350 μm . This structure collapses upon fixing a 50% compressive strain, but is fully restored following shape recovery. Analysis of SEM micrographs

further revealed an average pore interconnection size—openings between cuboidal macropores—of 58 μm in diameter. Surprisingly, these pore interconnections appeared much smaller than the interconnections observed in the semi-crystalline foams, and the pore structure was much more cuboidal for the amorphous foams. This suggests that pore interconnectivity was better for the semi-crystalline foam fabrication. The exact cause of this is unknown, but we hypothesize this is attributed to densification of the semi-crystalline foam which does not occur for the amorphous foam, or due to variability in the degree of salt fusion.

To demonstrate the concept of using expanding scaffolds to fill segmental defects, an in situ experiment was conducted using the 92tBA-8BA foams (**Figure 5-9**). A foam plug with a diameter of 3 mm and thickness of 4.5 mm was fixed in a compressed state. The foam was placed on a 25 G needle (simulating the intramedullary nail) and positioned in a 4 mm defect of a mouse femur. The foam was triggered to expand by submersion in 45 °C water, simulating intraoperative deployment, which triggered full recovery within 60 s.

5.4.2 Defect Stability and Graft Integration

Qualitative evaluation of graft integration and bone remodeling at 4, 8, and 12 weeks post-surgery was conducted by digital x-ray radiography. Analysis of limbs treated with semi-crystalline and amorphous SMP foams after 4 weeks revealed that semi-crystalline foams lacked the mechanical integrity to maintain defect stability (**Figure 5-10a**). The 80PCL-20PEG-20HA foam was unable to maintain the defect gap size of 4 mm, and catastrophic collapse of the defect was observed. The amorphous 92tBA-8BA foam, however, was able to maintain the 4 mm gap length. Further inspection of the compressive modulus for each foam showed that the 92tBA-8BA foam (16 MPa) was over 2 order of magnitude stiffer than the 80PCL-20PEG-20HA foam (0.06 MPa) (**Figure 5-10b**). Because the 80PCL-20PEG-20HA treatments resulted in

catastrophic collapse, all mice were euthanized within 4 weeks of surgery and no long-term studies using this foam were possible.

Digital x-ray radiographs of the 92tBA-8BA foams after 4, 8 and 12 weeks showed that defect stability was maintained throughout the 12 week period with animals permitted normal ambulation and activity (**Figure 5-11**). Bone formation was observed at the margins, indicating integration of the foam with the native bone; however, no gross *de novo* bone formation occurred into the scaffold during the 12 week period. By comparison, limbs treated with an allograft showed bone remodeling at the margins within the first 4 weeks. In cases where the allograft alignment was not perfect, however, remodeling was slowed.

Qualitative analysis of bone remodeling and foam integration by microcomputed tomography showed integration between the 92tBA-8BA foams and the native bone. Imaging artifacts resulting from the presence of the intramedullary nail rendered quantitative analysis of bone remodeling unattainable. Qualitative 3D reconstructions showed that mice implanted with the 92tBA-8BA foam demonstrate new bone formation at both margins of the native bone (**Figure 5-12**). Interestingly, bone formation occurred radially at the margins, suggesting bone formation around the SMP foam which had a larger diameter than the femoral shaft (3 mm and 1.6 mm for the shaft and bone, respectively). This radial growth was not evident at the margins for defects treated with an allograft (**Figure 5-12a, right**). Additionally, integration of the foam with the native defect margins can be observed as bony ingrowths with a size and geometry similar to pores in the foam (**Figure 5-12, right**).

5.4.3 Histology

Histology was performed on harvested limbs 12 weeks post-surgery to assess bone repair. Analysis of hematoxylin and eosin stained sections for a 92tBA-8BA foam (**Figure 5-13a**)

revealed no gross *de novo* bone formation occurred into the foam. Granulated tissue, however, was observed both in the outer pores of the foam and in the interior. This suggests that foams did enable cell penetration into the interior. Furthermore, no sign of infection or implant rejection through foreign body response was found, and bone marrow at the distal end appeared healthy. For the allograft control (**Figure 5-13b**), hematoxylin and eosin stained sections showed remodeling had begun at both proximal and distal margins, with healthy bone marrow present along the entire length of the femur.

5.4.4 Torsional Testing and Analysis

Biomechanical analysis of harvested limbs was performed to evaluate functional remodeling of segmental defects treated with 92tBA-8BA foams and allografts, with the contralateral femur used as an intact control. Torsional testing curve profiles were similar for limbs treated with foams and allografts (**Figure 5-14**), and in all cases failure occurred at either the proximal or distal margin. Analysis of the torsional testing revealed that the mechanical integrity of extracted limbs was comparable between foams and allografts (**Figure 5-15**). As would be expected from the known progression of healing in mouse segmental femoral defects of this type [28], both treatment groups had significantly lower torsional properties than did the contralateral intact femur (**Table 5-1**). Results indicated that integration of the foams with the native bone was present and bony bridging in the allograft groups has begun, but *de novo* bone formation and remodeling at the interfaces did not complete at 12 weeks, which was expected. Promisingly, there was less than one order of magnitude difference between both treatment groups and the intact control. Torsional stiffness for both treatment groups were similar, with a stiffness of $\sim 0.1 \text{ N-mm-deg}^{-1}$, whereas the torsional stiffness for the intact femur was eight times greater at $0.86 \text{ N-mm-deg}^{-1}$. Although not statistically significant, peak torque and energy-to-

failure of the foam was typically lower than that of the allograft group. The contralateral intact femur was significantly different from all treatment groups for all torsional properties tested.

5.5 Discussion

In this chapter, we have demonstrated the feasibility of intraoperative delivery and load-bearing of SMP grafts for treatment of mouse segmental defects. Here, two self-deployable SMP foams were employed as space-filling bone grafts. The softer, semi-crystalline foam was unable to maintain defect stability, whereas the stiffer, amorphous foam maintained defect stability throughout the 12 week study. SMP grafts demonstrated rapid deployment, within 55 s, *in situ* upon irrigation with 45 °C water—a clinically translatable triggering method (**Figure 5-9**), and were triggered to fill and conform to a 4 mm segmental defect.

An SMP foam based on PCL chemistry was developed due to PCL's biocompatibility, biodegradability [29, 30], and previous use in bone tissue engineering [21, 31, 32]. PEG was added to the chemistry to enable deployment at 37 °C[18] (**Chapter 4**). To provide bioactivity to the PCL-PEG scaffolds, hydroxyapatite (HA) nanoparticles were physically incorporated into the foam, as HA has been shown to increase osteoconductivity [22-24]. HA nanoparticles were successfully incorporated onto the surface of the PCL-PEG foams (**Figure 5-1**), however relying on physical incorporation of HA resulted in low loading efficiencies of only 40%. To improve HA loading efficiencies, HA nanoparticles could be functionalized [33] and chemically crosslinked into the PCL-PEG network through thiol-ene chemistry (preliminary results discussed in **Appendix 4**). Although loading efficiencies were low, HA incorporation proved robust with no observable loss of HA following a compressive shape memory cycle (**Figure 5-5**).

The findings demonstrate, for the first time, the feasibility of employing deployable stiff SMP grafts as synthetic bone substitutes in load-bearing applications, while also highlighting challenges associated with soft SMP grafts. A stiff 92tBA-8BA SMP graft was able to maintain the defect gap without significant defect shortening 4, 8, and 12 weeks post-surgery (**Figure 5-11**). In contrast, softer 80PCL-20PEG-20HA SMP grafts resulted in catastrophic collapse of the defect within the first 4 weeks, requiring euthanasia within days or weeks of operation (**Figure 5-10**). This suggests that SMPs that are glassy at body temperature are best suited for applications where partial or full load bearing may be required, due to the higher elastic modulus. With an apparent compressive elastic modulus of ~16 MPa at 37 °C (**Figure 5-10**), the amorphous SMP graft is less stiff than cortical (12–17 GPa [34]) and cancellous (0.1–4.5 GPa [35]) bone. For the small animal model used in this study, the amorphous SMP graft has a sufficient stiffness to maintain defect stability (**Figures 5-11 and 5-12**); however, for the SMP graft to be applied alone in a clinically-relevant animal model, a biodegradable chemistry is needed and the interconnectivity of the SMP graft must be increased. Promisingly, the SMP graft integrated with native defect surfaces, as was observed through bony ingrowth at the implant/defect margins with a size and geometry similar to that of pores (**Figure 5-12**). That integration was further supported by the torsional mechanical testing results, in which torsional stiffness, peak torque, and energy-to-failure for the SMP grafts were slightly lower but statically comparable to the allograft treatment (**Figure 5-15 and Table 5-1**). Furthermore, histology analysis (**Figure 5-13**) confirmed that the SMP graft did not elicit a negative biological response or cause infection in any of the animals tested. While the SMP graft was unable to promote gross *de novo* bone formation after 12 weeks, this is not unexpected as the graft contained no additional signaling factors or progenitor cells. Previous studies have shown that polymeric

scaffolds alone are poor at promoting remodeling [36], and incorporation of growth factors or stem cells into polymeric scaffolds can be used to promote better remodeling.

In addition to the promising results observed here, the present findings further help identify areas for improving SMP grafts moving forward. As previously mentioned, no gross *de novo* bone formation was observed after 12 weeks in the SMP graft. To enhance bone formation, growth factors such as bone morphogenetic proteins (BMPs) [37] could be incorporated into the scaffold. For instance, Rahman and colleagues loaded poly(lactic-*co*-glycolic acid)/poly(ethylene glycol) scaffolds with BMP-2 and found that in a mouse calvarial defect model there was a 55% increase in bone volume for defects treated with BMP-2 containing scaffolds compared to empty defect controls, whereas only a 31% increase was observed for scaffolds without BMP-2 [38]. Similarly, Oest et al. previously reported that poly(L-lactide-*co*-D,L-lactide) scaffolds loaded with BMP-2 and transforming growth factor- β 3 promoted significantly more bone after 16 weeks than unloaded scaffolds and empty controls in a rat segmental defect model [36]. Additionally, vascularization has been recognized as an important role for bone remodeling [39]; one way to accelerate vascularization is through incorporation of vascular endothelial growth factor (VEGF) in combination with BMP, which has been shown to have a synergistic effect for bone healing [40]. *De novo* bone formation could also be improved through seeding stem cells in the scaffold prior to implantation, as has been previously shown [41].

Results also suggest that pore interconnectivity of the current SMP graft could be increased to promote cell infiltration. We speculate that with the average interconnection size—openings between cuboidal macro-pores—being 58 μ m between pores, cell infiltration into the core of the scaffold may be limited. While histology showed some granular tissue formation into the interior of the foam (**Figure 5-13**), tissue density was lower than expected. Improved

interconnectivity can be achieved through modifications to the salt fusion protocol, such as mixing in water to promote greater salt fusion [42]. It is important to consider, however, that with increased interconnectivity, the mechanical integrity of the foams will decrease.

Furthermore, the current non-biodegradable amorphous SMP graft could be improved through employing a chemistry that is biodegradable, such as hydrolytic polyesters. One approach is to fabricate a porous scaffold using a biodegradable TPU with body temperature actuation that has been previously developed in our lab[43]. For this scenario, the TPU could be dissolved and added to a fused salt template. Upon solvent removal, the salt could be extracted resulting in a porous TPU scaffold. Alternatively, porous foams fabricated from biodegradable PLGA materials with tunable shape memory properties could be a promising approach [44].

5.6 Conclusion

In this chapter, we have demonstrated the feasibility of intraoperative delivery and load bearing of SMP foams for grafting of segmental defects. Two self-deployable SMP grafts were evaluated in a mouse segmental defect model *in vivo*. Soft, semi-crystalline foams were unable to maintain defect stability, while stiffer amorphous foams maintained defect stability and integrated with the native bone 12 weeks post-surgery, providing comparable torsional stability as an allograft treatment. SMP grafts show promise as synthetic bone grafts that can be used to fill complex bone defects. Incorporation of growth factors and employing biodegradable chemistries is expected to provide additional functionality for developing clinically-relevant treatment strategies for bone repair.

5.7 Acknowledgements

This work was performed in collaboration with Ling-Fang Tseng, a graduate student in Dr. James Henderson's lab, and with Dr. Megan Oest, an Assistant Professor in Orthopedic Surgery at Upstate Medical University. Ling-Fang Tseng developed and characterized contracting SMP sleeves that were tested in conjunction with the expanding SMP foams discussed in this chapter. All *in vivo* experiments, protocols, and analyses were performed together, in parallel. Dr. Oest performed the *in vivo* scaffold implantations and was instrumental in guiding and directing analysis of harvested limbs. I would also like to thank the Histology core lab at SUNY Upstate Medical University for their assistance in histological samples preparation. This work was sponsored by DARPA (DP12AP00271), and the content of the information does not necessarily reflect the position or the policy of the Government, and no endorsement should be inferred.

5.8 References

- [1] Owens BD, Kragh Jr JF, Macaitis J, Svoboda SJ, Wenke JC. Characterization of extremity wounds in operation Iraqi freedom and operation enduring freedom. *Journal of orthopaedic trauma*. 2007;21:254-7.
- [2] Owens BD, Kragh Jr JF, Wenke JC, Macaitis J, Wade CE, Holcomb JB. Combat wounds in operation Iraqi Freedom and operation Enduring Freedom. *Journal of Trauma and Acute Care Surgery*. 2008;64:295-9.
- [3] Reichert JC, Saifzadeh S, Wullschlegel ME, Epari DR, Schütz MA, Duda GN, et al. The challenge of establishing preclinical models for segmental bone defect research. *Biomaterials*. 2009;30:2149-63.

- [4] Burns TC, Stinner DJ, Mack AW, Potter BK, Beer R, Eckel TT, et al. Microbiology and injury characteristics in severe open tibia fractures from combat. *Journal of Trauma and Acute Care Surgery*. 2012;72:1062-7.
- [5] Lane JM, Tomin E, Bostrom MP. Biosynthetic bone grafting. *Clinical orthopaedics and related research*. 1999;367:S107-S17.
- [6] Dimitriou R, Mataliotakis GI, Angoules AG, Kanakaris NK, Giannoudis PV. Complications following autologous bone graft harvesting from the iliac crest and using the RIA: a systematic review. *Injury*. 2011;42:S3-S15.
- [7] Xie C, Reynolds D, Awad H, Rubery PT, Pelled G, Gazit D, et al. Structural bone allograft combined with genetically engineered mesenchymal stem cells as a novel platform for bone tissue engineering. *Tissue Eng*. 2007;13:435-45.
- [8] Kujala S, Ryhänen J, Danilov A, Tuukkanen J. Effect of porosity on the osteointegration and bone ingrowth of a weight-bearing nickel–titanium bone graft substitute. *Biomaterials*. 2003;24:4691-7.
- [9] Hing KA, Wilson LF, Buckland T. Comparative performance of three ceramic bone graft substitutes. *The Spine Journal*. 2007;7:475-90.
- [10] Johnson AJW, Herschler BA. A review of the mechanical behavior of CaP and CaP/polymer composites for applications in bone replacement and repair. *Acta biomaterialia*. 2011;7:16-30.
- [11] Sabir MI, Xu X, Li L. A review on biodegradable polymeric materials for bone tissue engineering applications. *Journal of Materials Science*. 2009;44:5713-24.
- [12] LeGeros RZ. Properties of osteoconductive biomaterials: calcium phosphates. *Clinical orthopaedics and related research*. 2002;395:81-98.

- [13] Bohner M. Design of ceramic-based cements and putties for bone graft substitution. *Eur Cell Mater.* 2010;20:3-10.
- [14] Cheung H-Y, Lau K-T, Lu T-P, Hui D. A critical review on polymer-based bio-engineered materials for scaffold development. *Composites Part B: Engineering.* 2007;38:291-300.
- [15] Krueger CA, Wenke JC, Ficke JR. Ten years at war: comprehensive analysis of amputation trends. *J Trauma Acute Care Surg.* 2012;73:S438-44.
- [16] Yakacki CM, Shandas R, Safranski D, Ortega AM, Sassaman K, Gall K. Strong, Tailored, Biocompatible Shape-Memory Polymer Networks. *Advanced functional materials.* 2008;18:2428-35.
- [17] Smith KE, Garcia M, McAnuff K, Lamell R, Yakacki CM, Griffis J, et al. Anterior cruciate ligament fixation: Is radial force a predictor of the pullout strength of soft-tissue interference devices? *The Knee.* 2012;19:786-92.
- [18] Baker RM, Henderson JH, Mather PT. Shape memory poly(ϵ -caprolactone)-co-poly(ethylene glycol) foams with body temperature triggering and two-way actuation. *Journal of Materials Chemistry B.* 2013;1:4916-20.
- [19] Henderson JH, Davis KA, Baker RM. Applications of shape memory polymers (SMPs) in mechanobiology and bone repair. *Biomaterials for Bone Regeneration: Novel Techniques and Applications.* 2014:111.
- [20] Zhang D, George OJ, Petersen KM, Jimenez-Vergara AC, Hahn MS, Grunlan MA. A bioactive "self-fitting" shape memory polymer scaffold with potential to treat cranio-maxillo facial bone defects. *Acta biomaterialia.* 2014;10:4597-605.

- [21] Liu X, Zhao K, Gong T, Song J, Bao C, Luo E, et al. Delivery of growth factors using a smart porous nanocomposite scaffold to repair a mandibular bone defect. *Biomacromolecules*. 2014;15:1019-30.
- [22] Causa F, Netti P, Ambrosio L, Ciapetti G, Baldini N, Pagani S, et al. Poly- ϵ -caprolactone/hydroxyapatite composites for bone regeneration: In vitro characterization and human osteoblast response. *Journal of Biomedical Materials Research Part A*. 2006;76:151-62.
- [23] Chuenjitkuntaworn B, Inrung W, Damrongsri D, Mekaapiruk K, Supaphol P, Pavasant P. Polycaprolactone/hydroxyapatite composite scaffolds: preparation, characterization, and in vitro and in vivo biological responses of human primary bone cells. *Journal of Biomedical Materials Research Part A*. 2010;94:241-51.
- [24] Kim SS, Ahn KM, Park MS, Lee JH, Choi CY, Kim BS. A poly (lactide-co-glycolide)/hydroxyapatite composite scaffold with enhanced osteoconductivity. *Journal of Biomedical Materials Research Part A*. 2007;80:206-15.
- [25] Lee H, Dellatore SM, Miller WM, Messersmith PB. Mussel-inspired surface chemistry for multifunctional coatings. *science*. 2007;318:426-30.
- [26] Arnold EV, Doletski BG, Dunn TM, Raulli RE, Mueller EP, Benedek KR, et al. Sterilization System and Device. In: Office USPaT, editor. US: Noxilizer, Inc.; 2011.
- [27] Arrington SA, Schoonmaker JE, Damron TA, Mann KA, Allen MJ. Temporal changes in bone mass and mechanical properties in a murine model of tumor osteolysis. *Bone*. 2006;38:359-67.
- [28] Yazici C, Takahata M, Reynolds DG, Xie C, Samulski RJ, Samulski J, et al. Self-complementary AAV2.5-BMP2-coated femoral allografts mediated superior bone healing versus

live autografts in mice with equivalent biomechanics to unfractured femur. *Mol Ther*. 2011;19:1416-25.

[29] Middleton JC, Tipton AJ. Synthetic biodegradable polymers as orthopedic devices. *Biomaterials*. 2000;21:2335-46.

[30] Sun H, Mei L, Song C, Cui X, Wang P. The in vivo degradation, absorption and excretion of PCL-based implant. *Biomaterials*. 2006;27:1735-40.

[31] Williams JM, Adewunmi A, Schek RM, Flanagan CL, Krebsbach PH, Feinberg SE, et al. Bone tissue engineering using polycaprolactone scaffolds fabricated via selective laser sintering. *Biomaterials*. 2005;26:4817-27.

[32] Rohner D, Hutmacher DW, Cheng TK, Oberholzer M, Hammer B. In vivo efficacy of bone-marrow-coated polycaprolactone scaffolds for the reconstruction of orbital defects in the pig. *Journal of Biomedical Materials Research Part B: Applied Biomaterials*. 2003;66:574-80.

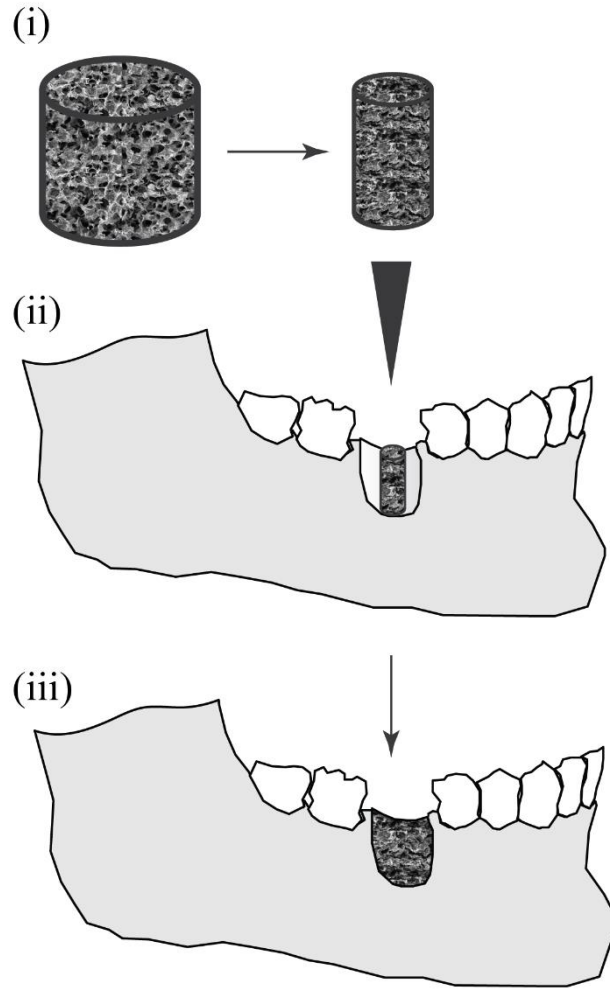
[33] Lee HJ, Choi HW, Kim KJ, Lee SC. Modification of hydroxyapatite nanosurfaces for enhanced colloidal stability and improved interfacial adhesion in nanocomposites. *Chemistry of materials*. 2006;18:5111-8.

[34] Reilly DT, Burstein AH. The elastic and ultimate properties of compact bone tissue. *Journal of biomechanics*. 1975;8:393-405.

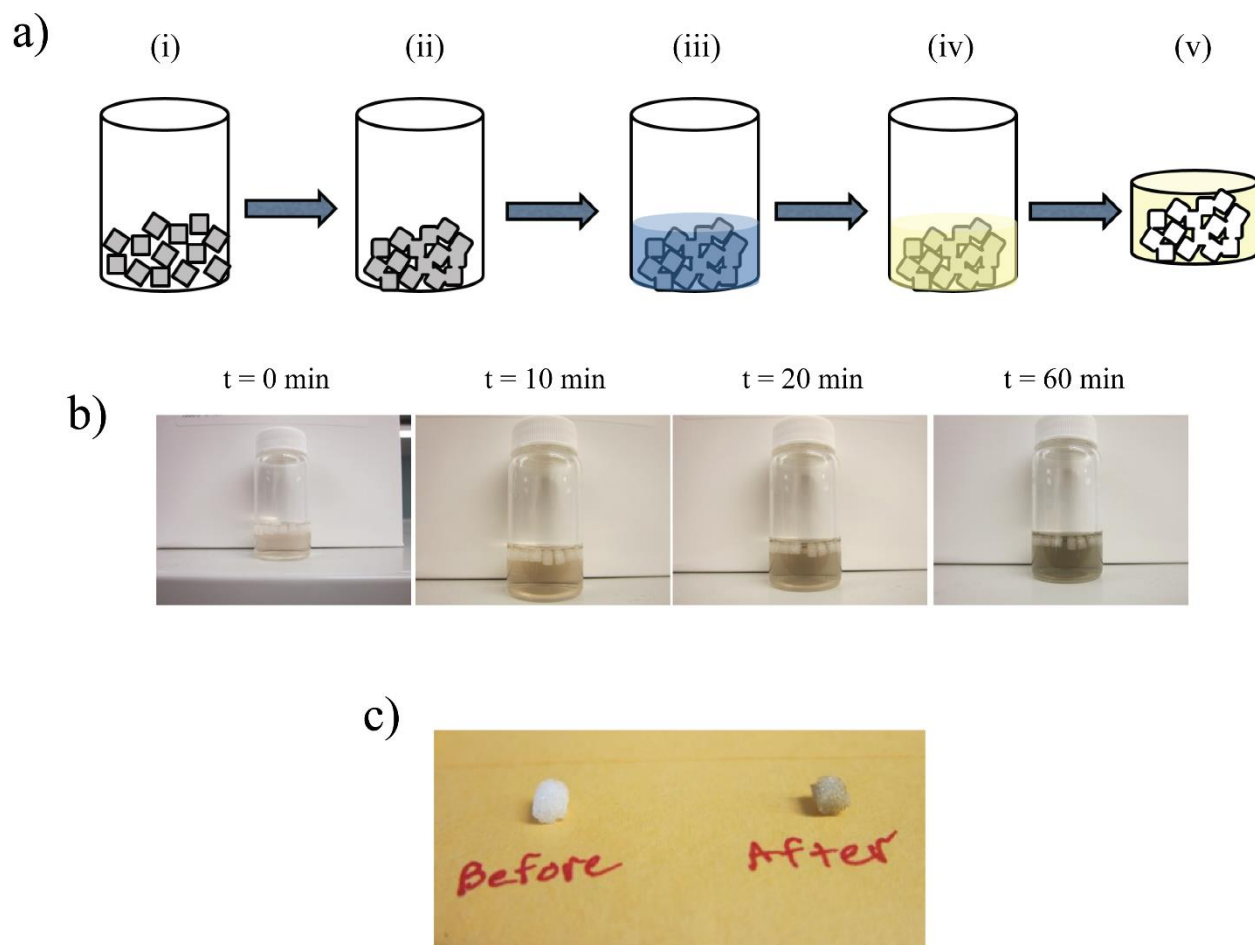
[35] Turner CH, Cowin SC, Rho JY, Ashman RB, Rice JC. The fabric dependence of the orthotropic elastic constants of cancellous bone. *Journal of biomechanics*. 1990;23:549-61.

[36] Oest ME, Dupont KM, Kong HJ, Mooney DJ, Guldberg RE. Quantitative assessment of scaffold and growth factor-mediated repair of critically sized bone defects. *Journal of orthopaedic research*. 2007;25:941-50.

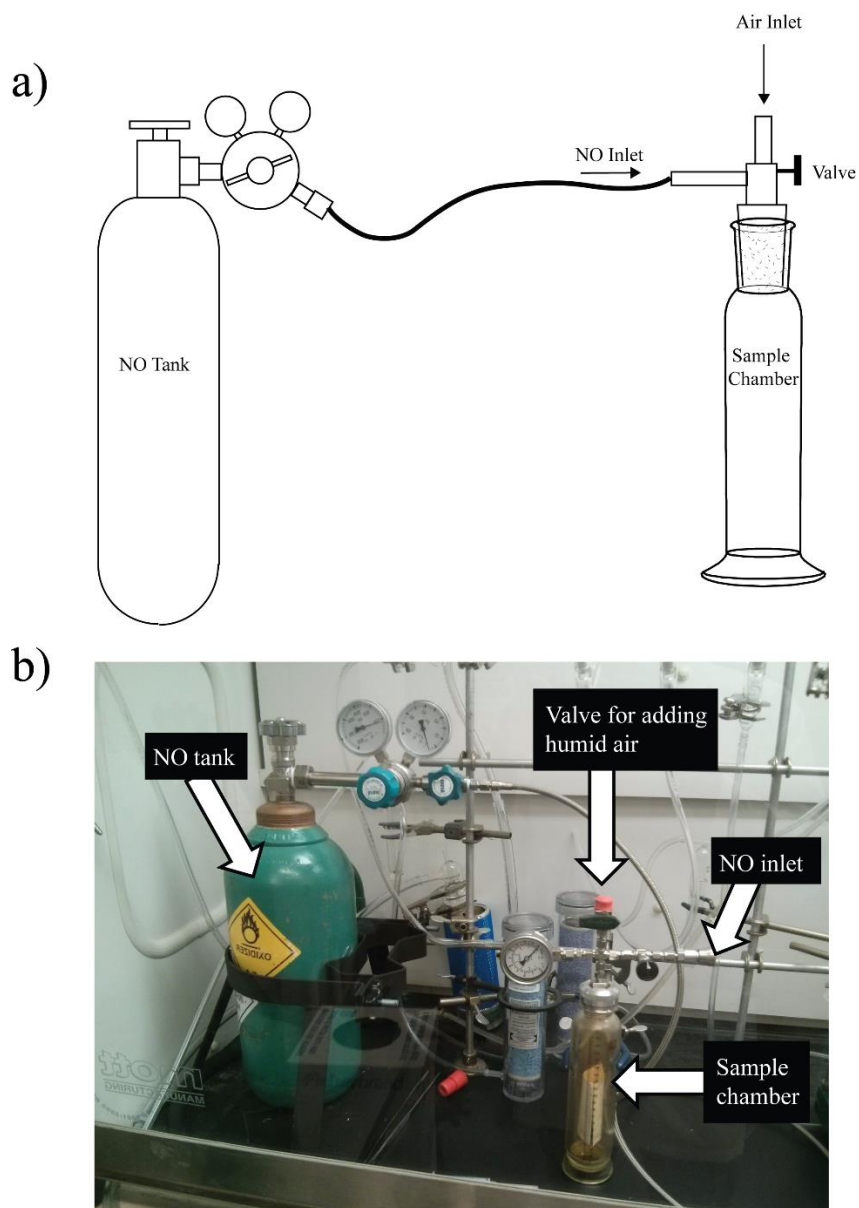
- [37] Oryan A, Alidadi S, Moshiri A, Bigham-Sadegh A. Bone morphogenetic proteins: A powerful osteoinductive compound with non-negligible side effects and limitations. *BioFactors*. 2014;40:459-81.
- [38] Rahman CV, Ben-David D, Dhillon A, Kuhn G, Gould TW, Müller R, et al. Controlled release of BMP-2 from a sintered polymer scaffold enhances bone repair in a mouse calvarial defect model. *Journal of tissue engineering and regenerative medicine*. 2014;8:59-66.
- [39] Mercado-Pagán ÁE, Stahl AM, Shanjani Y, Yang Y. Vascularization in Bone Tissue Engineering Constructs. *Annals of Biomedical Engineering*. 2015:1-12.
- [40] Peng H, Wright V, Usas A, Gearhart B, Shen H-C, Cummins J, et al. Synergistic enhancement of bone formation and healing by stem cell-expressed VEGF and bone morphogenetic protein-4. *The Journal of clinical investigation*. 2002;110:751-9.
- [41] Bruder SP, Kraus KH, Goldberg VM, Kadiyala S. The Effect of Implants Loaded with Autologous Mesenchymal Stem Cells on the Healing of Canine Segmental Bone Defects*. *The Journal of Bone & Joint Surgery*. 1998;80:985-96.
- [42] Zhang D, Burkes WL, Schoener CA, Grunlan MA. Porous inorganic-organic shape memory polymers. *Polymer*. 2012;53:2935-41.
- [43] Tseng LF, Mather PT, Henderson JH. Shape-memory-actuated change in scaffold fiber alignment directs stem cell morphology. *Acta biomaterialia*. 2013;9:8790-801.
- [44] Knight PT, Lee KM, Chung T, Mather PT. PLGA-POSS End-Linked Networks with Tailored Degradation and Shape Memory Behavior. *Macromolecules*. 2009;42:6596-605.



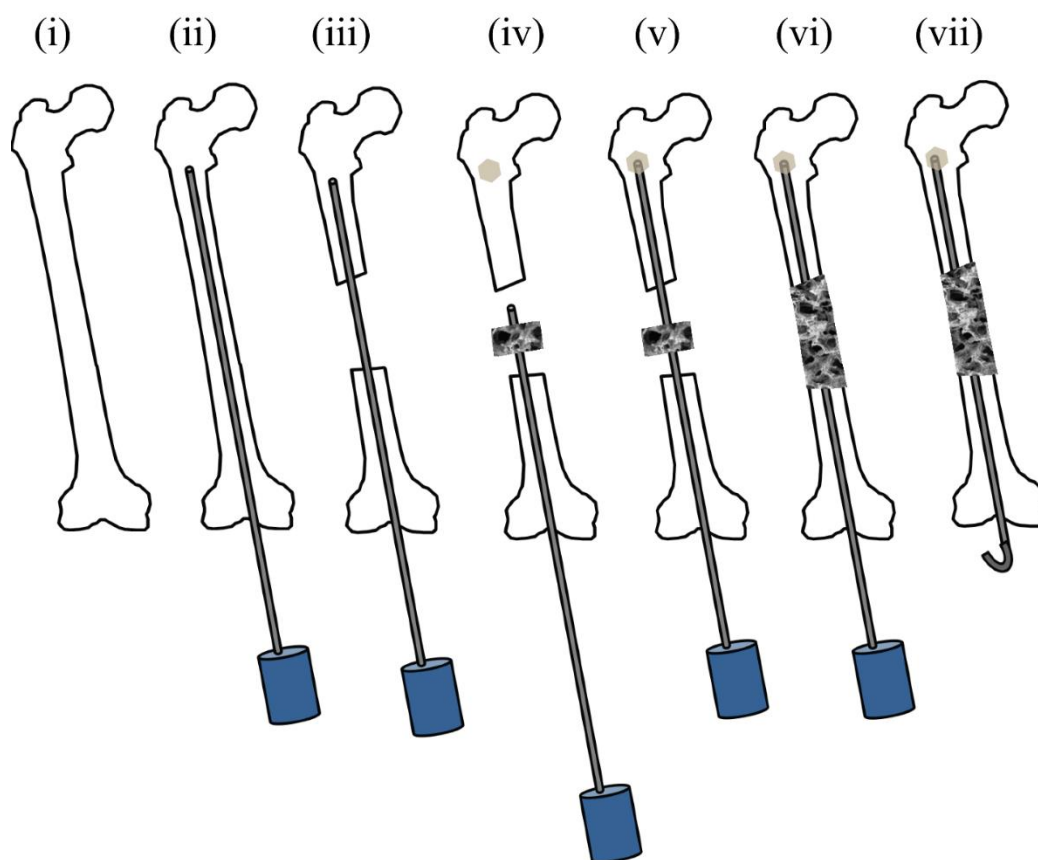
Scheme 5-1. Concept of deployable scaffolds for treatment of critical size defects. (i) An SMP scaffold could be radially compressed and fixed into a shape smaller than the defect site; (b) the SMP could then be delivered to the defect site where it remains in its stable temporary shape; (c) upon heating, the SMP would recover and expand to fill the defect. Adopted with permission from ref [19].



Scheme 5-2. Preparation of tBA/BA scaffolds coated with polydopamine. (a) A modified porogen-leaching technique is employed where (i) salt particles with the desired diameter are sieved and added to a 20 mL glass vial; (ii) salt particles are fused in a humidity chamber for 24 h; (iii) a comonomer solution consisting of tBA, BA, TEGDMA crosslinker, and DMPA photoinitiator are added to the salt template; (iv) the solution is UV cured for 2 h; (v) foams are removed from the glass vials, surface skins are cut off, and salt is extracted by soaking in water for 48 h. (b) Time progression images of polydopamine coating show a darkening of the polydopamine solution, indicating successful coating; (c) prior to polydopamine coating, tBA/BA scaffolds are white. After coating and drying, scaffolds turn dark brown/grey.



Scheme 5-3. Sterilization setup using NO_x. (a) Schematic and (b) picture of the NO sterilization setup. Programmed SMP foams are placed in Tyvek pouches and sealed in the sample chamber. NO gas is injected into the sample chamber through the NO inlet. After 1 h, 120 mL of humid air is injected into the sample chamber. After 18 h, sample pouches are removed and aerated.



Scheme 5-4. Surgical procedure for implanting deployable SMP scaffolds. (i) femur is exposed and (ii) a 25 G needle is inserted into the medullary cavity; (iii) a 4 mm segmental defect is cut into mid-diaphysis; (iv) programmed foams are inserted on the intramedullary nail and 50 uL of bone cement (brown circle) injected into the proximal end of the femur; (v) the intramedullary nail is inserted in the proximal end of the femur; (vi) SMP foam expansion is triggered by irrigating with 45 °C saline. Following expansion, foams are irrigated with room temperature saline to cool foams below their glass transition temperature; (vii) the intramedullary nail is cut and bent between the distal condyles.

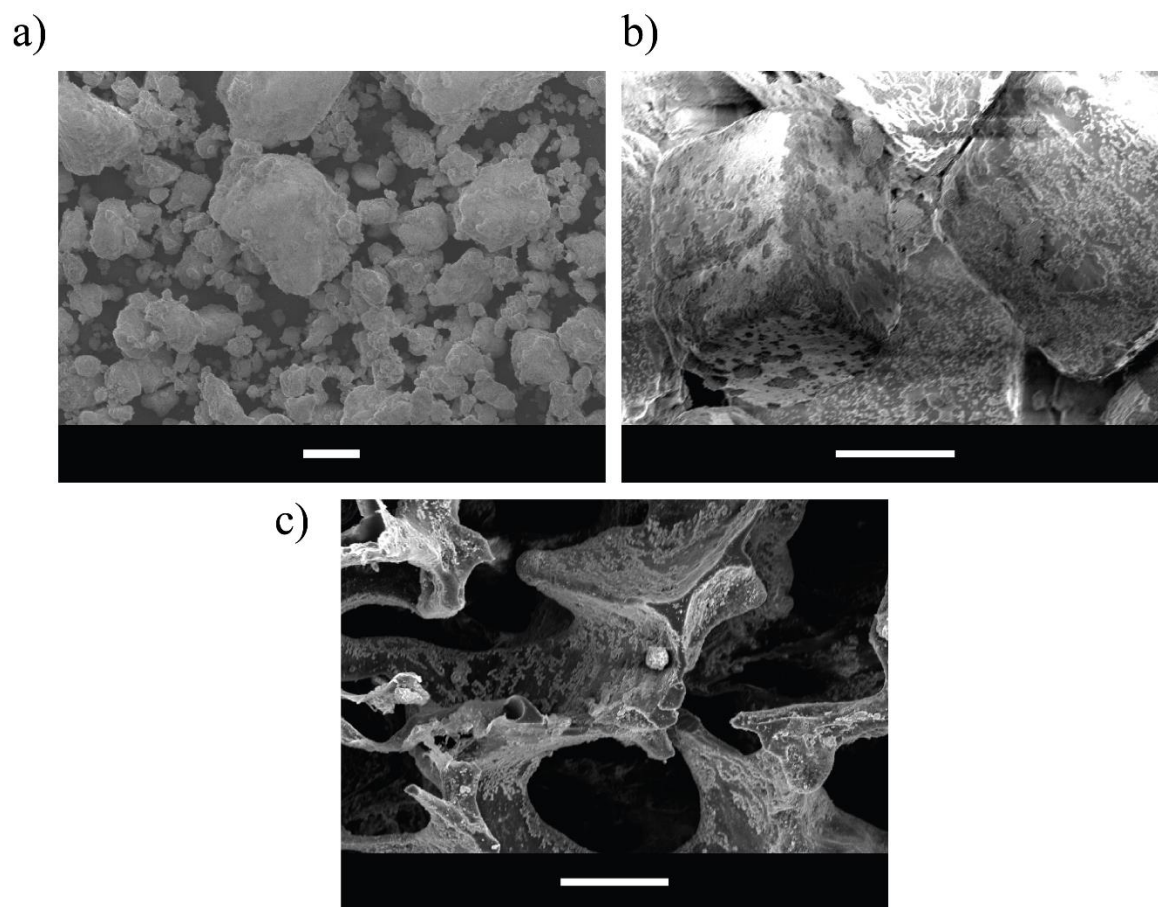


Figure 5-1. Scanning electron micrographs show successful incorporation of hydroxyapatite (HA) into 80PCL-20PEG foams. (a) HA nanoparticles (<200 nm according to vendor specifications) aggregate into larger particles; (b) following salt fusion in the presence of HA, cuboidal salt particles are coated with nano HA particles; (c) following foam fabrication and salt extraction, HA nanoparticles cover the pores and struts of the foam. Scale bars are 100 μm for all SEM micrographs.

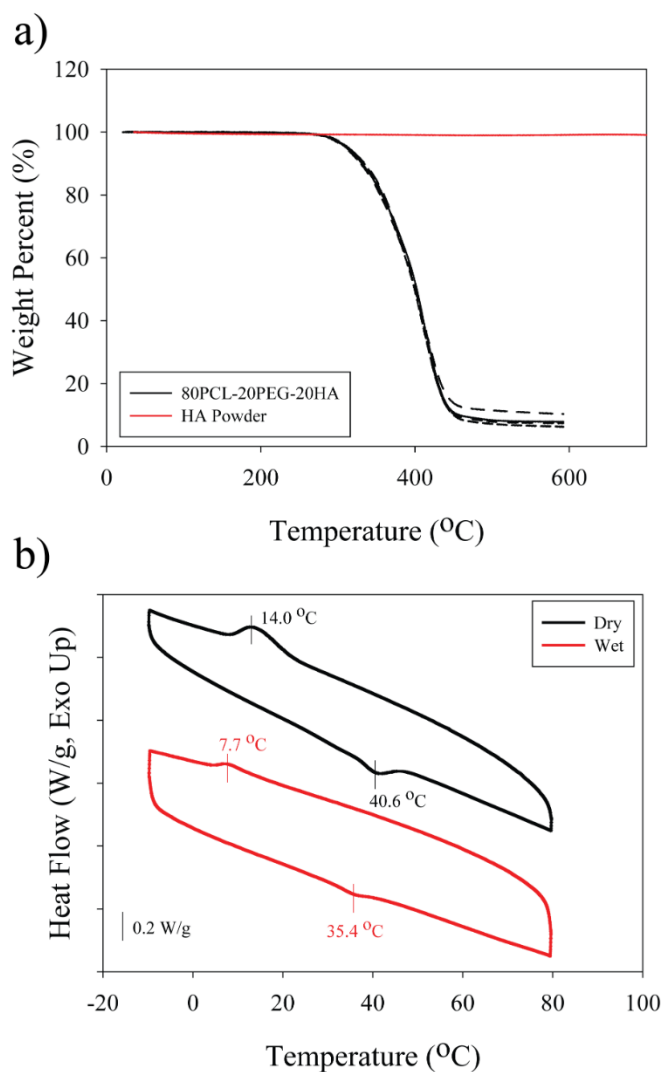


Figure 5-2. Thermal degradation and transition temperature of 80PCL-20PEG-20HA foams. (a) Thermogravimetric analysis (TGA) of HA-incorporated foams show an average of 8% mass remaining following degradation. Dotted black lines represent degradation profiles from different locations of the same foam. (b) DSC 2nd heating traces of dry and wet foams reveal a dry T_m of 40.6 °C that drops to 35.4 °C upon hydration. The sloped baseline in the DSC traces is an artifact from the DSC equipment. A heating rate of 20 °C-min⁻¹ was used for TGA, and a heating/cooling rate of 3 °C-min⁻¹ was used for DSC.

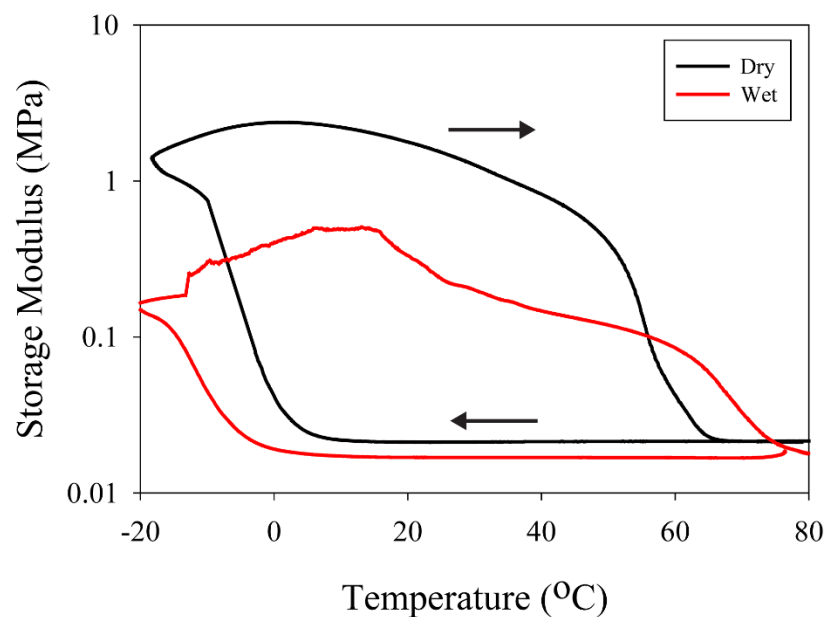


Figure 5-3. Temperature dependent dynamic mechanical response (1 Hz, under compression) of the 80PCL-20PEG-20HA foam. Foams have an apparent storage modulus of ~1 MPa below T_m (dry) that drops to ~10 kPa upon heating above T_m . Heating and cooling rates of $3\text{ }^{\circ}\text{C}\cdot\text{min}^{-1}$ were used.

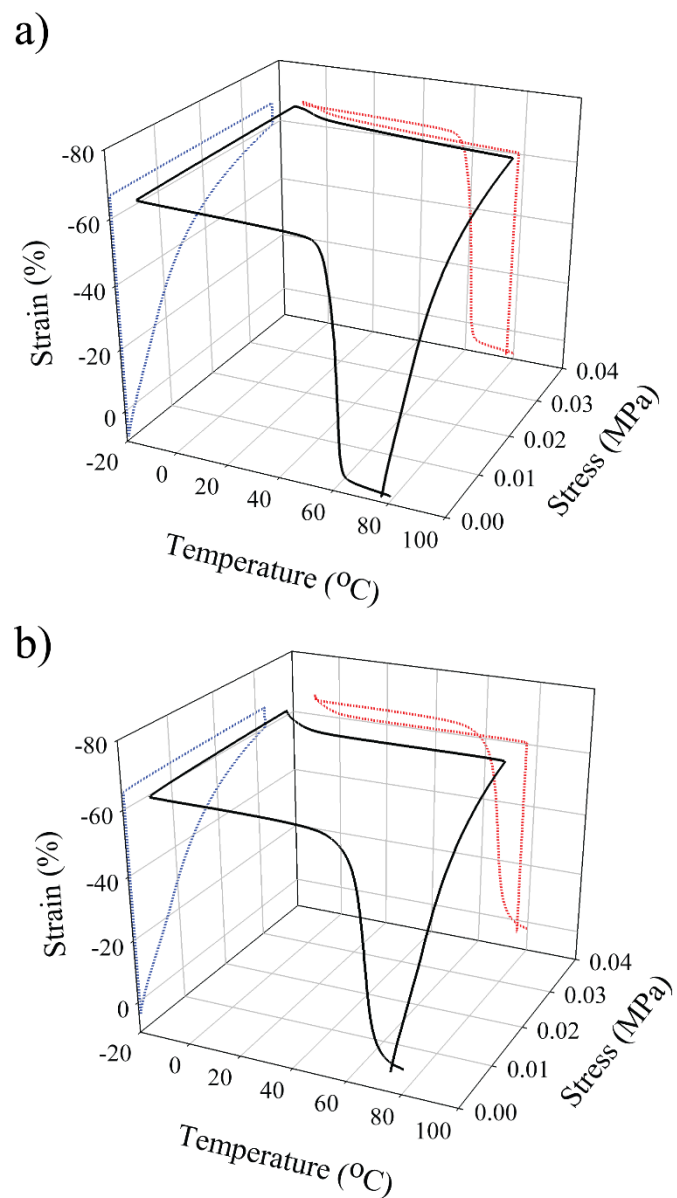


Figure 5-4. Shape memory behavior of the 80PCL-20PEG-20HA foams. One-way shape memory behavior (compression) of (a) dry and (b) wet foams reveal excellent shape fixing and shape recovery.

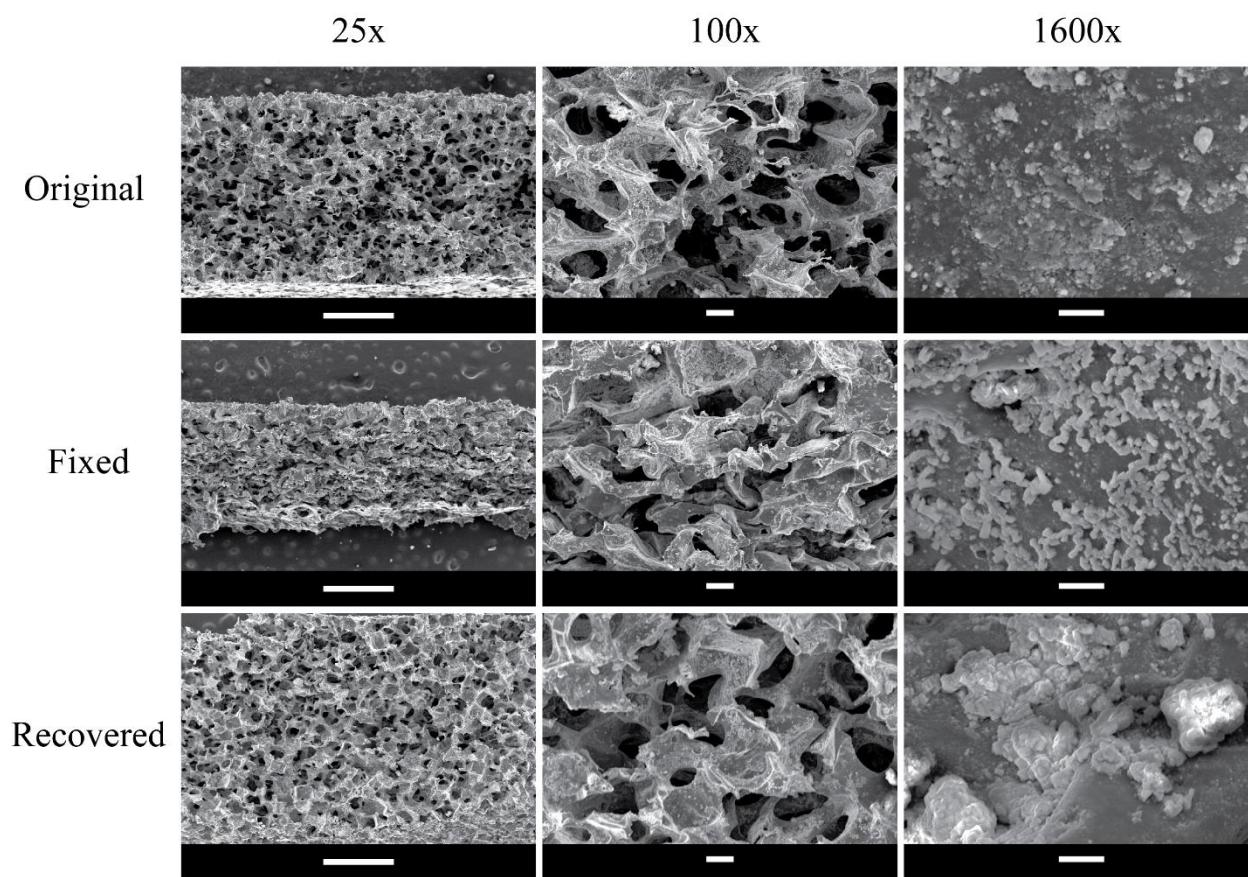


Figure 5-5. Scanning electron micrographs of 80PCL-20PEG-20HA foams during a one-way shape memory cycle. SEM micrographs of foams (top) before fixing, (middle) after fixing a 50% compressive strain, and (c) after recovery reveals the open, porous architecture collapses upon fixing but is restored upon shape recovery. Magnifications of (left) 25x, (middle) 100x, and (right) 1600x show the macroscopic and microscopic effect of shape memory on the foam architecture. Inspection of the 1600x micrographs reveals hydroxyapatite particles remain on the foam surface during all stages of the shape memory cycle. Scale bars are 1 mm, 100 μ m, and 10 μ m for magnifications of 25x, 100x, and 1600x, respectively.

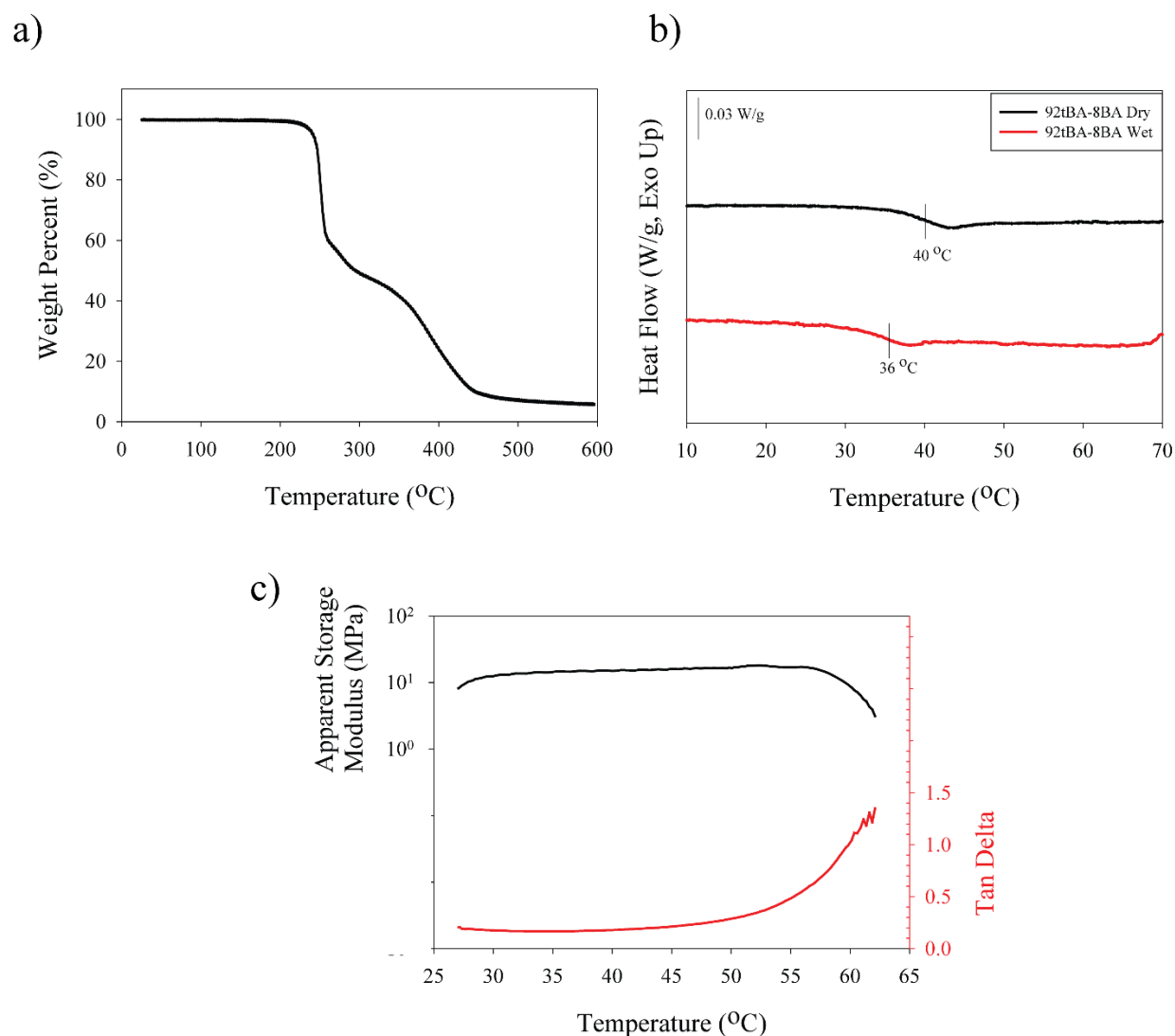


Figure 5-6. Thermal and thermomechanical properties of 92tBA-8BA SMP foams. (a) TGA reveals complete salt extraction upon heating to 600 °C; (b) DSC 2nd heating trace reveals a dry T_g of 40 °C that drops to 36 °C upon hydration; (c) dynamic mechanical analysis (DMA) of dry foam shows an apparent storage modulus of ~10 MPa below T_g. Heating rate used for TGA was 20 °C ·min⁻¹, heating/cooling rate for DSC was 3 °C ·min⁻¹, and heating rate for DMA was 3 °C ·min⁻¹.

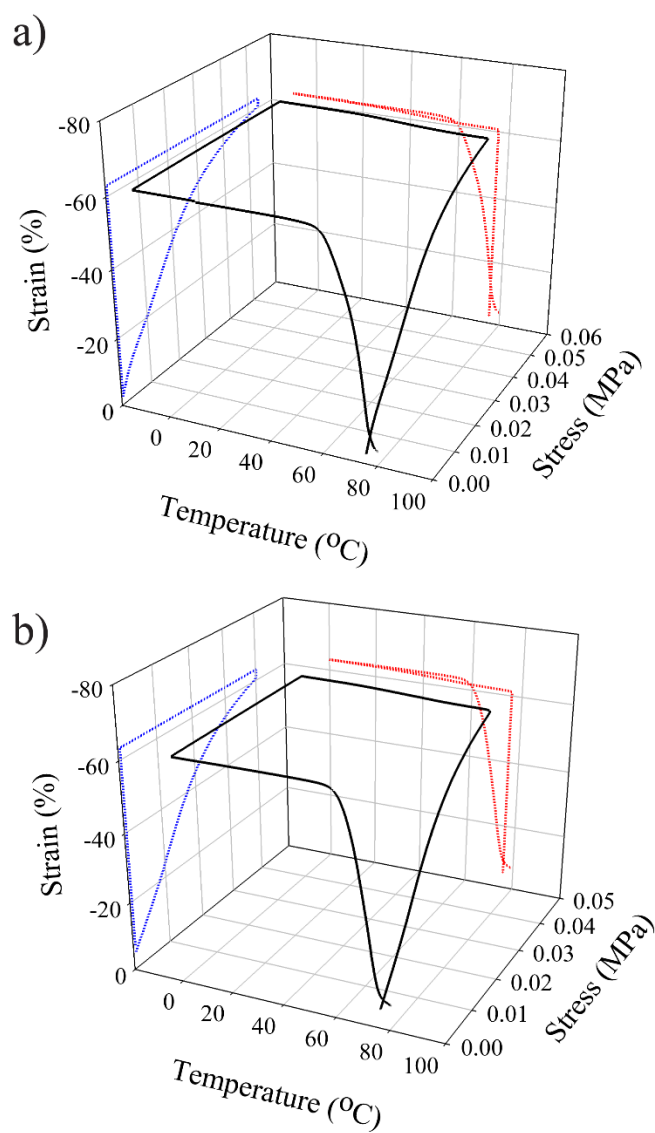


Figure 5-7. Shape memory behavior of 92tBA-8BA foams. One-way shape memory behavior (compression) of (a) dry and (b) wet foams reveal excellent shape fixing and shape recovery.

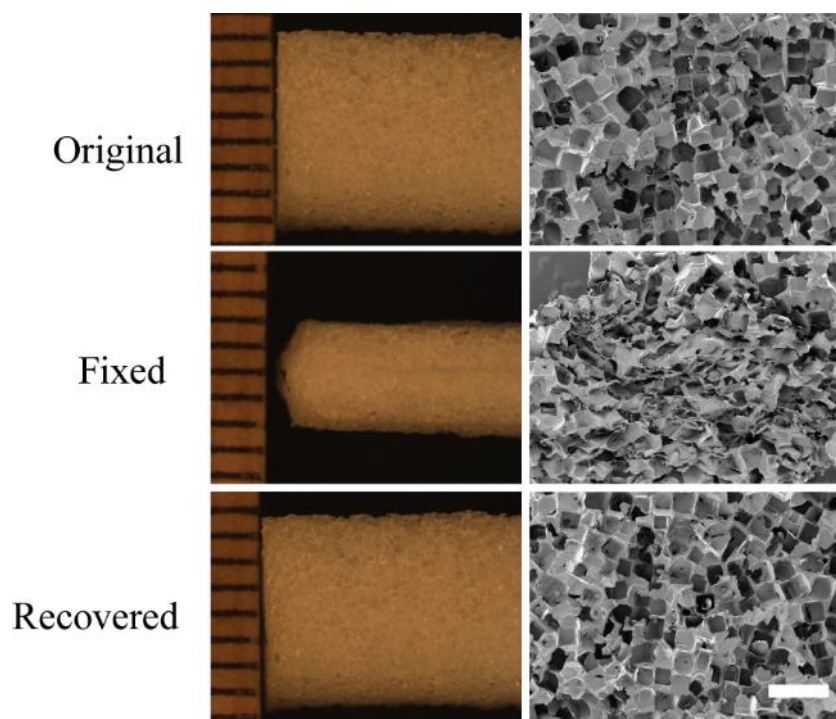


Figure 5-8. Optical micrographs and scanning electron micrographs of 92tBA-8BA foams during a one-way shape memory cycle. (left) optical micrographs and (right) SEM micrographs (top) before fixing, (middle) after fixing a 50% compressive strain, and (c) after recovery reveals the open, porous architecture collapses upon fixing but is restored upon shape recovery. Foams have a cuboidal pore morphology with small interconnecting openings between pores. Scale bar is 1 mm.

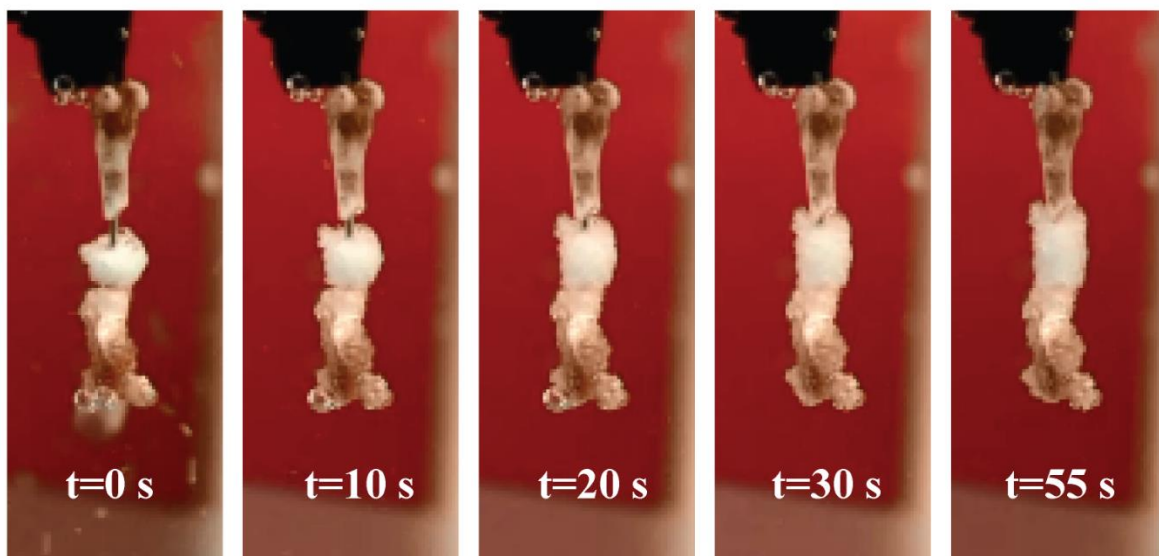


Figure 5-9. *In situ* recovery of a 92tBA-8BA foam in a mouse femoral segmental defect. A compressed foam was triggered to recover by submerging in 45 °C water, simulating intraoperative delivery. The foam expanded to fill the defect within 55 s.

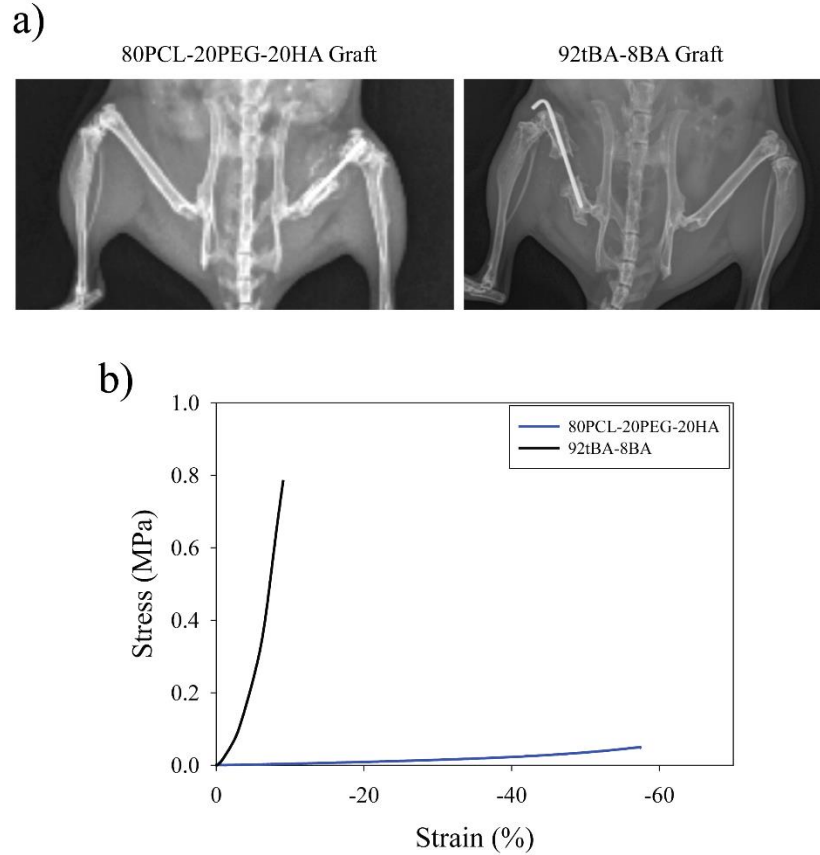


Figure 5-10. Comparison of the stability of soft (80PCL-20PEG-20HA) and stiff (92tBA-8BA) foams implanted *in vivo*. (a) x-ray radiographs of mice implanted with SMP foams 4 weekspost-surgery show significant limb shortening for 80PCL-20PEG-20HA foam treatment; no shortening occurs for 92tBA-8BA foam treatment. (b) compressive stress v. strain curves for foams hydrated at 37 °C for 24 h reveal compressive elastic moduli of 0.06 MPa and 16 MPa for soft and stiff foams, respectively.

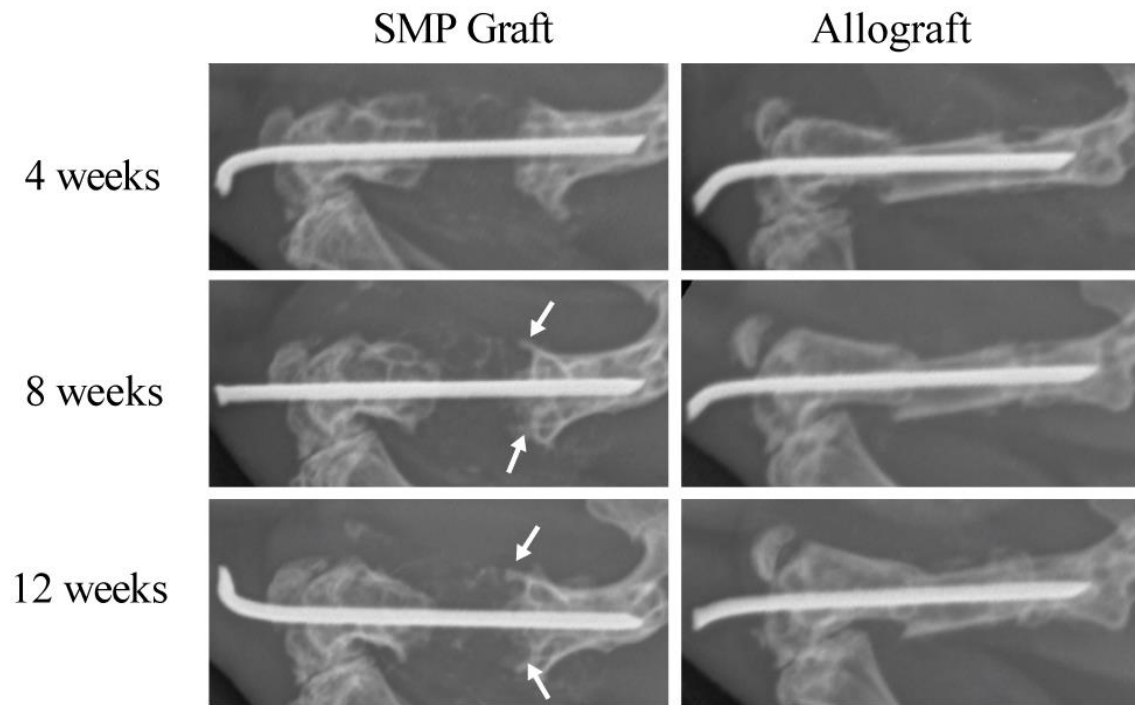


Figure 5-11. Representative radiographs of limbs treated with an SMP graft (92tBA-8BA) and a control allograft at 4, 8, and 12 weeks post-surgery. The SMP graft maintained the length of the segmental defect 12 weeks post-surgery. White arrows indicate bony formations at the margin.

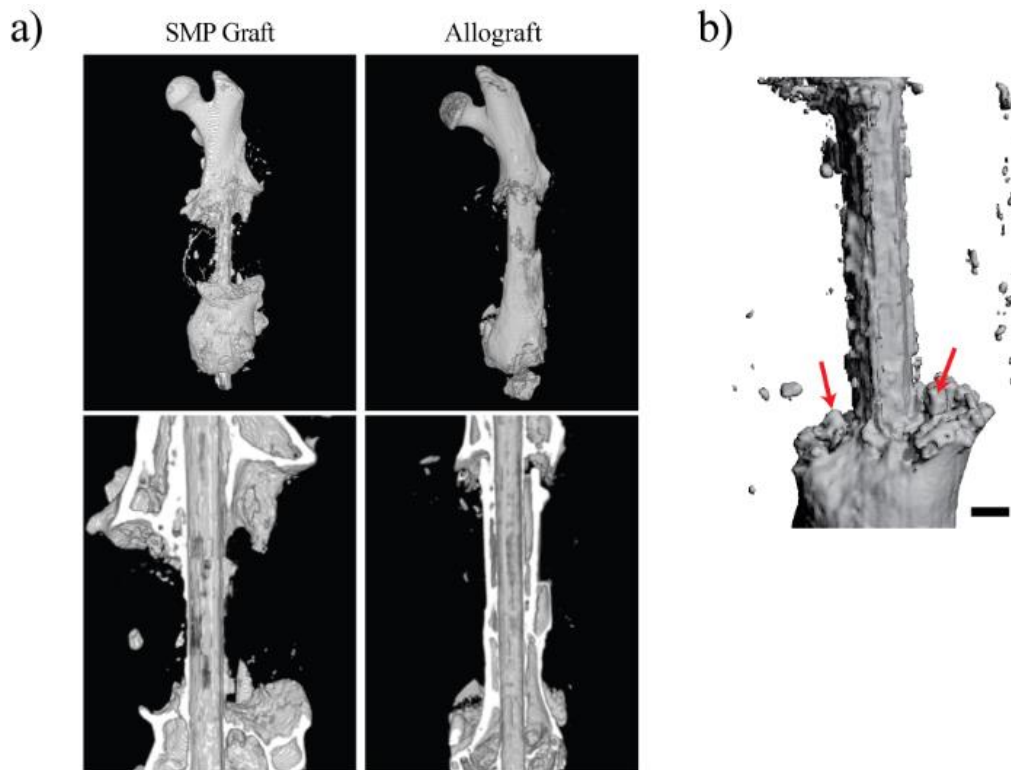


Figure 5-12. Representative reconstructed microcomputed tomography scans of limbs treated with an SMP graft (92tBA-8BA) and a control allograft 12 weeks post-surgery; (a)(top) 3D reconstruction of the entire femur, and (bottom) enlarged cross-sectional view of the defect site sho new bone formation at the margins between the grafts and the native bone. (b) 3D reconstruction of a defect treated with an SMP graft shows bony protrusions (red arrows) that have the same cuboidal morphology and size as the SMP pores. Scale bar in (b) is 300 μm .

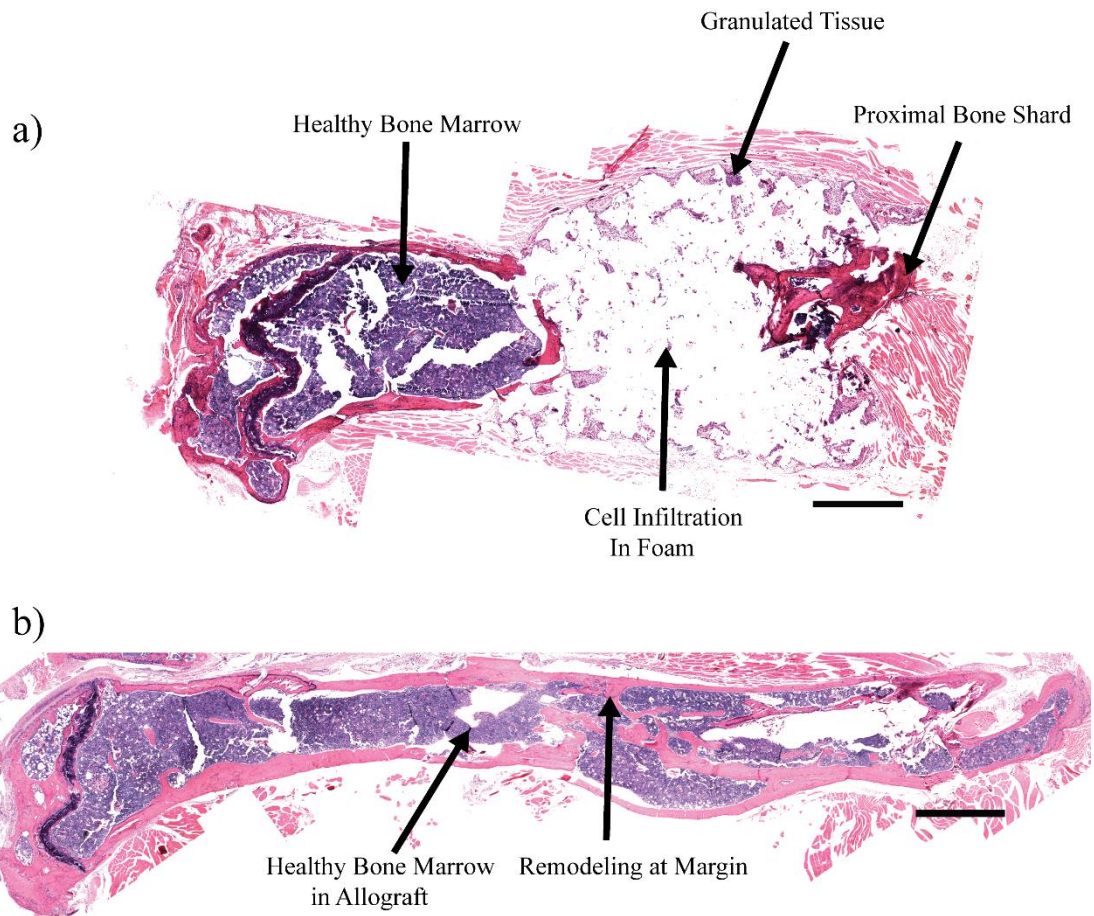


Figure 5-13. Histological analysis of limbs treated with (a) SMP grafts (92tBA-8BA) and (b) an allograft control 12 weeks post-surgery. Granulated tissue and cell infiltration is found into the SMP foam, and the distal native bone marrow appears healthy. Allograft treatment shows remodeling has begun at the margins. Scale bars are 1 mm.

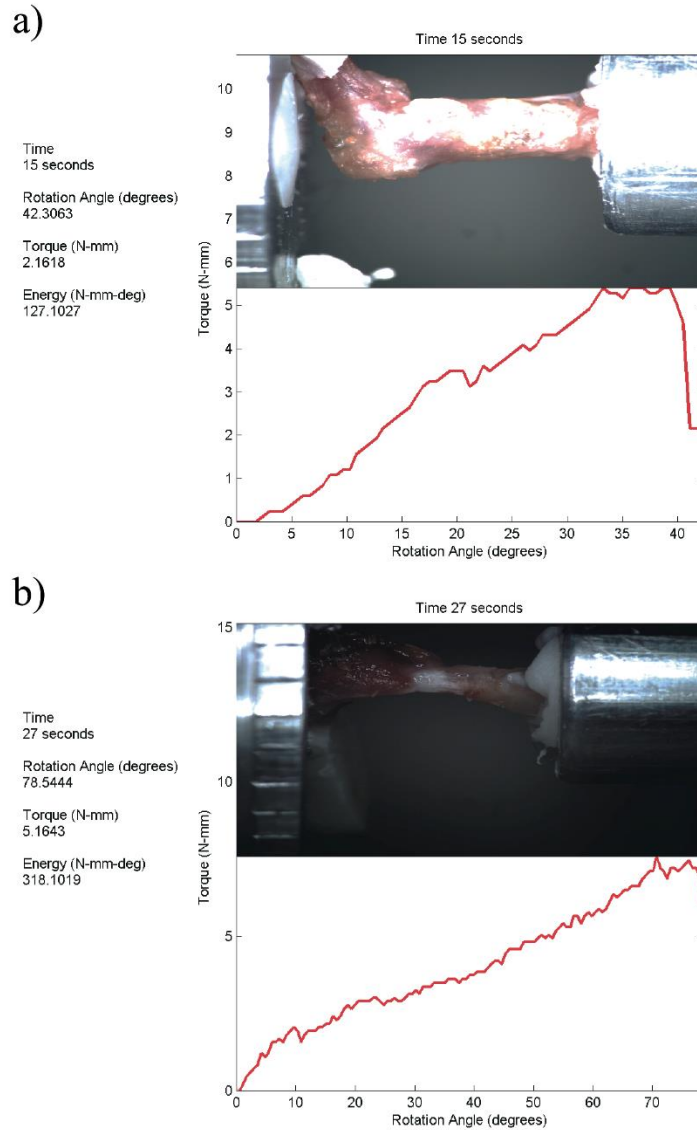


Figure 5-14. Example torsional testing output from custom MATLAB algorithm for limbs treated with (a) SMP grafts (92tBA-8BA) and (b) an allograft control 12 weeks post-surgery. Torque-rotation angle curves were generated with real-time testing images overlaid to assess in failure analysis. Torque, energy, and stiffness were determined for each trace.

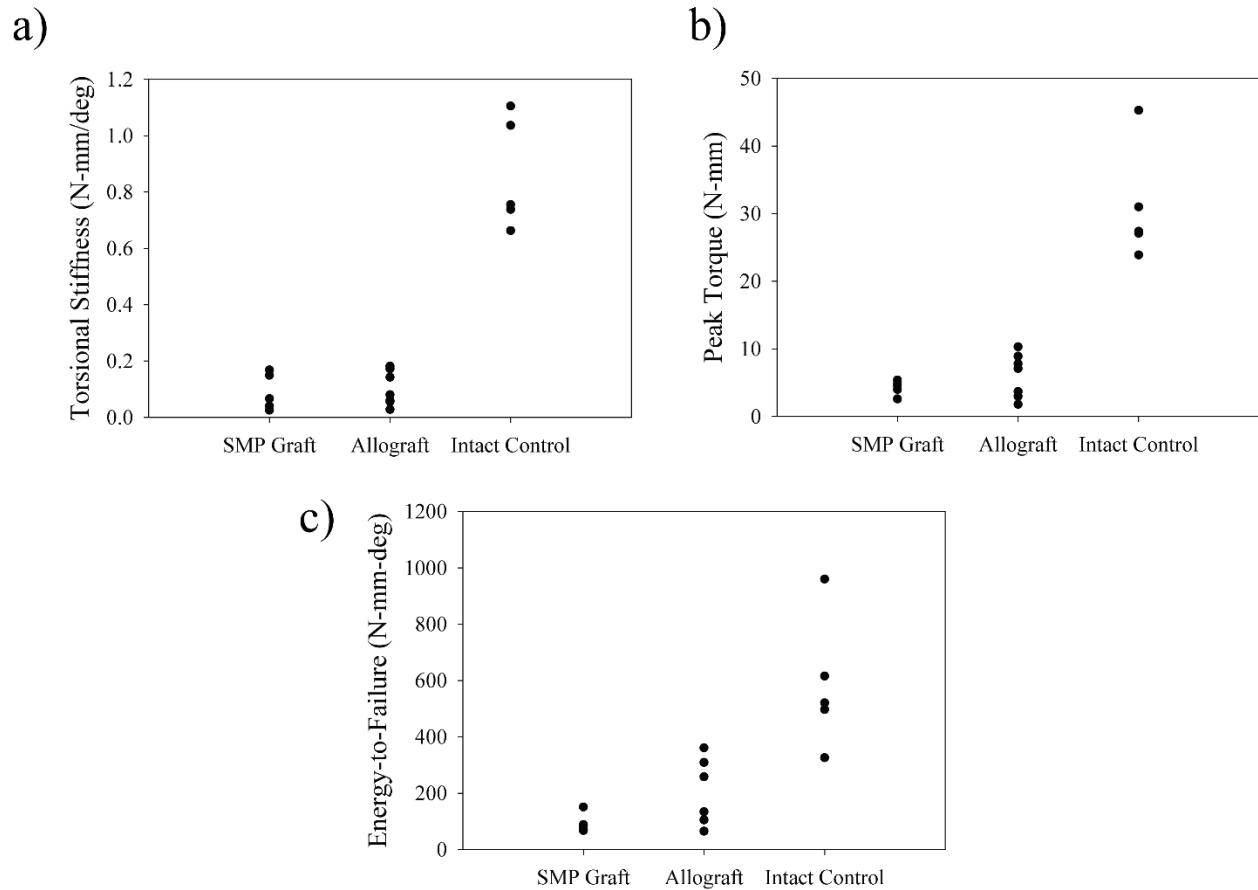


Figure 5-15. Torsional mechanical properties of limbs treated with SMP graft or allograft, and a contralateral intact femur control, 12 weeks post-surgery. (a) Torsional stiffness; (b) peak torque; (c) energy-to-failure. The SMP graft exhibited a trend of lower torsional mechanical properties compared to the allograft group, although not statistically significant. Mechanical properties of both treatment groups were significantly lower than the contralateral intact control.

Table 5-1. Summary of torsional mechanical properties for limbs treated with an SMP graft (92tBA-8BA) or an allograft control, and a contralateral intact control. The SMP graft exhibited a trend of lower torsional mechanical properties compared to the allograft group, although not statistically significant. Mechanical properties of both treatment groups were significantly lower than the contralateral intact control.

Group	Torsional Stiffness (N-mm-deg ⁻¹)	Peak Torque (N-mm)	Energy-to-Failure (N-mm-deg)
92tBA-8BA Foam	0.090 ± 0.065	4.28 ± 1.06	93 ± 34
Allograft	0.103 ± 0.062	6.09 ± 3.25	191 ± 116
Intact Control	0.860 ± 0.197	30.9 ± 8.4	584 ± 235

Chapter Six: Osteogenic Differentiation in Expanding Shape Memory Scaffolds[†]

6.1 Synopsis

Chapter 5 revealed that stiffer shape memory polymer (SMP) scaffolds show promise for use as bone repair constructs. While the SMP constructs are stable and integrate well with the native bone, there is limited bone growth and remodeling due to the lack of cells, lack of growth factors, and small interconnections between pores. To overcome these limitations, one option is seeding stem cells into scaffolds before implantation and triggering osteogenic differentiation. This chapter explores the possibility of seeding stem cells in SMP scaffolds programmed to expand, and how triggering expansion of these scaffolds may affect osteogenic differentiation. Osteogenic differentiation in expanding and control scaffolds is compared through protein expression, gene expression, and calcium deposition assays. The findings suggest that SMP scaffolds can be employed as promising candidates for deployable cell-based therapies to facilitate bone repair.

6.2 Introduction

As discussed in **Chapter 5**, critical size bone defects place a significant burden on the US healthcare system. Treatment of critical size defects or other bone defects requiring bone grafts costs over \$100 billion annually, worldwide [1]. While bone autografts remain the gold standard of treatment, recent efforts have focused on alternative treatment options including allograft, xenograft, and synthetic bone graft substitutes. When evaluating the effectiveness of a bone

[†] Adapted (in part) from LF. Tseng, J. Wang, R.M. Baker, P.T. Mather, and J.H. Henderson, **2015**, (*in preparation*)

graft, several elements should be considered: osteogenicity, osteoinductivity, osteoconductivity, and osteointegration [2, 3]. Osteogenicity refers to the presence of bone-forming cells in the donor graft; osteoinductivity refers to the ability of the graft to stimulate host stem cells to differentiate into bone-forming osteoblasts; osteoconductivity refers to the ability of the graft to enable ingrowth of new bone cells and capillaries; and osteointegration refers to bonding between the graft and the host bone. While traditionally synthetic bone graft substitutes possessed good osteoconductivity and osteointegration while lacking osteogenicity and osteoinductivity [3], recent advances in tissue engineering and material science have addressed these shortcomings. For instance, bone grafts composed of or incorporating ceramics such as hydroxyapatite [4, 5] and β -tricalcium phosphate [6, 7] have shown to significantly improve osteoinductivity. Additionally, osteoinductivity has been improved through the incorporation of growth factors, particularly bone morphogenic proteins[8-10].

One promising approach to improve osteogenicity of synthetic bone graft substitutes is to incorporate stem cells directly into the graft [11, 12]. Bruder et al. reported that incorporation of human mesenchymal stem cells in hydroxyapatite/ β -tricalcium phosphate ceramic blocks, compared to cell-free ceramic blocks, resulted in significantly more bone formation in a critical size segmental defect model [13]. Later, Petite and colleagues used a faster-resorbing coral scaffold in combination with marrow stromal cells (MSCs) to treat critical size defects in a sheep model [14]. In this study they found MSCs produced complete recorticalization and formed a medullary canal with mature bone after 4 months, and bone formation occurred at about the same rate as implant resorption. Several other studies have also demonstrated bone repair when using a cell-based therapy where porous scaffolds are combined with stem cells [15-17].

Recent advances in programmable SMP scaffolds developed for the treatment of critical size bone defects provide a new opportunity to combine SMP deployability with the osteogenicity of stem-cell seeded constructs. Within the past two years, the use of SMP scaffolds in bone repair strategies has gained significant attention [18-21]. Liu and colleagues developed a poly(ϵ -caprolactone) scaffold containing hydroxyapatite that was used as a synthetic bone graft in an *in vivo* rabbit mandibular critical size defect model [20]. Zhang et al. also developed a bioactive SMP foam that could “self-fit” into irregular bone defect geometries [19]; while no *in vivo* work was conducted, the ability of these bioactive SMP scaffolds to support osteoblast adhesion, proliferation, and osteogenic gene expression was reported. Bao et al developed an electrospun SMP scaffold that supported osteoblast adhesion, proliferation, and differentiation [18]; however, the effect of scaffold architecture change on cells was not investigated. Additionally, in **Chapter 5** we reported the use of expanding SMP foams for treating segmental defects in mice. Collectively, these studies demonstrate the potential of programmable SMP scaffolds as deployable bone repair strategies. Combining this deployability with stem cell-based therapy may provide a new strategy to minimal-invasively treat critical size defects in a rapid manner. Before this can be achieved, the effect of scaffold deployment on stem cell osteogenic differentiation capacity must be explored.

The goal of this study was to determine if osteogenic differentiation capacity is preserved following programmed architectural change in SMP foam scaffolds. We hypothesized that stem cell osteogenic differentiation could be preserved during and following programmed architectural change in expanding SMP foams when triggered under cytocompatible conditions. To test this hypothesis, human adipose-derived stem cells were seeded in SMP foam scaffolds programmed to expand when heated to 37 °C. Osteogenic differentiation capacity was assayed

before and after triggering scaffold expansion. Mineral deposition, protein expression, and gene expression were compared between programmed and control scaffolds.

6.3 Methods and Materials

6.3.1 Materials

Tert-butyl acrylate (tBA), butyl acrylate (BA), tetraethylene glycol dimethacrylate (TEGDMA), and 2,2-dimethoxy-2-phenyl acetophenone (DMPA) were purchased from Sigma Aldrich. Prior to use, tBA and BA were purified by passing through inhibitor removal columns (SDHR-4, Scientific Polymer). TEGDMA and DMPA were used as received.

6.3.2 Scaffold Preparation

Porous SMP foam scaffolds were fabricated following the procedure outlined in **Chapter 5 (Section 5.3.2.2)** to fabricate tBA-BA foams with a tunable glass transition temperature (T_g). For this study, a target T_g slightly higher than 37 °C was required to ensure stability of a programmed shape at 30 °C (discussed later). To fabricate foam scaffolds with a hydrated T_g of 42 °C, a comonomer wt-% ratio of 98-2 (tBA-BA) was used, with a constant 5 wt-% TEGDMA crosslinker and 1 wt-% DMPA photoinitiator. An example comonomer solution would consist of: 2 mL tBA (1.75 g), 40 μ L BA (37.5 mg), 82.6 μ L TEGDMA (89.4 mg), and 18.8 mg of DMPA. This solution was mixed and added to a fused salt template. The fused salt template was photo-cured for 2 h using UV light, after which the glass vial was broken and the cured foam removed. Foams contained a solid skin on each surface that was removed with a razor blade. Following skin removal, foams were placed in 60 °C water for 48 h to extract the salt. Foams were rinsed thoroughly and placed in methanol for 12 h to extract unreacted monomer and

photoinitiator. Foams were then dried in a vacuum oven for 24 h. Foam plugs were coated with polydopamine following the procedure described in **Chapter 5 (Section 5.3.2.2)**.

For cell studies, cylindrical foam plugs with a 3.5 mm diameter and 4–4.5 mm height were used. As-prepared foam scaffolds were used as the *static* control. *Active* shape-changing foam scaffolds were programmed into a temporary compact state by uniaxially compressing the foam plugs with 30% strain using calipers at room temperature. Upon unloading, foams elastically recovered approximately 5% strain, resulting in a fixed compressive strain of 25%. This approach to fixing a temporary deformation below the SMP T_g we previously termed “Reversible Plasticity Shape Memory (RPSM)” [22], and this study is the first to employ this approach in a porous foam structure.

6.3.3 Scaffold Characterization

Thermogravimetric analysis (TGA) was employed to confirm salt extraction of 98tBA-2BA foams. Samples weighing 5-10 mg of the foam scaffold were loaded in a Q500 (TA Instruments) thermogravimetric analyzer and heated to 600 °C at a rate of 20 °C-min⁻¹ under nitrogen purge.

Differential scanning calorimetry (DSC) was employed to determine the T_g of the 98tBA-2BA foams. DSC experiments were conducted using a Q200 (TA Instruments) equipped with a refrigerated cooling system. Samples with a mass of 3-5 mg were placed in Tzero aluminum pans (dry samples) or Tzero hermetic pans (wet samples) and were heated from -10 °C to 80 °C (first heat), cooled back to -10 °C (first cool), and finally heated back to 80 °C (second heat). All heating and cooling rates were 3 °C-min⁻¹. The T_g was determined using Universal Analysis Software (TA Instruments). Wet samples were soaked in 37 °C water for 24 h prior to testing.

The ability of *active* foams to maintain a stable programmed shape at 30 °C (cell seeding temperature) and be subsequently triggered to recover at 37 °C was investigated. Foams were programmed with a 25% compressive strain and hydrated with phosphate buffered saline (PBS) in a 30 °C water bath for 5 d, simulating cell culture conditions. Scaffold recovery was measured during the 5 d period using calipers to determine the stability of the programmed shape at 30 °C. After 5 d, samples were moved to a 37 °C water bath, triggering recovery, and the shape recovery was measured.

6.3.4 Scaffold Sterilization

Active and static scaffolds were sterilized following the procedure outlined in **Chapter 5 (Section 5.3.7)**.

6.3.5 Cell Culture

6.3.5.1 Cell Expansion

Human adipose-derived stem cells (hASCs) were used to investigate the effect of scaffold shape and architecture change on osteogenic differentiation. hASCs were chosen because they are commonly used in bone tissue engineering [23]. Prior to seeding on scaffolds, hASCs were expanded in basal growth medium: MesenPro RS medium with 2% MesenPro RS growth supplement, 1% GlutaMAX, and 1% penicillin/streptomycin in a 37 °C humidified incubator with 5% CO₂. Cells were passaged at 80% confluence using TrypLE Express solution. Cells were used at passage 6 for scaffold experiments. All cell culture products were purchased from Life Technologies.

6.3.5.2 Cell Seeding In Foams

To determine if osteogenic differentiation capacity is preserved following changes in foam architecture, hASCs were seeded in *static* and *active* foams that underwent a two-stage cell culture process. During the first stage, cells were cultured in foams at a cytocompatible temperature (30 °C) that does not trigger recovery of *active* foams; at the second stage, foams were heated to 37 °C to trigger recovery of the *active* foams. Prior to cell seeding, sterilized foams were immersed in antibiotic-antimycotic solution (Sigma-Aldrich) overnight at 4 °C to ensure the sterility, followed by rinsing in PBS.

To facilitate cell seeding into the foam scaffolds, a vacuum-assisted seeding approach was employed. Prior to cell seeding, foams were first equilibrated in growth medium for 20 min. Samples were then placed in transfection tubes containing 3 mL of cell suspension at a cell concentration of 500,000 cells·mL⁻¹. To each transfection tube, 30 foam scaffolds were added. To perform vacuum-assisted seeding, a 1-mL syringe with a 16 G needle tip was attached to house vacuum. Air from each transfection tube was evacuated by pulling house vacuum for 30 s, three times. By evacuating air, the cell suspension was forced into the interconnected pores of the foams, improving cell seeding into each foam scaffold. The scaffolds were incubated at 30 °C for 5 h allowing cells to attach to the scaffolds. During this seeding period, transfection tubes were lightly agitated every 30 min to keep cells in suspension. After 5 h, samples were placed in a 96-well plate and 230 µL of basal growth medium was added to each sample. Samples were incubated for 24 h at 30 °C.

After 24 h incubation at 30 °C, the basal growth medium was switched to osteogenic differentiation medium: BGJ_b medium (Life Technologies), 10 mM HEPES (Life Technologies), 10 mM β-glycerophosphate (Sigma-Aldrich), 1 nM dexamethasone (Sigma-Aldrich), 150 µM L-

ascorbic acid phosphate magnesium salt *n*-hydrate (Wako), 10% fetal bovine serum (Gibco), and 1% penicillin/streptomycin (Life Technologies). The osteogenic medium was changed every 2 d. After incubation at 30 °C for 5 d, foams were incubated at 37 °C, triggering expansion, for 23 d. Foams completely expanded within 24 h at 37 °C. Osteogenic specific characteristics were characterized at three time points: before triggering (30 °C for 5 d); 2 d post-triggering (37 °C 2 d); and 23 d post-triggering (37 °C 23 d). Three independent replicates consisting of cell expansion through the foam experiments were performed ($n = 3$).

6.3.6 Assessing Calcium Deposition

6.3.6.1 Xylenol Orange Staining

To detect calcium deposition, xylenol orange (XO) staining—a non-destructive staining method [24]—was used. XO powder (Sigma-Aldrich) was dissolved in deionized water and filtered to make a sterile stock solution of 20 mM and stored at 4 °C. The foams were cultured at the final concentration of 40 μ M XO in medium overnight before imaging. The XO-containing medium was replaced with fresh Hoechst-containing medium (0.1 mg/ml; Hoechst 33342, Life Technologies) 30 min before imaging to stain for cell nuclei. Fluorescent images of XO-stained foams were taken using a N3 filter cube and images of cell nuclei taken using an A4 filter cube using a Leica DMI 4000B inverted microscope.

6.3.6.2 Scanning Electron Microscopy[‡]

To qualitatively visualize mineral deposition, scanning electron microscopy (SEM) was performed using a JEOL JSM-5600 Scanning Electron Microscope. Foams were sputter-coated with gold prior to imaging. Representative images were taken to visualize foam architecture, cell

[‡] EDX scanning and analysis was performed with the help of Eric Oulette

coverage, and mineral deposition at the three different time points. Additionally, cell infiltration into the foams was assessed by imaging foam cross-sections of both *static* and *active* foams at the last time point. To confirm calcium deposition on the foams, energy-dispersive x-ray spectroscopy (EDS) was used.

6.3.6.3 Microcomputed Tomography

Three-dimensional analysis of mineral deposition was assessed using microcomputed tomography (Micro-CT 40; Scanco Medical). Foams were rinsed with PBS three times and fixed with 10% neutral buffered formalin overnight. Fixed foams were rinsed with deionized water before drying in an evacuated desiccator overnight. Dried foams were scanned at a nominal voxel size of 6 μm , and images were acquired at 55 kV, 144 μA , and with a 200 ms integration time. To determine mineral volume, a series of thresholds was applied to the reconstructed slices. First, a threshold of 40 (1/1000 units Scanco software) was applied to isolate foam+mineral and calculate the total volume. Next, a threshold of 70 was applied to determine if mineral could be isolated from the foam volume, as this threshold successfully isolated polymer from mineral in a separate SMP scaffold we explored [25]. However, this threshold was not high enough to completely isolate the mineral from the foam, so a threshold of 100 was used. The normalized mineral volume was calculated by dividing the mineral volume (V_{100}) by the foam+mineral volume (V_{40}). This ratio was compared between static and active foams from all three time points (n=3).

6.3.7 Alkaline Phosphatase Activity

To determine osteogenic protein expression, an alkaline phosphatase (ALP) colorimetric assay was performed using *p*-nitrophenyl phosphate (Sigma-Aldrich). Foams were prepared for

the assay by first rinsing three times with tris-buffered saline at room temperature. For each technical replicate, three foams were combined in a 1 mL Eppendorf tube and, and cells were lysed in 450 μ L of sterile deionized water. Three foams were combined for each technical replicate to increase cell number and ALP content. Cells were further lysed and homogenized by vigorous mixing using syringes with 20 G needles. Cell lysates were separated from the foams by centrifuging through nylon filters (Spin-X centrifuge filter tube, Costar). 50 μ L of cell lysates were added in three separate wells of a 96-well plate and reacted with 150 μ L of *p*-nitrophenyl phosphate (Sigma-Aldrich) at 37 °C for 1 h. The reaction was stopped by adding 50 μ L 3 N NaOH to each well. The absorbance was read at 405 nm in a plate reader (Synergy 2, BioTek). ALP concentration was determined using 4-nitrophenol solution (Sigma-Aldrich) and normalized by DNA content (PicoGreen dsDNA assay, Life Technologies).

6.3.8 Real-Time Polymerase Chain Reaction (qPCR)[‡]

To determine osteogenic gene expression, real-time qPCR was performed. Total RNA extraction and cDNA analysis were conducted prior to running qPCR. Real-time qPCR was performed in quadruplicate with 100 ng of cDNA in 20 μ L reaction volume containing Power SYBR Green Master Mix (Invitrogen) and primers (RealTimePrimers) on Mastercycler ep realplex (Eppendorf).

6.3.8.1 Total RNA Extraction and cDNA Analysis

To allow quantitative comparison of markers of osteogenic lineage, total RNA was extracted from cells seeded in foam scaffolds at the end of each time point. Foams were rinsed three times with sterile PBS and frozen at –80 °C. Total RNA was extracted using RNeasy Micro

[‡] All qPCR protocols, experiments, and analyses were developed and performed by Jing Wang

Kit (QIAGEN) per the manufacturer's instructions. Total RNA was then used for reverse-transcription reaction to synthesize cDNA using the QuantiTect Reverse Transcription Kit (QIAGEN). RNA and cDNA quantity were assessed by absorbance readings at 260 nm using spectrophotometry. Absorbance reading ratios of 260/280 and 230/280 were greater than 1.8, indicating a high purity of RNA and cDNA. For each replicate, nine foams were combined to increase cell number.

6.3.8.2 Determining Best Housekeeper Gene for qPCR

To determine the best housekeeping genes for foam scaffolds, ten housekeeping genes (ACTB, B2M, GAPD, GUSB, HPRT1, PGK, PP1A, RPL13A, TBP, TFRC; purchased from realtimeprimer.com) were tested on cells seeded in *static* and *active* scaffolds. Raw qPCR data was processed by LinRegPCR [26]. The resulting primer efficiencies and Ct values were used as inputs in Bestkeeper [27] to find the most stable housekeeping gene for the foam scaffolds. The most stable housekeeping gene (B2M) was used as the reference gene in the subsequent qPCR reactions.

6.3.8.3 qPCR Procedure

To examine osteogenic differentiation, characteristic gene expression of Runx2 and osteocalcin (OC) were examined and normalized to the reference gene B2M ($n = 3$). Gene expression fold change was calculated as the expression level normalized to the static control group at the first time point, using the Pfaffl method [28]. Since results were normalized to the static control group, a fold change higher than 1 indicates gene up-regulation, while a fold change lower than 1 indicates gene down-regulation.

6.3.9 Histology

To visualize mineral deposition in each foam, histological analysis was performed using Alizarin Red staining. Foams were first rinsed with PBS three times and fixed with 10% neutral buffered formalin overnight. Next, foams were stained with 2% Alizarin red with pH adjusted to 4.2 for 30 s ($n = 3$). Stained whole samples were extensively rinsed with deionized water. Only samples at the last time point (37 °C for 23 d) were collected for staining.

6.3.10 Statistics

Statistical analyses were performed on the ALP, qPCR, and microcomputed tomography results to compare *static* and *active* groups, as well as to compare between time points within each group. Paired t-tests were performed using the Data Analysis Package in Excel (Microsoft Office 2013). Holms-Sidak correction was applied to correct for multiple comparisons (3 comparisons). Significance was determined at the 95% confidence level.

6.4 Results

6.4.1 Scaffold Architecture Reorganization

Foam scaffolds with a composition of 98tBA-2BA were prepared via a modified porogen-leaching method. TGA analysis confirmed that salt extraction was complete (**Figure 6-1a**) which is consistent with results from **Chapter 5** using the same material system. Increasing the composition to 98tBA-2BA resulted in a foam with a higher T_g than the 92tBA-8BA foams fabricated in **Chapter 5**. Here, a T_g of 43 °C in the hydrated state was achieved (**Figure 6-1b**).

The ability of programmed foams to maintain their fixed shape at 30 °C and recover to their permanent shape at 37 °C was determined under simulated cell culture conditions (**Figure**

6-2). Programmed foams initially recovered 13% of the programmed strain following sterilization (prior to cell culture), a limitation of the RPSM programming method. We speculate this is due to a combination of programming the foam below its glass transition temperature and exposing the foam to a humid environment during sterilization. Foams programmed with a compressive strain remained stable at 30 °C, as only 5% of the programmed strain was recovered over the 5 d period (**Figure 6-2**). Upon triggering recovery at 37 °C, the foam scaffold completely recovered within 24 h. SEM micrograph insets show a collapsed pore morphology following programming that remains stable after 5 d in 30 °C PBS (**Figure 6-2**); pore morphology opened following triggering at 37 °C. Programmed pore architecture change was further confirmed by microcomputed tomography 3D reconstructions of *active* and *static* foam scaffold cross-sections (**Figure-6-3**). Prior to triggering pore morphology change, *active* scaffolds had a collapsed pore structure; within 2 d of triggering at 37 °C, pore architecture opened and resembled the cuboidal pore morphology of the *static* control scaffolds.

6.4.2 Cell Seeding in Programmed Scaffolds

A vacuum-assisted seeding approach was employed to seed cells into foam scaffolds at a concentration of 500,000 cells-mL⁻¹. Hoechst nuclear dye revealed cells attached to the pores of the scaffolds and proliferated over time (**Figure 6-4**). Cells seeded in both *active* and *static* scaffolds had comparable cell densities before and after triggering architecture change. Cell densities before transition (5 d at 30 °C) and 2 d following transition (2 d at 37 °C) were comparable between both groups, and cells appeared to cover the scaffold pores (**Figure 6-4, left and middle**). After 4 weeks of total culture (5 d at 30 °C + 23 d at 37 °C), cell density had significantly increased for both groups and a confluent cell layer had covered the scaffolds, spanning across the pores (**Figure 6-4, right**). SEM micrographs of the scaffold surface (**Figure**

6-5, top) and scaffold cross-sections (**Figure 6-5, middle and bottom**) after 4 weeks of culture confirmed that cells had proliferated to form a cell sheet covering the scaffold and showed that cells had infiltrated into the interior pores of the scaffolds for both *active* and *static* groups. Cell sheets were observed to be well-adhered to the interior pore walls and had penetrated to the center of the scaffolds. This suggests pore interconnectivity was sufficient for cell infiltration and nutrient diffusion.

6.4.3 Mineral Formation

To detect mineralized nodule formation on the foam scaffolds, XO staining, SEM analysis and microcomputed tomography analyses were performed.

6.4.3.1 Xylenol Orange (XO) Analysis

XO staining revealed that mineral deposition was qualitatively comparable between *active* and *static* control samples across all time points (**Figure 6-6a**). No detectable mineral deposition was observed on scaffolds before triggering architecture change (5 d at 30 °C). After triggering at 37 °C for 2 d, a few small mineralized nodules were detected on *active* and *static* foam scaffolds (black arrows). After 23 d at 37 °C, a significant increase in the size and number of mineralized nodules was detected, with no observable different between *active* and *static* groups. To determine if the mineralized nodules were a result of precipitation from the osteogenic induction medium onto the surface of the foam scaffolds or a result of deposition by attached cells, control samples containing no cells were cultured under the same conditions and stained with XO. After 4 weeks, results from 3 different samples showed that no significant mineral deposition occurred on the scaffolds (**Figure 6-6b**), suggesting that the mineralized

nodules observed on cell-containing scaffolds were not due to spontaneous mineral precipitation from the medium but instead due to deposition by the attached cells.

6.4.3.2 Scanning Electron Microscopy (SEM) Analysis

SEM analysis was employed to qualitatively compare mineral deposition between *active* and *static* foam scaffolds. Before triggering architecture change (5 d at 30 °C) and 2 d after triggering (2 d at 37 °C) no significant mineral deposition was found on active or static foam scaffolds (**Figure 6-7**). After 23 d at 37 °C, scaffolds were covered in mineralized nodules (white specks in the SEM micrographs) for both groups. No qualitative differences were observed between *active* and *static* scaffolds across all time points. To determine if the mineralized nodules were a type of calcium phosphate, EDS was performed in conjunction with SEM, and the composition of a mineralized nodule and of the cell sheet were investigated (**Figure 6-8a**). EDS analysis of the mineral nodule showed strong phosphorous and calcium peaks in the resulting spectrum (**Figure 6-8b**). Similarly, when exploring a large area of a cell sheet, large phosphorous and calcium peaks are present, indicating calcified nodules deposited by adherent cells. A large gold peak is present due to the gold coating during sample preparation for SEM.

6.4.3.3 Microcomputed Tomography Analysis

Microcomputed tomography was performed to qualitatively and quantitatively compare mineral deposition on *active* and *static* foam scaffolds. To determine the amount of mineral deposition on each scaffold, a series of three thresholds was applied, and the resulting 3D reconstructions and material volumes compared (**Figure 6-9**). When applying a threshold of 40 (1/1000 units from Scanco Software), both scaffold and material were included (**Figure 6-9, top**). Increasing the threshold to 70 resulted in partial scaffold loss, but was unable to completely

isolate the mineral (**Figure 6-9, middle**). Upon increasing the threshold to 100, mineral was completely isolated from scaffold, and an increase in mineral deposition was found after 4 weeks of culture (**Figure 6-9, bottom**).

Comparison of active and static scaffolds over 4 weeks revealed no significant difference between the two groups (**Figure 6-10** and **Table 6-1**). For both groups, a trend of increased mineral deposition over time was qualitatively observed (**Figure 6-10**), with minimal mineral deposition before transition and 2 d after transition and significant mineral deposition 23 d after transition. This trend was seen consistently with all samples from two independent replicates. However, with a third independent replicate inconsistent results were found (**Table 6-1, Replicate 1**); a large amount of mineral deposition was observed before transition, however minimal deposition was observed after 4 weeks. Further inspection of these samples using SEM revealed that a cell sheet had formed on these scaffolds during the initial seeding period (**Figure 6-11, top**). Furthermore, large mineral deposits were confirmed with SEM (**Figure 6-11, bottom**). Based on the SEM, we speculate the inconsistent microcomputed tomography results are attributed to inconsistencies with cell seeding for this independent replicate. Due to this variability and the small sample size, a statistically significant difference in mineral deposition over time was not achieved.

6.4.4 Protein Expression

Protein expression was assessed by performing an ALP calorimetric assay. ALP is an early marker for osteogenic differentiation and plays an important role in mineral nodule formation, which is a functional indication of osteogenic differentiation [29]. Quantitative analysis of ALP activity showed no difference between *active* and *static* foams across all time points (**Figure 6-12**). With the exception of one replicate from the before transition *static* group,

a trend of increased ALP expression after the transition was observed, albeit not statistically significant.

6.4.5 Gene Expression

Real-time PCR was employed to examine gene expression of osteogenic differentiation markers Runx2 and osteocalcin (OC) for *active* and *static* foam scaffolds at all three time points. When normalizing to the static group before transition (5 d at 30 °C), a trend of upregulation of Runx2 was observed over time for both groups, with fold changes upwards of 10 found after 4 weeks of culture (**Figure 6-13a**). Although the fold changes for active and static scaffolds were higher at 4 weeks compared to before the transition, results were not statistically significant due to large variability between replicates. Upregulation of Runx2 over time suggests that hASCs differentiated toward an osteogenic lineage over time. Inspection of OC, a late osteogenic marker, revealed that OC expression decreased after 4 weeks for both *active* and *static* groups, although not statistically significant (**Figure 6-13b**). This result was unexpected, as OC expression typically increases over time as it is a later stage indicator of osteogenesis [30]. For both Runx2 and OC, no difference was found between *active* and *static* scaffolds across all time points.

6.4.6 Histology

Calcium deposition was further qualitatively assessed by performing Alizarin Red staining on *active* and *static* scaffolds following 4 weeks of culture. Alizarin Red staining confirmed that calcium deposition was achieved on both active and static scaffolds (**Figure 6-13**), as shown by multiple samples staining positive (red). No observable difference was found between the two groups. To determine if calcium deposition was attributed to precipitation from

medium, control scaffolds with no cells were cultured under the same conditions for 4 weeks and stained with Alizarin Red (**Figure 6-13**). The control sample did not stain positive, suggesting calcium deposition was a result of adherent cells on the *active* and *static* scaffolds. These results agree with the XO, SEM, and microcomputed tomography results discussed above.

6.5 Discussion

In this chapter, we have demonstrated osteogenic differentiation of human adipose-derived stem cells when cultured in 3D porous SMP foam scaffolds following dynamic changes in architecture. SMP foams were programmed to change from a collapsed pore architecture to an open pore architecture with attached and viable cells. Gratifyingly, changes in pore architecture did not inhibit osteogenic differentiation of adherent stem cells, as indicated by comparable levels of mineral deposition, protein expression, and gene expression between *active* and *static* scaffolds.

SMP foam scaffolds maintained a stable temporary state and supported cell growth and attachment. Programmed scaffolds had minimal recovery when cultured at 30 °C for 5 d (**Figure 6-2**), and cells readily attached and proliferated in the scaffold (**Figure 6-4**). Interestingly, scaffolds recovered 13% of the programmed deformation following sterilization (**Figure 6-2**). We attribute this to the mode of strain fixing for this study, which relied on fixing of inelastic deformation by deforming the sample below its thermal transition temperature [22, 31], as compared to the traditional approach of deforming above the thermal transition temperature followed by subsequent cooling. While an initial recovery occurred during sterilization, samples remained stable upon culture at 30 °C for 5 d, demonstrating the effectiveness of this fixing approach. Additionally, complete recovery of the scaffolds was achieved within 24 h of triggering using a cytocompatible triggering temperature of 37 °C (**Figure 6-2**). We found that

triggering deployment of the foam scaffolds did not inhibit osteogenic differentiation capacity of adherent stem cells, as was observed through comparable levels of protein expression (**Figure 6-12**), gene expression (**Figure 6-13**), and mineral deposition (**Figures 6-6, 6-7, 6-10, and 6-13**) between *active* and *static* scaffolds. This shows promise for employing SMP foam scaffolds as deployable cell-based therapies, where a stable temporary shape is required long-term for cell attachment and growth and body temperature triggering could be used to deploy the scaffold without affecting the differentiation capacity of the attached cells.

While previous studies have demonstrated that SMP scaffolds can support bone repair using terminally differentiated osteoblasts [18, 19] or bone marrow stem cells [20], this study is the first to report osteogenic differentiation following SMP shape change. Four separate assays confirmed functional osteogenic differentiation of stem cells through calcium deposition following 4 weeks of culture. SEM micrographs revealed by 4 weeks cells had formed sheets spanning the pores of both active and static scaffolds, with significant cell infiltration (**Figure 6-5**). Inspection of the surface of the cell sheets showed significant mineral deposition (**Figure 6-7**) which EDS confirmed was calcium phosphate (**Figure 6-8**). EDS spectra of the mineral nodule and of the cell sheet were comparable to a reported EDS spectrum of mineral deposition from mesenchymal stem cells that had committed down an osteogenic lineage [32]. The presence of calcium and phosphate is promising, and a more detailed study into the composition of the mineralized nodules, particularly the Ca:P ratio, could reveal more information about the type of calcium phosphate (e.g. amorphous, carbonate hydroxyapatite, etc.) present [33]. Quantitative analysis of mineralized nodule formation from microcomputed tomography also showed calcium deposition for both active and static scaffolds following 4 week culture, with the exception of one independent replicated (**Figure 6-10** and **Table 6-1**). We hypothesize this may be due to

inconsistencies in the initial cell seeding density, where cell sheets had formed early on for the independent replicate with inconsistent mineral deposition. Previous studies have reported that osteogenic differentiation of stem cells is affected by cell density [34-36]. In a report by Kim et al, higher cell seeding density on poly(propylene fumarate) disks resulted in more mineral deposition within 8 d of culture, and it was suggested that late stage osteogenic differentiation could be enhanced by higher cell seeding density, while cell proliferation and early osteogenic differentiation could be stimulated by lower cell seeding density [35]. Although we observed these inconsistencies, a trend of mineralized nodule formation after 4 weeks was found, indicating functional osteogenic differentiation of hASCs was achieved in SMP scaffolds, and no differences were found between *active* and *static* scaffolds.

In addition to observing no difference in mineral deposition between *active* and *static* scaffolds, we also found no difference in protein expression or gene expression levels between the two groups (**Figure 6-12** and **Figure 6-13**), indicating scaffold architecture change did not elicit a negative response. Inspection of ALP protein expression for *active* and *static* groups revealed no significant change over time, although a slight increase after transition compared to before transition was observed (**Figure 6-12**). While we expected an increase in ALP protein expression over time, we attribute the lack of an increase to the use of fetal bovine serum (FBS) in the induction medium, which has been reported to result in low ALP protein expression in hASCs tested with several different osteogenic induction media [37]. Future studies could use human-serum as a replacement for FBS, as human-serum resulted in a significant increase of ALP protein expression [37]. A trend of increased expression of Runx2—an essential transcription factor in osteoblast differentiation [38, 39]—at 4 weeks was observed, suggesting an increase in osteogenic differentiation (**Figure 6-13a**). We expected a similar trend for

osteocalcin—a late stage marker for osteogenic differentiation—however osteocalcin expression was lower at 4 weeks compared to 5 d at 30 °C (**Figure 6-13b**). We speculate this is attributed to the combination of hASCs and the osteogenic induction medium used in this study. In a study comparing different serum conditions on the osteogenic differentiation of hASCs, all serum conditions were reported to have only modest expression levels of osteocalcin, with no increase in expression observed over time [37]. Serum conditions explored in this study used the same induction components (ascorbic acid, dexamethasone, and beta-glycerophosphate) and similar concentrations for each with the exception of dexamethasone. Furthermore, other studies have also reported unexpected osteocalcin expression during osteogenic differentiation of adipose-derive stem cells, with a significant drop in expression after 7 d of culture in induction medium and only a modest increase between 7 and 14 d [40]. Nonetheless, these results combined with the mineral deposition results indicate that the SMP 3D scaffold is capable of supporting not only cell attachment and proliferation, but also stem cell differentiation capacity, which are essential for tissue engineering applications of SMPs.

The SMP foam scaffold reported here also shows promise as a 3D platform to study the cell mechanobiological response to dynamic changes *in vitro*. As discussed in detail in **Chapter 1**, SMPs are a promising technology for studying cell-material interactions in dynamic *in vitro* environments (termed *Active Cell Culture*), and most studies to date have been limited to 2D [41-43]. The tBA-BA system used in this study was previously employed as a dynamic 2D substrate to study cell-material interactions [44, 45], as detailed in **Chapters 2-3**. Recent efforts have now focused on expanding this work to 3D scaffolds which more closely mimic the 3D environment cells experience *in vivo*. To-date, our group has reported the only 3D SMP scaffold for application in *Active Cell Culture*, where an SMP fiber mat was applied [46]. The SMP fiber

mat, however, would be difficult to adapt to applications requiring large volumes. Furthermore, a fibrous architecture may not be suitable for tissue engineering applications such as bone tissue engineering. The SMP foam scaffold presented here can serve as a new *Active Cell Culture* 3D scaffold with a pore morphology different in size and shape compared to the fibrous SMP web. The large cuboidal pores also serve as a more functional morphology for bone tissue engineering applications. Potential for *Active Cell Culture* was demonstrated by the scaffold's ability to maintain a programmed shape with attached and viable cells for 5 d at 30 °C, and to subsequently expand within 24 h upon heating to 37 °C (**Figure 6-2**). Here we have also demonstrated stem cell attachment, proliferation, and differentiation are supported in the SMP foam scaffold. As a natural extension of this work, expanding foam scaffolds could be investigated to determine if pore expansion can be used as a biologically-relevant stimulus to induce differentiation in the absence of, or in combination with, induction medium. Supporting this concept, recent work on topography changing 2D substrates has demonstrated that SMP actuated topography change can be used to direct stem cell lineage commitment [47].

6.6 Conclusion

We have demonstrated osteogenic differentiation of adipose-derived stem cells in programmable SMP foam scaffolds following dynamic changes in scaffold architecture with attached and viable cells. Foam scaffolds transitioned from a temporarily collapsed-pore architecture to a permanently open-pore architecture upon shape memory actuated expansion at 37 °C. Stem cells seeded in *active* scaffolds—scaffolds that underwent programmed architecture change—expressed comparable levels of osteogenic characteristics to stem cells seeded in *static* control scaffolds, as indicated by osteogenic gene expression, ALP protein expression, and mineral deposition. These findings suggest that programmable SMP scaffolds have the potential

to be explored as deployable cell-based therapies to facilitate bone repair. Additionally, the cytocompatible programmed shape change suits these SMP foams well for use as *Active Cell Culture* 3D scaffolds.

6.7 References

- [1] O'Keefe RJ, Mao J. Bone Tissue Engineering and Regeneration: From Discovery to the Clinic-An Overview Introduction. Tissue Engineering Part B-Reviews. 2011;17.
- [2] Van der Stok J, Van Lieshout EM, El-Massoudi Y, Van Kralingen GH, Patka P. Bone substitutes in the Netherlands—a systematic literature review. Acta biomaterialia. 2011;7:739-50.
- [3] Giannoudis PV, Dinopoulos H, Tsiridis E. Bone substitutes: an update. Injury. 2005;36:S20-S7.
- [4] Lin L, Chow KL, Leng Y. Study of hydroxyapatite osteoinductivity with an osteogenic differentiation of mesenchymal stem cells. Journal of Biomedical Materials Research Part A. 2009;89:326-35.
- [5] Ripamonti U, Crooks J, Khoali L, Roden L. The induction of bone formation by coral-derived calcium carbonate/hydroxyapatite constructs. Biomaterials. 2009;30:1428-39.
- [6] Yuan H, De Bruijn J, Li Y, Feng J, Yang Z, De Groot K, et al. Bone formation induced by calcium phosphate ceramics in soft tissue of dogs: a comparative study between porous α -TCP and β -TCP. Journal of materials science: materials in medicine. 2001;12:7-13.
- [7] Yuan H, Yang Z, de Bruijn JD, de Groot K, Zhang X. Material-dependent bone induction by calcium phosphate ceramics: a 2.5-year study in dog. Biomaterials. 2001;22:2617-23.
- [8] Li C, Vepari C, Jin HJ, Kim HJ, Kaplan DL. Electrospun silk-BMP-2 scaffolds for bone tissue engineering. Biomaterials. 2006;27:3115-24.

- [9] Oest ME, Dupont KM, Kong HJ, Mooney DJ, Guldberg RE. Quantitative assessment of scaffold and growth factor-mediated repair of critically sized bone defects. *Journal of orthopaedic research*. 2007;25:941-50.
- [10] Wozney JM. The bone morphogenetic protein family and osteogenesis. *Molecular reproduction and development*. 1992;32:160-7.
- [11] Rosset P, Deschaseaux F, Layrolle P. Cell therapy for bone repair. *Orthopaedics & Traumatology: Surgery & Research*. 2014;100:S107-S12.
- [12] Ciapetti G, Granchi D, Baldini N. The combined use of mesenchymal stromal cells and scaffolds for bone repair. *Current pharmaceutical design*. 2011;18:1796-820.
- [13] Bruder SP, Kurth AA, Shea M, Hayes WC. Bone regeneration by implantation of purified, culture-expanded human mesenchymal stem cells. *Journal of Orthopaedic Research*. 1998;16:155.
- [14] Petite H, Viateau V, Bensaid W, Meunier A, de Pollak C, Bourguignon M, et al. Tissue-engineered bone regeneration. *Nature biotechnology*. 2000;18:959-63.
- [15] Manassero M, Viateau V, Deschepper M, Oudina K, Logeart-Avramoglou D, Petite H, et al. Bone regeneration in sheep using acropora coral, a natural resorbable scaffold, and autologous mesenchymal stem cells. *Tissue Engineering Part A*. 2013;19:1554-63.
- [16] Kon E, Muraglia A, Corsi A, Bianco P, Marcacci M, Martin I, et al. Autologous bone marrow stromal cells loaded onto porous hydroxyapatite ceramic accelerate bone repair in critical-size defects of sheep long bones. *Journal of biomedical materials research*. 2000;49:328-37.

- [17] Quarto R, Mastrogiacomo M, Cancedda R, Kutepov SM, Mukhachev V, Lavroukov A, et al. Repair of large bone defects with the use of autologous bone marrow stromal cells. *New England Journal of Medicine*. 2001;344:385-6.
- [18] Bao M, Lou X, Zhou Q, Dong W, Yuan H, Zhang Y. Electrospun biomimetic fibrous scaffold from shape memory polymer of PDLA-co-TMC for bone tissue engineering. *ACS applied materials & interfaces*. 2014;6:2611-21.
- [19] Zhang D, George OJ, Petersen KM, Jimenez-Vergara AC, Hahn MS, Grunlan MA. A bioactive “self-fitting” shape memory polymer scaffold with potential to treat cranio-maxillo facial bone defects. *Acta biomaterialia*. 2014;10:4597-605.
- [20] Liu X, Zhao K, Gong T, Song J, Bao C, Luo E, et al. Delivery of growth factors using a smart porous nanocomposite scaffold to repair a mandibular bone defect. *Biomacromolecules*. 2014;15:1019-30.
- [21] Rychter P, Pamula E, Orchel A, Posadowska U, Krok-Borkowicz M, Kaps A, et al. Scaffolds with shape memory behavior for the treatment of large bone defects. *J Biomed Mater Res A*. 2015.
- [22] Rodriguez ED, Luo X, Mather PT. Linear/network poly (ϵ -caprolactone) blends exhibiting shape memory assisted self-healing (SMASH). *ACS applied materials & interfaces*. 2011;3:152-61.
- [23] Yoon E, Dhar S, Chun DE, Gharibjanian NA, Evans GR. In vivo osteogenic potential of human adipose-derived stem cells/poly lactide-co-glycolic acid constructs for bone regeneration in a rat critical-sized calvarial defect model. *Tissue Eng*. 2007;13:619-27.

- [24] Kuhn LT, Liu Y, Advincula M, Wang YH, Maye P, Goldberg AJ. A nondestructive method for evaluating in vitro osteoblast differentiation on biomaterials using osteoblast-specific fluorescence. *Tissue engineering Part C, Methods*. 2010;16:1357-66.
- [25] Tseng LF. *Shape Memory Electrospun Scaffolds for Cell Mechanobiology and Bone Regenerative Applications*: Syracuse University; 2015.
- [26] Ramakers C, Ruijter JM, Deprez RHL, Moorman AFM. Assumption-free analysis of quantitative real-time polymerase chain reaction (PCR) data. *Neuroscience Letters*. 2003;339:62-6.
- [27] Pfaffl M, Tichopad A, Prgomet C, Neuvians T. Determination of stable housekeeping genes, differentially regulated target genes and sample integrity: BestKeeper – Excel-based tool using pair-wise correlations. *Biotechnology Letters*. 2004;26:509-15.
- [28] Pfaffl MW, Horgan GW, Dempfle L. Relative expression software tool (REST©) for group-wise comparison and statistical analysis of relative expression results in real-time PCR. *Nucleic acids research*. 2002;30:e36-e.
- [29] Hoemann CD, El-Gabalawy H, McKee MD. In vitro osteogenesis assays: influence of the primary cell source on alkaline phosphatase activity and mineralization. *Pathol Biol (Paris)*. 2009;57:318-23.
- [30] Liu Q, Cen L, Yin S, Chen L, Liu G, Chang J, et al. A comparative study of proliferation and osteogenic differentiation of adipose-derived stem cells on akermanite and β -TCP ceramics. *Biomaterials*. 2008;29:4792-9.
- [31] Gu X, Mather PT. Entanglement-based shape memory polyurethanes: Synthesis and characterization. *Polymer*. 2012;53:5924-34.

- [32] Thibault RA, Mikos AG, Kasper FK. Protein and mineral composition of osteogenic extracellular matrix constructs generated with a flow perfusion bioreactor. *Biomacromolecules*. 2011;12:4204-12.
- [33] LeGeros RZ. Calcium phosphate-based osteoinductive materials. *Chemical reviews*. 2008;108:4742-53.
- [34] Kim K, Dean D, Lu A, Mikos AG, Fisher JP. Early osteogenic signal expression of rat bone marrow stromal cells is influenced by both hydroxyapatite nanoparticle content and initial cell seeding density in biodegradable nanocomposite scaffolds. *Acta biomaterialia*. 2011;7:1249-64.
- [35] Kim K, Dean D, Mikos AG, Fisher JP. Effect of initial cell seeding density on early osteogenic signal expression of rat bone marrow stromal cells cultured on cross-linked poly (propylene fumarate) disks. *Biomacromolecules*. 2009;10:1810-7.
- [36] Zhou H, Weir MD, Xu HH. Effect of cell seeding density on proliferation and osteodifferentiation of umbilical cord stem cells on calcium phosphate cement-fiber scaffold. *Tissue Engineering Part A*. 2011;17:2603-13.
- [37] Kyllönen L, Haimi S, Mannerström B, Huhtala H, Rajala KM, Skottman H, et al. Effects of different serum conditions on osteogenic differentiation of human adipose stem cells in vitro. *Stem Cell Res Ther*. 2013;4:17.
- [38] Komori T, Yagi H, Nomura S, Yamaguchi A, Sasaki K, Deguchi K, et al. Targeted disruption of *Cbfa1* results in a complete lack of bone formation owing to maturational arrest of osteoblasts. *cell*. 1997;89:755-64.
- [39] Ducy P, Zhang R, Geoffroy V, Ridall AL, Karsenty G. *Osf2/Cbfa1*: a transcriptional activator of osteoblast differentiation. *cell*. 1997;89:747-54.

- [40] Shafiee A, Seyedjafari E, Soleimani M, Ahmadbeigi N, Dinarvand P, Ghaemi N. A comparison between osteogenic differentiation of human unrestricted somatic stem cells and mesenchymal stem cells from bone marrow and adipose tissue. *Biotechnology Letters*. 2011;33:1257-64.
- [41] Davis KA, Burke KA, Mather PT, Henderson JH. Dynamic cell behavior on shape memory polymer substrates. *Biomaterials*. 2011;32:2285-93.
- [42] Ebara M, Uto K, Idota N, Hoffman JM, Aoyagi T. Shape-Memory Surface with Dynamically Tunable Nano-Geometry Activated by Body Heat. *Advanced Materials*. 2012;24:273-8.
- [43] Le DM, Kulangara K, Adler AF, Leong KW, Ashby VS. Dynamic Topographical Control of Mesenchymal Stem Cells by Culture on Responsive Poly (ϵ -caprolactone) Surfaces. *Advanced Materials*. 2011;23:3278-83.
- [44] Yang P, Baker RM, Henderson JH, Mather PT. In vitro wrinkle formation via shape memory dynamically aligns adherent cells. *Soft Matter*. 2013;9:4705-14.
- [45] Baker RM, Brasch ME, Manning ML, Henderson JH. Automated, contour-based tracking and analysis of cell behaviour over long time scales in environments of varying complexity and cell density. *Journal of The Royal Society Interface*. 2014;11:20140386.
- [46] Tseng LF, Mather PT, Henderson JH. Shape-memory-actuated change in scaffold fiber alignment directs stem cell morphology. *Acta biomaterialia*. 2013;9:8790-801.
- [47] Gong T, Zhao K, Yang G, Li J, Chen H, Chen Y, et al. The control of mesenchymal stem cell differentiation using dynamically tunable surface microgrooves. *Advanced healthcare materials*. 2014;3:1608-19.

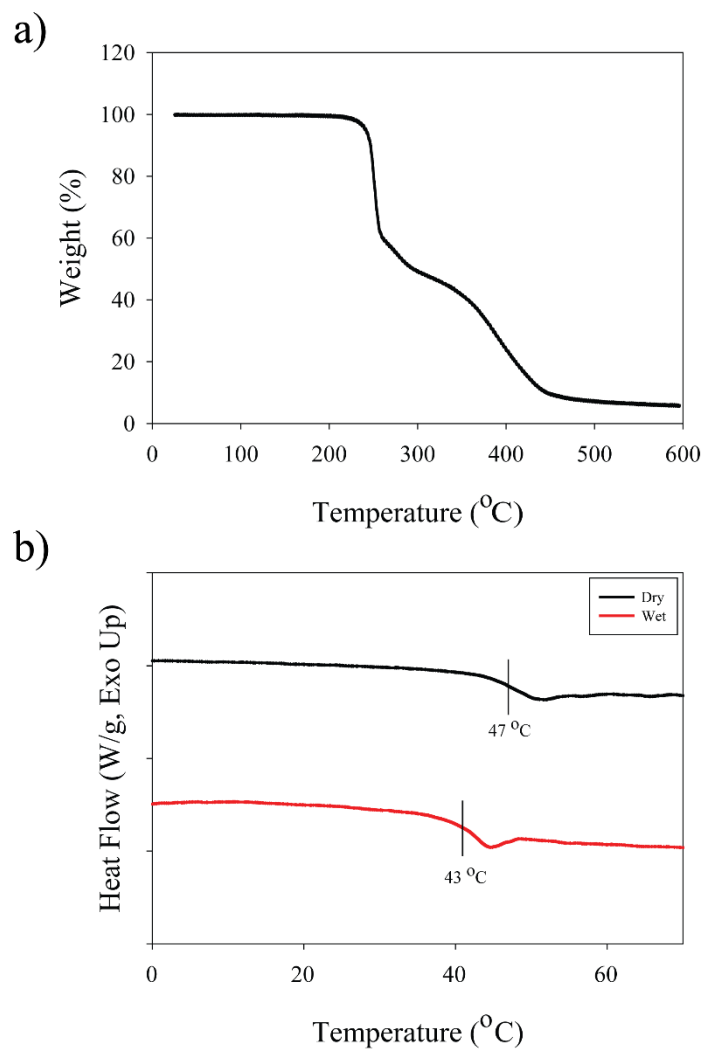


Figure 6-1. Thermal properties of 92tBA-8BA foam scaffolds. (a) TGA degradation profile indicates salt was extracted; (b) DSC 2nd heat traces show a dry T_g of 47 °C that drops to 43 °C upon hydration. Heating rate for TGA was 20 °C·min⁻¹; heating rate for DSC was 3 °C·min⁻¹.

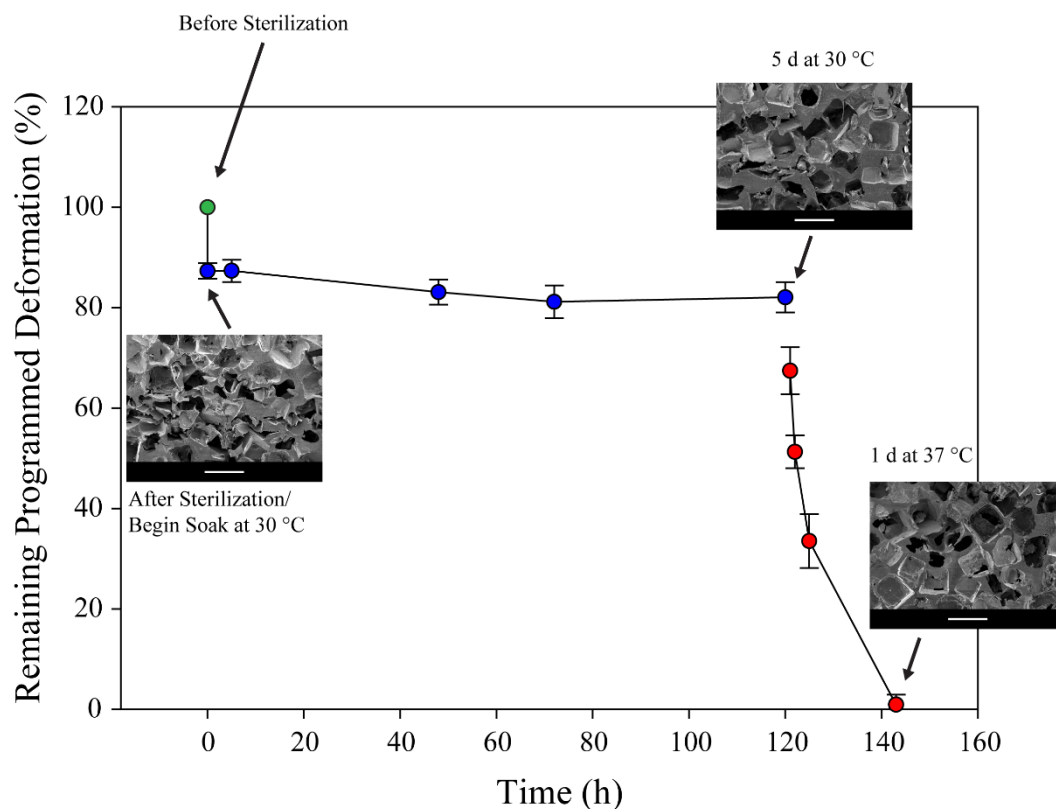


Figure 6-2. Shape recovery of 92tBA-8BA scaffolds under simulated *active cell culture* conditions. After sterilization, scaffolds initially recovered 13% of the programmed deformation (25% programmed uniaxial compressive strain). When cultured at 30 °C for 5 d (blue symbols) the scaffold remained stable in its programmed state; upon triggering recovery at 37 °C (red symbols), the scaffold recovers within 24 h. Inset scanning electron micrographs show the architecture remains collapsed during culture at 30 °C and restores its open cuboidal morphology after recovery. Scale bars are 500 μm .

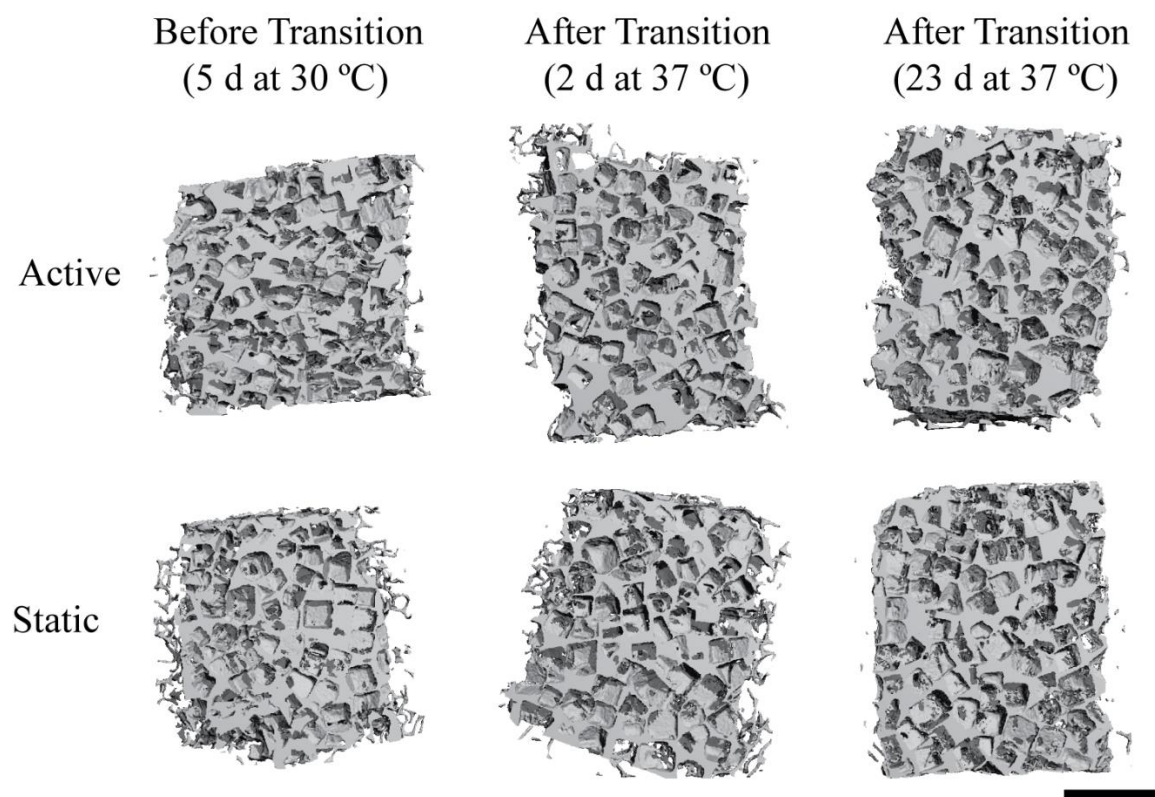


Figure 6-3. Reconstructed 3D microcomputed tomography of active and static cross-sections during culture. Before transition, *active* scaffolds have a collapsed pore architecture that is restored within the first 2 d after transition. *Static* scaffold pore morphology is open and cuboidal for all time points. Scale bare is 1 mm.

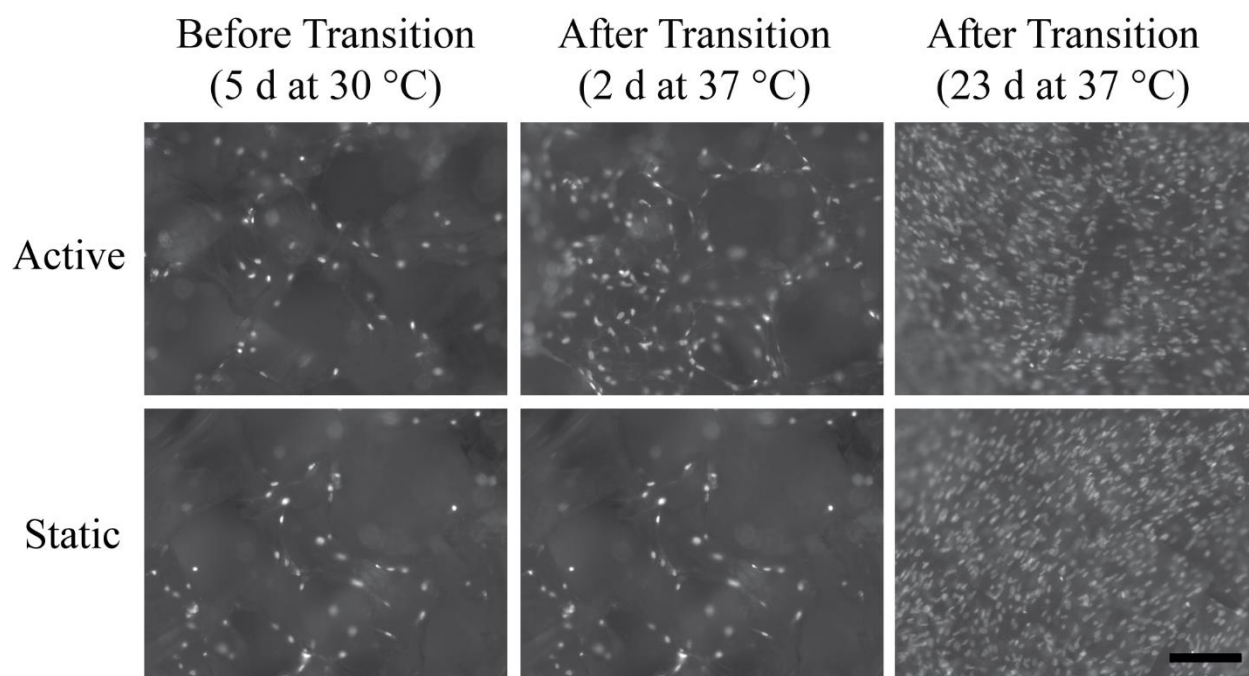


Figure 6-4. Hoechst nuclear staining for cells seeded in *active* and *static* foam scaffolds. Cell nuclear staining using Hoechst 33342 at three time points show cells attach and proliferate, with cell sheets forming on both *active* and *static* scaffolds after 4 weeks of culture. Cell densities for *active* and *static* foams were comparable. Scale bar is 200 μm .

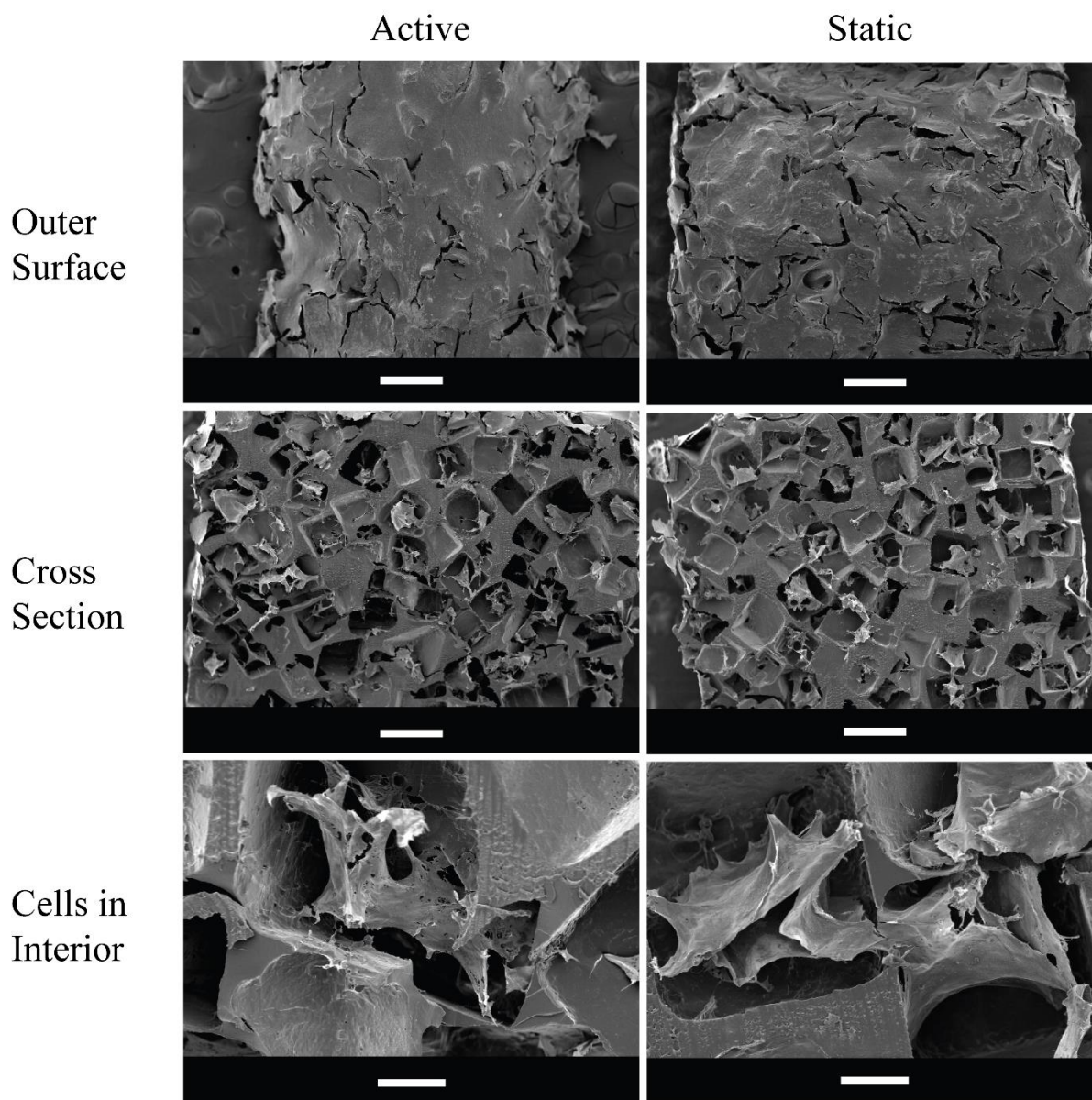


Figure 6-5. SEM micrographs of active and static foams following culture for 4 weeks. After 4 weeks of culture (5 d at 30 °C + 23 d at 37 °C) a cell sheet formed on the (top) outer surface of both active and static scaffolds; (middle) cross-section SEM micrographs reveal cell significant cell infiltration into the center of the scaffolds, which is further illustrated in (bottom) magnified SEM micrographs showing cells filling the interior pores. Scale bars are 500 μm for (top) and (middle), and 100 μm for (bottom).

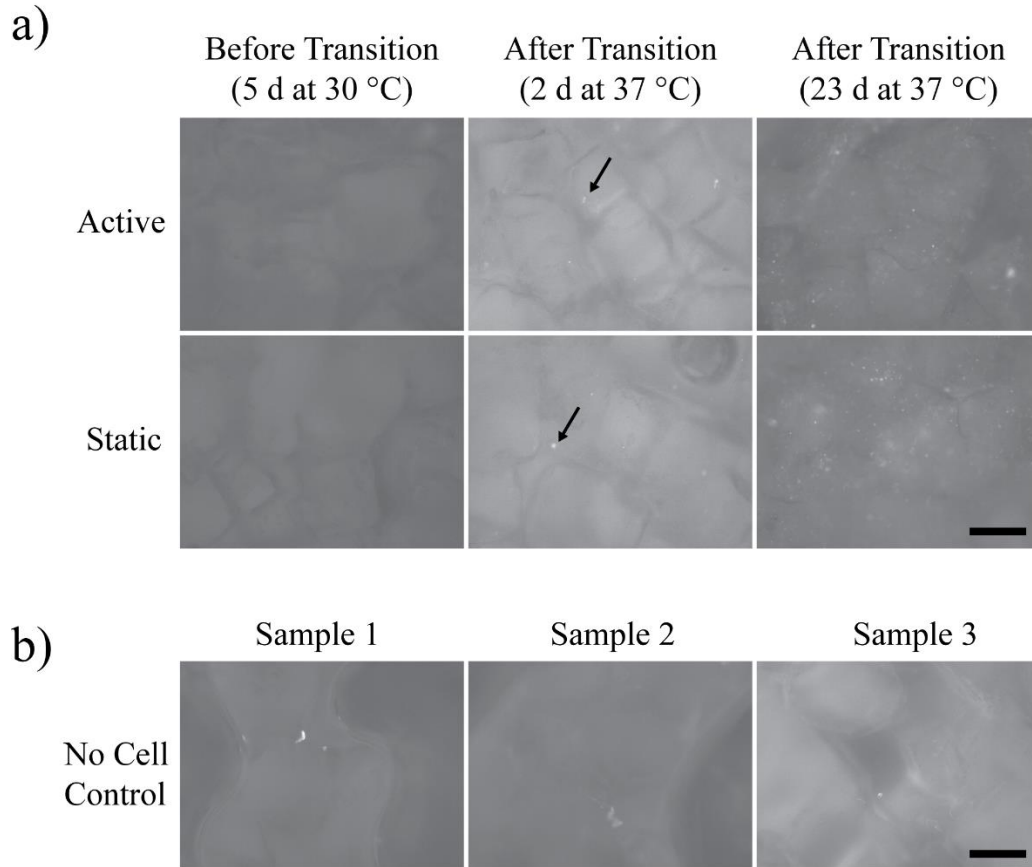


Figure 6-6. Xylenol orange (XO) staining for calcium deposition on *active* and *static* foam scaffolds. (a) for both *active* and *static* foam scaffolds, no calcium nodules were detectable before transition; following transition at 37 °C for 2 d small calcium nodules were detected (black arrows) but in limited quantity; after 23 d at 37 °C, a significant increase in the size and number of calcium nodules is detected, with no observable different between *active* and *static* groups. (b) Three empty control scaffolds (no cells) that were cultured under the same conditions as the active and static scaffolds show no calcium deposition after 4 weeks, indicating the calcium deposition observed in (a) was deposited by the adhered cells. Scale bars are 200 μ m. Histogram stretching was performed on the raw images to allow visualization of calcium nodules.

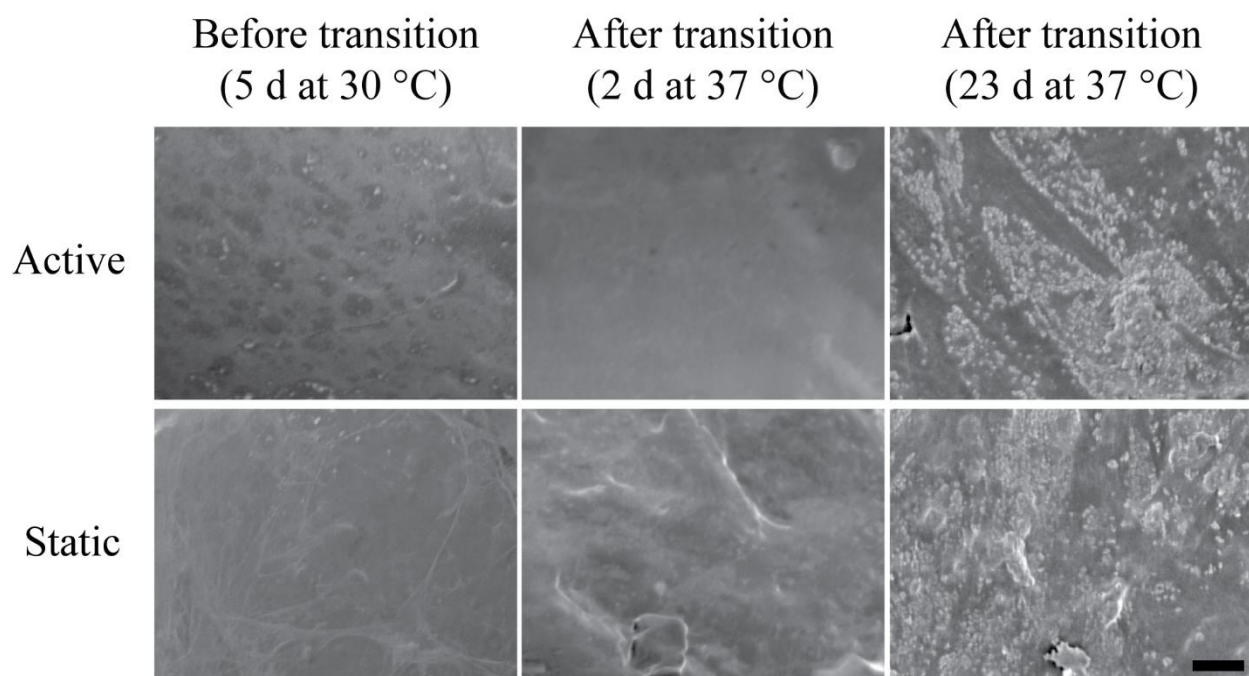


Figure 6-7. SEM micrographs of *active* and *static* foam scaffolds reveal mineral deposition. Before transition and 2 d after transition no significant mineral deposition was found on active or static foam scaffolds. After 23 d at 37 °C, scaffolds were covered in mineralized nodules (white specs) for both active and static scaffolds. Scale bar is 20 μ m.

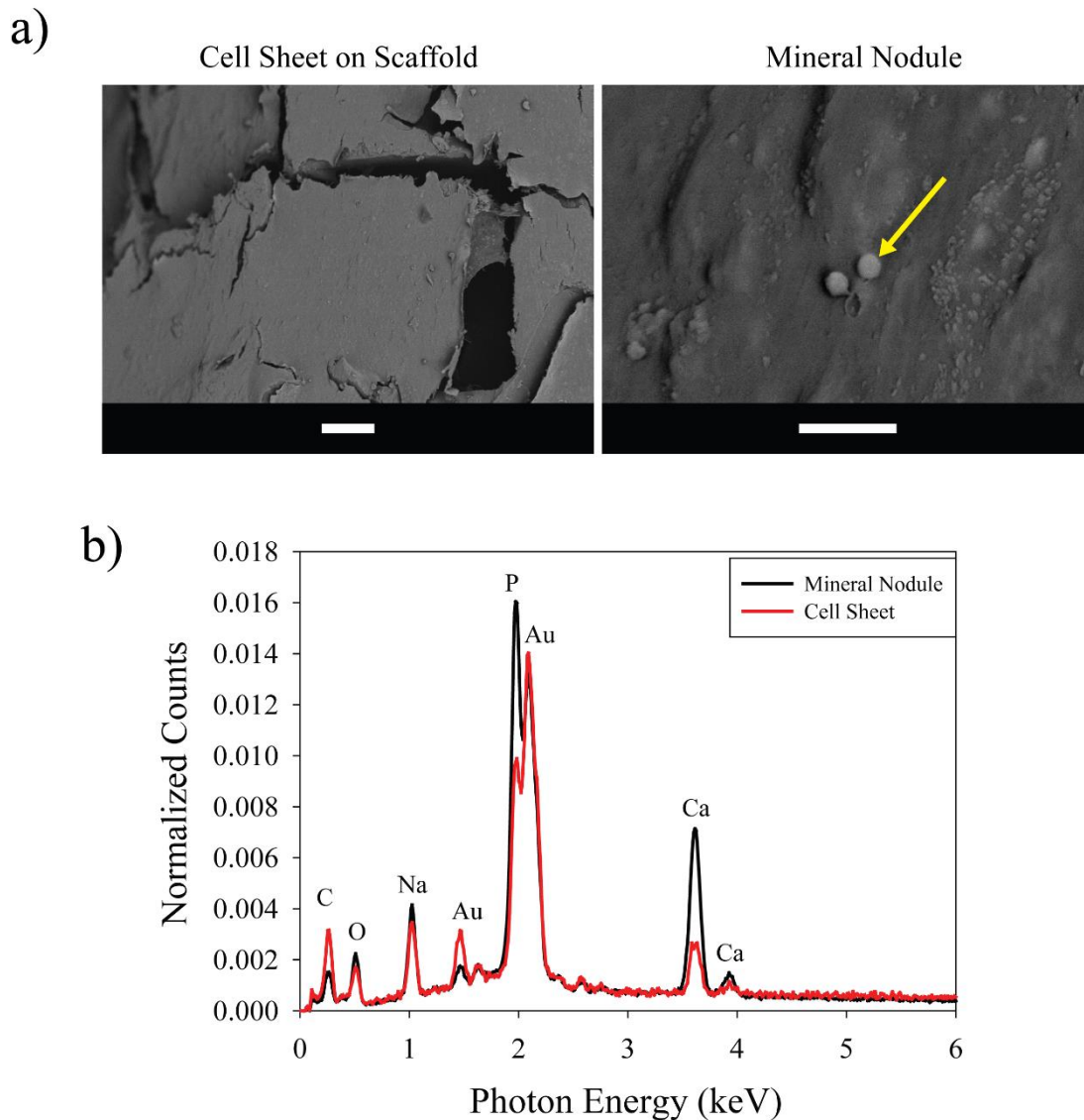


Figure 6-8. Energy dispersive spectroscopy (EDS) of mineral deposition shows minerals contain calcium. (a) SEM images from backscattered electrons of a cell sheet covering the foam scaffold and of a magnified view of a mineralized nodule. (b) EDS traces of the cell sheet and of the mineralized nodule show a significant amount of calcium and phosphorous. Scale bars in (a) are 100 μm for the cell sheet and 10 μm for the mineral nodule.

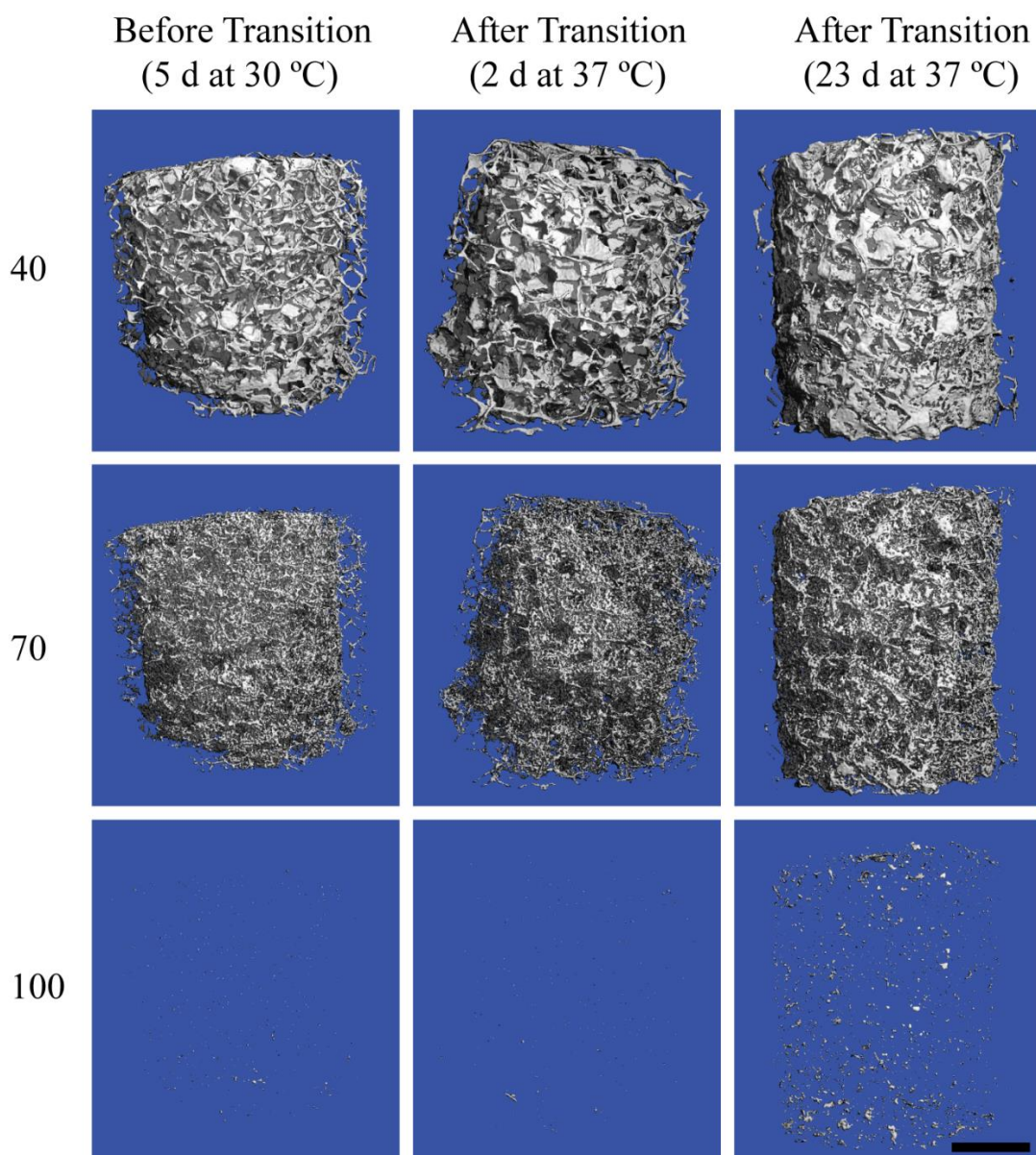


Figure 6-9. Microcomputed tomography 3D reconstructions when applying three different thresholds. With an applied threshold of (top) 40, both mineral and foam are included; for a threshold of (middle) 70, the foam is partially removed; for a threshold of (bottom) 100, the mineral is completely isolated from the foam. Using a threshold of 100, the progression of mineral deposition over time was observed. The foam scaffold shown in this figure is a *static* foam. Scale bar is 1 mm.

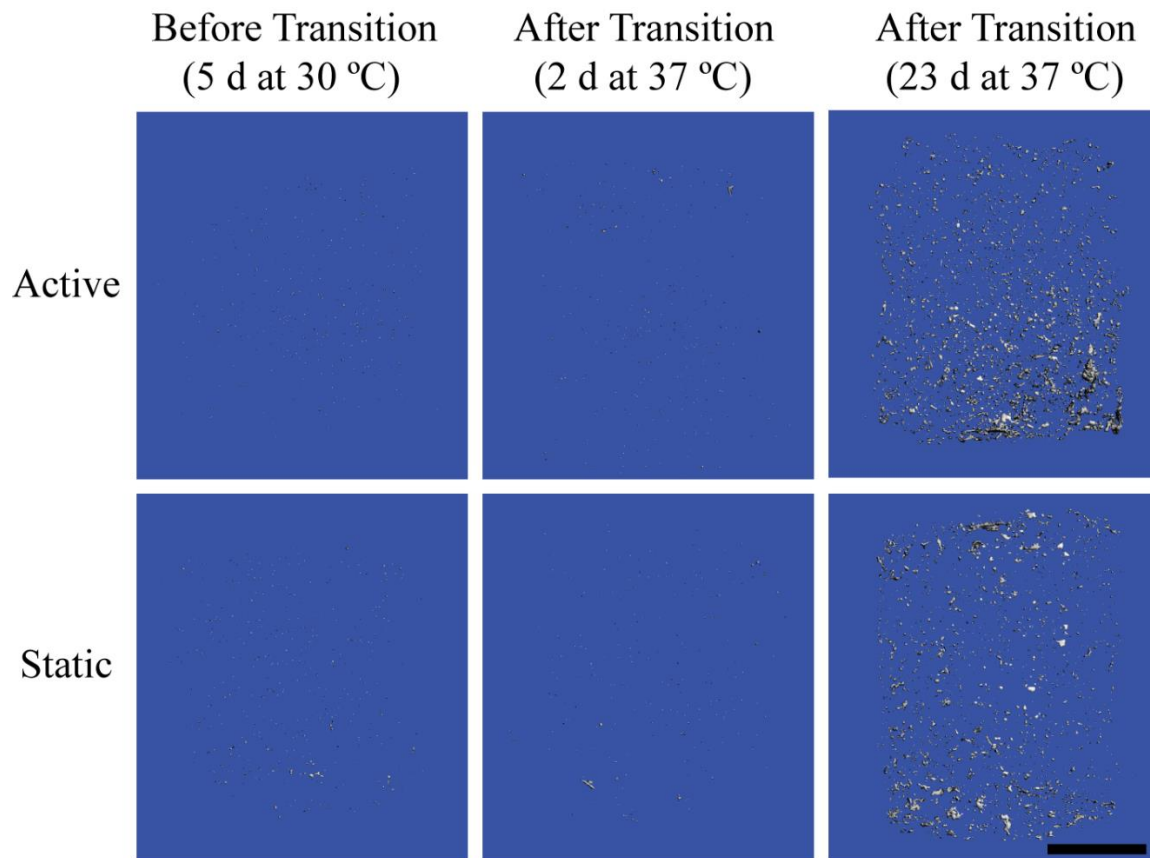


Figure 6-10. Microcomputed tomography 3D reconstructions of active and static foam scaffolds show mineral deposition over time. For both *active* and *static* scaffolds, small quantities of minerals were detected, and mineral size was small before transition and 2 d after transition. Significant increase in mineral volume and size was found on both groups 23 d after transition. A threshold of 100 was used to isolate mineral. Scale bar is 1 mm.

Table 6-1. Mineral fractions (V_{100}/V_{40}) of *active* and *static* foam scaffolds over time. Three replicates for (top) active and (bottom) static scaffolds reveal that average mineral fractions for replicates 2 and 3 are consistent and increasing over time, while the mineral fraction for replicate 1 is high at the early time point and decreases at the later time points. This inconsistency for replicate 1 is attributed to inconsistent initial cell seeding density. No significant difference was found between *active* and *static* groups.

Active Foam Scaffolds V_{100}/V_{40} (%)			
Replicate	5 d at 30 °C	2 d at 37 °C	23 d at 37 °C
1	0.734	0.554	0.032
2	0.016	0.038	0.398
3	0.005	0.005	0.502

Static Foam Scaffolds V_{100}/V_{40} (%)			
Replicate	5 d at 30 °C	2 d at 37 °C	23 d at 37 °C
1	0.854	0.449	0.062
2	0.040	0.091	0.295
3	0.015	0.009	0.280

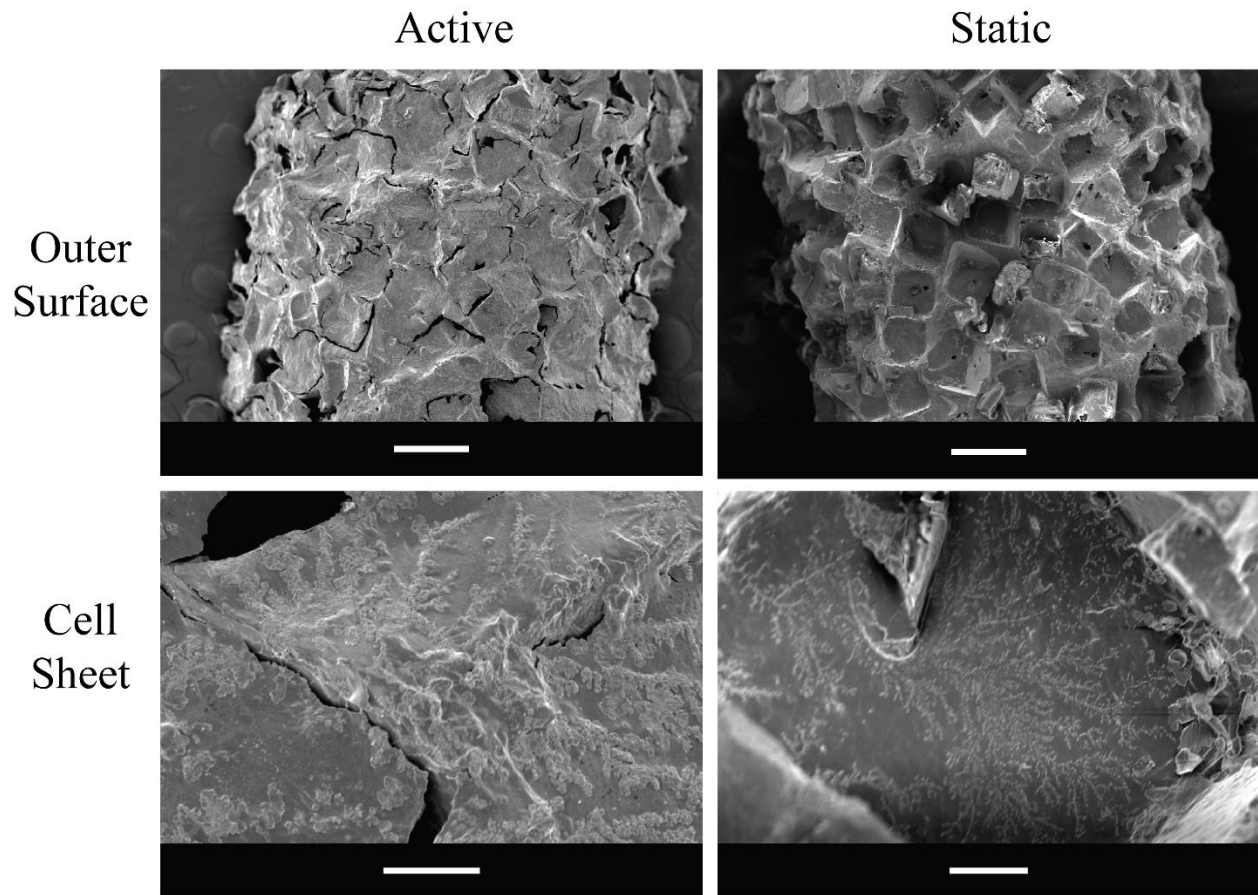


Figure 6-11. SEM micrographs of independent replicate with cell sheet formation before transition. For the independent replicate where significant mineral deposition was observed before transition, both *active* and *static* scaffolds had a confluent cell sheet covering the (top) outer surface. Inspection of the (bottom) surface of the cell sheet shows large mineral deposits. Scale bars are (top) 500 μm and (bottom) 50 μm .

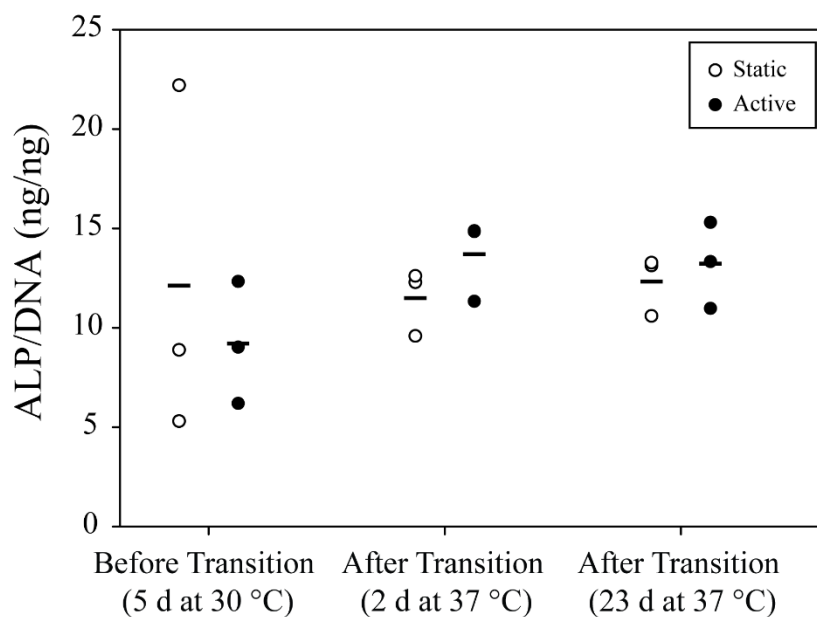


Figure 6-12. Alkaline phosphatase (ALP) activity for *active* and *static* foam scaffolds before and after transition. No significant difference in ALP activity was found between active and static scaffolds. While a trend of increased ALP activity is seen for after transition (37 °C 2 d and 37 °C 23 d) compared to before transition (30 °C 5 d), no statistically significant difference was found. Horizontal lines indicate averages over 3 independent replicates.

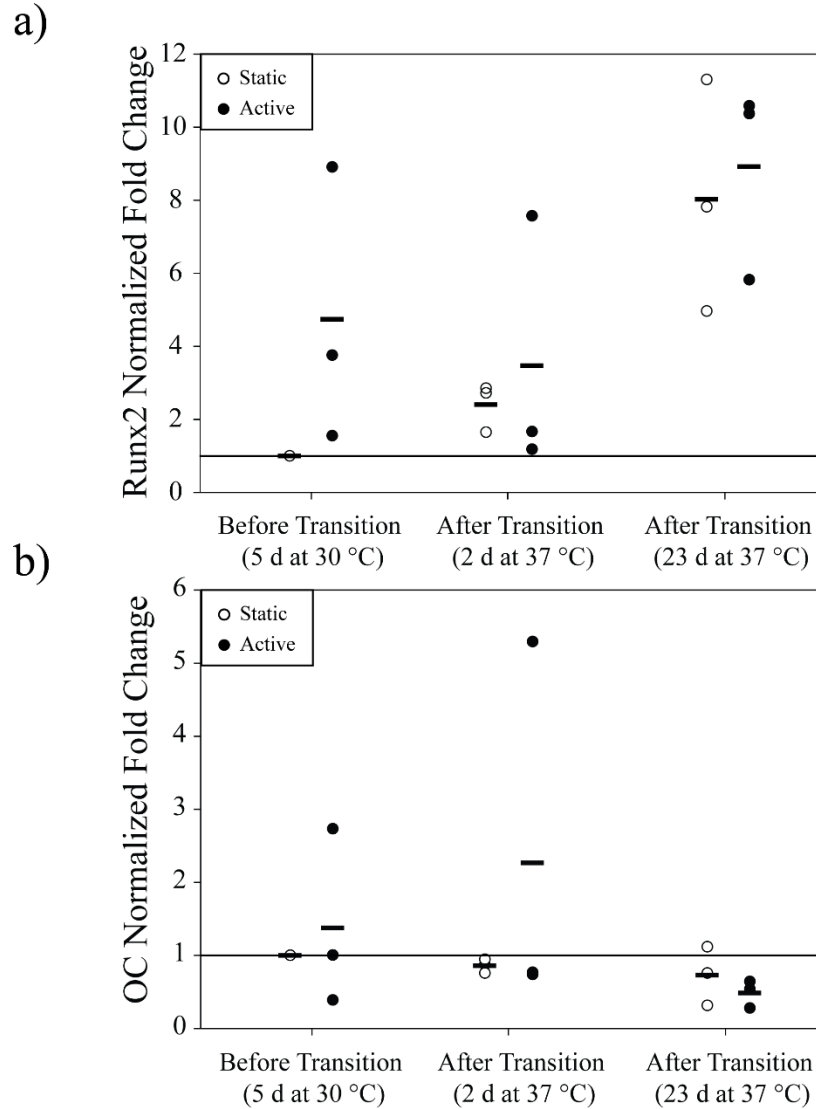


Figure 6-13. Real-time PCR (qPCR) expression of osteogenic markers Runx2 and osteocalcin (OC) for *active* and *static* foam scaffolds. (a) A trend of increasing (upregulation) Runx2 over time was observed for *active* and *static* scaffolds, although significance was not achieved; (b) a trend of decreasing (downregulation) OC was observed for *active* and *static* scaffolds, but no significance was found. There was no difference between *active* and *static* scaffolds in both markers across all time points. Horizontal lines indicate averages over 3 independent replicates.

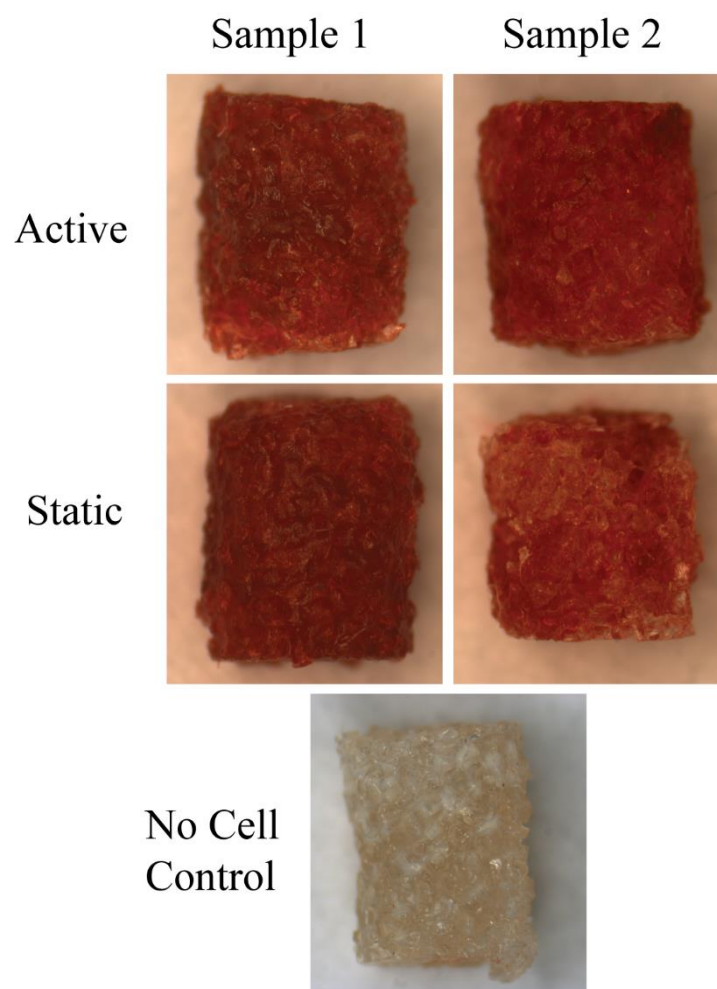


Figure 6-14. Alizarin red staining of *active* and *static* foam scaffolds 4 weeks after culture. Calcium deposition (red stain) was observed throughout the entire scaffold for both *active* and *static* scaffolds. An empty control scaffold (no cells) cultured under the same conditions showed no staining, suggesting calcium deposition is from the adhered cells and not deposition from the medium onto the scaffold. No observable difference was found between *active* and *static* scaffolds.

Chapter Seven: Conclusions and Future Directions

7.1 Overall Conclusion

This work describes the fabrication and application of dynamic 2D substrates and 3D scaffolds for use in cell mechanobiology and tissue engineering. Shape memory polymers (SMPs) with the capacity to undergo programmed changes in shape at body temperature were developed, characterized, and applied *in vitro* and *in vivo*.

In **Chapters 2 and 3**, a novel bilayer system capable of forming nano-scale wrinkles under cytocompatible conditions was developed and applied *in vitro* as an *Active Cell Culture* substrate. **Chapter 2** described the fabrication of shape memory actuated wrinkle formation, where body temperature recovery of an SMP substrate induced buckling of a thin gold coating. This system provided the ability to easily tune the wrinkle properties by changing the programming conditions of the SMP. When increasing the amount of programmed strain in the SMP substrate, wrinkle orientation and amplitude increased. As a result, we were able to increase the degree of cell alignment by seeding cells on substrates with increasing programmed strain, until reaching a point of saturation. The tunability of surface properties afforded by this bilayer approach is advantageous over other SMP systems which rely on surface embossing or molding and typically require multiple embossers or molds to achieve different topographies. Additionally, when employed as an *Active Cell Culture* substrate, the bilayer system was able to “turn-on” cell alignment by changing from a flat topography to a wrinkled topography with attached and viable cells. The ability to turn-on a cell behavior may prove important as scientists continue developing functional tissue engineered constructs.

In **Chapter 3**, the wrinkle bilayer system was applied *in vitro* to ascertain the effect the ordered nanotopography had on cell motility. A custom tracking algorithm, *ACTIVE* (automated contour-based tracking for *in vitro* environments), was developed that, for the first time, enabled accurate tracking of large cell populations over long timescales, while also identifying cell divisions. Cell motility was described using a set of physics-based metrics that revealed subtle differences between cell motility on wrinkled, flat gold substrates, and flat tissue culture polystyrene substrates. Application of *ACTIVE* and the imaging methods described in Chapter 3 is expected to enable researchers to investigate how cell-cell interactions, coupled with cell-material interactions, can direct cell behavior in complex environments.

Having achieved topography changing 2D substrates and successfully applying them *in vitro*, we expanded our efforts in **Chapters 4-7** to develop shape changing 3D scaffolds and applying those *in vitro* and *in vivo*. In **Chapter 4** a modified porogen-leaching approach was developed to fabricate highly porous, interconnected SMP foams. A simple method for forming a fused salt template was employed, and a poly(ϵ -caprolactone)-co-poly(ethylene glycol) (PCL-PEG) network was formed through thiol-ene mediated crosslinking. The resulting PCL-PEG recovery temperature was tuned to body temperature by changing the composition, where increasing hydrophilic PEG resulted in a lowering of the melt transition temperature in the hydrated state. A second approach to tuning the functional recovery temperature was control the programming condition, in particular the deformation temperature during a one-way shape memory cycle. This phenomenon has been reported for other systems, however the mechanism of this system is unique as it is not based on a broad melting transition temperature or inelastic deformation of amorphous chains below their glass transition temperature. Additionally, this system is the first to report a two-way shape memory behavior in compression, a characteristic

that may prove useful for tissue engineered scaffolds with reversible actuation. The approach for fabricating porous SMP foams and the chemistry employed in this Chapter can be used as a simple way to fabricate porous shape-changing scaffolds, with applicability in 3D *Active Cell Culture*, minimally-invasive medical devices, and deployable tissue engineered constructs.

In **Chapter 5**, the porogen-leaching technique and PCL-PEG chemistry developed in **Chapter 4** were used to fabricate expanding semi-crystalline SMP foam scaffolds as synthetic bone grafts. A stiffer amorphous SMP foam was also explored combining the chemistry from **Chapter 2** with the porogen-leaching approach from **Chapter 4**. The feasibility of employing SMP foams as synthetic bone substitutes was explored by implanting SMP foam grafts in a mouse critical size segmental defect model *in vivo*. For such a load-bearing application, soft semi-crystalline foams were unable to maintain defect stability and resulted in euthanasia of mice within 4 weeks. The stiffer amorphous foam, however, maintained defect stability while also integrating with the native bone interface at the defect site and providing torsional stability comparable to an allograft control. This work demonstrated that SMP foams show promise as deployable, space-filling synthetic bone substitutes. Significant improvements to the SMP foam chemistry and architecture must be made before applying these foam in a clinically relevant defect model, as the foams in their current state are not biodegradable and did not promote gross *de novo* bone formation. Current efforts are focused on addressing these needs, as is discussed below in the future work.

Finally, in **Chapter 6**, the stiff amorphous SMP foam developed in **Chapter 5** was applied *in vitro* to determine the effect of expansion on stem cell differentiation capacity. An approach to improve bone regeneration *in vivo* that has received significant attention recently is incorporation of osteogenic progenitor cells into synthetic bone substitutes. For SMP foams to be

employed as deployable synthetic bone substitutes containing osteogenic progenitor cells, it is important to understand how deployment may affect osteogenic differentiation capacity. We found that SMP foam expansion of 25% had no detectable negative effect on the osteogenic differentiation capacity of adherent stem cells. Foams cultured with stem cells for 4 weeks expressed significant amounts of calcium deposition, which was confirmed to be cell-mediated deposition. Furthermore, scaffolds promoted cell growth and infiltration into the interior of the foam, where cell sheets were found spanning the pore surfaces. This work demonstrated the feasibility of applying SMP foams as a deployable cell-therapy based treatment to facilitate bone repair. Properties of this system, in particular the long-term stability of the programmed state at 30 °C coupled with shape-change triggering at 37 °C, also show promise for applying this system as an *Active Cell Culture* scaffold. Such scaffolds that can dynamically change shape under cytocompatible conditions are expected to reveal new insights into cell-material interactions in a more biomimetic environment.

Overall, the SMP substrate and scaffolds developed in this dissertation show great potential for use in *Active Cell Culture* and as tissue engineering scaffolds. Their tunability and facile fabrication enable them to be applied in a wide range of applications. Some suggestions for future work relating to the systems developed in this dissertation, as well as for SMP *Active Cell Culture* work in general, are discussed below.

7.2 Recommendations for Future Work

7.2.1 Shape Memory 2D Substrates for Active Cell Culture

The SMP bilayer system described in **Chapter 2** demonstrated that active wrinkling during cell culture could be used to turn-on cell alignment. In this study, only the equilibrium

states before and after wrinkle formation were investigated. However, we recognize the possibility that different rates of wrinkle formation may have drastically different effects on cell behavior. An advantage of this bilayer system is the acrylate-based chemistry enables easy tuning of the recovery temperature and recovery kinetics. By fabricating a series of SMP bilayer systems with different recovery kinetics, wrinkle formation on timescales much slower than, similar to, and faster than that of cell cytoskeletal reorganization may be achieved. Results from such studies may provide new insights into how cell cytoskeletal reorganization can be controlled to elicit different cell responses, revealing new understandings about cell mechanobiology in a dynamic environment.

While not explored as part of this dissertation, shape memory functionality may further be exploited to fabricate new *Active Cell Culture* substrates capable of undergoing dynamic changes in surface chemistry and elasticity. For example, the shape-changing capacity of SMPs could be used to program micropatterned topographies that can dynamically change pattern shape and area, which could elicit significant changes in cell behavior. Micropatterned adhesive islands on static substrates have been previously used to control cell shape and cell spreading, resulting in the ability to direct cells to grow or undergo apoptosis [1]. SMPs could be used to turn-on such an effect by micropatterning large islands that are triggered to shrink into smaller islands. This may enable the ability to program cells from a growth state to a cell-death state, which could be useful for studying cancer cell mechanobiology. Additionally, dynamic changes in micropattern shape have the potential to be used to actively direct stem cell lineage commitment. Cell aspect ratio atop different micropatterns was shown to influence stem cell lineage commitment down either an osteogenic path or adipogenic path [2]. SMP actuated

changes in micropattern aspect ratio could be used to switch stem cell lineage specification on demand.

Another aspect of SMP functionality that can be exploited for *Active Cell Culture* substrates is the ability of SMPs to undergo large drops in stiffness (up to 3 orders of magnitude) upon heating through a thermal transition temperature. Although SMPs fabricated to-date have moduli that are too stiff to regulate cell behavior *in vitro*, advances in substrate fabrication now enable the use of microposts to lower the effective stiffness felt by cells [1]. SMP substrates with a micropost topography could be used to induce a change in the effective stiffness felt by cells, and these changes could be used to change cell behaviors such as motility, morphology, and stem cell lineage commitment which have been reported to be elasticity-sensitive (discussed in **Chapter 1**). The use of SMPs for substrates with dynamic topographies, surface chemistries, and elasticities is a promising application that will likely reveal new and significant understandings of how dynamics *in vivo* play a role in regulating cell behavior.

7.2.2 Cell Tracking in Dynamic Environments

The SMP bilayer system was applied in **Chapter 3** to investigate the effect of wrinkle topography on cell motility. In this study, only tracking analyses of cells on static substrates (substrates that did not dynamically form wrinkles with attached cells) were conducted. Current efforts now focus on expanding these methods to tracking cells before, during, and after wrinkle formation. Accurate tracking of cells during dynamic topography changes is expected to reveal the kinetics of cells reorientation, motility change, and division orientations. Constructing accurate tracks during translation will not be trivial, as additional tracking challenges will arise. As wrinkling occurs, substrates may translate, rotate, or shift out of focus, which must be minimized experimentally and accounted for in the *ACTIVE* tracking algorithm. Analysis of cell

motility in these environments also requires tracking of cells over longer periods of time to study the dynamic cell-material interactions on these non-equilibrium substrates.

In addition to addressing the challenges associated with tracking during a dynamic topography change, application of cell tracking should be expanded to 3D scaffolds. While interesting cell motility characteristics can be found in 2D tracking, cell migration in 3D is much different than cell migration in 2D [3]. Our group has developed 3D fibrous scaffolds capable of undergoing dynamic changes in fiber realignment under cytocompatible conditions [4]. Application of tracking in this fibrous 3D environment that more closely mimics extracellular matrix (ECM) dynamics than 2D substrates will likely have a major impact in the field of cancer cell mechanobiology. *In vivo*, tumor cells directly remodel fibers of the ECM from a random orientation to a radial orientation to promote cell invasion and metastasis [5]. Investigating tumor cell migration in fibrous scaffolds that undergo biomimetic changes in fiber orientation can provide a better understanding of the interaction between tumor cells and the underlying ECM.

7.2.3 SMP Scaffolds for Bone Tissue Engineering

The application of SMP scaffolds for bone tissue engineering (**Chapter 5**) has received significant interest over the past two years [6-8]. The work in Chapter 5 demonstrated the feasibility of applying expanding SMP foams as space-filling substitutes for treating critical size bone defects. While the PCL-PEG scaffold was too soft to provide adequate stability in a load-bearing application, it may serve as a functional bone repair strategy in non load-bearing applications, such as craniofacial defects. PCL is a biocompatible, biodegradable [9, 10], FDA approved polymer that shows promise for such application. Incorporation of hydroxyapatite (HA) will improve the osteoconductivity and osteoinductivity of the PCL-based scaffold. However, physical incorporation of HA into SMP foams proved inefficient, and modifications to

the HA could be made to chemically incorporate it into the scaffold (work which is discussed in **Appendix 4**).

One major limitation of the current stiff amorphous SMP foam is the acrylate-based chemistry is not biodegradable. This prevents its use as a clinically-relevant bone repair strategy. The next steps for exploring expanding SMP scaffolds is to develop stiff, biodegradable foams. One approach to achieve this is to use a poly(D,L lactide) based chemistry that has been previously developed in our lab as a biodegradable stent coating [11, 12] and later developed as an SMP fiber mat [4]. Efforts for using this chemistry to fabricate SMP foams is discussed in **Appendix 5**. Biodegradable, stiff foams should be explored in a larger, clinically-relevant animal model such as sheep or dogs to determine the limitations of its load-bearing capacity. While the stiff foams were able to maintain defect stability in a mouse model, it remains unclear how the foam will function in a larger animal model.

7.2.4 SMP Scaffolds as Deployable Cell-Based Therapy

In **Chapter 6** we found that SMP foam scaffolds show promise for use as a deployable cell-based therapy to facilitate bone repair, as SMP deployment did not inhibit osteogenic differentiation of adherent stem cells. As a natural next step, SMP foams seeded with osteogenic progenitor cells should be evaluated *in vivo* to determine if bone repair is facilitated. Combining the methods of **Chapter 5** (intraoperative delivery of SMP bone grafts) and **Chapter 6** (inducing osteogenic differentiation in programmed scaffolds) can enable this application to be explored. The effect of pore interconnectivity should be considered when developing these constructs, as larger pore interconnections would be desired to facilitate nutrient transport through the scaffold while promoting cell infiltration. As a consequence, however, the mechanical integrity of the foams will decrease as the pore interconnectivity increases. Additionally, the ability of

expanding SMP foams to conform to complex defects should be investigated, as this is an attractive property that SMPs possess that many other non-deployable synthetic grafts do not. Conformation to the defect site may promote faster integration of the construct if sufficiently stability is afforded.

7.2.5 SMP Scaffolds as 3D Active Cell Culture Scaffolds

The SMP foam developed in Chapter 6 also possessed properties that are required of *Active Cell Culture* materials. The foam maintained a stable temporary shape long-term while promoting cell growth and infiltration, and was triggered to expand completely at a cytocompatible triggering temperature. Several studies have investigated cell-material interactions on 2D SMP substrates [13-15], but to-date only one 3D scaffold has been used as an *Active Cell Culture* SMP scaffold to study cell-material interactions during dynamic architecture change [4]. The SMP foam developed here can serve as an alternate *Active Cell Culture* scaffold with cuboidal pores that can undergo large expansion ratios and apply large tensile strains to attached cells. Expanding foam scaffolds could be investigated to determine if pore expansion can be used as a biologically-relevant stimulus to induce differentiation in the absence of, or in combination with, induction medium, which has been demonstrated on 2D SMP substrates [16].

7.2.6 Shape Memory Assisted Cell Seeding (SMACS)

An alternative idea for exploiting the expanding capability of SMP foams is to trigger foam expansion in the presence of cell-containing medium to force, through suction, cells into the interior of the scaffold. This concept, termed “Shape Memory Assisted Cell Seeding” (SMACS), may serve as a useful method to homogeneously seed large numbers of cells into

large 3D scaffolds. The methodology and preliminary results for investigating SMACS is discussed in **Appendix 6**.

7.3 References

- [1] Chen CS, Mrksich M, Huang S, Whitesides GM, Ingber DE. Micropatterned surfaces for control of cell shape, position, and function. *Biotechnology Progress*. 1998;14:356-63.
- [2] Peng R, Yao X, Ding J. Effect of cell anisotropy on differentiation of stem cells on micropatterned surfaces through the controlled single cell adhesion. *Biomaterials*. 2011;32:8048-57.
- [3] Doyle AD, Wang FW, Matsumoto K, Yamada KM. One-dimensional topography underlies three-dimensional fibrillar cell migration. *The Journal of cell biology*. 2009;184:481-90.
- [4] Tseng L-F, Mather PT, Henderson JH. Shape-memory-actuated change in scaffold fiber alignment directs stem cell morphology. *Acta biomaterialia*. 2013;9:8790-801.
- [5] Provenzano PP, Eliceiri KW, Campbell JM, Inman DR, White JG, Keely PJ. Collagen reorganization at the tumor-stromal interface facilitates local invasion. *BMC medicine*. 2006;4:38.
- [6] Liu X, Zhao K, Gong T, Song J, Bao C, Luo E, et al. Delivery of growth factors using a smart porous nanocomposite scaffold to repair a mandibular bone defect. *Biomacromolecules*. 2014;15:1019-30.
- [7] Zhang D, George OJ, Petersen KM, Jimenez-Vergara AC, Hahn MS, Grunlan MA. A bioactive "self-fitting" shape memory polymer scaffold with potential to treat cranio-maxillo facial bone defects. *Acta biomaterialia*. 2014;10:4597-605.

- [8] Rychter P, Pamula E, Orchel A, Posadowska U, Krok-Borkowicz M, Kaps A, et al. Scaffolds with shape memory behavior for the treatment of large bone defects. *Journal of Biomedical Materials Research Part A*. 2015.
- [9] Middleton JC, Tipton AJ. Synthetic biodegradable polymers as orthopedic devices. *Biomaterials*. 2000;21:2335-46.
- [10] Sun H, Mei L, Song C, Cui X, Wang P. The in vivo degradation, absorption and excretion of PCL-based implant. *Biomaterials*. 2006;27:1735-40.
- [11] Guo Q, Knight PT, Mather PT. Tailored drug release from biodegradable stent coatings based on hybrid polyurethanes. *Journal of Controlled Release*. 2009;137:224-33.
- [12] Knight PT, Lee KM, Qin H, Mather PT. Biodegradable thermoplastic polyurethanes incorporating polyhedral oligosilsesquioxane. *Biomacromolecules*. 2008;9:2458-67.
- [13] Davis KA, Burke KA, Mather PT, Henderson JH. Dynamic cell behavior on shape memory polymer substrates. *Biomaterials*. 2011;32:2285-93.
- [14] Ebara M, Uto K, Idota N, Hoffman JM, Aoyagi T. Shape-Memory Surface with Dynamically Tunable Nano-Geometry Activated by Body Heat. *Advanced Materials*. 2012;24:273-8.
- [15] Le DM, Kulangara K, Adler AF, Leong KW, Ashby VS. Dynamic Topographical Control of Mesenchymal Stem Cells by Culture on Responsive Poly (ϵ -caprolactone) Surfaces. *Advanced materials*. 2011;23:3278-83.
- [16] Gong T, Zhao K, Yang G, Li J, Chen H, Chen Y, et al. The control of mesenchymal stem cell differentiation using dynamically tunable surface microgrooves. *Advanced healthcare materials*. 2014;3:1608-19.

Appendix One: MATLAB Analysis for Wrinkle Amplitude and Cell Nuclear Alignment

A1.1 MATLAB Algorithm for Wrinkle Amplitude Analysis

Overview

To calculate the average amplitude of wrinkles formed in our bilayer system (**Chapter 2**), we have developed a custom MATLAB algorithm that analyzes the resulting text file from an AFM scan. The code is designed to analyze uniaxial wrinkles only. Additionally, the code is only designed to analyze AFM scans where wrinkles are aligned vertically or horizontally (not at an off-axis).

Main M-File: Determining_Average_PeaktoValley.m

This m-file prompts the user to select an excel file that contains the AFM scan data and calls on the function `Peak_To_Valley.m` to calculate the average amplitude (peak-valley amplitude) and its standard deviation. This m-file also generates a histogram of peak-valley amplitudes for the AFM scan. As displayed below, this code will analyze AFM scans where uniaxial wrinkles are vertical. For horizontal wrinkles, uncomment “`Mydata_Transpose = Mydata;`” and comment out “`Mydata_Transpose = transpose(Mydata);`” The output variables of interest are “**Average**” and “**Standard_Deviation**” which are the average and standard deviation of the calculated wrinkle amplitude.

```

%%%%%%%%%%%%%%%%%%%%%%%%%%%%%%%%%%%%%%%%%%%%%%%%%%%%%%%%%%%%%%%%%%%%%%%%
%
% Determining_Average_PeaktoValley.m
%
clear all;
%
% Ask the user to select the excel file corresponding to the AFM trace
[filename, pathname] = uigetfile('*.xlsx', 'Select an Excel file');
Mydata = xlsread(filename);
%
% Adjust the data so the lowest valley starts at a position of "0"
MinValue = min(min(Mydata));
Mydata = Mydata-MinValue;
%
% Mydata_Transpose = Mydata; % Use this if wrinkles are horizontal in AFM
% scan
Mydata_Transpose = transpose(Mydata); % Use this if wrinkles are vertical
%
x=5; % Number to "average" over, must be greater than 3; Large numbers may
%     lose peaks or valleys
%
% Calculate the amplitude for each peak-valley distance for the first
% scan(horizontal row) of the AFM data
Peak_Valley(:,1) = Peak_To_Valley(Mydata_Transpose(:,1),x);
%
% Loop to calculate the amplitude for each peak-valley distance for the
% remaining scans (horizontal rows) of the AFM data; these values are all
% combined into one vector, Peak_Valley
for i = 2:size(Mydata_Transpose,2);
    New_Peak_Valley(:,1) = Peak_To_Valley(Mydata_Transpose(:,i),x);
    Peak_Valley = [Peak_Valley; New_Peak_Valley];
    clear New_Peak_Valley;
end
%
% Plot a histogram of all the peak-valley amplitudes
figure(1);
hist(Peak_Valley,30);
title('Histogram with Averaged Valleys');
xlabel('Pixel Height Bin')
ylabel('Count')
%
% Calculate the average and standard deviation of peak-valley amplitudes
Average = mean(Peak_Valley)
Standard_Deviation = std(Peak_Valley)
%%%%%%%%%%%%%%%%%%%%%%%%%%%%%%%%%%%%%%%%%%%%%%%%%%%%%%%%%%%%%%%%%%%%%%%%

```

Function: Peak_To_Valley.m

This function takes in a vector corresponding to one line profile of the AFM scan and an averaging window, “x”, to isolate peaks and valleys from the rest of the trace. The height between consecutive peaks and valleys is calculated and stored in an output vector, Peak_Valley. This vector will thus contain all the peak-height values for a given line profile of the AFM scan.

```
function [Peak_Valley] = Peak_To_Valley(Mydata_Vector,x)
%%%%%%%%%%%%%%%%%%%%%%%%%%%%%%%%%%%%%%%%%%%%%%%%%%%%%%%%%%%%%%%%%%%%%%%%
%   Inputs:
%       - Mydata_Vector: Vector of heights for a line profile of the AFM
%       scan
%       - x: An averaging number used to isolate peaks and valleys; higher
%       values remove noise and "false" peaks/valleys, but too large of a
%       number will result in losing real peaks/valleys. Number must be
%       odd and >= 3. Range of 3-11 works well for our typical scans.
%
%   Outputs:
%       - Peak_Valley: Vector of all Peak - Valley heights
%%%%%%%%%%%%%%%%%%%%%%%%%%%%%%%%%%%%%%%%%%%%%%%%%%%%%%%%%%%%%%%%%%%%%%%%
%   Allocating vector space and determining loop size
y = size(Mydata_Vector,1)-x;
My_Max_Vector = zeros(y, 1);
My_Min_Vector = zeros(y, 1);
My_Matrix = zeros(y,4);
%
%   Loop creates matrix of peak (max) and valley (min) heights based on
%   using at a moving range of "x" points
for i=1:y;
    My_Vector = zeros(x, 1);
    for j = 1:x;
        My_Vector(j,1) = Mydata_Vector(i+j-1);
    end
    My_Max_Vector(i,1) = max(My_Vector);
    My_Min_Vector(i,1) = min(My_Vector);
    My_Matrix(i,1) = i;
    My_Matrix(i,2) = Mydata_Vector(i+ceil(x/2),1);
    My_Matrix(i,3) = My_Max_Vector(i,1);
    My_Matrix(i,4) = My_Min_Vector(i,1);
end;
%
My_NewMatrix = zeros((y-3),4);
My_NewMax_Vector = zeros((y-3),1);
My_NewMin_Vector = zeros((y-3),1);
%
%   Loop sets non-peak points to "0" and non-valley points to "-1". This
%   makes calculating di
for k=1:(y-3);
    s = -1; % Dummy variable for altering non-minimum points
```

```

        if My_Max_Vector(k,1) == My_Max_Vector(k+1,1) && My_Max_Vector(k,1)
== My_Max_Vector(k+2,1) && My_Max_Vector(k,1) == My_Max_Vector(k+3,1);
            My_NewMax_Vector(k,1) = My_Max_Vector(k,1);
        else My_NewMax_Vector(k,1) = 0;
        end;
        if My_Min_Vector(k,1) == My_Min_Vector(k+1,1) && My_Min_Vector(k,1)
== My_Min_Vector(k+2,1) && My_Min_Vector(k,1) == My_Min_Vector(k+3,1);
            My_NewMin_Vector(k,1) = My_Min_Vector(k,1);
        else My_NewMin_Vector(k,1) = s;
        end;
        My_NewMatrix(k,1) = k;
        My_NewMatrix(k,2) = My_Matrix(k,2);
        My_NewMatrix(k,3) = My_NewMax_Vector(k,1);
        My_NewMatrix(k,4) = My_NewMin_Vector(k,1);
    end;

%
% Loop that calculates the number of peaks and valleys, and stores the
% heights of those peaks and valleys in vectors called "Max" and "Min",
% respectively.
z = 0; % counter for number of peaks
v = 0; % counter for number of valleys
for l=1:(y-4)
    if My_NewMax_Vector(l,1) > 0 && My_NewMax_Vector(l+1,1) == 0;
        z = z + 1;
        Max(z,1) = My_NewMax_Vector(l,1);
    end;
    if My_NewMin_Vector(l,1) >= 0 && My_NewMin_Vector(l+1,1) == s;
        v = v + 1;
        Min(v,1) = My_NewMin_Vector(l,1);
    end;
end;

%
% Calculate the difference in height between consecutive peaks and
% valleys
w = min(z,v); % Determines if there are less peaks or valleys
counter = 0;
for c = 1:w-1;
    Peak_Valley(c+counter,1) = Max(c)-Min(c);
    Peak_Valley(c+counter+1,1) = Max(c+1) - Min(c);
    counter = counter + 1;
end;
end
%%%%%%%%%%%%%%%%%%%%%%%%%%%%%%%%%%%%%%%%%%%%%%%%%%%%%%%%%%%%%%%%%%%%%%%%

```

A1.2 MATLAB Algorithm for Calculating Nuclear Angle Spread

Overview

To calculate the angular spread of cell nuclei, a custom MATLAB algorithm was developed where the standard deviation of cell angular spread was calculated. Cell angles were adjusted and rotated in 1° increments to determine the angle that resulted in maximum alignment. The resulting standard deviation, angle resulting in max alignment, and the adjusted cell angles are output and can be used for further analysis and histogram plotting.

Function: AngleSpread2.m

This function takes a vector of cell nuclear angles (in degrees) and first passes them to a sub-function, AngleAlign.m, that adjusts the cell angles so they are positive and centered around 90° . After obtaining adjusted angles, this function calculates the truncated standard deviation of the nuclear angles and then subtracts 1° from all of the angles and calculates a new truncated standard deviation. This happens for all 180° to get the reference angle that results in max alignment (minimum standard deviation). This function returns the minimum standard deviation (max alignment), the corresponding reference angle, and the adjust cell angles centered about this reference angle.


```

function [FinalStd, MaxAngle, HistogramMaxVector] =
AngleSpread2 (AngleVector)
%%%%%%%%%%%%%%%%%%%%%%%%%%%%%%%%%%%%%%%%%%%%%%%%%%%%%%%%%%%%%%%%%%%%%%%%
% Input:
% - AngleVector: A vector of nuclear angles in Degrees
% Outputs:
% - FinalStd: Standard deviation of the nuclear angles
% - MaxAngle: The rotation angle that leads to maximum alignment
% - HistogramMaxVector: Vector of adjusted cell angles that can be
% used to make a histogram where 90 Degrees is the angle of max
% alignment
%%%%%%%%%%%%%%%%%%%%%%%%%%%%%%%%%%%%%%%%%%%%%%%%%%%%%%%%%%%%%%%%%%%%%%%%
% Determines the minimum standard deviation of an angle vector by rotating
% by 1 degree at a time for 180 degrees
AngleVector = AngleVector(~isnan(AngleVector));
StdVector = zeros(180,1);
MinStd = 1000000;
NonTruncStdVector = zeros(180,1);
for i = 1:180;
    AlignedAngleVector = AngleAlign(AngleVector);
    AlignedAngleVector = AlignedAngleVector - 90;
% If for some reason angles are outside of -90 to +90, something went
% wrong; make sure angles are in degrees
    if max(AlignedAngleVector) > 90
        disp('error max angle')
        continue
    end
    if min(AlignedAngleVector) < -90
        disp('error min angle')
    end

%
% Calculate the standard deviation of angles; then adjust the angles.
% Uses the truncated standard deviation formula derived by Davidson et
% al. Acta Biomaterialia. 2010;62590-2598
    NonTruncStdVector(i)
    (sum(AlignedAngleVector.^2)/size(AlignedAngleVector,1))^0.5;
    StdVector(i) = 52/(1+543*NonTruncStdVector(i)^(-1.96));
%
% If this rotation angle results in lower standard deviation, store it
% and update the MinStd, otherwise do nothing.
    if StdVector(i) < MinStd;
        MaxAngleVector = AngleVector;
        MinStd = StdVector(i);
        MaxAngle = i;
    end;
    AngleVector = AngleVector - 1; % rotate cell angles by 1 Degree
end;
%
% Adjust the cell angles to be centered about 90 Degrees, which now
% corresponds to angle of most alignment;
ModMaxAngleVector = AngleAlign(MaxAngleVector);
HistogramMaxVector = ModMaxAngleVector;
FinalStd = std(HistogramMaxVector);
%%%%%%%%%%%%%%%%%%%%%%%%%%%%%%%%%%%%%%%%%%%%%%%%%%%%%%%%%%%%%%%%%%%%%%%%

```

Function: AngleAlign.m

This function simply takes a vector of angles and adjust them so they are all positive (between 0 and 180) and they are centered about 90°.

```
function AngleVectorMod2 = AngleAlign(AngleVector)
%%%%%%%%%%%%%%%%%%%%%%%%%%%%%%%%%%%%%%%%%%%%%%%%%%%%%%%%%%%%%%%%%%%%%%%%
%   Input:
%       - AngleVector: A vector of nuclear angles in Degrees
%
%   Outputs:
%       - AngleVectorMod2: A vector of nuclear angles that are adjusted so
%       they are positive (between 0-180 Degrees) and centered about 90
%       Degrees.
%%%%%%%%%%%%%%%%%%%%%%%%%%%%%%%%%%%%%%%%%%%%%%%%%%%%%%%%%%%%%%%%%%%%%%%%
% Allocate space and determine loop size
x = size(AngleVector,1);
AngleVectorMod = zeros(x(:,1),1);
AngleVectorMod2 = zeros(x(:,1),1);
%
% Loop that adjusts all angles to be between 0 and +180
for y = 1:x;
%
%   Make all angles positive
if AngleVector(y) < 0;
    AngleVectorMod(y) = AngleVector(y) + 360;
else AngleVectorMod(y) = AngleVector(y);
end
%
%   Make all angles between 0 and 180
if AngleVectorMod(y) > 180
    AngleVectorMod(y) = AngleVectorMod(y) - 180;
end
%
%   Centers the angles about 90 Degrees
if AngleVectorMod(y) < 90;
    AngleVectorMod2(y) = 90 - AngleVectorMod(y);
else AngleVectorMod2(y) = AngleVectorMod(y)*(-1) + 270;
end
end
%%%%%%%%%%%%%%%%%%%%%%%%%%%%%%%%%%%%%%%%%%%%%%%%%%%%%%%%%%%%%%%%%%%%%%%%
```

Appendix Two: ACTIVE Tracking User's Manual

Overview

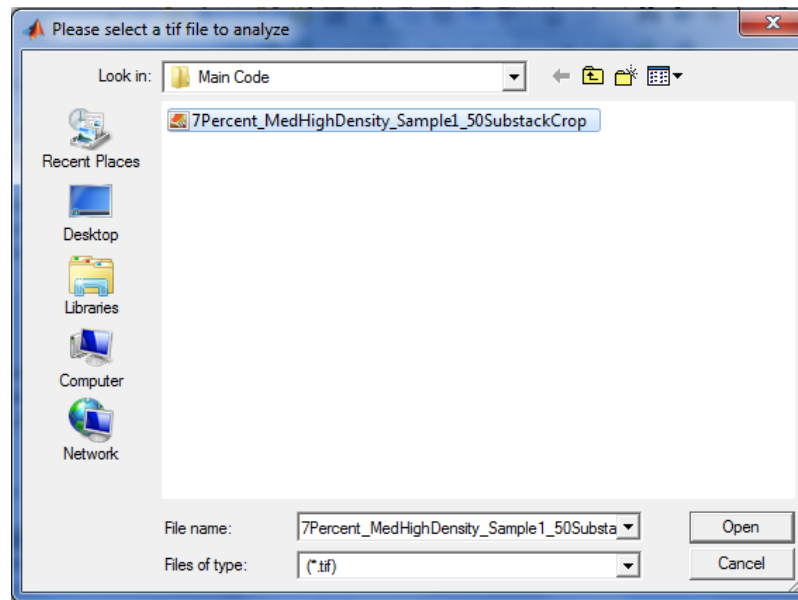
The Automated Contour-based Tracking for *In Vitro* Environments (ACTIVE) approach was designed for automated nuclear cell tracking and was created using MATLAB version 2011a. It requires a valid MATLAB license to run. This user's manual details the main parameters used and the general operation of the tracking code as it was implemented in "Automated, contour-based tracking and analysis of cell behavior over long timescales in environments of varying complexity and cell density"[1]. While the suggested parameters are specifically tailored to the aforementioned study, the system was developed to work well for tracking in images that display fluctuations in intensity within a single image or for a series of images that display significant variations in contrast over time. The complete tracking algorithm and a sample set of images can be downloaded at: <http://henderson.syr.edu/downloads/>

Image Preparation

The code is equipped to read 16-bit grayscale image stacks. The stacks must be .tiff, and can be converted to the proper format with ImageJ:

Open stack in Image J --> Image --> Type --> 16-bit --> File --> Save as --> Tiff

There are currently no requirements for the tiff stack name, apart from standard naming conventions relevant to MATLAB (e.g., no symbols, spaces, etc.). Once initialized, the program will direct the user to select the tiff stack for analysis:



Though it is not required, it is suggested that the tiff stack be placed in the same directory as the unzipped tracking code for convenience.

Operation

The `ACTIVE` approach operates entirely from the wrapper function, `run_tracking_contour2.m`. Briefly, contour segmentation of images is first achieved through implementation of the `makecontourparentarray.m` function and ellipse fitting is accomplished through `find_particles_fixed.m`. Once segmented, cells are tracked using the modified Kilfoil function `trackmem_new.m`. Post tracking correction is then completed using the `sib_matrix_creation.m`, `collision_corrector_rtc2.m`, `collision_tags_rtc2_3.m`, and `relabeling.m` functions. An additional division correction was performed for the current study prior to relabeling to account for frustrated divisions. Analysis of outputs from the

run_tracking_contour2.m function can then be assessed using the supplemental analysis code to generate mean squared displacement, velocity autocorrelation, and asphericity plots, similar to those displayed in the tracking manuscript.

Detailed Tracking Instructions

1. Download the full tracking code from <http://henderson.syr.edu/downloads/>
2. Unzip the file and place all of the functions into a new folder within a stable directory. Navigate to this directory within MATLAB and open the function file labeled run_tracking_contour_rtc2.m.
3. Right click (control click for Mac) on the "Main Code" folder and select "Add to Path" --> "Selected Folders" to add the main code to the current function path.
4. Initialize the run_tracking_contour_rtc2 function within MATLAB. This can be achieved by copying the following code into the command window and pressing enter (return on Macs):

```
[ xyzs_id, xyzs_id_columns, filename, framerate] = run_tracking_contour2();
```

*Note that both of the above lines contribute to the single function call.

5. A basic GUI window will pop up with a series of parameters that the user can manipulate. At the current time, these parameters must be manually adjusted. The default setting for these parameters is optimized for a C3H10T1/2 mouse fibroblast dataset with a cell density of 87,500 cells-mL⁻¹ stained at a Hoechst 33342 dye concentration of 0.01 µg-mL⁻¹. Parameter details are described below:

- a. **Plot Toggle:** Determines whether individual frame images (contour and ellipse plots) are displayed. It is of note that turning on this functionality will produce two plots for each image assessed. For example, in a standard 480 frame tiff stack used in the tracking manuscript, this would result in 960 images produced. For most computers, this will result in an error in MATLAB, due to insufficient memory. Thus, it is recommended that plot toggle is turned off, unless using a relatively small substack. Plotting individual images significantly increases run time (value of 1 = on, value of 0 = off). Plot Toggle can be used to look at segmentation results (both contour fitting and ellipse fitting), allowing a user to view how changing parameters affects segmentation.
- b. **Number of Contours:** Maximum number of total contour levels into which a single cell's intensity profile can be sectioned. Note that the current tracking version uses a built in MATLAB histogram stretching function (`imadjust`) to improve contour fitting. Increasing the number of contours in most cases improves segmentation at the cost of significantly increasing run time.
- c. **Half Particle Diameter:** A half size measurement of a typical cell/object in pixels (must be an odd integer for image filtering purposes). Changing this parameter can be used to

Plot Toggle (1=on; 0=off):	0
Number of Contours:	10
Half Particle Diameter (must be an odd integer)	13
Noise Wavelength (pixels):	2
Collision Plot Toggle (1=yes; 0=no)	0
Maximum Area (pixels ²)	260
Minimum Area (pixels ²)	10
Maximum Displacement (pixels)	20
Frame Time (min)	3
Maximum Collision Time (frames)	10
<input type="button" value="OK"/> <input type="button" value="Cancel"/>	

optimize segmentation. We found that a value slightly larger than the particle radius worked best for our experimental data.

- d. Noise Wavelength: Characteristic noise value for each image (in pixels). This value can be changed to affect the bandpass filtering of the image and consequently the segmentation. Values of 1-3 typically work best.
- e. Collision Plot Toggle: Determines whether collision event plots/videos are produced. Tracks for a subset of division/collision are produced (~10-15) depending on the total number of collisions identified by the code. These videos can be used to look at cell interactions before and after post-processing to evaluate if post-processing is correctly switching mislabeled cell IDs
- f. Maximum Area: Maximum area threshold for a single cell. Particles with an area greater than this parameter are deleted.
- g. Minimum Area: Minimum area threshold for a single cell. Particles with an area smaller than this parameter are deleted.
- h. Maximum Displacement: Maximum distance a single particle moves, frame to frame (in pixels). This parameter is used for linking and larger values may lead to combinatorics issues. If the parameter leads to combinatorics issues, a warning message is displayed. A typical value is the diameter of an average cell.
- i. Frame Time: Time step between two consecutive images (minutes), as defined during experimental capture of the image stack
- j. Maximum Collision Time: Maximum time cells can be completely occluded during a merging event. This parameter is used to construct complete merging events during post-processing.

The above parameters were set to the following values for all samples run in the tracking manuscript:

Parameter	Value
Plot Toggle	0
Number of Contours	15
Half Particle Diameter	13
Noise Wavelength	2
Collision Plot Toggle	0
Maximum Area	260
Minimum Area	10
Maximum Displacement	20 or 17*
Frame Time	3
Maximum Collision Time	10

*All high density samples for the presented tracking paper were run with a maximum displacement of 17 pixels due to complex combinatorics issues preventing tracking completion or resulting in significantly increased run time. All low and medium density samples were run with a max displacement of 20 pixels.

Once processing is complete, a .mat file will appear, saved as the same filename of the tiff stack used. This .mat file includes the following information:

A. **xyzs_id**: the main output matrix containing all cell information stored for all frames.

For the current version of ACTIVE, xyzs_id contains the following column outputs:

1. x-position: the x-position for the center of mass of a cell in a specific frame
2. y-position: the y-position for the center of mass of a cell in a specific frame
3. major axis: long-axis length of the fitted cell ellipse
4. minor axis: short-axis length of the fitted cell ellipse
5. theta/angle information: positional orientation of the fitted cell ellipse ($-\frac{3}{4}\pi$ to $\frac{3}{4}\pi$)

6. area: calculated area of the fitted ellipse
7. intensity: calculated intensity for the fitted ellipse
8. a sibling cell tag within a specific frame (used for sibling identification)
9. a sibling cell tag for overall particles (used for matching cell sibling IDs)
10. an individual reference number for each cell in all frames (used for matching cell sibling IDs)
11. frame number
12. cell identification tag
13. overall color number reference for colored ellipse plotting
14. color number reference tailored to Matlab's pre-set color system
15. original cell ID before relabeling

B. ***xyzs_id_columns***: the column number in *xyzs_id* containing cell IDs after linking

C. ***t_matrix***: same outputs as *xyzs_id* (columns 1-11), prior to linking; full cell information matrix resulting from segmentation portion only. This matrix can be used to adjust linking parameters (e.g., Max Displacement).

D. ***frame_avg***:

1. Average major axis value per frame
2. Average minor axis value per frame
3. Average aspect ratio per frame
4. Average angle of orientation of cells per frame
5. Average area of cells per frame
6. Average integrated intensity of cells per frame
7. Average intensity of cells per frame

E. *event_array*:

1. Cell 1 index into xyzs_id
2. Cell 1 ID
3. Cell 2 ID
4. Frame
5. Color number reference (relates to columns 13/14 in xyzs_id)
6. Type of collision (division, collision, or continuing collision only)
7. Index used to build the event array
8. Event number
9. Cell 2 index into xyzs_id

F. *event_array2*: An updated event_array (same information as above), with cell IDs in the events updated post division-correction

Once completed, the system will save a .mat file with the above information (A-F) in a new analysis folder in the directory directly above where the image data is stored. This new .mat file will have the same filename as the image stack assessed.

Detailed Correlation Analysis Instructions

1. Correlation analyses can be directly run after running run_tracking_contour2.m and storing the output. You can additionally load the saved .mat file (directory noted above).
2. Right click (control click for Mac) on the "Correlation Analyses" folder and select "Add to Path" --> "Selected Folders" to add the correlation code to the current function path.

3. The main code for the correlation analyses is `corr_analysis.m`. This function runs the MSD, velocity auto-correlation, diffusion plot generation, and cell track asphericity calculations. The call to the function is:

```
[MSD_mat, decomp_MSD_mat, vel_mat, asphericity] = corr_analysis(xyzs_id, xyzs_id_columns, framerate, filename, new_dir, theta, accuracy, plot_toggle)
```

4. The parameters `xyzs_id`, `xyzs_id_columns`, `framerate`, `filename`, and `new_dir` are part of the output of `run_tracking_contour2.m` and do not need to be specified. The parameters `theta`, `accuracy`, and `plot_toggle` do need to be specified, and a description of each is below:

- a. `theta`: The angle of anisotropy, if any, clockwise from the horizontal (default is 0).
- b. `accuracy`: The number of points to include in the finite difference calculation for determining cell velocities. Must be 2, 4, 6 or 8 (default is 8).
- c. `plot_toggle`: When this toggle is on, the correlation analysis plots are generated and saved. When this toggle is off, only the calculations are performed and no plots are generated (default is 1, or “on”)

5. Call the function with the appropriate parameters specified.

Once processing is complete, a `.mat` file will appear, saved as the name ‘Final_Analysis.mat’ located in a new folder in the directory with the original `.mat` file from `run_tracking_contour2`. This `.mat` file includes the following information:

- A. ***MSD_mat***: cell array with the first row of cells containing parameter labels and the second row containing the parameter values for the MSD analysis. The columns of the cell array are:

1. Short timescale slope

2. Long timescale slope
3. Mobility parameter (Intercept of line fit to long timescale data)

B. ***Decomp_MSD_mat***: cell array with the first row of cells containing parameter labels and the second row containing the parameter values for the decomposed MSD analysis. The columns of the cell array are:

1. X-Short timescale slope
2. X-Long timescale slope
3. X-Mobility parameter
4. Y-Short timescale slope
5. Y-Long timescale slope
6. Y-Mobility parameter

C. ***vel_MAT***: cell array with the first row of cells containing parameter labels and the second row containing the coefficients of the exponential decay fit for the velocity auto-correlation analysis. The columns of the cell array are:

1. X-Amplitude
2. X-Decay constant
3. X-Offset
4. Y-Amplitude
5. Y-Decay constant
6. Y-Offset

D. ***asphericity***: A vector containing the cell track asphericity values, with each row corresponding to a unique cell

Along with saving a .mat file containing the parameter values, the following plots will be generated and saved if plot_toggle is turned on: (Note all plots will be saved to a new folder that is created in the new_dir path)

1. filename_full_tracks: This is a plot of all cell tracks
2. filename_full_alpha: This is a semilog plot of the Gaussian parameter αv time for the complete MSD analysis.
3. filename_full_MSD: This is a log10 MSD v. log10 Δt plot containing lines fit to the short timescale and long timescale data of the MSD profiles.
4. filename_MSD_decomp: This is a log10 MSD v. log10 Δt plot containing lines fit to the short timescale and long timescale data for both the x and y direction MSD profiles.
5. filename_alpha_power_fit: This is a semilog plot of the Gaussian parameter αv time, for both the x and y directions, for the decomposed MSD analysis. This plot also contains power law fits to the alpha traces.
6. filename_alpha_no_fit: This is a semilog plot of the Gaussian parameter αv time, for both the x and y directions, for the decomposed MSD analysis. This plot also does not contain power law fits to the alpha traces.
7. filename_velocity: This is a plot of the velocity auto-correlation v. Δt in both the x and y directions. An exponential decay is fit to each trace and the fit coefficients displayed.
8. filename_gyration_plot: This is a plot of the terminal cell positions, with respect to a common origin, rotated by the principle eigenvector direction for

each cell track. The anisotropy of the terminal positions is directly proportional to track asphericity.

9. filename_diffusion_plot: This is a plot of the terminal cell positions for all cells with respect to a common origin. The anisotropy of the terminal positions qualitatively shows the degree of collective anisotropic cell motility.
10. Diffusion and gyration tiff plots: In a new folder in this same directory, a series of tiff images containing the cell positions from (8) and (9) above for each frame, rather than terminal position, is saved. From these images videos can be generated to show how the cells diffuse and track asphericity develops as a function of time.

Acknowledgements

The *ACTIVE* approach builds upon IDL code written by Timon Idema and colleagues for segmentation [2] and code initially written by John Crocker in IDL [3] and updated for execution in MATLAB by Maria Kilfoil for linking [4]. Cell division and merging event identification, as well as the post-processing and analysis code, are original to the *ACTIVE* system.

Conditions and terms of use:

- The software packages provided here are M-files executable in MATLAB, a proprietary numerical computing environment developed by [MathWorks](#).
- You are free to use this software for research purposes, but you should not redistribute it without the consent of the authors.
- In addition, end users are expected to include adequate citations and acknowledgments whenever results or derivatives that are based on the software are presented or published.
 - Citation to *ACTIVE* should include the following:

- Baker RM, Brasch ME, Manning ML, and Henderson JH. Automated, contour-based tracking and analysis of cell behavior over long timescales in environments of varying complexity and cell density. *Journal information to be updated when available*.
- Citations to work foundational to ACTIVE are suggested to include the following, at a minimum:
 - Idema T. A new way of tracking motion, shape, and divisions. *European Biophysics Journal*. 2013;1-8.
 - Crocker JC, Grier DG. Methods of digital video microscopy for colloidal studies. *Journal of Colloid and Interface Science*. 1996;179(1):298-310.
 - Gao Y, Kilfoil ML. Accurate detection and complete tracking of large populations of features in three dimensions. *Optics Express*. 2009;17(6):4685-704.

References:

- [1] Baker RM, Brasch ME, Manning ML, Henderson JH. Automated, contour-based tracking and analysis of cell behaviour over long time scales in environments of varying complexity and cell density. *Journal of The Royal Society Interface*. 2014;11:20140386.
- [2] Idema T, Dubuis JO, Manning ML, Nelson PC, Liu AJ. Wavefronts and Mechanical Signaling in Early Drosophila Embryos. *Biophysical Journal*. 2013;104:329A-A.
- [3] Crocker JC, Grier DG. Methods of digital video microscopy for colloidal studies. *Journal of Colloid and Interface Science*. 1996;179:298-310.
- [4] Gao Y, Kilfoil ML. Accurate detection and complete tracking of large populations of features in three dimensions. *Optics Express*. 2009;17:4685-704.

Appendix Three: MATLAB Analysis for Biomechanical Torsion

Testing of Femurs

Overview

A custom MATLAB algorithm was developed to help analyze the torsional testing results in **Chapter 5**. Torsional testing data was collected using a materials testing unit (QTest, MTS Corporation), and images of the femur were acquired in real-time during testing at a frequency of 1 Hz. The MATLAB algorithm overlays the testing images with the loading trace, allowing the user to better interpret the loading trace based on visual observations of the femur. Additionally, the algorithm calculates torque, energy, and stiffness values from the loading trace.

Using the Code

When using the code, you will be asked to select a .tif stack (images of the testing) and a corresponding .txt file (MTS output text file). For this study, the .txt file contained the signal names in the 5th line, and the data values starting in the 7th line, and the the code is written to read a .txt file with this structure. Changes to the “textscan” call can be made if reading in a different .txt layout is required. The code next will ask for a start time and an end time to read the data. All data that is read will be analyzed, so if users want to remove the toe region from the loading curve they should specify a start time accordingly.

The code will use this information and generate a series of plots at the same frequency as the image acquisition (1 Hz in this case). For a frequency of 1 Hz, a plot will be generated for each second of testing, with the loading curve up to that second plotted, and the corresponding image overlaid. Sequential images will be saved as individual .tiff images. The code will then

calculate max torque, energy-to-failure, and torque and energy at 70 Degree rotation (used as maximum rotation angle in our study). Additionally the code will calculate stiffness by performing linear regression on the “start_angle” and “end_angle” parameters specified in the code (user should hard code change these).

Code

```
% %%%%%%%%%%%%%%%%%%%%%%%%%%%%%%%%%%%%%%%%%%%%%%%%%%%%%%%%%%%%%%%%%%%%%%%%%%
%
% Allow user to select .tiff stack and video of mechanical testing, then
% combine those into one plot
%
% GLOBAL PARAMETERS
image_frequency = 1; % Specify the image frequency in Hz
radius = 12.01; % Specify the torque system radius in mm (used in plotting to
% calculate torque)
start_angle = 0; % Beginning angle for calculating stiffness (beginning of
% linear region)
end_angle = 30; % End angle for calculating stiffness (end of linear region)
%
% Open the tif stack of the tested images to be loaded
[filename, pathname] = uigetfile({'*.tif'}, 'Select a tif stack');
stackname = [pathname filename];
image_info = imfinfo(stackname);
number_images = numel(image_info);
%
% Open the .txt file, and store the values and headers
[filename2, pathname2] = uigetfile('*.txt', 'Pick the text file to open');
fileID = fopen([pathname2 filename2]);
headers = textscan(fileID, '%q %q %q %q', 1, 'HeaderLines', 5, 'Delimiter', ',');
values = textscan(fileID, '%f %f %f %f', 'HeaderLines', 7, 'Delimiter', ',');
%
% Define the load and displacement vectors (should always be column 3 and 1
% for our testing setup; can check headers to make sure)
load = values{1};
time = values{2};
displacement = values{3};
frequency = values{4};
%
% % Find where in the data the frequency generator is turned on and adjust
% % the data accordingly
% index = find(frequency == 1, 1, 'first');
index = find(displacement ~= 0, 1, 'first');
load = load(index:length(load));
time = time(index:length(time));
displacement = displacement(index:length(displacement));
%
% Adjust the time so it now starts at time = 0
time = time - time(1);
```

```

%
%%%%%%%%%%%%%%%%%%%%%%%%%%%%%%%%%%%%%%%%%%%%%%%%%%%%%%%%%%%%%%%%%%%%%%%%
% This is added to allow the user to specify a start and end point for the
% data.
prompt = {'Start Time (s):', 'End Time (s):'};
dlg_title = 'Testing Parameters';
num_lines = 1;
def = {'0', num2str(time(length(time)))};
answer = inputdlg(prompt, dlg_title, num_lines, def);
%
start_time = str2num(answer{1});
end_time = str2num(answer{2});
%%%%%%%%%%%%%%%%%%%%%%%%%%%%%%%%%%%%%%%%%%%%%%%%%%%%%%%%%%%%%%%%%%%%%%%%
%
% Now adjust the data based upon start and end time
bool_data = time >= start_time & time <= end_time;
time = time(bool_data);
load = load(bool_data);
displacement = displacement(bool_data);
time = time - time(1);
displacement = displacement - displacement(1);
load = load - load(1);
%
%Determine plotting boundaries
xmin = min(displacement*180/pi/radius); % Converted to degrees
xmax = max(displacement*180/pi/radius);
ymin = min(radius*load); % Converted to Torque
ymax = max(radius*load);
%
% Specify save location
[~, figbase, ~] = fileparts(filename);
mkdir(pathname, figbase);
addpath(pathname, figbase);
%
% Index for while loop
i = start_time*image_frequency + 1;
testing_time = max(time) + 1/image_frequency;
current_time = time(1);
%
% Loop that generates and saves tiff images for each "frame" of testing
while current_time <= testing_time
    if i <= number_images
        image = imread(stackname, i, 'Info', image_info);
        image = padarray(image, 5, 5);
    else
        image = imread(stackname, 1, 'Info', image_info)*0;
    end
%
    % Isolate data only before loading time; Convert to Angle v. Torque
    bool_test = time <= current_time;
    displacement_plot = displacement(bool_test)*180/pi/radius; % In degrees
    load_plot = load(bool_test)*radius; % Torque in N-mm
%
    % Calculate the energy up to loading time
    if sum(bool_test) > 1
        energy = trapz(displacement_plot, load_plot);
    else

```

```

        energy = 0;
    end
%
% Plot data up to loading time; Include torque, displacement, and
% energy on plot
h = figure(i);
ax1 = axes('Position',[0 0 1 1],'Visible','off');
ax2 = axes('Position',[.3 .1 .6 .8]);
plot(ax2,displacement_plot, load_plot,'r','LineWidth',2);
axis([xmin xmax ymin 2*ymax]);
xlabel('Rotation Angle (degrees)')
ylabel('Torque (N-mm)')
title(['Time ' num2str(current_time,3) ' seconds'])
hold on
imagesc([xmin xmax], [2*ymax ymax],image)
%
text_block = {'Time';
[num2str(current_time,3) ' seconds'];
' ';
'Rotation Angle (degrees)';
num2str(displacement_plot(length(displacement_plot)));
' ';
'Torque (N-mm)';
num2str(load_plot(length(load_plot)));
' ';
'Energy (N-mm-deg)';
num2str(energy)};
%
axes(ax1); % sets ax1 to current axes
text(.025,0.6,text_block)
hold off
%
figname = [figbase, '_',num2str(i)];
saveas(h, [pathname, figbase, '\', figname] , 'tif');
close(h);
current_time = current_time + 1/image_frequency; % Advance the time
i = i + 1;
end
%%%%%%%%%%%%%%%%%%%%%%%%%%%%%%%%%%%%%%%%%%%%%%%%%%%%%%%%%%%%%%%%%%%%%%%%
% Now let's calculate some values
torque = load*radius;
angle = displacement*180/pi/radius;
%
% Perform linear regression on first 60 degree worth of data
bool_regression = angle >= start_angle & angle <= end_angle;
p = polyfit(angle(bool_regression),torque(bool_regression),1);
yfit = polyval(p,angle(bool_regression));
yresid = torque(bool_regression) - yfit;
SSresid = sum(yresid.^2);
SStotal = (length(torque(bool_regression))-1)*var(torque(bool_regression));
stiffness = p(1); % Stiffness is slope of regression curve
r_squared = 1 - SSresid/SStotal; % Calculate R squared for the regression
%
% Max Torque and energy
max_torque = max(torque);
index1 = find(torque==max(torque),1,'First');
angle_max_torque = angle(index1);

```

```

energy_max_torque = trapz(angle(1:index1),torque(1:index1));
%
% Energy at end of testing
energy_break = trapz(angle,torque);
%
% Torque and Energy at 70 Degree Rotation
index2 = find(angle >= 70,1,'First');
torque_70 = torque(index2);
energy_70 = trapz(angle(1:index2),torque(1:index2));
%%%%%%%%%%%%%%%%%%%%%%%%%%%%%%%%%%%%%%%%%%%%%%%%%%%%%%%%%%%%%%%%%%%%%%%%

```

Sample .txt Format (comma delimited): (Note: Digital Input was from frequency generator that controlled data collection and image acquisition)

"""

"Test Method","MEO_torsion_mouse_femur.msm"

"Sample I. D.", "Sample7.mss"

"Specimen Number", "8"

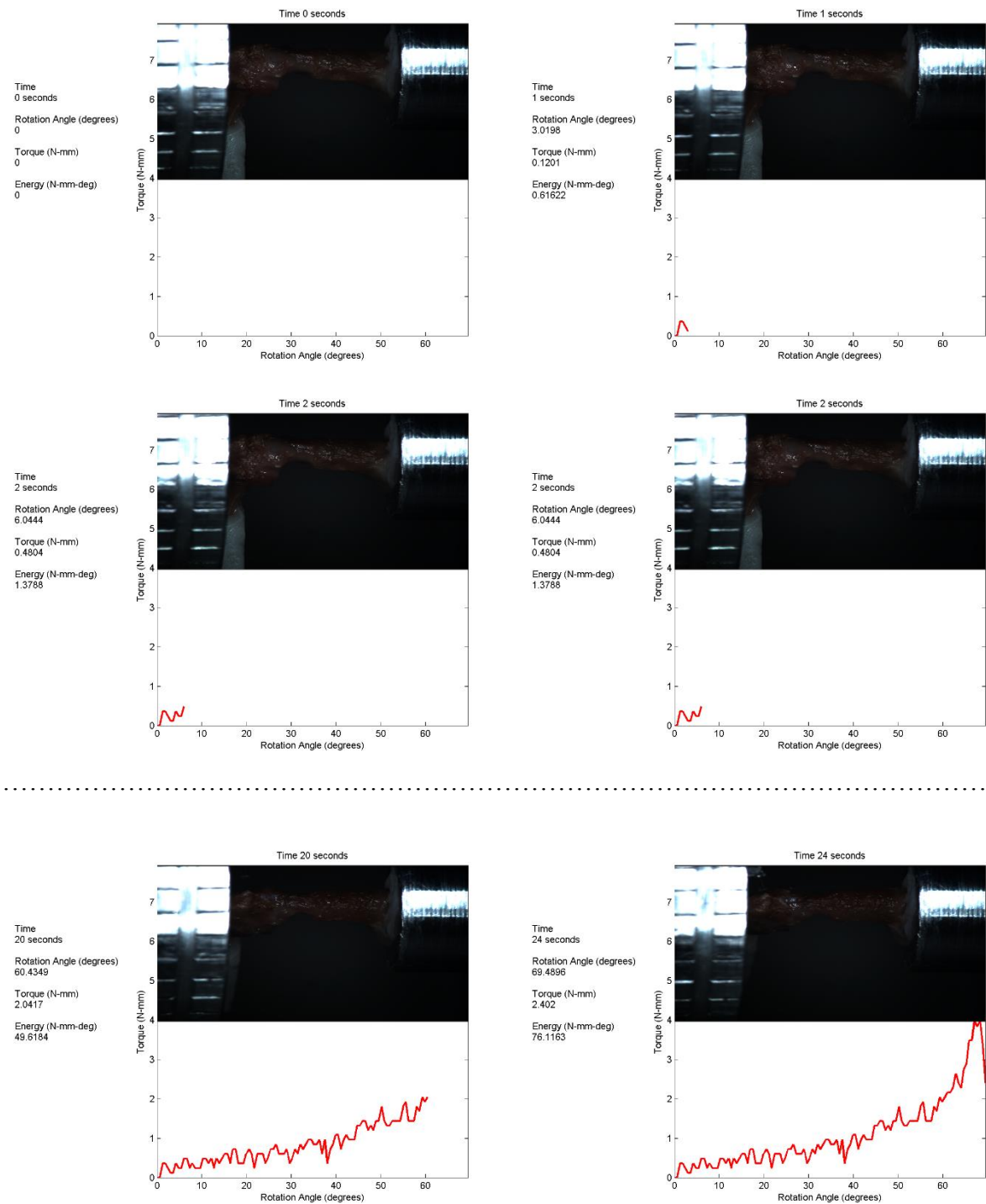
"Load (N)", "Time (s)", "Crosshead (mm)", "_DigitalInput1 ()"

```

-0.06,0.400,0.000,0.000
0.01,0.800,0.000,0.000
0.00,1.000,0.000,0.000
0.00,1.200,0.000,0.000
0.00,1.400,0.000,0.000
0.00,1.600,0.000,0.000
-0.01,1.690,0.000,1.000
0.00,2.000,0.164,1.000
0.00,2.600,0.545,0.000
0.00,2.800,0.670,1.000
0.00,3.000,0.796,1.000
0.00,3.200,0.924,1.000
0.00,3.400,1.050,0.000

```

Sample Image Sequence:



Appendix Four: Functionalized Hydroxyapatite

Motivation

For the SMP PCL-PEG foams used in **Chapter 5**, we incorporated hydroxyapatite, a bioactive molecule, physically into the foam during fabrication. Relying on physical incorporation, however, resulted in low loading efficiencies of 40% (refer to **Figure 5-2a**). One method that may improve the loading efficiency is to functionalize HA nanoparticles and chemically crosslink them into the network. To do this, HA can be functionalized using the same reactive end-group that was used for PEG functionalization in Chapter 4 (**Section 4.3.1.2**). The approach for achieving this as well as preliminary results are discussed below.

Method

HA nanoparticles were functionalized (**Scheme A4-1**) with vinyl end-groups. Following a published protocol[1], hydroxyl groups on HA nanoparticles were grafted with hexamethylene diisocyanate, followed by addition of ethylene glycol (EG) (**Scheme A4-2a**) to add a reactive hydroxyl group to the grafted chain. This functionalized HA was then reacted with allyl isocyanate (**Scheme A4-2b**), yielding a reactive vinyl group that can be end-linked through thiol-ene chemistry with the functionalized PCL and PEG macromers. Detailed reaction steps for each step are shown in **Scheme A4**.

To determine if grafting was successful, fourier transform infrared spectroscopy (FTIR) and thermogravimetric analysis (TGA) was performed on unmodified and modified HAp particles. For FTIR, HAp powder was mixed with potassium bromide salt and compressed to form a thin film for scanning. An average of 15 scans were recorded and the absorption peaks compared between unmodified and modified HAp. For TGA analysis, samples were heated at 20

°C-min⁻¹ to 700 °C and the thermal degradation profiles compared. Furthermore, 80PCL-20PEG-20HA (20% loading of HAp) foams were fabricated following the modified porogen leaching technique described in **Chapter 4 (Section 4.3.2)**, with the only difference being modified HAp particles were mixed with the polymer solution before adding the solution to the fused salt template. TGA analysis was performed on the resulting foam to determine the loading efficiency.

Preliminary Results

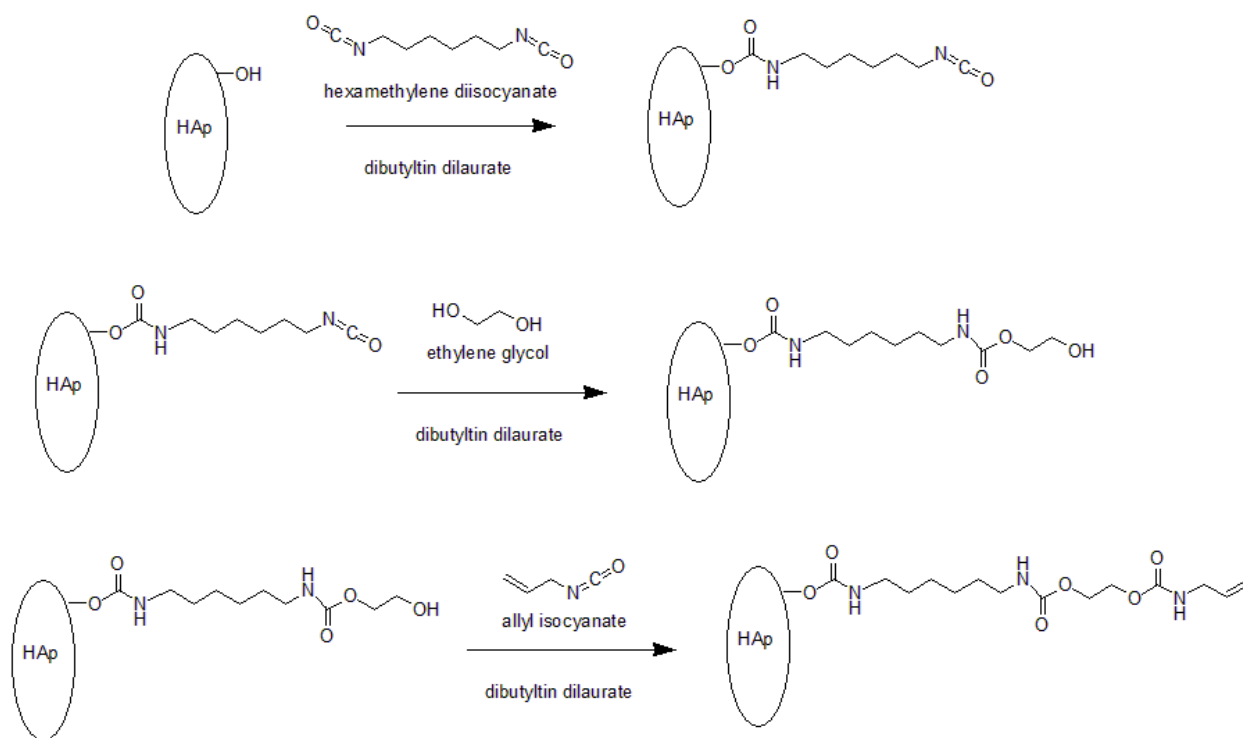
Functionalization of hydroxyapatite was confirmed by FTIR and TGA. FTIR analysis (**Figure A4-1a**) showed the presence of absorption bands at 1610 cm⁻¹ and 1580 cm⁻¹ for the functionalized HA which are not present in the unmodified HA, suggesting grafting was successful. The absorption bands at 1610 cm⁻¹ and 1580 cm⁻¹ are from the presence of –NHCO– [1]. No absorption band was present at 2255 cm⁻¹, which would be present if free isocyanate remained, suggesting EG was grafted to the isocyanate band. However, no observable difference in absorption spectra were found between HAp-EG and HAp-EG-DA, so it was unclear if this last reaction step was successful. TGA analysis of unmodified HAp revealed minimal weight loss when heated to 700 °C, whereas functionalized HAp exhibited a weight loss of 11% when heated to 700 °C (**Figure A4-1b**), supporting our findings that a polymer chain was grafted to the HAp.

80PCL-20PEG-20HA foams were fabricated using the modified HAp, and TGA analysis of those foams showed 14% weight remaining following heating to 700 °C, which suggests a loading efficiency of ~70% (79% if we account for the EG degradation that is assumed to be grafted on the HAp particle). This preliminary results suggest this method of HA incorporation may be more efficient than physical incorporation, however further studies should be done to

determine grafting efficiency, whether DA was successfully grafted, and if the modified HA is chemically linked to the PCL-PEG scaffold.

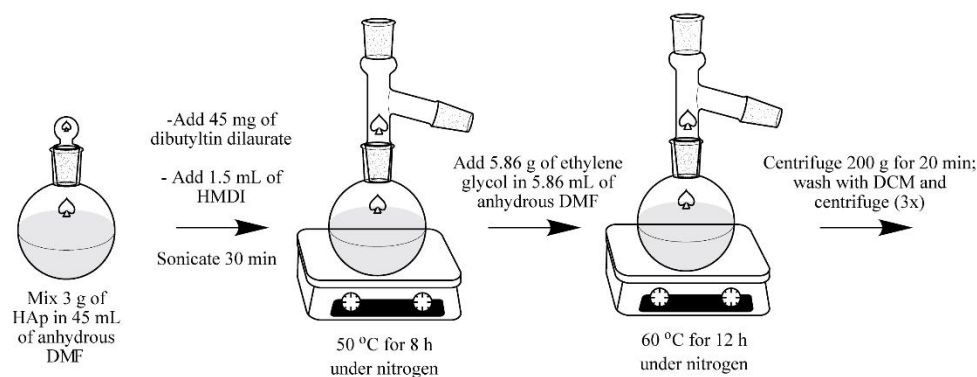
References

[1] Lee HJ, Choi HW, Kim KJ, Lee SC. Modification of hydroxyapatite nanosurfaces for enhanced colloidal stability and improved interfacial adhesion in nanocomposites. *Chemistry of materials*. 2006;18:5111-8.

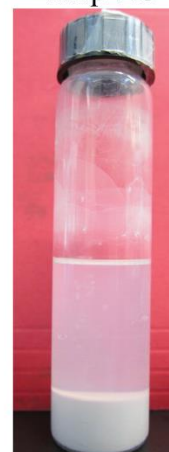


Scheme A4-1. Hydroxyapatite nanoparticles (HAp) are functionalized with a reactive vinyl group following a 3-step process. First unmodified HAp is grafted with hexamethylene diisocyanate with dibutyltin dilaurate as the catalyst. Next ethylene glycol is added to the reaction flask and grafted to the free isocyanate group on the modified HAp. Finally allyl isocyanate is reacted with the hydroxyl groups of the grafted ethylene glycol to add a vinyl terminated end group to the HAp. Detailed reaction processes for steps 1 and 2 are shown in **Scheme A4-2a**, and a detailed reaction process for step 3 is shown in **Scheme A4-2b**.

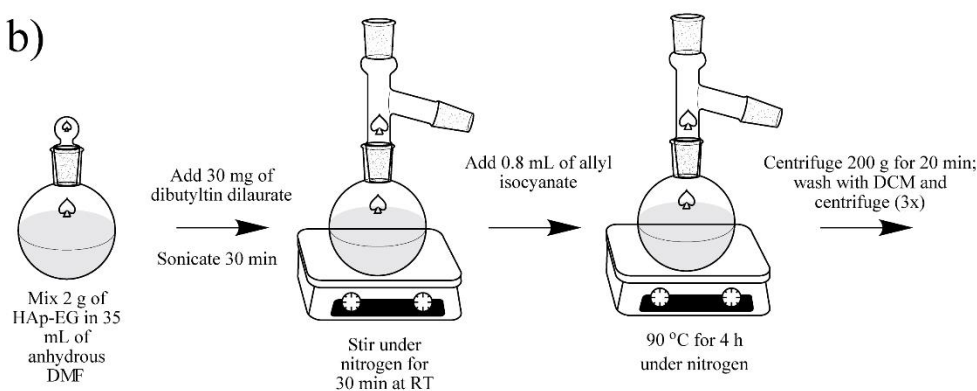
a)



HAp-EG



b)



HAp-EG-DA



Scheme A4-1. Reaction protocol for (a) grafting ethylene glycol (EG) to HAp to form HAp-EG and (b) end-capping allyl isocyanate to the HAp-EG particles for form functionalized HAp-EG-DA. For (a) HAp particles are reacted with hexamethylene diisocyanate, using dibutyltin dilaurate as a catalyst, for 8 h at 50 °C in DMF; next ethylene glycol is added to the reaction flask and the reaction carried out at 60 °C for 12 h; finally the HAp-EG particles were centrifuged and washed 3 times with DCM. For (b) the HAp-EG particles were reacted with allyl isocyanate, using dibutyltin dilaurate as the catalyst, at 90 °C for 4 h, followed by centrifugation and washing with DCM 3 times, and finally drying.

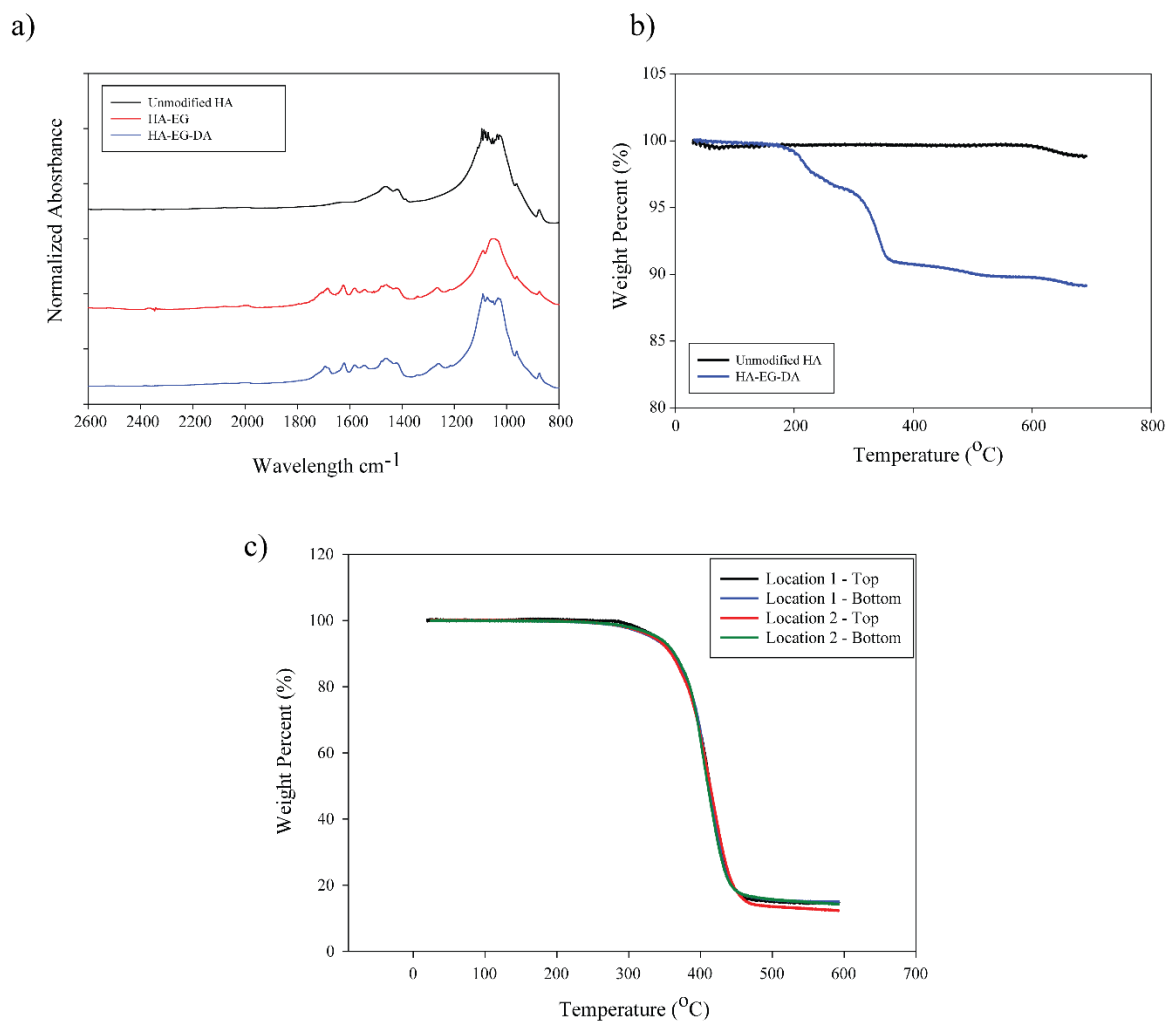


Figure A4-1. Functionalization of HA nanoparticles. (a) Fourier transform infrared spectroscopy (FTIR) comparison of functionalized and unmodified HA particles indicate new absorption bands at 1610 cm^{-1} and 1580 cm^{-1} , indicative of successful EG grafting; however, no detectable changes in band absorption were found after grafting with DA. (b) TGA degradation traces show a polymeric degradation for the functionalized HA-EG-DA particles when compared to the unmodified particles, which exhibit minimal weight loss up to $700\text{ }^{\circ}\text{C}$. (c) 80PCL-20PEG-20HA scaffolds had an average of 14% weight remaining, indicating a loading efficiency of 70%, which is better than the 40% from physical HA incorporation in **Chapter 5**.

Appendix Five: Biodegradable Amorphous SMP Foams

Motivation

In **Chapter 5**, we showed that an amorphous, glass transition (T_g) based shape memory polymer (SMP) foam was able to serve as a stable synthetic bone substitute in a critical size segmental defect model. In that study we employed an acrylate-based system that was not biodegradable, which limits its use as a clinically-relevant synthetic bone substitute. Moving forward, if SMP foams are to be applied in clinical applications it is necessary to use a biodegradable chemistry. As a step towards achieving that goal, we have begun exploring a biodegradable poly(D,L-lactide) (PDLLA) chemistry that was developed previously in our lab as a biodegradable stent coating[1, 2] and later applied as an SMP fibrous mat for *Active Cell Culture* and orthopedic applications[3]. Here we have begun exploring two approaches for fabricating PDLLA SMP foams: 1) thiol-ene mediated crosslinking of PDLLA macromers (similar to PCL-PEG system in **Chapter 4**); and 2) thermoplastic polyurethane PDLLA foams. Below we detail the methods for fabricating these foams as well as some preliminary results for their thermal and thermomechanical properties.

Method

Thiol-ene mediated crosslinked networks: Chemically crosslinked networks of PDLLA were synthesized using thiol-ene mediated chemistry (**Scheme A5-1**). First, a PDLLA diol was fabricated using ring opening polymerization of D,L Lactide initiated by 1,4 butanediol, following a previously reported procedure[3]. PDLLA diols with molecular weights of $M_n = 3$ kDa and $M_n = 16$ kDa were synthesized. Next, each PDLLA diol was functionalized following the same protocol described in **Chapter 4** for PEG end-capping (**Section 4.3.1.1**), forming

PDLLA diallyl acrylamide. Foams of the PDLLA diallyl acrylamide were fabricated following the same procedure detailed in **Chapter 4 (Section 4.3.2)**.

PDLLA-POSS polyurethane foams: PDLLA-POSS polyurethane (TPU) foams were fabricated by solvent casting PDLLA-POSS TPU in a fused salt template. The PDLLA-POSS TPU (**Scheme A5-2**) was kindly provided by Ling-Fang Tseng. TPUs with molecular weights of $M_w = 128$ kDa and $M_w = 160$ kDa were used. Foams were fabricated by first dissolving the TPU in chloroform in a 3:1 solvent:polymer ratio. This solution was stirred at 55 °C to lower the viscosity. The solution was syringed into a fused salt template (5.5 g of salt) with a ratio of 5:1 salt:polymer. Since the solution was too viscous to completely infiltrate the salt, vacuum was pulled to assist infiltration. After vacuum infiltration, the chloroform was evaporated at room temperature for 12 h and then in a 50 °C vacuum oven for 24 h. The permanent shape of the TPU was then set by heating the polymer/salt construct to 140 °C (temperature above the melt transition temperature of POSS) for 10 min and cooling at room temperature to recrystallize the POSS. Next the samples were placed in 60 °C water for salt extraction. Foams were dried in a vacuum oven and their thermal and thermomechanical properties tested.

Characterization: Thermal characterization of the foams was conducted using thermogravimetric analysis (TGA) to confirm salt extraction and differential scanning calorimetry (DSC) to determine thermal transition temperatures. Shape memory characterization was performed using a dynamic mechanical analyzer in compression, following a typical one-way shape memory cycle.

Preliminary Results

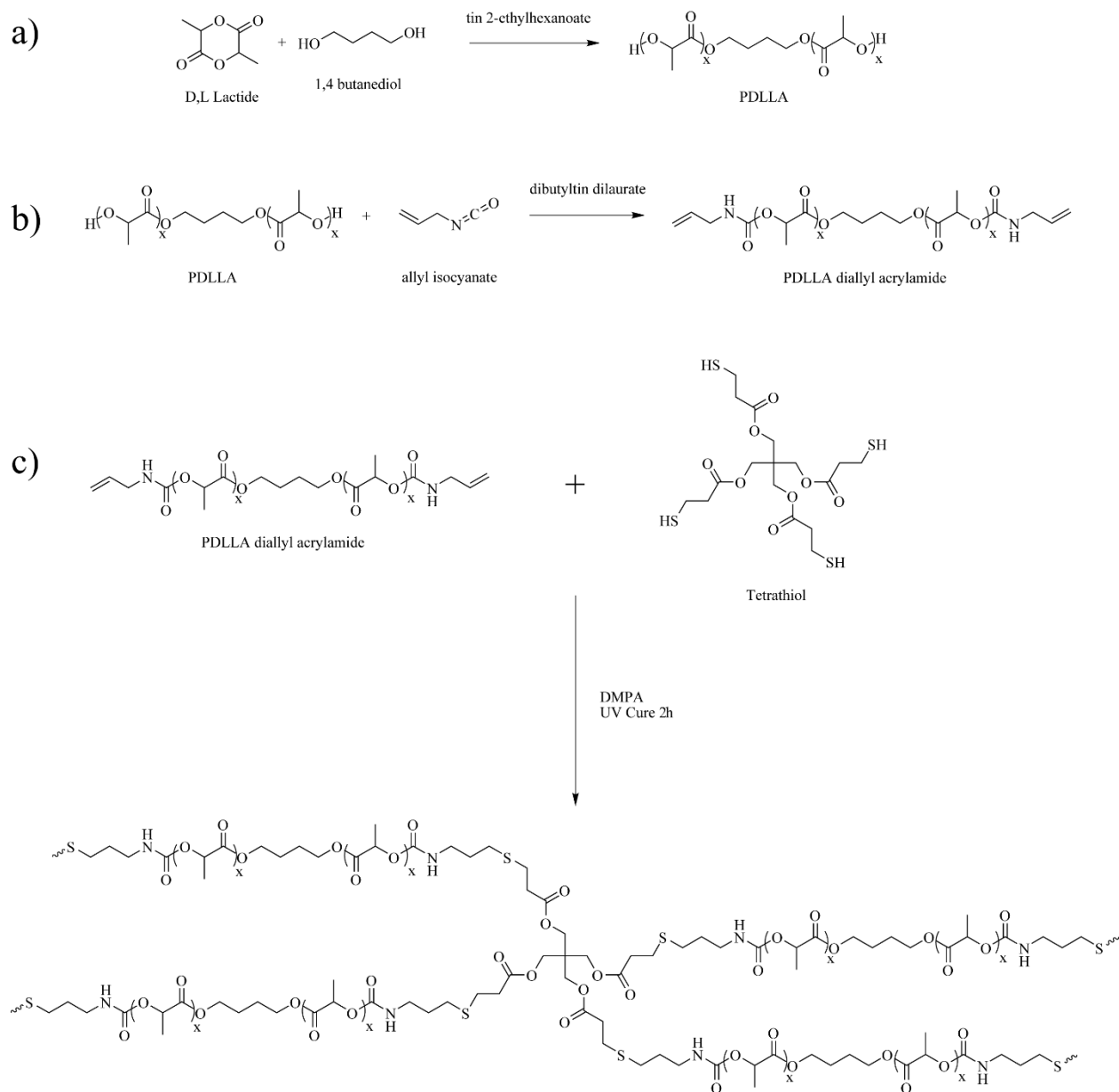
Thiol-ene mediated crosslinked networks: TGA analysis of salt-extracted foams showed that salt removal was complete and the degradation profile of the PDLLA foams was similar to the PDLLA diol and macromer (**Figure A5-1a**). Interestingly the onset of degradation was higher for the foams than the macromer or diol, which could be due to crosslinking with tetrathiol or an artifact of heat transfer. The thermal properties of the resulting foams were investigated using DSC, where the glass transition temperature (T_g) was found to be influenced by PDLLA molecular weight and hydration (**Figure A5-1b**). PDLLA with a molecular weight of 3 kDa resulted in foams with a dry T_g of 42 °C, whereas PDLLA with a molecular weight of 16 kDa resulted in foams with a dry T_g of 51 °C. Upon hydration for 24 h at 37 °C, the T_g of each foam decreased by 13 °C. With this system, a hydrated T_g near body temperature was achieved. Shape memory analysis of foams programmed at 80 °C to 60% strain revealed foams had excellent shape fixing, but shape recovery was very low (**Figure A5-1c**). Low shape recovery is likely attributed to the low gel fraction obtained for these scaffolds (80% gel fraction). Low gel fractions are likely a result of incomplete functionalization of the PDLLA macromer and low polymer concentrations during curing. To address these issues, we should investigate the effect of polymer concentration on sample curing and gel fraction, as well as investigate different functionalization techniques to improve the degree of functionalization. HNMR could be used to quantitatively find the degree of functionalization. Furthermore, changing to an acrylate end-cap (as was used for the PCL functionalization in **Chapter 4, Section 4.3.1.1**) may provide better crosslinking.

PDLLA-POSS polyurethane foams: DSC analysis of PDLLA-POSS TPU foams revealed that in the dry state, foams had a T_g of 51 °C which was similar for the PDLLA-POSS TPU before dissolving and fabricating a foam (**Figure A5-2a**). The POSS hard block of the TPU has a melt transition temperature (T_m) of 127 °C, showing that the setting temperature of 140 °C as discussed above is appropriate. Upon hydration, the T_g of the TPU and TPU foam dropped to ~41 °C (data not shown), consistent with our previous study[3]. Shape memory testing of the TPU foam using a dynamic mechanical analyzer revealed that the foams have excellent shape fixing and shape recovery in compression (**Figure A5-2b**). Samples were heated to 60 °C and uniaxially compressed to 40% strain, cooled to -10 °C to fix the strain, unloaded, and then heated to 85 °C for recovery. Samples had >99% fixing ratio and >97% recovery ratio. The effect of deformation temperature on the shape memory behavior of the TPU foams was investigated to determine if the recovery temperature had a strong dependence on the deformation temperature. Results show that when the deformation temperature decreases, the onset of recovery also decreases (**Figure A5-2c**). This enables programming at a lower temperature to ensure recovery will happen when heated at body temperature. One interesting observation was when deforming at 80 °C the sample did not fully recover. We hypothesize this may be due to crystallization of the POSS domains (T_c ~72 °C according to **Figure A5-2a**) which may alter the permanent shape during deformation at 80 °C. Additionally, stress relaxation of the thermoplastic PDLLA chains may contribute to incomplete recovery.

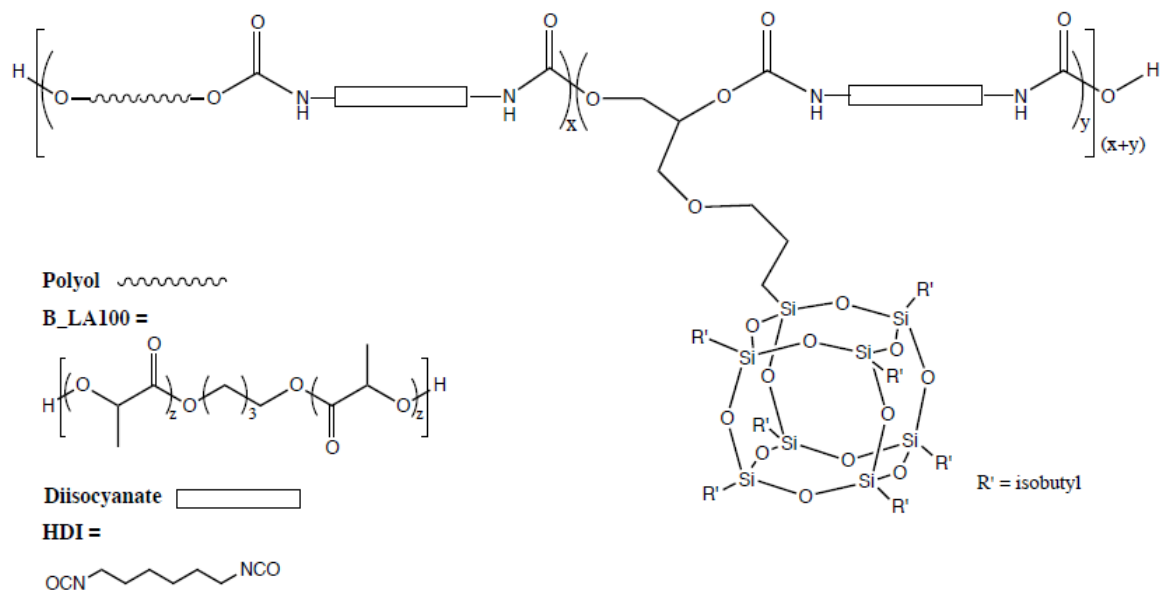
References

- [1] Guo Q, Knight PT, Mather PT. Tailored drug release from biodegradable stent coatings based on hybrid polyurethanes. *Journal of Controlled Release*. 2009;137:224-33.

- [2] Knight PT, Lee KM, Qin H, Mather PT. Biodegradable thermoplastic polyurethanes incorporating polyhedral oligosilsesquioxane. *Biomacromolecules*. 2008;9:2458-67.
- [3] Tseng L-F, Mather PT, Henderson JH. Shape-memory-actuated change in scaffold fiber alignment directs stem cell morphology. *Acta biomaterialia*. 2013;9:8790-801.



Scheme A5-1. Thiol-ene mediated crosslinking of PDLLA macromers. (a) PDLLA diol is fabricated using ring opening polymerization of D,L Lactide initiated by 1,4 butanediol; (b) the PDLLA diol is functionalized by end-capping with allyl isocyanate to fabricate a PDLLA diallyl acrylamide; (c) The PDLLA diallyl acrylamide is crosslinked via thiol-ene mediation.



Scheme A5-2. Chemical structure of the PDLLA thermoplastic polyurethane (TPU). PDLLA diol (polyol) was reacted with hexamethylene diisocyanate (HDI) and polyhedral oligomeric silsesquioxane (POSS) under typical urethane polymerization conditions. Reprinted with permission from ref [3].

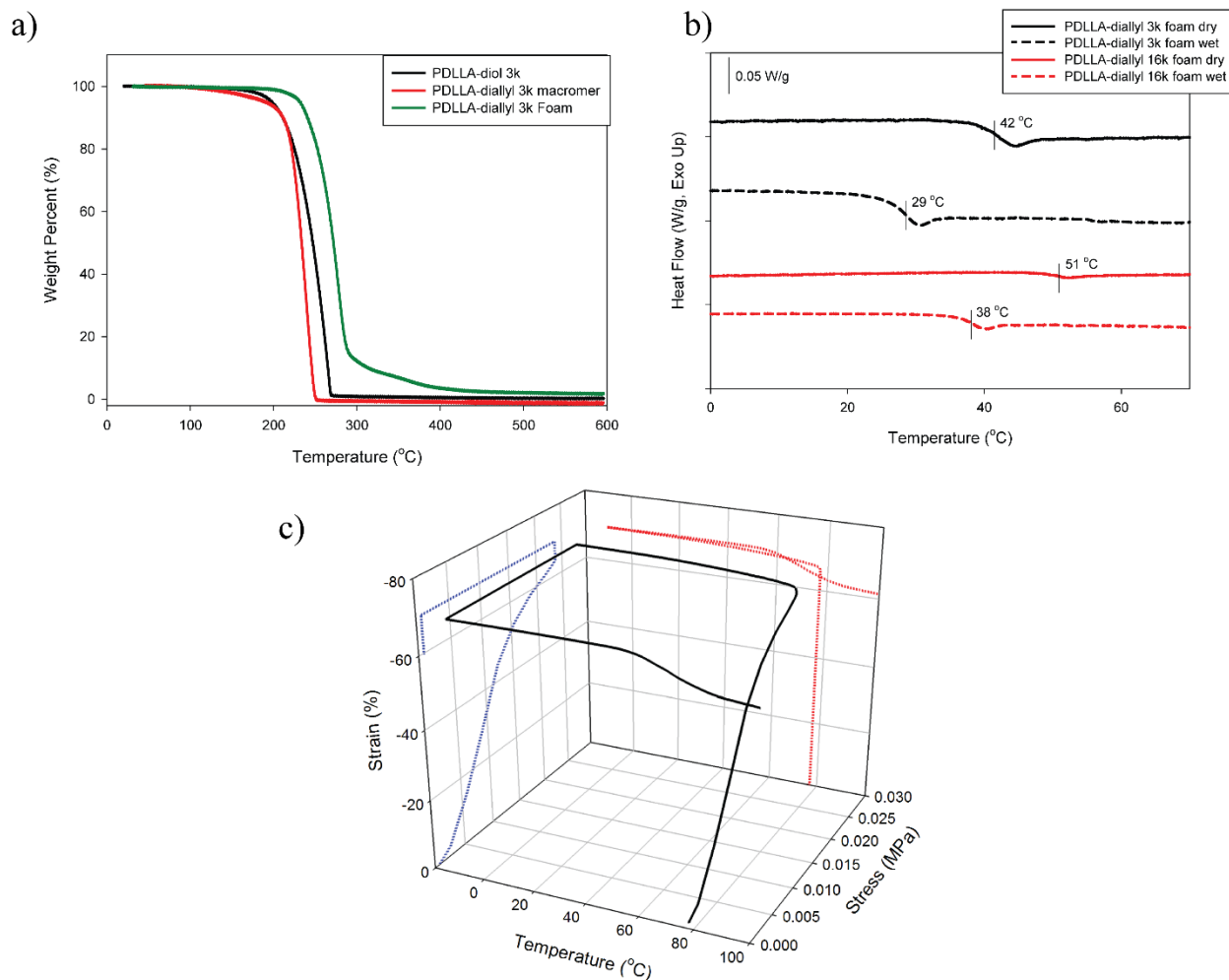


Figure A5-1. Thermal and thermomechanical characterization of thiol-ene mediated PDLLA foams. (a) TGA analysis shows salt was completely extracted from foams; (b) DSC 2nd heat traces reveal a lower T_g for the 3 kDa foam compared to the 16 kDa foam, and hydration plasticizes the T_g causing a drop of ~ 11 °C in T_g ; (c) one-way shape memory in compression shows that a sample deformed at 80 °C had excellent shape fixing upon cooling to -10 °C, however recovery was very limited (14% recovery).

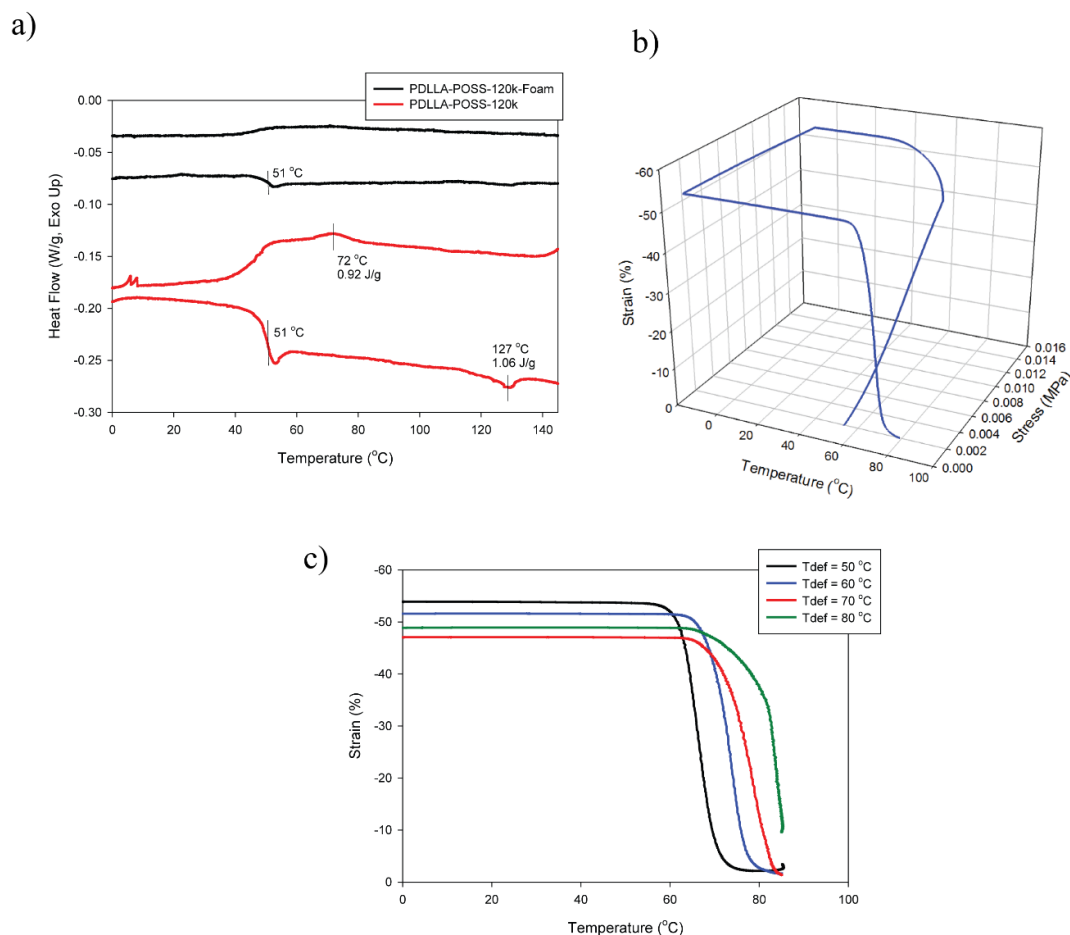


Figure A5-2. Thermal and thermomechanical properties of PDLLA TPU foams. (a) DSC 2nd heating trace of both the TPU foam (black) and the TPU before foam fabrication (red) had a dry T_g of 51 °C. This T_g drops to 41 °C (not shown) due to plasticization when placed in water; (b) one-way shape memory behavior in compression reveals excellent shape fixing and shape recovery of a TPU foam deformed at 60 °C; (c) the effect of deformation temperature during a one-way shape memory cycle shows that deforming near T° (51 °C) results in the lowest onset of recovery temperature. Higher deformation temperature results in a higher onset of recovery temperature. All deformation temperatures with the exception of 80 °C result in full recovery of the sample. All heating/cooling rates were 3 °C·min⁻¹

Appendix Six: Shape Memory Assisted Cell Seeding (SMACS)[†]

Motivation

Control over the seeding density and distribution of cells cultured on 3D scaffolds is critical to tissue formation within the scaffolds. Cell seeding density has been reported to affect bone mineralization in poly(lactide-co-glycolide) scaffolds with a seeding density of 1×10^6 cells- cm^{-3} leading to more bone mineralization than a seeding density of 0.5×10^6 cells- cm^{-3} , whereas minimal difference was observed between seeding densities of 1×10^6 cells- cm^{-3} and 10×10^6 cells- cm^{-3} [1]. However, homogenous cell distribution throughout the scaffolds was better at higher seeding densities. Similarly, seeding densities of chondrocytes in agarose gels have been reported to affect the resulting mechanical properties, with higher seeding densities resulting in better mechanical properties[2].

Typical cell seeding in 3D constructs is achieved through static methods, such as droplet seeding or solution seeding. These methods however may result in low seeding efficiencies and heterogeneity in the cell distribution within the scaffolds[3-5]. As an alternative to static seeding methods, dynamic seeding methods such as perfusion bioreactors have been developed[6, 7]. Bioreactors have greatly improved seeding efficiency and distribution homogeneity, but require purchasing or building complex bioreactors. One possibility to improving static seeding methods the use of suction to facilitate cell seeding. This concept has been reported successfully with an elastomeric poly(L-lactide-co-caprolactone) sponge where a custom cell seeding apparatus was developed to compress and induce suction into the polymer sponges[8]. This study, however, required the use of external mechanical loading to induce suction into the scaffold. Shape memory polymers (SMPs) may serve as a novel approach to improve cell seeding using the

[†] This work was performed in collaboration with Ling-Fang Tseng and Jing Wang, who contributed equally.

shape changing properties of SMPs. In this study, we aimed to develop a series of methods to test the hypothesis that shape memory triggered expansion in cell-containing medium can facilitate cell penetration into the interior of a porous scaffold. We have termed this approach “Shape Memory Assisted Cell Seeding,” or “SMACS”.

To achieve this, we first investigated an alternative salt fusion approach to improve pore interconnectivity compared to the scaffolds fabricated in **Chapters 4-6**. We then fabricated a series of scaffolds with glass transition temperatures (T_g) ranging from room temperature to 37 °C, which we expected to have different recovery kinetics when triggered to change shape at 37 °C (lower T_g leading to faster recovery). To test whether SMACS can improve cell seeding, we investigated cell distribution into scaffolds triggered to expand. We explored 3 main variables thought to contribute significantly to SMACS: 1) degree of interconnectivity (controlled by water % during fusion); 2) SMP scaffold compression ratio; 3) recovery kinetics (changing scaffold composition).

To-date, we have established the protocols to investigate SMACS, from sample preparation to cell culture and imaging. Below we discuss the methods and preliminary results, and note that we are currently developing the methods for analyzing the cell images acquired.

Method

Salt Fusion: To improve pore interconnectivity, we modified the salt leaching technique that was used in **Chapters 4-6**. Here, 6 g of salt (300-500 μm) was added to a 20 mL glass vial. Next, water was added to the salt at 6, 10, or 15% by weight, and the salt and water were mixed with a 22 G needle tip until fully mixed. The hydrated salt was then compressed using a 10 mL syringe plunger to form a compact “puck” of hydrated salt. These pucks were then centrifuged at

4000 rpm for 15 min to further compact the pucks. After centrifugation, vials were left in a fumehood over night to allow water to evaporate. The vials of salt were then completely dried in a vacuum dessicator for 24 h. After drying, these fused salt pucks were used to fabricate foams.

Foam Fabrication: Foams of tert-butyl acrylate (tBA) and butyl acrylate (BA) were fabricated following the same procedure discussed in **Chapter 5 (Section 5.3.2.2)**, using the new fused salt templates. In this study, we fabricated tBA-BA foams with 5 different compositions to determine the effect of composition on recovery temperature and recovery kinetics at 37 °C. Foams with compositions of 95-5, 91-9, 87-13, 83-17, and 79-21 were fabricated, and each sample was coated with polydopamine.

Foam Characterization: To determine the effect of foam composition on thermal properties, thermogravimetric analysis (TGA) and differential scanning calorimetry (DSC) were employed. For TGA, samples were heated to 600 °C at 20 °C-min⁻¹ in a Q500 thermogravimetric analyzer. DSC was performed using a Q200 differential scanning calorimeter to determine the effect of composition on the glass transition temperature (T_g) of the SMP foams. Second heating traces of samples heated to 80 °C at 3 °C-min⁻¹ were analyzed.

The effect of composition on compressive shape memory properties was investigated using a Q800 dynamic mechanical analyzer. Cylindrical foam plugs were heated to 90 °C and compressed to 60% strain. Samples were cooled to -10 °C at 3 °C-min⁻¹ to fix the deformation, unloaded, and then heated at 3 °C-min⁻¹ to 90 °C to observe recovery. The effect of composition on hydrated recovery at 37 °C was also investigated by programming cylindrical foams with a 50-60% compressive strain and submerging them in 37 °C water for 10 min.

Groups for Cell Culture: For cell experiments, we explored the effects of composition, salt fusion, and compression ratio on SMACs effectiveness. Three compositions (95-5, 87-13, and 79-21 of tBA-BA), three salt fusion conditions (6%, 10%, and 15% water), and three compression ratios (25%, 50%, and 75% fixed strain) were used. Compression ratios were only explored for the 79-21 tBA-BA sample to limit sample size. A positive control of vacuum-assisted seeding in a non-programmed sample was used. A negative control of no seeding assistance in a non-programmed sample was used. A total of 21 samples were used for cell culture experiments (**Table A6-1**).

Preparing Samples for Cell Culture: Cylindrical plugs with a 5 mm diameter and 5 mm height were cut for each group. Samples were programmed by heating in 55 °C water and compressing to the target strain (25, 50, or 75%) using calipers. The compressed strain was fixed by soaking in ice water for 20 s. Samples were dried in a dessicator store at 4 °C. One day prior to cell culture, samples were sterilized by soaking in an antibiotic-antimycotic solution at 4 °C.

Cell Culture: For cell experiments, C3H10T1/2 mouse fibroblasts were first expanded in complete growth medium (BME, 10 % FBS, 1 % penicillin/streptomycin, 1 % GlutaMAX) on T-175 flasks, with initial seeding at 5,000 cells-cm⁻². Expansion was conducted in a humidified incubator with 5% CO₂ at 37 °C. Medium was changed after 3 d, and cells were passaged at 80% confluence using 0.25% Trypsin. Cells at passage 15 were used for experiments.

Prior to seeding cells in programmed and control foams, foams were rinsed in 4 °C complete medium to remove the antibiotic-antimycotic solution. Foams were then placed in

wells of a 96-well plate. To prevent the foams from floating to the surface once medium was added, sterilized 22 G needle tips, cut to 6 mm, were wedged in each well. Next, 230 μL of cell solution at a concentration of $500,000 \text{ cells}\cdot\text{mL}^{-1}$ and a temperature of 37°C was added to each well, triggering expansion of the programmed samples. Samples were incubated in a 37°C humidified incubator for 5 h, then samples were moved to a new well and 230 μL of fresh medium was added. This was to prevent cells attached to the body of the well during seeding from infiltrating into the foams. Samples were cultures for an additional 19 h and then prepared for imaging.

Cell Imaging: After 24 h of culture (5 h seeding + 19 h additional culture), samples were rinsed in phosphate buffered saline (PBS) and fixed in a 10% formalin solution for 1 h. Samples were then stained with Hoechst 33342 nuclear dye at a concentration of $0.1 \text{ mg}\cdot\text{mL}^{-1}$ for 30 min. The exterior of each sample was imaged using a Leica DMI 4000B inverted microscope. Images were captured with a Leica DFC 340FX camera using a 10x/0.22 NA objective and the A4 filter. After imaging the exterior, each sample was cut in half parallel to the long axis of the cylinder. The interior of each sample was then imaged to determine the cell penetration profile. A Leica DMI 6000B inverted microscope with an automated stage was used to acquire images, along with an Andor Luca R camera and a 5x objective. To construct a complete profile of the foam cross-section, a 4x4 grid of each sample was imaged, and a z-stack ranging from -240 to 240 μm with 30 μm increments of each grid position was acquired. Micro-manager 1.4 was used for image acquisition. Following imaging of each sample, the Extended Depth of Field Plugin in ImageJ was used on each z-stack to get a single in-focus image for each grid location. Next, the

in-focus images from each grid position were then stitched using the Stitch plugin from Micro-Manager. This enabled construction of an in-focus image of the entire foam cross-section.

Preliminary Results

New Salt Fusion Approach: Compared to scanning electron microscopy (SEM) micrographs from the tBA-BA scaffolds in **Chapter 5 (Figure 5-8)**, we qualitatively observed increased pore interconnectivity with the new salt fusion approach employed here (**Figure A6-1**). Interestingly, increasing the weight % of water during salt fusion resulted in increased pore interconnectivity. With 6% water, pore morphology is cuboidal and small openings between pores were observed (**Figure A6-1, left**); when the water was increased to 10%, larger interconnected openings were observed between the pores with the architecture also appearing less cuboidal(**Figure A6-1, middle**); with 15% water, the cuboidal morphology is lost and an open, highly-interconnected architecture is revealed(**Figure A6-1, right**). However, with 15% water, the foam became more brittle as observed when punching cylindrical plugs of the materials (no quantitative analysis has been performed to-date). Results suggest that this new salt fusion approach enables control over the pore interconnectivity and architecture.

Foam characterization: Foam characterization was performed on tBA-BA scaffolds with a range of compositions to determine the effect of composition on thermal properties and shape memory behavior. For these experiments, foams were fabricated using the original salt fusion technique (**Chapter 4**) and not the approach described above. TGA analysis of foams with compositions of 95-5, 87-13, 83-17, and 79-21 tBA-BA revealed similar thermal degradation profiles independent of composition, and salt was extracted from all foams (**Figure A6-2a**). DSC

analysis showed that by varying the composition of the foams, a range of T_g from 26.3 °C to 45.1 °C achieved for dry foams (**Figure A6-2b, Table A6-2**). Foams with a composition of 79tBA-21BA had a T_g near room temperature, and as a result this is the lowest composition that can be used for testing SMACS; lower T_g would not maintain a stable programmed shape at room temperature.

Shape memory characterization of foams with different compositions showed all compositions had excellent shape fixing and shape recovery (**Figure A6-3a**). Additionally, the onset of recovery temperature decreased as the amount of tBA in the composition decreased (**Figure A6-3b**). Inspection of the recovery kinetics of programmed scaffolds hydrated at 37 °C showed that decreasing the amount of tBA in the system increased the recovery speed (**Figure A6-4**). The 79tBA-21BA sample recovered most of its programmed strain within the first minute; by 9 minutes, the 83tBA-17BA had also fully recovered; the samples with the higher T_g (e.g. 95-5) only recovered a small percentage of their strain within the first 9 min. This demonstrates that the expansion rate during cell seeding can be controlled, which may affect cell infiltration into the scaffolds.

Cell Imaging: Employing the methods discussed above, we were able to successfully construct in-focus images of entire foam cross-sections following cell culture (**Figure A6-5**). Although quantitative analysis has not yet been completed, qualitatively we can see a difference between the 79tBA-21BA sample programmed 75% and the 95tBA-5BA sample programmed 75%, with the 79tBA-21BA containing more cells in the interior for all salt fusion conditions. This suggests that recovery kinetics play a role in cell seeding, as the 79tBA-21BA recovers on

the order of minutes, while the 95tBA-5BA recovers on the order of hours. We are currently finalizing an automated approach in MATLAB to analyze these results.

Conclusion

Here we have developed a series of methods to test how SMP recovery kinetics, SMP compression ratio, and pore interconnectivity can influence SMACS. Additionally, we have reported a new salt fusion approach that resulted in increased and controllable pore interconnectivity. Mechanical testing should be performed on scaffolds fabricated with varying degrees of salt fusion, as the mechanical properties are expected to decrease with increased interconnectivity. Current efforts are focused on developing an automated image analysis algorithm in MATLAB to analyze the reconstructed images of cell nuclei in the foam cross-section.

References

- [1] Holy CE, Shoichet MS, Davies JE. Engineering three-dimensional bone tissue in vitro using biodegradable scaffolds: investigating initial cell-seeding density and culture period. *Journal of biomedical materials research*. 2000;51:376-82.
- [2] Mauck RL, Seyhan SL, Ateshian GA, Hung CT. Influence of seeding density and dynamic deformational loading on the developing structure/function relationships of chondrocyte-seeded agarose hydrogels. *Annals of biomedical engineering*. 2002;30:1046-56.
- [3] Li Y, Ma T, Kniss DA, Lasky LC, Yang ST. Effects of filtration seeding on cell density, spatial distribution, and proliferation in nonwoven fibrous matrices. *Biotechnology progress*. 2001;17:935-44.

- [4] Kim B-S, Putnam AJ, Kulik TJ, Mooney DJ. Optimizing seeding and culture methods to engineer smooth muscle tissue on biodegradable polymer matrices. 1998.
- [5] Unsworth J, Rose F, Wright E, Scotchford C, Shakesheff K. Seeding cells into needled felt scaffolds for tissue engineering applications. *Journal of Biomedical Materials Research Part A*. 2003;66:425-31.
- [6] Martin I, Wendt D, Heberer M. The role of bioreactors in tissue engineering. *TRENDS in Biotechnology*. 2004;22:80-6.
- [7] Wendt D, Marsano A, Jakob M, Heberer M, Martin I. Oscillating perfusion of cell suspensions through three-dimensional scaffolds enhances cell seeding efficiency and uniformity. *Biotechnology and bioengineering*. 2003;84:205-14.
- [8] Xie J, Jung Y, Kim SH, Kim YH, Matsuda T. New technique of seeding chondrocytes into microporous poly (l-lactide-co- ϵ -caprolactone) sponge by cyclic compression force-induced suction. *Tissue engineering*. 2006;12:1811-20.

Table A6-1. Sample groups used for each salt fusion template for cell culture. A total of 7 groups were used for each salt fusion condition investigated (6%, 10%, 15% water), for a final total of 21 groups for the cell experiments.

	tBA-BA	Programmed Strain (%)
	95-5	75
	87-13	75
	79-21	75
	79-21	50
	79-21	25
Positive Control	79-21	0
Negative Control	79-21	0

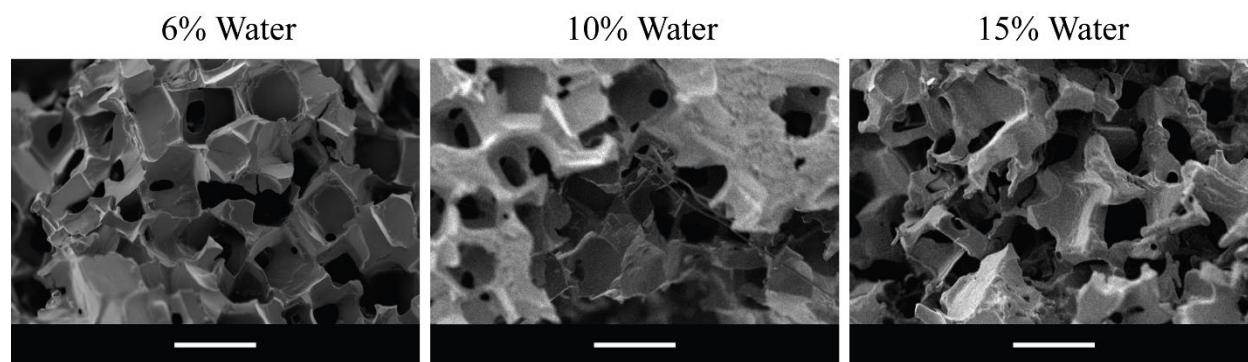


Figure A6-1. SEM micrographs of SMP foams fabricated using new salt fusion technique. Salt fusion with 6% water mixed in resulted in cuboidal pores with small interconnection openings; with 10% water, pores had larger interconnections sizes and were more open; increasing the water to 15% resulted in highly interconnected pores with a loss in cuboidal morphology. Scale bars are 500 μm .

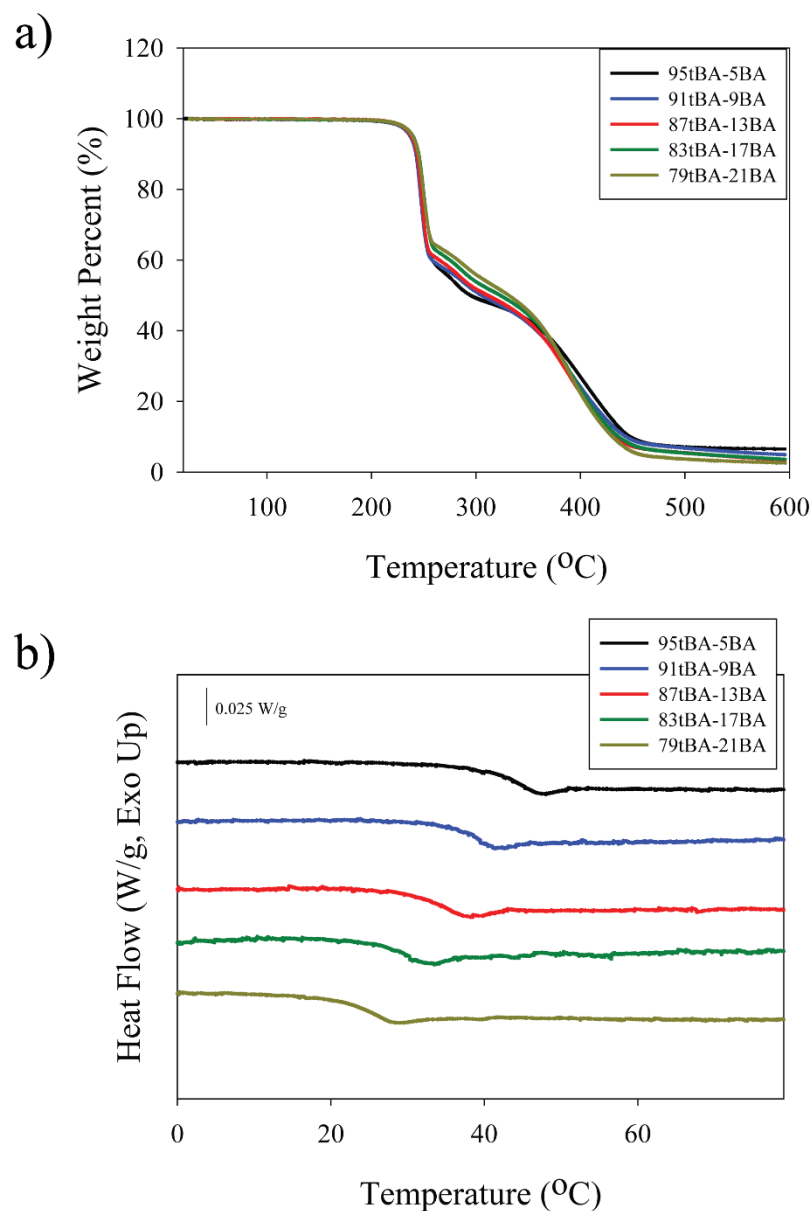


Figure A6-2. Thermal properties of tBA-BA foams with different compositions. (a) TGA analysis reveals salt is completely extracted for all foams; (b) DSC 2nd heat traces show a trend of decreasing T_g with decreasing tBA weight-%.

Table A6-2. Composition effect on Dry and Wet T_g. A range of T_gs were achieved from 45.1 °C to 26.3 °C in the dry state, and a range of 38.3 °C to 20.3 °C in the wet state.

tBA-BA	Dry T _g (°C)	Wet T _g (°C)
95-5	45.1	38.3
91-9	39	34.9
87-13	35.1	31.2
83-17	29.9	24.7
79-21	26.3	20.3

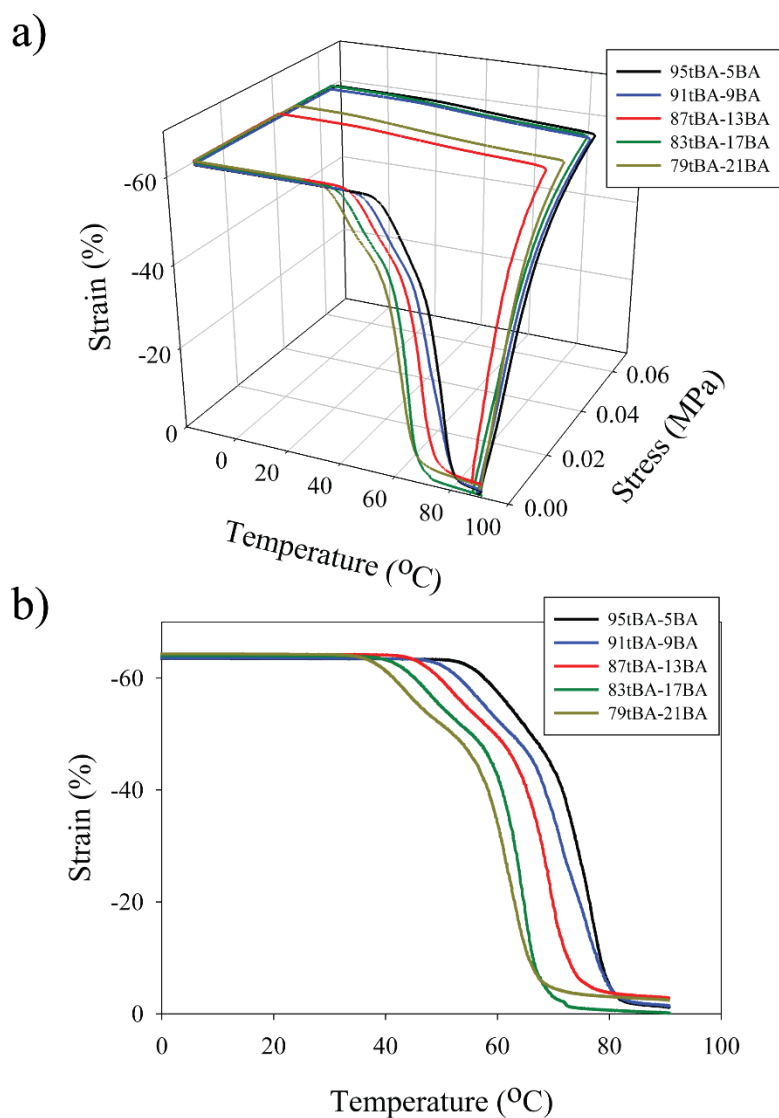


Figure A6-3. Shape memory behavior of tBA-BA foams with different compositions. (a) compressive one-way shape memory traces show all foams have excellent shape fixing and shape recovery; (b) recovery profiles of foams with different compositions shows that as tBA weight-% decreases, the onset of recovery temperature also decreases.

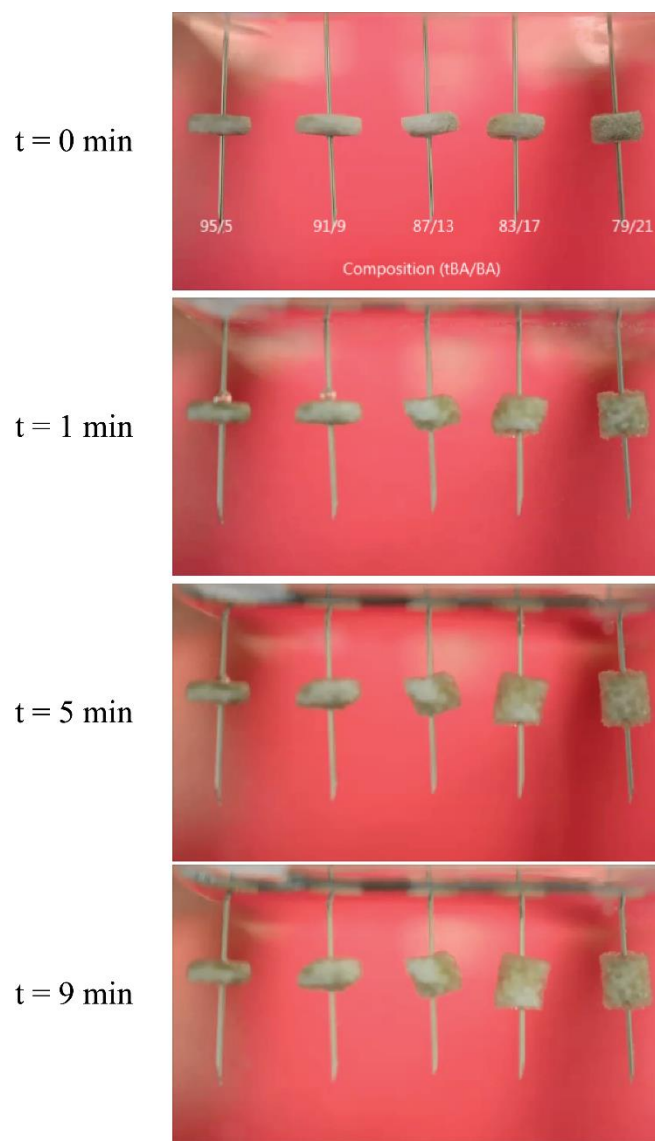


Figure A6-4. Recovery of tBA-BA foams in 37 °C water. As the amount of tBA in the foams decreases, the recovery rate at 37 °C increases; foams with the lowest tBA composition (79-21) recovered most of the programmed strain within one min; foams with the highest tBA composition (95-5) had minimal recovery within the first 9 min.

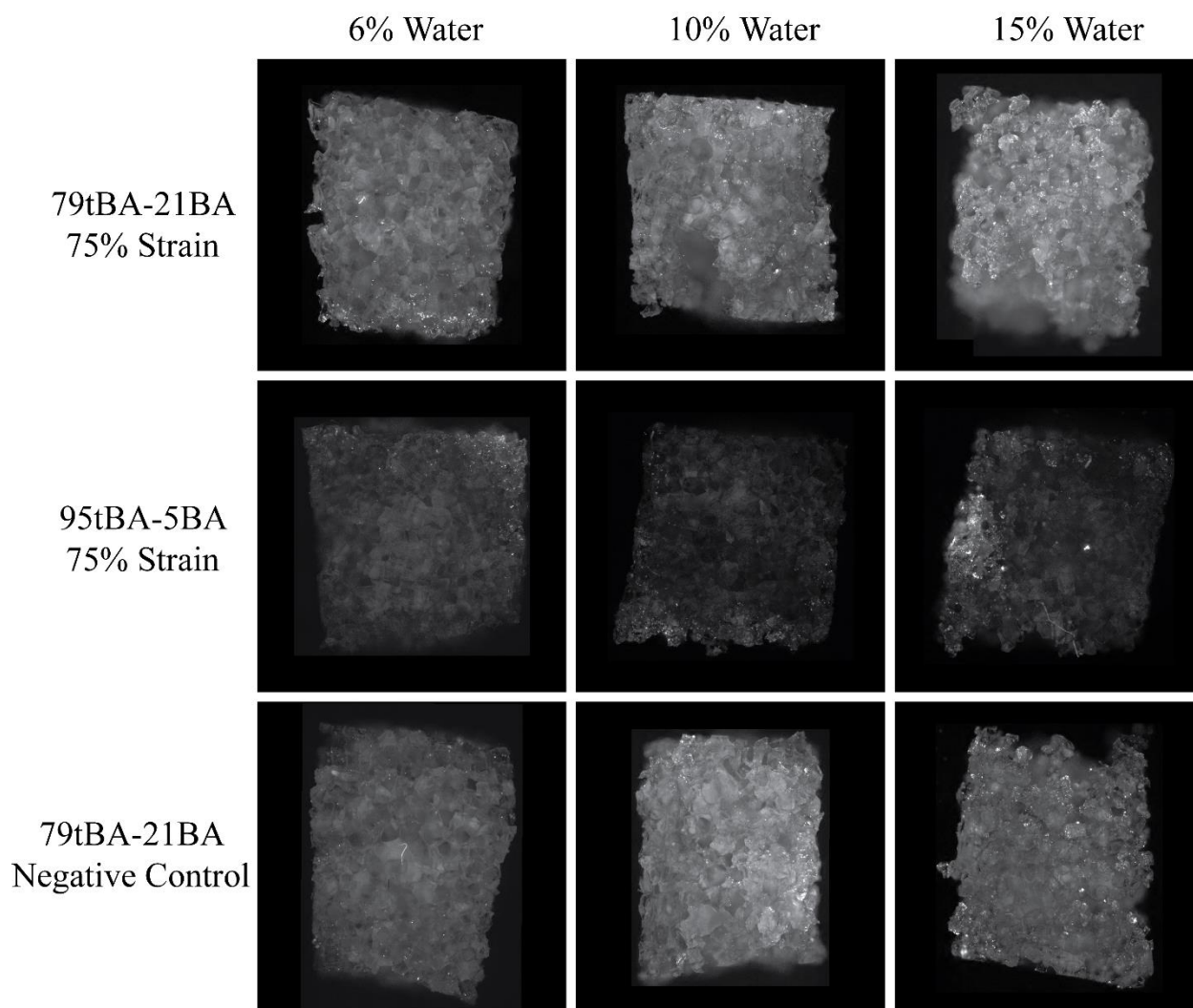


Figure A6-5. Example cell infiltration micrographs after stitching. The small bright circles in each image are cell nuclei. Qualitatively, an increase in cell infiltration with increasing water-% was observed. Additionally, programmed 79tBA-21BA foams had increased cell infiltration compared to programmed 95tBA-5BA foams.

VITA

NAME OF AUTHOR: Richard M. Baker

PLACE OF BIRTH: Cincinnati, Ohio, USA

DATE OF BIRTH: February 21st, 1987

EDUCATION:

B.S. in Biomedical Engineering, Rose-Hulman Institute of Technology (2009)

B.S. in Mechanical Engineering, Rose-Hulman Institute of Technology (2009)

Ph.D. in Bioengineering, Syracuse University (2009-present)

PUBLICATIONS:

Tan C, **Baker RM**, and Mather PT. Shape memory foam composites as self-biasing reversible actuators. Manuscript in preparation.

Baker RM*, Tseng LF*, Wang J*, Mather PT, and Henderson JH. Osteogenic differentiation in shape memory polymer foams and electrospun fiber mats. Manuscript in preparation

Baker RM*, Tseng LF*, Oest ME, and Henderson JH. Self-deploying shape memory polymer scaffolds for grafting and stabilization of complex fractures: a mouse femoral segmental defect study, *in revision*.

Robertson J, Torbati A, Rodriguez ED, Mao Y, **Baker RM**, Qi J, Mather PT. Mechanically programmed shape change in laminated elastomeric composites. *Soft Matter*, 2015.

Birjandi Nejad H; **Baker RM**; Mather PT. Preparation and characterization of triple shape memory composite foams. *Soft Matter*, 2014.

Baker RM*, Brasch ME*, Manning ML, and Henderson JH. Automated, contour-based tracking and analysis of cell behaviour over long timescales in environments of varying complexity and cell density. *Journal of the Royal Society Interface*, 2014.

Baker RM*, Davis KA*, and Henderson JH. Shape memory applications in mechanobiology and bone repair. In: Biomaterials for bone regeneration: novel techniques and applications, Woodhead Publishing Series in Biomaterials, Edited by P. Dubruel and S. Van Vlierberghe, 2014.

Baker RM, Henderson JH, and Mather PT. Shape memory poly(epsilon-caprolactone)-co-poly(ethylene glycol) foams with body temperature triggering and two-way actuation. *Journal of Materials Chemistry B*, 2013.

Baker RM*, Yang P*, Henderson JH, and Mather PT. In vitro wrinkle formation via shape memory dynamically aligns adherent cells. *Soft Matter*, 2013.